EXTENSIONAL TECTONICS IN A CONVERGENT MARGIN SETTING: DEFORMATION OF THE NORTHERN CHILEAN FOREARC

A Dissertation

Presented to the Faculty of the Graduate School

of Cornell University

in Partial Fulfillment of the Requirements for the Degree of

Doctor of Philosophy

by

John Peter Loveless

January 2008

EXTENSIONAL TECTONICS IN A CONVERGENT MARGIN SETTING: DEFORMATION OF THE NORTHERN CHILEAN FOREARC

John Peter Loveless, Ph.D.

Cornell University 2008

The Coastal Cordillera of the northern Chilean forearc overlies a portion of the plate boundary where great subduction zone earthquakes originate. Geological structures in this region exhibit deformation that has accumulated over millions of years as a result of the subduction earthquake cycle. These structures primarily demonstrate extension in the direction of convergence between the Nazca and South American plates. The details of the permanent strain field have significant implications for the long-term interaction between the forearc and subduction zone processes. In this thesis, I combine observations of faults and surface cracks, radar interferometric analyses of ground deformation, and numerical modeling of the stress, strain, and displacement fields produced in the forearc by the subduction zone earthquake cycle to provide new insight into this interaction.

I present spatially-complete maps of meter-scale surface cracks throughout the forearc. Through analysis of crack strikes, morphological observations, and elastic dislocation modeling of stress fields generated by subduction zone earthquakes, I find that the distribution of cracks is consistent with formation by repeated interplate seismic events. Concentrations of stress along upper plate faults can explain the enhanced opening of cracking. Movement on the upper plate faults themselves also results from stresses related to the subduction earthquake cycle. Models pre-

sented in this thesis show consistency between the complicated deformation field expressed by the forearc structures and the varying stress fields associated with the subduction zone. Interseismic deformation encourages failure on normal faults, while strong underthrusting earthquakes are capable of pushing these faults toward either normal or reverse failure. Minor reverse motion superimposed on dominantly normal faults is described for several locations in the forearc. The dependency of the upper plate stress field on the distribution of subduction zone strain accumulation and release and the sense of forearc faulting have implications for fault mechanics. The style of permanent deformation observed in the forearc can be used to constrain the distribution of interseismic strain accumulation and coseismic slip. Additionally, because the upper plate faults respond to low-magnitude stress perturbations induced by the seismic cycle, the absolute level of stress on these structures must be very low.

BIOGRAPHICAL SKETCH

John (Jack) Peter Loveless was born May 30, 1980 in Northampton, Massachusetts to Joan and Peter Loveless. As young children, Jack and his older sister, Julie, spent much time flipping through the pages of a world atlas with their father, pointing out places with interesting names and gaining an appreciation of geography. In second grade, a student teacher named Ms. Sullivan introduced Jack's class to basic concepts of astronomy, including the names, relative locations, and characteristics of the then 9 planets. These facts fascinated Jack, which became so apparent to Ms. Sullivan that she gave him "My Very First Book About Space," parts of which he memorized. Despite his fascination with geography and astronomy, Jack's early thoughts of potential careers were dominated by visions of playing Major League Baseball, a naïve dream that was nurtured by his brief brush with fame after being the winning pitcher in the Northampton Little League 1992 city championship game (Eagles 19, Elks 0).

While attending Northampton High School, Jack and longtime friend Daniel Gray were sent to the hospital with minor wounds after a physics class experiment gone awry. Not to be thwarted by piddling shards of cast iron flung from a rotating electric motor and imbedded in their skin, Jack and Dan both pursued scientific studies in college. Earlier in high school, Jack was leaning towards majoring in astronomy, but his burgeoning love of the outdoors — fed by backpacking and climbing trips with Dan — pointed him in the direction of geology.

After graduating from high school in 1998, Jack followed his sister to college at the University of New Hampshire, where he quickly declared geology as a major but then proceeded to fall asleep during the majority of introductory lectures. This habit was short lived, however, and Jack soon became engrossed in his course-

work, though DJing at WUNH-FM competed for his time and attention. In 2000, following his sophomore year, he was hired by Professors Wallace Bothner and Jo Laird to map the Epping, NH quadrangle for the U.S. Geological Survey's EDMAP program. Later that summer, he served as the field assistant for then Boston University PhD. student, now James Madison University Professor Steven Whitmeyer in the San Luis province of Argentina. Having become quite fond of structural geology through courses with Dr. Bothner and then having been introduced to the wonders of South America, Jack decided that seeking a graduate program in Andean tectonics would be a good idea. Professor Richard Allmendinger at Cornell graciously agreed, and following Jack's graduation with a B.S. in Geology from UNH in 2002, thankfully avoiding academic physical harm, he moved to Ithaca to being his doctoral studies.

Upon Cornell's acquisition of high-resolution satellite imagery for the Salar Grande region of northern Chile in fall 2002, Jack began the first part of his graduate training: the art of clicking a mouse to trace linear features on a computer screen. After five years (almost a tenth of which were spent in South America) and many mouse clicks, Jack will return, along with his fiancée Claire Lobdell and their two cats, to the Commonwealth in the fall of 2007 to begin a post-doctoral position with Professor Brendan Meade at Harvard University.

In loving memory of my father, Peter Loveless, who taught me, amongst so much else, to appreciate and question the natural world, and to persevere — skills that have been essential not only for completing my dissertation, but for living and enjoying life in general.

ACKNOWLEDGEMENTS

Many people have made my experience at Cornell extraordinarily enjoyable and educational, including the four members of my thesis committee. First and foremost, I thank my principal advisor, Richard Allmendinger, for his encouragement, scientific intuition, and patience. From Rick I learned how to think critically, consider all possible solutions to a problem, and present my findings effectively, or at the very least in an aesthetically pleasing manner. I always enjoyed our conversations, whether they were about geology, computers, coffee, politics and public policy, or strategies for teaching and learning effectively. Rick sat through countless practice talks before conferences, encouraged me when the going got tough, and has in many other ways been a fantastic mentor.

Matthew Pritchard has also been a constant source of support and inspiration. His work ethic and well-roundedness make learning from and working with him very enjoyable and rewarding. He walked me through many problems I encountered when processing radar data and did so with the utmost patience and clarity. Matt's insistence on scientific rigor tended to result in a few more analyses carried out or paragraphs written, but I deeply appreciate his instilling this tenet in me. Both Matt and Rick read through many rough drafts of thesis chapters, and I thank them for offering their complementary editing styles to help me to improve my writing.

Bryan Isacks made possible my initial foray into the geology of northern Chile and has been a reliable source of constructive criticism and encouragement. A humble giant of geosciences, Bryan always raised important points during my Andes seminars that forced me to take a more careful look at my interpretations and conclusions. Alan Zehnder set me straight numerous times when it came to

concepts about mechanics. His ability to instantly grasp geological problems and propose mechanical solutions to them consistently impressed me.

Many other professors and researchers in the Department of Earth and Atmospheric Sciences contributed substantially to the education I received at Cornell. Teresa Jordan, John Gephart, and Robert Kay posed thought-provoking and insightful questions during Andes seminars, making these presentations extremely beneficial for shaping my future research. Conversations with Jason Phipps Morgan and Christopher Andronicos made me consider alternate hypotheses to explain my observations and ideas, and I'll fondly remember their shared tendency to strike up very interesting chats with me about my research or related topics. Suzanne Mahlburg Kay was a valuable resource for Andean geology and provided me the fantastic experience of serving as the teaching assistant for the Cornell summer field camp in Argentina. Arthur Bloom was always eager to dig up references pertinent to my research and provide valuable advice, both scientific and grammatical. Muawia Barazangi rarely passed up an opportunity to a) remind me that it's never too late to become a seismologist, b) encourage (i.e., order) me to get married, or c) drink afternoon espresso with me, and he still managed to find time to provide A-plus scientific feedback and an interesting perspective on Middle East politics.

Working in northern Chile gave me the opportunity to experience a new and very different landscape, but more importantly it introduced me to some wonderful scientists without whose assistance and collaboration my work would not exist. Gabriel González at the Universidad Católica del Norte in Antofagasta provided endless logistical and scientific help during my field campaigns and became a good friend, teacher, and honorary member of my thesis committee. He gracefully balanced his departmental, academic, and family duties while willingly making

time to meet with me during my visits to the city. Daniel Carrizo accompanied me in the field on my first trip to Chile and instantly became a great friend and colleague. Conversations with Daniel, whether in his office or over lunch with his welcoming family, were always enjoyable, educational, and thought-provoking. I feel extremely lucky to have Gabriel and Daniel as collaborators and *amigos*. José Cembrano, Felipe Aron, Javier Verdejo, and the staff of the Hotel Tatio also provided much appreciated assistance and hospitality during my visits to Chile.

Francisco "Paco" Gomez (University of Missouri-Columbia) introduced me to radar interferometry, hosted me during a week-long visit to Missouri where I learned the details of processing, joined me in Chile during my first field season, and became a good friend in the process. Many thanks to Michele Cooke (University of Massachusetts-Amherst), who hosted me on several occasions for discussions about boundary element modeling, as well as (now-EAS professor) Rowena Lohman, Yu Xie Mukherjee (Department of Theoretical and Applied Mechanics, Cornell), George Hilley (Stanford University), Kelin Wang (Canadian Pacific Geoscience Centre), David Pollard (Stanford University), Frantz Maerten (IGEOSS), Debi Kilb (University of California-San Diego), Joan Gomberg (USGS), Jürgen Klotz (GFZ-Potsdam), Terry Engelder (Penn State University), and David Ruppert (School of Operations Research and Industrial Engineering, Cornell) for providing technical and/or editorial help during graduate school. I thank Professors Wallace Bothner, Jo Laird, William Clyde, Francis Birch, and Karen Von Damm, all at the University of New Hampshire, for their support and mentoring during my undergraduate years. Without the introduction to geological research that they provided me, I probably wouldn't have continued on to graduate school.

The organizational skills and friendliness of EAS department staff members

Linda Hall, Elena Welch, Lynda Swafford, Nadine Porter, Cathy Lopez, and Amy Colvin made the logisitical details of being a graduate student phenomenally easy. Thanks in particular to Linda for her miracle work in arranging the details of seminar speaker visits, thereby saving me much time. Without the technical expertise of Steve Gallow, Mike Brodsky, and Aaron Wade, no computers used in this thesis would be running nearly as smoothly as they are. Thanks also to Steve for sharing stories of his running adventures, and in general for making Snee Hall a great place to spend my days.

Rick Allmendinger told me in my first few days of graduate school that the relationships with my peers would be what truly get me through my time at Cornell, and now having gotten through it, I couldn't agree more. Doctors Gregory Hoke and Brian Ruskin took me under their wings early in my first semester, and through our shared late-night slap-happiness, rampant acronym construction, and coffee guzzling, I quickly felt at home in Ithaca. Adam Goss, Neil McGlashan, and Stephanie Devlin — my fellow Entering Class of '02ers — have provided five wonderful years of friendship and scientific exchange. Néstor Cardozo, Holly Caprio, and Phoebe Judge have been fantastic people with whom to share the Structure Lab. Thanks also to Holly for assisting me in the field in 2004 and 2006. Thanks to Jacob "Cubbie" Moore, Greg Kirkpatrick, Carrie Brindisi, Chris Garvin, Meghan Herz, and Herdis Schopka for their friendship and company on numerous cycling adventures around the Finger Lakes region. Peter Nester, Gabriela Depine, and Joey Rosario, in addition to being good friends, were quality roommates in various Chilean hotels. Post-doc. Noah Finnegan and I bonded through countless discussions about ROI_PAC, Matlab, and other facets of geodynamic life, and I appreciate the advice he gave me concerning post-graduate school plans. Jordan

Garroway, an undergraduate who spent many hours searching for cracks in the virtual northern Chilean desert, consistently impressed me and was a pleasure to have working in the lab. Julie Pett-Ridge, Louise McGarry, Melissa Stephenson, Danielle Glasgow, Chao Shi, Katie Tamulonis, Tiffany Tchakirides, Ursula Smith, Dave Wolf and others also became great friends and colleagues, and I look forward to keeping in touch. While not a graduate student at Cornell, Dan Gray (University of Rochester) and I went through graduate school concurrently. As he has for over a decade, Dan helped me through tough times, in part by accompanying me on much-needed stress-relieving jaunts to Salmon River Gorge, the Gunks, and the Adirondacks. During the car rides to these places, we drew several who-would've-thought parallels between InSAR imaging of earthquake deformation and *in vivo* laser imaging of simian retinae.

I gratefully acknowledge the financial support that Rick gave me through grants EAR-0087431 and EAR-0337496 from the National Science Foundation. I deeply appreciate the three years of funding I received from NASA Earth Systems Science graduate fellowship NGT5-05R-0000-0064. This fellowship not only provided salary and health insurance but also funded my 2006 field season and allowed for no-cost acquisition of the MODIS data used in Chapter 4. Additional, much appreciated support came from the Department of Earth and Atmospheric Sciences McConnell and Long fellowships, Cornell University Graduate School travel grants, and the Sidney Kaufman travel funds. An International Quality Network grant to Manfred Strecker the Universität Potsdam, Germany sponsored my visit and participation in a short course in 2003, while the Geological Society of America provided me support to attend the Backbone of the Americas meeting in Mendoza, Argentina in 2006 and the annual meeting of its northeast section in 2007. NASA

grant NAG5-11424 (to Bryan Isacks) funded the purchase of the IKONOS satellite imagery instrumental to Chapters 1, 2, and 3. Fondo Nacional De Desarrollo Cientifico y Tecnologico Chile grant 1040389 (to Gabriel González) further funded the research presented in Chapter 1. Financial support for Chapter 4 came in part from NSF grant EAR-0510719 (to Matt Pritchard).

My entire family — both immediate and extended — has been a constant source of enthusiasm and inspiration. Infinite thanks to my parents, Joan and Peter Loveless, for putting me through college and perpetually encouraging me, and to my sister Julie, stepmother Cindy, and stepbrother Tyler for their support. My uncles Mike and Norm, with their natural sense of scientific curiosity, were always keen on hearing about my research at family gatherings, and I've appreciated their encouragement particularly in the past several months. Finally, I thank Claire Lobdell for her endless patience, compassion, interest in my work, and companionship. For the past four and a half years, Claire's confidence in me has allowed me to face challenges in all facets of life; for this I am eternally grateful.

TABLE OF CONTENTS

LIST OF TABLES

LIST OF FIGURES

CHAPTER 0

INTRODUCTION

0.1 Background

The world's largest earthquakes occur in subduction zones. As an oceanic plate subducts beneath an overriding continent, frictional coupling between the two plates results in the accumulation of elastic strain, which is occasionally released through underthrusting earthquakes. While geodetic and seismic data provide detailed information about the contemporary behavior of subduction zones, different types of analyses are required to understand subduction tectonics over long periods of time. In this thesis, I discuss extensional structures in the coastal regions of northern Chile, which represent the surficial expression of the Andean subduction earthquake cycle accumulated over time scales ranging from a single earthquake to millions of years. An understanding these structures and their connections to the underlying subduction zone processes allows for a more complete classification of the seismic cycle as it evolves through time.

The Andean margin defines one end-member model of subduction zones (*Uyeda and Kanamori*, 1979) in which the oceanic plate subducts at a shallow angle (20°–30°) beneath of the continental plate. Countless great earthquakes have ruptured the plate boundary, including the 1960 $M\sim$9.5 Valdivia earthquake in central Chile — the largest earthquake ever recorded. Much of the portion of the South American plate overlying the seismogenic region of the plate interface, where underthrusting earthquakes occur, lies offshore, inhibiting studies of the surficial effects of plate boundary seismicity.

The Coastal Cordillera in northern Chile, however, is an ideal locality to study

the surface expression of plate tectonic processes. The mountain range overlies the downdip extent of the locked plate boundary — defined by kinematic modeling of geodetic data (e.g., *Norabuena et al.*, 1998; *Bevis et al.*, 2001; *Klotz et al.*, 2001; *Khazaradze and Klotz*, 2003) and spatial analysis of underthrusting earthquakes (e.g., *Bevis and Isacks*, 1984; *Cahill and Isacks*, 1992; *Tichelaar and Ruff*, 1991) — where strain accumulates between great earthquakes and is catastrophically released during these events. The hyperarid climate of the Atacama Desert, which has prevailed for at least the last 6 Myr (*Hartley and Chong*, 2002) if not more than 13–18 Myr (*Dunai et al.*, 2005; *Rech et al.*, 2006), creates a unique set of geological conditions that simultaneously facilitate and complicate structural observation. Much of the region is covered in gypsum-indurated sediment, which creates a durable surface crust capable of preserving small-scale features for long periods of time, particularly given the lack of precipitation. Neotectonic studies of the region thus rely on tectonic geomorphology, using the present topography as a proxy for accumulated tectonic deformation. The lack of vegetation permits an uninhibited view of the surface, which is ideal for making both field and remote sensing based observations.

The aridity of the region permits the blanket of regolith to cover bedrock features, hiding traditional structural geology data such as exposed fault planes and slip indicators. Furthermore, the erosion constants required for morphological dating of fault scarps are unknown for the Atacama Desert, complicating the use of this technique to assess fault activity (e.g., *González and Carrizo*, 2003). The lack of vegetation translates into a lack of charcoal preserved in stratigraphic layers, eliminating radiocarbon dating of horizons offset by motion on faults as a candidate technique for assessing the age of neotectonic structures.

0.2 Worldwide examples of forearc deformation

The kinematics of upper plate faults have been described for several forearcs worldwide (Figure 0.1). The lateral component of oblique convergence in Japan and Sumatra is accommodated by dominantly dextral motion on upper plate faults, notably the Median Tectonic Line (Japan) and Sumatra Fault (e.g., *Fitch*, 1972; *Genrich et al.*, 2000; *Tabei et al.*, 2003). Where the relative plate convergence is more orthogonal, as is the case in New Zealand (*Cashman and Kelsey*, 1990; *Chanier et al.*, 1999), Central America (*Kuijpers*, 1980; *McIntosh et al.*, 1993; *Marshall and Anderson*, 1995), and along much of the Andean margin (*Arabasz*, 1971; *Delouis et al.*, 1998; *González et al.*, 2003; *Melnick et al.*, 2006, this thesis), dip slip forearc faulting is more commonly observed. With the exception of northern Chile and southern Peru, the more humid climates of these forearcs reduces the quality of long-term preservation of upper plate structures. Nonetheless, the cited studies provide additional examples of observable structures that represent deformation caused by subduction zone processes.

0.3 Short- and long-term records of the subduction zone seismic cycle

Different types of data are required in order to characterize the surficial expression of the subduction zone seismic cycle on a variety of time scales (Figure 0.2). Geodetic and seismic observations provide detailed information regarding the contemporary effects of the subduction zone seismic cycle. Such data are used to infer the distribution of strain accumulation on the subduction interface, the patterns of moment release during strong subduction earthquakes, and the distribution of

Figure 0.1: Map of the Pacific Rim region providing examples of upper-plate fault kinemetics for several forearcs. Black arrows show approximate direction of relative plate convergence at each subduction zone, and captions indicate the style of forearc deformation observed. See text for more details.

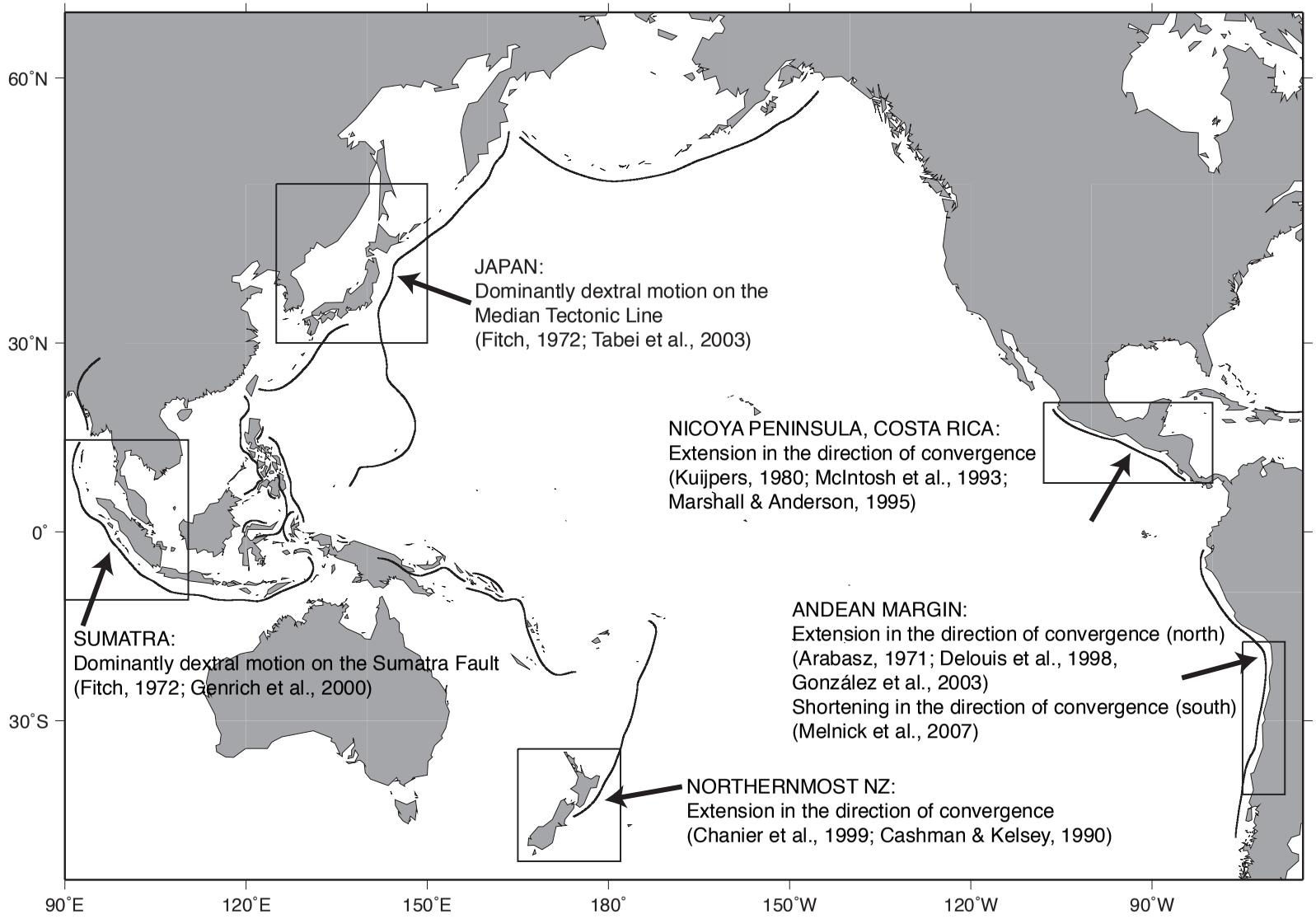
60˚N
30˚N
0˚
30˚S
90˚E
120˚E
150˚E
180˚
150˚W
120˚W
90˚W
JAPAN:
Dominantly dextral motion on the
Median Tectonic Line
(Fitch, 1972; Tabei et al., 2003)
NICOYA PENINSULA, COSTA RICA:
Extension in the direction of convergence
(Kuijpers, 1980; McIntosh et al., 1993;
Marshall & Anderson, 1995)
SUMATRA:
Dominantly dextral motion on the Sumatra Fault
(Fitch, 1972; Genrich et al., 2000)
ANDEAN MARGIN:
Extension in the direction of convergence (north)
(Arabasz, 1971; Delouis et al., 1998,
González et al., 2003)
Shortening in the direction of convergence (south)
(Melnick et al., 2007)
NORTHERNMOST NZ:
Extension in the direction of convergence
(Chanier et al., 1999; Cashman & Kelsey, 1990)

aftershocks and postseismic phenomena, which are important for constructing a seismic hazard analysis for a given region. Geodetic and seismic methods place tight constraint on these patterns. Four GPS networks in northern Chile have captured a snapshot of the horizontal deformation field caused by the interseismic period, as well as several subduction zone earthquakes (*Ruegg et al.*, 1996; *Norabuena et al.*, 1998; *Klotz et al.*, 1999; *Ruegg et al.*, 2001; *Bevis et al.*, 2001; *Brooks et al.*, 2003; *Chlieh et al.*, 2004; *Pritchard et al.*, 2007). Interferometric Synthetic Aperture Radar (InSAR) complements these measurements, providing a more spatially-complete picture of co- and postseismic deformation related to strong earthquakes (*Pritchard et al.*, 2002; *Xia et al.*, 2003; *Chlieh et al.*, 2004; *Pritchard et al.*, 2006; *Pritchard and Simons*, 2006; *Pritchard et al.*, 2007). Local seismic networks around the Antofagasta region have yielded additional information about the nature of subduction zone seismicity (*Comte et al.*, 1994; *Delouis et al.*, 1996, 1997; *Husen et al.*, 1999; *Sobiesiak*, 2004).

Given the 100–150 year recurrence interval of great subduction zone earthquakes along the Andean margin (*Dorbath et al.*, 1990; *Comte and Pardo*, 1991), a complete seismic cycle has yet to be recorded by modern instrumentation. Historical records allow for estimation of earthquake size and rupture extent for the past 3–4 seismic cycles, but the low population density throughout much of northern Chile limits the amount of information that can be extracted from these reports. It appears, however, that great earthquakes rupture distinct segments of the plate boundary, and the boundaries of these segments have remained relatively constant for at least the past several earthquake cycles (*Comte and Pardo*, 1991), indicating that the properties of the subduction interface are similar from one earthquake cycle to the next.

Deformation on thousand- to million-year time scales, manifested in paleoseismological data, changes in the geomorphology, and geologic structures in the forearc, provides a longer-term record of subduction zone behavior (Figure 0.2). Several studies have focused on the neotectonics of the Antofagasta-Paposo region (23°–25°S latitude) in the northern Chile forearc and have found that, in general, the structural signal is typified by extension in the direction of plate convergence, represented by normal slip on north striking faults (*Arabasz*, 1971; *Niemeyer et al.*, 1996; *Delouis et al.*, 1998; *González et al.*, 2003; *González and Carrizo*, 2003). Farther north in the Salar Grande region (21°S), dextral-normal slip on northwest striking faults is kinematically consistent with this deformation regime (*González et al.*, 2003). A suite of east-west striking reverse faults between 19° and 21.6°S shows that permanent strain in the forearc not only indicates margin-normal extension, but also margin-parallel shortening (*Allmendinger et al.*, 2005). Near the city of Caldera (27°S), *Marquardt et al.* (2004) describes faults accommodating NW-SE directed extension, while *Heinze* (2003) describes ENE-WSW directed extension shown by normal faulting between 30° and 31°S. Substantially farther south (37°S), *Melnick et al.* (2006) describe active reverse motion on north-south striking crustal faults, indicating an along-strike change in the modern intraplate strain regime.

The change in the long-term strain pattern from north to south is consistent with variations in the extent of interplate locking inferred from modeling of GPS data. Using a network spanning 18°–42°S, *Khazaradze and Klotz* (2003) find that an interplate zone locked to ∼35 km fits GPS data between 25°–30°S, while an increased extent of coupling — to 50 km depth — is required to match velocities south of 30°S. As noted by *Savage* (1983), a wider extent of strain accumulation

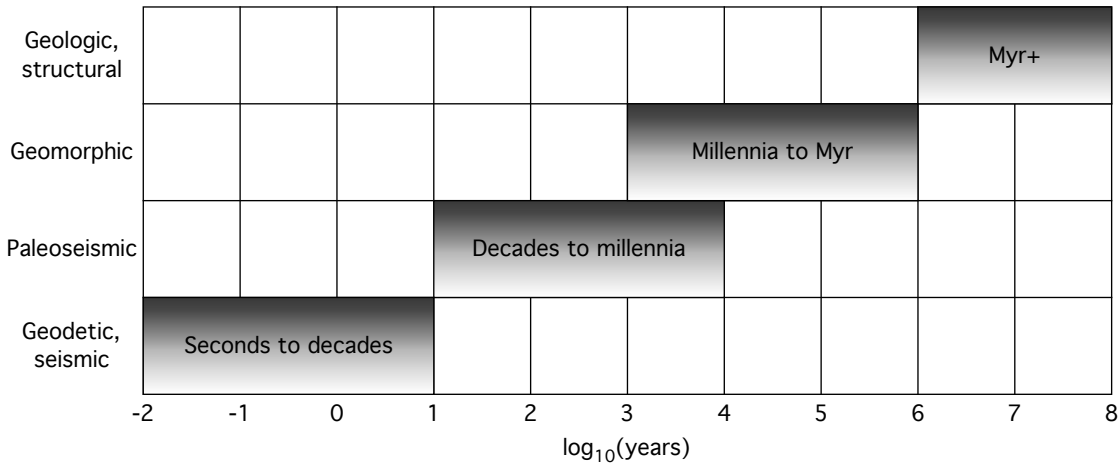

Figure 0.2: Deformation induced at the surface by the subduction zone seismic cycle is captured by different data types on different time scales. Seismic and geodetic data record snapshots of modern deformation, ranging from that which takes place during an earthquake to one complete seismic cycle. Paleoseismology characterizes the past several seismic cycles, while changes induced by tectonic processes on the regional geomorphology occur on millennial to million-year time scales. Geologic structures record deformation accumulated over million-year time scales. In all cases, the time periods recorded by each data type are not as distinct as shown here; upper-plate fault slip triggered by a recent earthquake, for example, blends the shortest- and longest-term data types. Modified from *Friedrich et al.* (2003).

on the plate interface results in a surface strain field characterized everywhere by shortening in the direction of convergence. However, given a narrower zone of interplate locking, some regions within the forearc experience extension in that direction (*Savage*, 1983). The along-strike change in locking depth inferred from GPS data (*Khazaradze and Klotz*, 2003) is thus consistent with the long-term strain patterns exhibited by forearc structures.

0.4 Variations in plate interface behavior: Observations and causes

What controls these spatial variations in the inter- and intraplate deformation regimes? The downdip extent of the locked zone is thought to represent a transition from an interface characterized by stick-slip behavior (unstable sliding) to one that shows stable sliding behavior Figure 0.3. While there have been semantic debates regarding what is meant by a "coupled" plate interface (*Wang and Dixon*, 2004a; *Lay and Schwartz*, 2004; *Wang and Dixon*, 2004b), in general, the unstably sliding, locked portion of the interface is considered to represent both the zone over which interseismic strain accumulates, and the zone that generates great subduction earthquakes. The rough equivalence has been shown through studies of the depths of teleseismic underthrusting earthquakes (e.g., *Tichelaar and Ruff*, 1991) and the extent of kinematic coupling that satisfactorily models interseismic GPS velocity measurements at the surface (e.g., *Norabuena et al.*, 1998; *Bevis et al.*, 2001; *Khazaradze and Klotz*, 2003). Within the regions above and below the locked seismogenic zone, the two plates are inferred to slide stably past one another and little interseismic strain is accumulated (Figure 0.3).

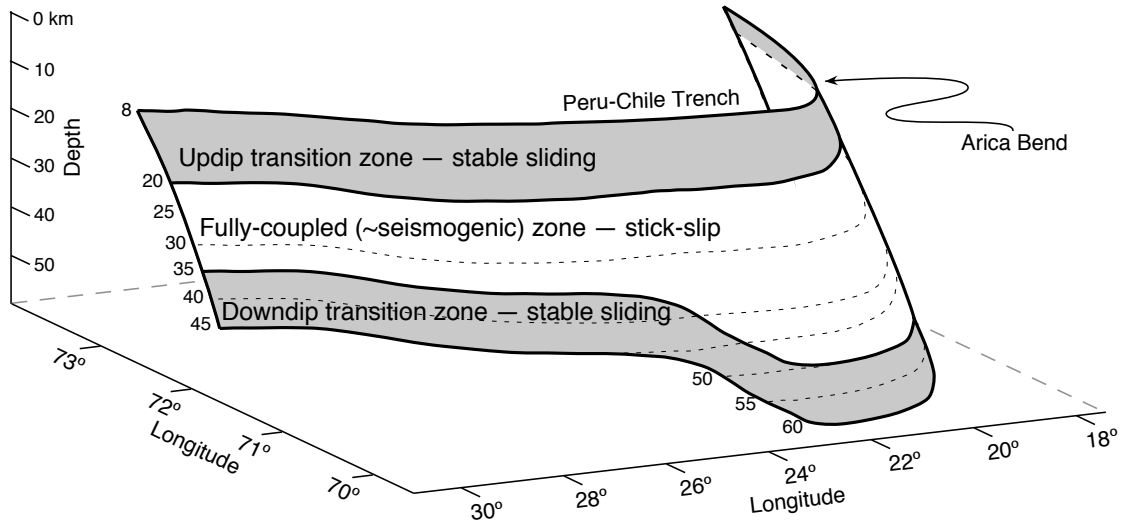

Figure 0.3: Schematic diagram showing the approximate distribution of plate interface conditions along the Andean margin. The two gray regions show zones in which the interplate behavior is characterized by stable-sliding, and so little interseismic strain accumulates. The white region between these zones is the fully-coupled zone, characterized by unstable sliding or stick-slip behavior. This region is interpreted to approximately represent the extent of the seismogenic zone where great earthquakes originate.

The depths at which these transitions occur is thermally regulated; stick-slip behavior dominates the interface for temperatures between about 100°C and 350°C, with stable sliding occurring below and above this range (*Oleskevich et al.*, 1999). Thus, variations in the thermal regime along a subduction zone would give rise to changes in the extent of interplate coupling. Factors that influence the depth of the 350°C isotherm, and therefore the downdip extent of interplate coupling, include the age of the subducting oceanic plate, the subduction zone geometry, the thickness of sediments atop the slab, which serve as insulation between the two plates, the plate convergence rate, and the amount of radiogenic heat production in the overriding plate (e.g., *Oleskevich et al.*, 1999). *Khazaradze and Klotz* (2003, and references therein) argue that both the age of the plate and the thickness of insulating sediments vary along the strike of the Andean margin in a way that disagrees with the modeled changes in locking extent. Following the relationships of *Oleskevich et al.* (1999), the modeled north-to-south increase in locking depth should reflect an increase in the age of the Nazca Plate and/or a decrease in sediment cover, which are opposite the actual characteristics. *Khazaradze and Klotz* (2003) instead propose that a "slab anchor" force, which increases the *degree* but not necessarily the *extent* of plate coupling, is responsible for the changes invoked in their model.

Additional observation of along-strike variations in the nature of interplate coupling relates the interface behavior to the forearc gravity anomaly field. By analyzing several subduction zones worldwide, *Wells et al.* (2003) and *Song and Simons* (2003) found a correlation between the slip distribution of great earthquakes and the spatial extent of negative anomalies in the gravity field. The negative anomalies, which mark the locations of forearc basins (negative topography),

tend to overlie regions that experienced the greatest magnitude of slip during recent subduction zone earthquakes. *Song and Simons* (2003) interpret the negative anomalies in gravity and topography to reflect regions that have been depressed through time by strong coupling of the underlying plate interface. *Bürgmann et al.* (2005) extend this hypothesis to their analysis of interseismic strain accumulation along the Kamchatka subduction zone. Based on dislocation modeling of GPS data, they find that portions of the plate interface characterized by greater coupling are roughly correlated with negative gravity anomalies, and less coupled regions coincide with positive gravity anomalies. The forearc gravity anomaly field is a long-lived physical characteristic, yet it shows remarkable predictive power in terms of the spatial variation in interseismic strain accumulation and coseismic moment release, which suggests that the physical properties of the subduction interface as measured on decadal time scales by geodesy are consistent over long periods of time.

0.5 Thesis outline

This thesis combines observational and theoretical approaches to assess further the compatibility between the short-term stress fields produced by the subduction earthquake cycle and the accumulated deformation represented by forearc structures. This strategy incorporates the type of field- and remote sensing observations that have described the neotectonic behavior of the region (*Arabasz*, 1971; *Niemeyer et al.*, 1996; *Delouis et al.*, 1998; *González et al.*, 2003; *González and Carrizo*, 2003; *Loveless et al.*, 2005) with the regional-scale modeling of subduction zone processes used to model geodetic data (e.g., *Ruegg et al.*, 1996; *Norabuena et al.*, 1998; *Klotz et al.*, 1999; *Pritchard et al.*, 2002; *Xia et al.*, 2003; *Chlieh et al.*,

2004; *Pritchard et al.*, 2006). Whereas the geodetic modeling studies sought to fit measurements of surface displacement, I use modeling to calculate the stress fields generated by subduction processes and explore their relationships with the permanent strain markers of the forearc.

Chapters 1–3 focus on meter-scale cracks that are preserved in the gypcrete surface crust. Despite their small size, the ubiquity of these features makes them useful for characterizing stress fields throughout the region. Chapter 1 provides a description and interpretation of over 37,000 of these features that we mapped using high-resolution IKONOS satellite imagery over the Salar Grande region. This chapter was published in the December 2005 issue of *Geology*. Gregory Hoke assisted both in the digital mapping of the cracks, as well as with initial field studies. Richard Allmendinger, Gabriel González, Bryan Isacks, and Daniel Carrizo all provided valuable discussions, conceptual guidance, assistance in the field and/or lab, and editorial comments on the manuscript.

In Chapter 2, I present a more detailed analysis of the cracks in the Salar Grande region. I used field- and remote sensing-based studies to reveal various characteristics of these features: the magnitude of finite strain they accommodate, relative age information, and the density of their distribution. One clear pattern seen in the distribution of cracks is their spatial correlation with upper plate fault scarps. From field observations, it is apparent that cracks along fault traces show enhanced opening. Using boundary element models, I find that the faults, as discontinuities in the Earth's crust, perturb the regional stress field produced by the seismic cycle; these stress perturbations can explain the enhancement of cracking. This chapter is in preparation for submission to the *Journal of Structural Geology*.

Chapter 3 provides a regional summary of crack observations, documenting

their occurrence throughout the forearc of northernmost Chile and southernmost Peru. Even though more than 37,000 cracks cut the surface of the ∼500 km^2 Salar Grande region, they provide but a point sample on the scale of the forearc. Using freely available Google Earth imagery, we have identified 16 additional localities where cracks are concentrated. Using elastic dislocation models, I compare the stress fields expected at the surface as a result of large subduction zone earthquakes in order to evaluate the hypothesis that these cracks form coseismically and represent a long-term record of plate boundary segmentation. This chapter is being prepared for publication with Jordan Garroway, an undergraduate research assistant who has been instrumental in mapping the cracks, Richard Allmendinger, who initially noted the availability of meter-scale resolution imagery in Google Earth and suggested its use for a regional survey of cracks, Matthew Pritchard, and Gabriel González as coauthors.

In Chapter 4, I examine in detail the effects of the 1995 Antofagasta earthquake on upper plate structures. Seven maps of coseismic slip have been published, and I use these slip distributions to calculate the near-surface deformation. I also examine co- and postseismic synthetic aperture radar interferograms in order to detect surface deformation on these structures. This chapter is in preparation for *Geophysical Journal International*, with Matthew Pritchard as coauthor. Pritchard provided three slip distributions from his previous work that I used in my deformation calculations, processed several of the radar interferograms, guided me through my own InSAR processing, and provided editorial commentary.

Chapter 5 serves as a summary chapter for the thesis, discussing on a regional scale the relationships between the subduction zone earthquake cycle and the upper plate structures of the forearc. Both the inter- and coseismic periods of the

earthquake cycle exert stress on these structures and, through modeling of these stress fields, I find consistency between the complex short- and long-term deformation fields. This chapter is being prepared for submission to *Tectonics* with Richard Allmendinger, Matthew Pritchard, and Gabriel González.

BIBLIOGRAPHY

Allmendinger, R. W., G. González, J. S. Yu, G. D. Hoke, and B. L. Isacks (2005), Trench-parallel shortening in the Northern Chilean forearc: Tectonic and climatic implications, *Bulletin of the Geological Society of America*, *117*(1/2), 89–104, doi:10.1130/B25505.1.

Arabasz, W. J. (1971), Geological and geophysical studies of the Atacama fault zone, in northern Chile, PhD. thesis, California Institute of Technology, Pasadena, CA.

Bevis, M., and B. L. Isacks (1984), Hypocentral trend surface analysis: Probing the geometry of benioff zones, *Journal of Geophysical Research*, *89*(B7), 6153–6170.

Bevis, M., E. Kendrick, R. Smalley Jr., B. Brooks, R. W. Allmendinger, and B. L. Isacks (2001), On the strength of interplate coupling and the rate of back arc convergence in the central Andes: An analysis of the interseismic velocity field, *Geochemistry, Geophysics, Geosystems*, *2*, doi:10.1029/2001GC000198.

Brooks, B. A., M. Bevis, R. Smalley Jr., E. Kendrick, R. Manceda, E. Lauria, R. Maturana, and M. Araujo (2003), Crustal motion in the Southern Andes (26°—36°S): Do the Andes behave like a microplate?, *Geochemistry, Geophysics, Geosystems*, *4*(10), 1085, doi:10.1029/2003GC000505.

Bürgmann, R., M. G. Kogan, G. M. Steblov, G. Hilley, V. E. Levin, and E. Apel (2005), Interseismic coupling and asperity distribution along the Kamchatka subduction zone, *Journal of Geophysical Research*, *110*, B07405, doi:10.1029/2005JB003648.

Cahill, T. A., and B. L. Isacks (1992), Seismicity and shape of the subducted Nazca Plate, *Journal of Geophysical Research*, *97*(B12), 17,503–17,529.

Cashman, S. M., and H. M. Kelsey (1990), Forearc uplift and extension, southern Hawke's Bay, New Zealand: Mid-Pleistocene to present, *Tectonics*, *9*(1), 23–44.

Chanier, F., J. Ferrière, and J. Angelier (1999), Extensional deformation across an active margin, relations with subsidence, uplift, and rotations: The Hikurangi subduction, New Zealand, *Tectonics*, *18*(5), 862–876, doi:10.1029/1999TC900028.

Chlieh, M., J. B. de Chabalier, R. J. C., R. Armijo, R. Dmowska, J. Campos, and K. Feigl (2004), Crustal deformation and fault slip during the seismic cycle in the North Chile subduction zone, from GPS and InSAR observations, *Geophysical Journal International*, *158*(2), 695–711, doi:10.1111-j.1365-246X.2004.02326.x.

Comte, D., and M. Pardo (1991), Reappraisal of great historical earthquakes in the northern Chile and southern Peru seismic gaps, *Natural Hazards*, *4*(1), 23–44, doi:10.1007/BF00126557.

Comte, D., M. Pardo, L. Dorbath, C. Dorbath, H. Haessler, L. Rivera, A. Cisternas, and L. Ponce (1994), Determination of seismogenic interplate contact zone and crustal seismicity around Antofagasta, northern Chile using local data, *Geophysical Journal International*, *116*(3), 553–561, doi:10.1111/j.1365-246X.1994.tb03279.x.

Delouis, B., A. Cisternas, L. Dorbath, L. Rivera, and E. Kausel (1996), The Andean subduction zone between 22 and 25°S (northern Chile): Precise geometry and state of stress, *Tectonophysics*, *259*, 81–100.

Delouis, B., T. Monfret, L. Dorbath, M. Pardo, L. Rivera, D. Comte, H. Haessler, J. P. Caminade, L. Ponce, E. Kausel, and A. Cisternas (1997), The M_W = 8.0 Antofagasta (Northern Chile) earthquake of 30 July 1995: A precursor to the end of the large 1877 gap, *Bulletin of the Seismological Society of America*, *87*(2), 427–445.

Delouis, B., H. Philip, L. Dorbath, and A. Cisternas (1998), Recent crustal deformation in the Antofagasta region (northern Chile) and the subduction process, *Geophysical Journal International*, *132*, 302–338, doi:10.1046/j.1365-246x.1998.00439.x.

Dorbath, L., A. Cisternas, and C. Dorbath (1990), Quantitative assessment of great earthquakes in Peru, *Bulletin of the Seismological Society of America*, *80*, 551–576.

Dunai, T. J., G. A. González L., and J. Juez-Larré (2005), Oligocene–Miocene age of aridity in the Atacama Desert revealed by exposure dating of erosion-sensitive landforms, *Geology*, *33*(4), 321–324, doi:10.1130/G21184.1.

Fitch, T. J. (1972), Plate convergence, transcurrent faults, and internal deformation adjacent to southeast Asia and the western Pacific, *Journal of Geophysical Research*, *77*(23), 4432–4460.

Friedrich, A. M., B. P. Wernicke, N. A. Niemi, R. A. Bennett, and J. L. Davis (2003), Comparison of geodetic and geologic data from the Wasatch region, Utah, and implications for the spectral character of Earth deformation at periods of 10 to 10 million years, *Journal of Geophysical Research*, *108*(B4), 2199, doi:10.1029/2001JB000682.

Genrich, J. F., Y. Bock, R. McCaffrey, L. Prawirodirdjo, C. W. Stevens, S. S. O. Puntodewo, C. Subarya, and S. Wdowinski (2000), Distribution of slip at the northern Sumatran fault system, *Journal of Geophysical Research*, *105*(B12), 28,327–28,341, doi:10.1029/2000JB900158.

González, G., and D. Carrizo (2003), Segmentación, cinemática y chronología relativa de la deformación tardía de la Falla Salar del Carmen, Sistema de Fallas Atacama, (23°40′S), norte de Chile, *Revista Geológica de Chile*, *30*(2), 223–244.

González, G., J. Cembrano, D. Carrizo, A. Macci, and H. Schneider (2003), The link between forearc tectonics and Pliocene-Quaternary deformation of the Coastal Cordillera, northern Chile, *Journal of South American Earth Sciences*, *16*, 321–342, doi:10.1016/S0895-9811(03)00100-7.

Hartley, A. J., and G. Chong (2002), Late Pliocene age for the Atacama Desert: Implications for the desertification of western South America, *Geology*, *30*(1), 43–46, doi:10.1130/0091-7613(2002)030<0043:LPAFTA>2.0.CO;2.

Heinze, B. (2003), Active intraplate faulting in the forearc of north central Chile (30°–31°S): Implications from neotectonic field studies, GPS data, and elastic dislocation modeling, PhD. thesis, Freie Universität Berlin, Berlin, Germany.

Husen, S., E. Kissling, E. Flueh, and G. Asch (1999), Accurate hypocentre determination in the seismogenic zone of the subducting Nazca Plate in northern Chile using a combined on-/offshore network, *Geophysical Journal International*, *138*(3), 687–701, doi:10.1046/j.1365-246x.1999.00893.x.

Khazaradze, G., and J. Klotz (2003), Short- and long-term effects of GPS measured crustal deformation rates along the south central Andes, *Journal of Geophysical Research*, *108*(B6), 2289, doi:10.1029/2002JB001879.

Klotz, J., D. Angermann, G. W. Michel, R. Porth, C. Reigber, J. Reinking, J. Viramonte, R. Perdomo, V. H. Rios, S. Barrientos, R. Barriga, and O. Cifuentes (1999), GPS-derived deformation of the Central Andes including the 1995 Antofagasta $M_w = 8.0$ earthquake, *Pure and Applied Geophysics*, *154*, 709–730, doi:10.1007/s000240050249.

Klotz, J., G. Khazaradze, D. Angermann, C. Reigber, R. Perdomo, and O. Cifuentes (2001), Earthquake cycle dominates contemporary crustal deformation in Central and Southern Andes, *Earth and Planetary Science Letters*, *193*(3-4), 437–446, doi:10.1016/S0012-821X(01)00532-5.

Kuijpers, E. P. (1980), The geologic history of the Nicoya Ophiolite Complex, Costa Rica, and its geotectonic significance, *Tectonophysics*, *68*, 233–255.

Lay, T., and S. Y. Schwartz (2004), "Coupling" semantics and science in earthquake research: Comment, *EOS Transactions, AGU*, *85*(36), 339–340.

Loveless, J. P., G. D. Hoke, R. W. Allmendinger, G. González, B. L. Isacks, and D. A. Carrizo (2005), Pervasive cracking of the northern Chilean Coastal Cordillera: New evidence for forearc extension, *Geology*, *33*(12), 973–976, doi:10.1130/G22004.1.

Marquardt, C., A. Lavenu, L. Ortlieb, E. Godoy, and D. Comte (2004), Coastal neotectonics in Southern Central Andes: Uplift and deformation of marine terraces in Northern Chile (27°S), *Tectonophysics*, *394*, 193–219, doi:10.1016/j.tecto.2004.07.059.

Marshall, J. S., and R. S. Anderson (1995), Quaternary uplift and seismic cycle deformation, Peninsula de Nicoya, Costa Rica, *Geological Society of America Bulletin*, *107*(4), 463–473.

McIntosh, K., E. Silver, and T. Shipley (1993), Evidence and mechanisms for forearc extension at the accretionary Costa Rica convergent margin, *Tectonics*, *12*(6), 1380–1392.

Melnick, D., B. Bookhagen, H. P. Echtler, and M. R. Strecker (2006), Coastal deformation and great subduction earthquakes, Isla Santa María, Chile (37°S), *Bulletin of the Geological Society of America*, *118*(11/12), 1463–1480, doi:10.1130/B25865.1.

Niemeyer, H., G. González, and E. Martinez-de los Ríos (1996), Evolución tectónica cenozoica del margen continental activo de Antofagasta, norte de Chile, *Revista Geológica de Chile*, *23*(2), 165–186.

Norabuena, E., L. Leffler-Griffin, A. Mao, T. Dixon, S. Stein, I. S. Sacks, L. Ocola, and M. Ellis (1998), Space geodetic observations of Nazca-South America convergence across the Central Andes, *Science*, *279*(5349), 358–362.

Oleskevich, D. A., R. D. Hyndman, and K. Wang (1999), The updip and downdip limits to great subduction earthquakes: Thermal and structural models of Cascadia, south Alaska, SW Japan, and Chile, *Journal of Geophysical Research*, *104*(B7), 14,965–14,991, doi:10.1029/1999JB900060.

Pritchard, M. E., and M. Simons (2006), An aseismic slip pulse in northern Chile and along-strike variations in seismogenic behavior, *Journal of Geophysical Research*, *111*, b08405, doi:10.1029/2006JB004258.

Pritchard, M. E., M. Simons, P. A. Rosen, S. Hensley, and F. H. Webb (2002), Coseismic slip from the 1995 July 30 $M_w = 8.1$ Antofagasta, Chile earthquake as constrained by InSAR and GPS observations, *Geophysical Journal International*, *150*, 362–376, doi:10.1046/j.1365-246X.2002.01661.x.

Pritchard, M. E., C. Ji, and M. Simons (2006), Distribution of slip from 11 $M_w > 6$ earthquakes in the northern Chile subduction zone, *Journal of Geophysical Research*, *111*, B10302, doi:10.1029/2005JB004013.

Pritchard, M. E., E. O. Norabuena, C. Ji, R. Boroschek, D. Comte, M. Simons, T. Dixon, and P. A. Rosen (2007), Geodetic, teleseismic, and strong motion constraints on slip from recent southern Peru subduction zone earthquakes, *Journal of Geophysical Research*, *112*, B03307, doi:10.1029/2006JB004294.

Rech, J. A., B. S. Currie, G. Michalski, and A. M. Cowan (2006), Neogene climate change and uplift in the Atacama Desert, Chile, *Geology*, *34*(9), 761–764, doi:10.1130/G22444.1.

Ruegg, J., J. Campos, R. Armijo, S. Barrientos, P. Briole, R. Thiele, M. Arancibia, J. Cañuta, T. Duquesnoy, M. Chang, D. Lazo, H. Lyon-Caen, L. Ortlieb, J. Rossignol, and L. Serruier (1996), The $M_w = 8.1$ Antofagasta (North Chile) Earthquake of July 30, 1995: First results from teleseismic and geodetic data, *Geophysical Research Letters*, *23*(9), 917–920.

Ruegg, J., M. Olcay, and D. Lazo (2001), Co-, post- and pre-seismic displacements associated with the M_w 8.4 southern Peru earthquake of 23 June 2001 from continuous GPS measurements, *Seismological Research Letters*, *72*(6), 673–678.

Savage, J. C. (1983), A dislocation model of strain accumulation and release at a subduction zone, *Journal of Geophysical Research*, *88*(B6), 4984–4996.

Sobiesiak, M. M. (2004), Fault Plane Structure of the 1995 Antofagasta Earthquake (Chile) Derived From Local Seismological Parameters, PhD. thesis, Universität Potsdam, Potsdam, Germany.

Song, T.-R. A., and M. Simons (2003), Large trench-parallel gravity variations predict seismogenic behavior in subduction zones, *Science*, *301*(5633), 630–633, doi:10.1126/science.1085557.

Tabei, T., M. M. S. Hashimoto, and Y. Ohta (2003), Present-day deformation across the southwest Japan Arc: Oblique subduction of the Philippine Sea Plate and lateral slip of the Nankai Forearc, *Earth, Planets and Space*, *55*(10), 643–647.

Tichelaar, B. W., and L. J. Ruff (1991), Seismic coupling along the Chilean subduction zone, *Journal of Geophysical Research*, *96*(B7), 11,997–12,022.

Uyeda, S., and H. Kanamori (1979), Back-arc opening and the mode of subduction, *Journal of Geophysical Research*, *84*(B3), 1049–1061.

Wang, K., and T. Dixon (2004a), "Coupling" semantics and science in earthquake research, *EOS Transactions, AGU*, *85*(18), 180–181.

Wang, K., and T. Dixon (2004b), "Coupling" semantics and science in earthquake research: Reply, *EOS Transactions, AGU*, *85*(36), 340.

Wells, R. E., R. J. Blakely, Y. Sugiyama, D. W. Scholl, and P. A. Dinterman (2003), Basin-centered asperities in great subduction zone earthquakes: A link between slip, subsidence, and subduction erosion?, *Journal of Geophysical Research*, *108*(B10), 2507, doi:10.1029/2002JB002072.

Xia, Y., G. Michel, C. Reigber, J. Klotz, and H. Kaufmann (2003), Seismic unloading and loading in northern central Chile as observed by differential Synthetic Aperture Radar Interferometry (D-INSAR) and GPS, *International Journal of Remote Sensing*, *24*(22), 4375–4391.

CHAPTER 1

PERVASIVE SURFACE CRACKING OF THE NORTHERN CHILEAN COASTAL CORDILLERA: NEW EVIDENCE FOR FOREARC EXTENSION*

1.1 Abstract

Despite convergence across the strongly coupled seismogenic interface between the South American and Nazca plates, the dominant neotectonic signature in the forearc of northern Chile is arc-normal extension. We have used 1-m resolution IKONOS satellite imagery to map nearly 37,000 cracks over an area of 500 km^2 near the Salar Grande (21°S). These features, which are best preserved in a ubiquitous gypcrete surface layer, have both nontectonic and tectonic origins. However, their strong preferred orientation perpendicular to the plate convergence vector suggests that the majority owe their formation to approximate east-west extension associated with plate boundary processes such as interseismic loading, co- and postseismic strain, and long-term instability resulting from subduction erosion. Similar structures were formed during or shortly after the 1995 $M_w = 8.0$ earthquake near the city of Antofagasta, south of Salar Grande, and in conjunction with the 2001 $M_w = 8.2$–8.4 Arequipa, Peru, event. Cracks such as these may form in other forearcs but remain largely unexposed because of vegetative cover or marked fluvial erosion — factors that are absent in northern Chile as a result of its hyperarid climate.

*Originally published as: Loveless, J.P., G.D. Hoke, R.W. Allmendinger, G. González, B.L. Isacks, and D.A. Carrizo (2005), Pervasive cracking of the northern Chilean forearc: New evidence for forearc extension, *Geology*, *33*, 973–976, doi:10.1130/G22004.1. Reprinted with permission of the Geological Society of America.

1.2 Introduction

As the Nazca plate subducts beneath South America, strong coupling between the two plates from ∼20- to 50-km depth (*Tichelaar and Ruff*, 1991) allows for the accumulation of elastic strain in the overriding continent (*Klotz et al.*, 1999; *Bevis et al.*, 2001). However, no structures in the forearc indicate permanent arc-normal shortening resulting from such loading. Instead, many features demonstrate extension nearly parallel to the direction of convergence. Approximately north-south–striking normal faults are observed both off- and onshore (*Arabasz*, 1971; *Delouis et al.*, 1998; *von Huene et al.*, 1999; *González et al.*, 2003; *von Huene and Ranero*, 2003). Displacement on normal faults is primarily dip-slip (*Delouis et al.*, 1998), suggesting an extension nearly perpendicular to the fault strike. Most faults are mapped as steeply landward dipping (*Arabasz*, 1971; *Delouis et al.*, 1998), although dips as low as 45° have been documented on the Mejillones Peninsula (∼23.5°S latitude, *González et al.*, 2003).

In addition to these well-known normal faults, mode 1 (opening) cracks are present in the forearc (*González et al.*, 2003). We describe here a dense suite of cracks west of Salar Grande, located in the Chilean Coastal Cordillera near 21°S latitude (Figures 1.1 and 1.2). Through mapping of a 500-km^2 area by high-resolution IKONOS imagery and fieldwork, we find a consistent crack orientation normal to the direction of plate convergence. The regularity in strike and broad distribution imply a genetic relationship between cracks and plate boundary processes. We discuss the origins of the cracks and suggest that they are driven primarily by tectonic processes.

1.3 Tectonic setting

Over the past 25 Ma, convergence between the Nazca and South American plates across a strongly coupled plate interface has resulted in crustal shortening and thickening, giving rise to the modern Andes. Great interplate thrust earthquakes ($M \geq 8$) are thought to rupture individual segments of the margin with recurrence intervals of ∼100–150 yr (*Comte and Pardo*, 1991). The southern Peru segment (16° to 18°S) ruptured in 2001, partially filling the post-1868 seismic gap, and the segment immediately south of the Mejillones Peninsula (∼23°S) ruptured in 1995 (Figure 1.1). The ∼420-km-long segment of northernmost Chile last experienced a great earthquake in 1877, the epicenter of which was estimated at 21.00°S, 70.25°W, just offshore of Salar Grande (Figure 1.1; *Comte and Pardo*, 1991).

Global Positioning System (GPS) data show orogen-scale interseismic shortening of the Central Andes in the direction of plate convergence on decadal timescales (Figure 1.1; *Bevis et al.*, 2001)). The velocity field has been modeled by using an elastic half-space with dislocations applied to the plate boundary that is locked between depths of 20 and 50 km during interseismic times (*Klotz et al.*, 1999; *Bevis et al.*, 2001). This model for the plate boundary is consistent with the conclusions of *Tichelaar and Ruff* (1991), who used seismic waveform inversion to analyze the variation in degree and extent of coupling along the Chilean margin.

GPS (*Klotz et al.*, 1999) and interferometric radar (*Pritchard et al.*, 2002) data spanning the 1995 $M_w = 8.0$ Antofagasta earthquake show a coseismic surface displacement gradient opposite that of the interseismic velocity field of northern Chile (Figure 1.1). The increase in westward displacement (relative to stable South America) from east to west shows that the Coastal Cordillera was extended during this earthquake. Surface cracking and 15–20 cm of normal fault slip occurred

during the event (*Delouis et al.*, 1998; *González et al.*, 2003), consistent with the coseismic strain captured by geodetic measurements. *Delouis et al.* (1998) proposed that other fresh-looking fault scarps in this region also developed as secondary features related to Quaternary subduction earthquakes. Near the coastal city of Ilo, southern Peru, substantial ground cracking and landslides accompanied the 2001 $M_w = 8.1$ Arequipa earthquake. These cracks are thought to be coseismically reactivated features that initially formed during the great 1604 earthquake that originated near Ilo (*Keefer and Moseley*, 2004).

The bedrock of the Coastal Cordillera represents the remnant of a Late Jurassic–Early Cretaceous magmatic arc. Original arc structures such as the Atacama Fault Zone influence neotectonic deformation (*Arabasz*, 1971). The presence of a Mesozoic arc remnant so close to the modern trench suggests long-term tectonic removal and subduction of material at the trench (subduction erosion), causing ∼1 km/Ma of trench retreat (*Rutland*, 1971; *von Huene and Scholl*, 1991). This tectonic erosion and underplating of subducted material beneath the Coastal Cordillera may cause uplift and extension (*von Huene et al.*, 1999; *von Huene and Ranero*, 2003).

1.4 Cracks in the Salar Grande region

We focus our study of cracks on a region located at ∼21°S latitude between the Salar Grande and the Pacific Ocean (Figure 1.2). The study area is located within the hyperarid Atacama Desert and is perched atop the 400–1200-m-high coastal escarpment of northern Chile. The persistence of the dry climatic conditions for at least 6 Ma (*Hartley and Chong*, 2002) and consequent preservation of landforms allow us to use present topography as a proxy for neotectonic deformation.

Cracks in the Salar Grande region are best preserved in the gypsum-indurated

Figure 1.1: Seismotectonic setting of northern Chile and southern Peru. Gradients in interseismic GPS velocities (vector scale I; from *Bevis et al.*, 2001) and coseismic displacements (vector scale C; from *Klotz et al.*, 1999) demonstrate shortening and extension, respectively. Epicenters of great earthquakes are shown as black dots; approximate rupture areas are enclosed by ellipses (2001 rupture area outlined with dashed line). Box near Salar Grande shows area of Figure 2.

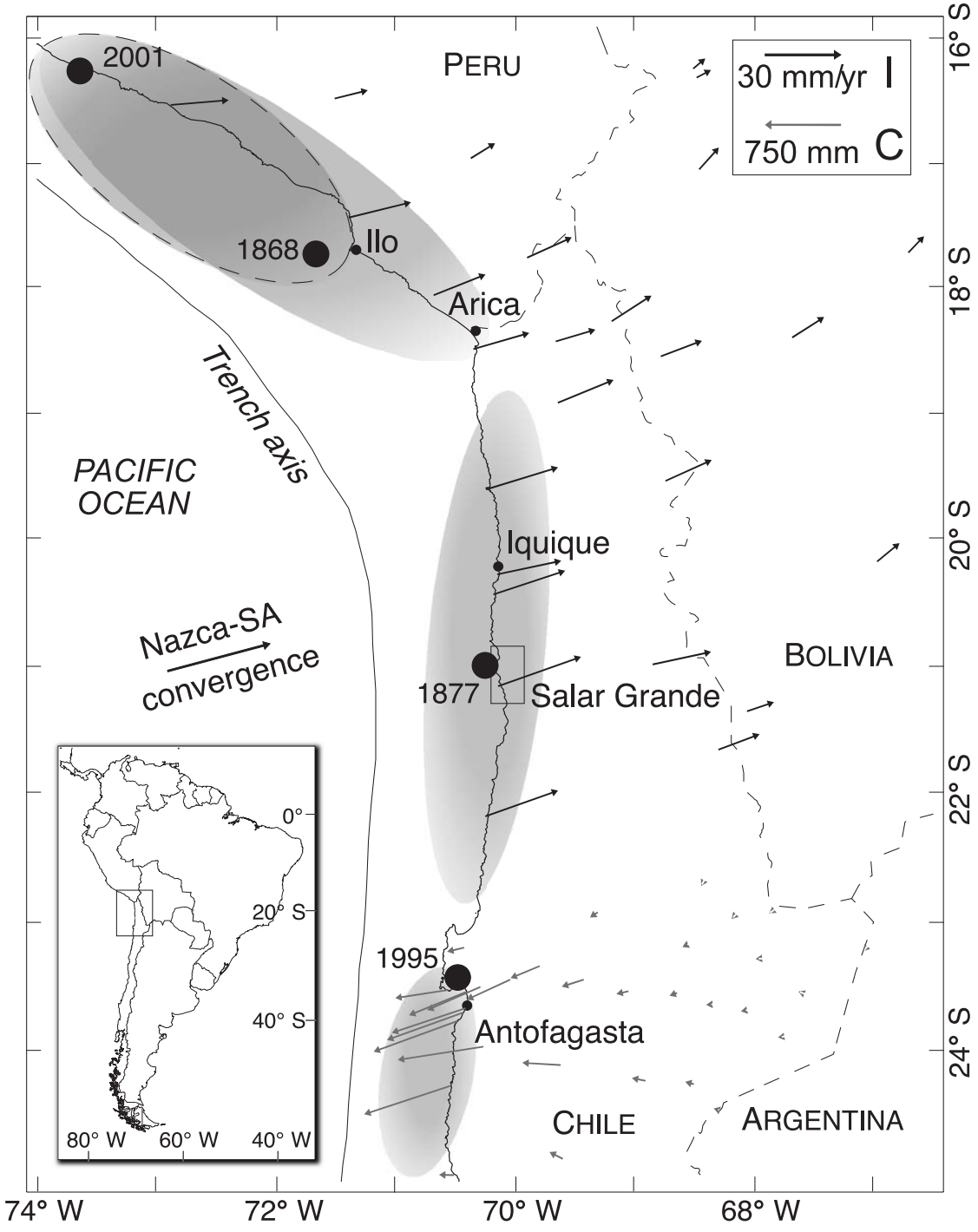
2001
1868
Ilo
Arica
PERU
30 mm/yr I
750 mm C
Trench axis
PACIFIC
OCEAN
Iquique
Nazca-SA
convergence
1877
Salar Grande
BOLIVIA
1995
Antofagasta
CHILE
ARGENTINA
0°
20° S
40° S
80° W
60° W
40° W
16° S
18° S
20° S
22° S
24° S
74° W
72° W
70° W
68° W

gravel (gypcrete) that blankets large areas of coastal northern Chile, but they also penetrate as deep as 8 m into bedrock. The latter are commonly parallel to bedrock joint sets, suggesting that some bedrock joints have propagated through the gypcrete. Surface cracks showing no correlation to bedrock joints are also present. Cracks are less evident in nonindurated sediments, indicating that characteristics of the gypcrete enhance preservation of the structures. Some cracks have been sealed by precipitated gypsum, but most are open. Vertical offset of up to 1 m is observed in a few locations; we suggest that most cracks are mode 1, but some mixed-mode cracks also exist. Apertures range from a few centimeters to 2.5 m, with many on the order of 0.5 m. Erosion of the gypcrete modifies crack morphology, rounding initially sharp edges and transporting wall material to the crack base. Fault scarp and crack morphologies, crack interaction patterns, and variation in aperture and depth give insight into relative ages of structures, but because material diffusion constants are unknown in the Atacama Desert, absolute dating is not possible.

Remote sensing and field-based observations allow us to divide cracks into two groups: those with nontectonic origins, and those likely formed by tectonic processes.

1.4.1 Nontectonic cracks

Cracks with millimeter- to centimeter-scale apertures commonly connect to form polygonal shapes centimeters to meters across within the gypsum- or locally halite-indurated gravel. This patterned ground probably formed by shrinking and swelling that resulted from fluctuations in temperature and moisture content (*Tucker*, 1978). The thick fog that blankets much of coastal northern Chile, particularly dur-

ing the winter, is the source of both the gypsum (*Rech et al.*, 2003) and moisture. Because cracks of this type are generally too small to detect by means of remote sensing, they have not been considered in our statistical analyses or measurements of regional strain. Locally, hillsides of cracked, 1–2-m-thick layers of gypcrete are delimited by a lobelike front, suggesting some downslope movement of gypcrete layers. The cracks in these areas parallel topographic contours, suggesting that gravitational forces are responsible for their formation.

1.4.2 Tectonic cracks

The nonuniform strikes and isolated occurrences of the nontectonic features described above contrast the strong preferred orientation and broad distribution of the cracks observed through remote sensing. We used IKONOS satellite imagery, which offers 1 m spatial resolution in the panchromatic band, to map more than 37,000 cracks over 500 km^2 (Figure 1.2). The mapped structures have consistent strike, with a length-weighted mean azimuth of 347° (circular variance of 0.21), which is similar to the trends of both the coastline and plate boundary and which is perpendicular to the plate convergence vector (Figure 1.2E).

Many cracks cluster spatially around mapped fault scarps (Figure 1.2A–E); faults and cracks have similar, but not identical, orientations (mean strikes of 325° and 347°, respectively; Figure 1.2E, F). Near the Hombre Muerto fault (Figure 1.2A), for example, narrow, shallow cracks of regional extent are oriented oblique to the fault scarp. With decreasing distance to the scarp, crack aperture and depth increase, reaching maxima at the scarp crest. In general, crack formation may precede faulting, but continued propagation of the cracks likely occurs as a secondary response to fault slip. In some cases, faults seem to have perturbed the

Figure 1.2: Crack mapping in Salar Grande region. (A) Morphological features and cracks mapped using IKONOS imagery. Numerous cracks (black lines) cluster around faults (gray lines), but this relationship is not unique. HM–Hombre Muerto fault. (B) Detail of crack mapping near two fault scarps. (C) IKONOS satellite image showing clusters of cracks around fault scarps in region of B). (D) Field photograph of cracks parallel to fault scarps. Road in center of photo is 2 m wide. (E, F) Rose diagrams showing strike distribution of cracks (E) and faults in Salar Grande region (F), with length-weighted mean orientation and direction of relative plate convergence (PC) indicated by arrows.

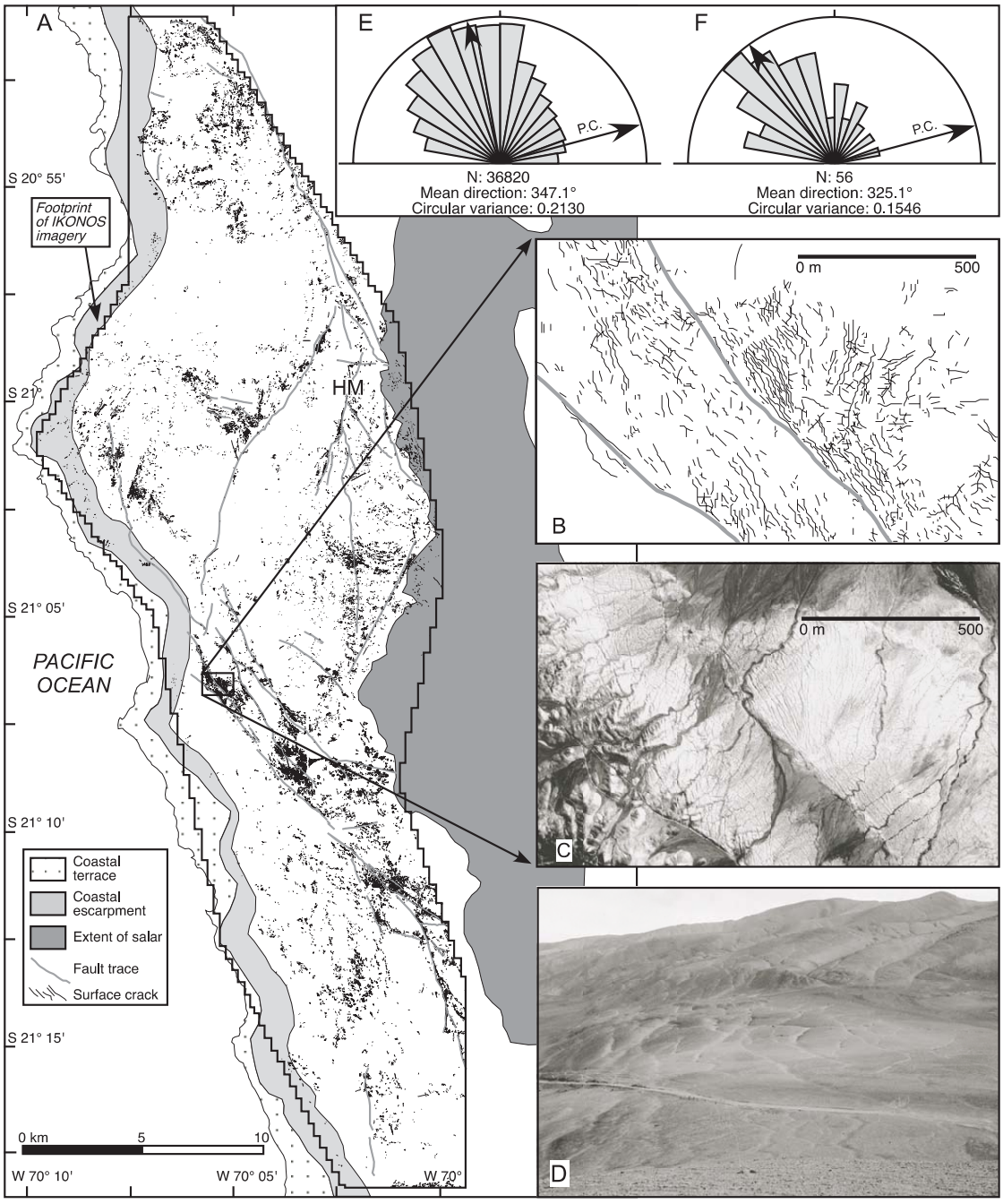
A
E
F
P.C.
P.C.
N: 36820
Mean direction: 347.1°
Circular variance: 0.2130
N: 56
Mean direction: 325.1°
Circular variance: 0.1546
S 20° 55'
Footprint of IKONOS imagery
S 21°
HM
S 21° 05'
PACIFIC OCEAN
S 21° 10'
S 21° 15'
Coastal terrace
Coastal escarpment
Extent of salar
Fault trace
Surface crack
0 km
5
10
W 70° 10'
W 70° 05'
W 70°
0 m
500
B
0 m
500
C
D

stress field in which the cracks propagate, causing curvature of strike near the fault (Figure 1.2B, C). Such perturbations can result from asperities that concentrate stress on the fault surface (*Rawnsley et al.*, 1992).

1.4.3 Quantification of extension

To determine the magnitude of finite extension represented by cracks in the imagery, we counted cracks intersecting transects trending perpendicular to the mean strike. Strain values along transects measured in the field were used to calibrate average crack aperture in the imagery-based profiles, allowing a simple count of cracks to roughly estimate extension magnitude. Along transects crossing the entire IKONOS data set, extension values reach ∼1.25%. Adjacent to faults, greater calculated extension of 5%–10% (over several hundred meters) is consistent with the observations of crack concentration around faults.

1.5 Discussion

The documented coseismic extension from field observations (*Delouis et al.*, 1998) and GPS measurements (*Klotz et al.*, 1999) of the 1995 Antofagasta earthquake provide evidence that extensional structures deform during or shortly after earthquakes. The displacement gradient tensor determined from the 1995 GPS data indicates maximum extensional strain of $8.93 \times 10^{-4}\%$ along an azimuth N63E. Salar Grande lies well north of Antofagasta, but we compare effects of the 1995 event to the cracks we have described because no great earthquake has occurred in northernmost Chile since 1877. The discrepancy between GPS-based and our crack-based strain estimates is several orders of magnitude, indicating that strain accompanying one great earthquake is insufficient to explain the cracking. Cracks

may represent extension associated with many earthquakes, a possibility supported by field observations of repeated opening and filling of cracks. If crack propagation occurs only during and/or shortly after earthquakes, we estimate, on the basis of the comparisons above, that $\sim 1 \times 10^3$ great earthquakes would be required to account for the finite extension. Given the 100–150-yr recurrence interval of *Comte and Pardo* (1991), this number of events has occurred over the past 100–150 ka. Although the climatic conditions of the Coastal Cordillera may preserve features of this age, we suggest that other sources of strain, such as interseismic loading and subduction erosion, also contribute to crack propagation, decreasing the time span represented by the structures.

Our simple dislocation models of interseismic loading (based on *Okada*, 1985) predict that coastal regions of a simulated Andean margin with a plate boundary locked between depths of 20 and 50 km experience ~E–W extensional strain on the order of 1×10^{-3}%. GPS stations are spaced such that they do not capture this narrow longitudinal zone of extension. This magnitude of strain is about equal to that demonstrated by the coseismic GPS data and is applied over a much longer time period (100 yr), yielding lower strain rates. The sense of predicted interseismic strain is similar to that due to the Antofagasta earthquake. This seems counterintuitive but results from different loading geometries: interseismic strain accumulation presumably occurs across the entire extent of the locked plate interface, whereas the Antofagasta earthquake ruptured only a portion of the fault. The dimensions of slip on the subduction thrust directly affect the surface deformation. The interseismic strain may itself cause brittle deformation of the forearc, or it may precondition the region for failure when more rapid coseismic strains are applied, as proposed by *Delouis et al.* (1998).

Long-term extension and uplift associated with subduction erosion processes have also been proposed as mechanisms for normal faulting in the forearc (*Delouis et al.*, 1998; *von Huene and Ranero*, 2003). Gravitational instability induced by the removal of material at the toe of the continental slope leads to extensional failure of the slope and forearc, demonstrated by normal faults observed offshore (*von Huene and Ranero*, 2003). Additionally, underplating of subduction-eroded material may contribute to uplift and surface extension of the forearc (*Delouis et al.*, 1998).

Dynamic stresses accompanying shear rupture propagation during great earthquakes may also generate mode 1 surface cracks. *Dalguer et al.* (2003) indicate that cracks formed by this mechanism are characterized by branched ends, which we do not observe in the Salar Grande region. *Savalli and Engelder* (2005) suggest that static, subcritical joint propagation is the most prominent mechanism of crack development in Earth's crust. Subcritical propagation, or crack growth that occurs even though the stress intensity at the tips is less than the critical level predicted by fracture mechanics, can occur as a result of fluid and/or chemical activity that facilitate crack propagation (*Atkinson and Meredith*, 1987). *Segall* (1984) states that strains applied continuously cause crack growth, whereas the material response to loads that fluctuate rapidly in magnitude may be elastic and thus not conducive to crack growth, even if critical stress intensity conditions are met. Therefore, static loading from interseismic convergence, subduction erosion processes, and co- and postseismic phenomena is the likely mechanism for crack propagation in the Salar Grande region, with dynamic shear rupture during earthquakes playing a lesser role.

The plate boundary-scale interseismic loading and regional seismicity suggest

that cracks similar to those seen at Salar Grande and Ilo, Peru, should be distributed throughout the forearc, yet we have not observed such concentrations in our reconnaissance visits to other locations, which suggests that the Salar Grande and Ilo regions are anomalous. The elevated concentration of faults (*Yu and Isacks*, 1999) and several bedrock joint sets near Salar Grande demonstrate weakness in the uppermost crust that locally allows surface cracking when tectonically loaded. Additionally, because the degree of gypsum induration of the sediment cover dictates the quality of crack preservation, variations in surface composition could help to explain the different concentrations of cracks in the forearc. Gypcrete covers a substantial portion of the Coastal Cordillera, but its material properties around our study area may enhance preservation of cracks. It is likely that cracks similar to those we describe here are present in other forearcs but may not be observed because of rapid landscape modification under wetter climatic conditions. The unique, hyperarid environment of northern Chile has literally laid bare the true extent of brittle deformation.

BIBLIOGRAPHY

Arabasz, W. J. (1971), Geological and geophysical studies of the Atacama fault zone, in northern Chile, PhD. thesis, California Institute of Technology, Pasadena, CA.

Atkinson, B. K., and P. G. Meredith (1987), The theory of subcritical crack growth with applications to minerals and rocks, in *Fracture Mechanics of Rock*, edited by B. K. Atkinson, pp. 111–166, Academic Press, London.

Bevis, M., E. Kendrick, R. Smalley Jr., B. Brooks, R. W. Allmendinger, and B. L. Isacks (2001), On the strength of interplate coupling and the rate of back arc convergence in the central Andes: An analysis of the interseismic velocity field, *Geochemistry, Geophysics, Geosystems*, *2*, doi:10.1029/2001GC000198.

Comte, D., and M. Pardo (1991), Reappraisal of great historical earthquakes in the northern Chile and southern Peru seismic gaps, *Natural Hazards*, *4*(1), 23–44, doi:10.1007/BF00126557.

Dalguer, L. A., K. Irikura, and J. D. Riera (2003), Simulation of tensile crack generation by three-dimensional dynamic shear rupture propagation during an earthquake, *Journal of Geophysical Research*, *108*(B3), 2144, doi:10.1029/2001JB001738.

Delouis, B., H. Philip, L. Dorbath, and A. Cisternas (1998), Recent crustal deformation in the Antofagasta region (northern Chile) and the subduction process, *Geophysical Journal International*, *132*, 302–338, doi:10.1046/j.1365-246x.1998.00439.x.

González, G., J. Cembrano, D. Carrizo, A. Macci, and H. Schneider (2003), The link between forearc tectonics and Pliocene-Quaternary deformation of the Coastal Cordillera, northern Chile, *Journal of South American Earth Sciences*, *16*, 321–342, doi:10.1016/S0895-9811(03)00100-7.

Hartley, A. J., and G. Chong (2002), Late Pliocene age for the Atacama Desert: Implications for the desertification of western South America, *Geology*, *30*(1), 43–46, doi:10.1130/0091-7613(2002)030<0043:LPAFTA>2.0.CO;2.

Keefer, D. K., and M. E. Moseley (2004), Southern Peru desert shattered by the great 2001 earthquake: Implications for paleoseismic and paleo-El Niño-Southern Oscillation records, *Proceedings of the National Academy of Sciences*, *101*, 10,878–10,883, doi:10.1073/pnas.0404320101.

Klotz, J., D. Angermann, G. W. Michel, R. Porth, C. Reigber, J. Reinking, J. Viramonte, R. Perdomo, V. H. Rios, S. Barrientos, R. Barriga, and O. Cifuentes (1999), GPS-derived deformation of the Central Andes including the 1995 Antofagasta $M_w = 8.0$ earthquake, *Pure and Applied Geophysics*, *154*, 709–730, doi:10.1007/s000240050249.

Okada, Y. (1985), Surface deformation due to shear and tensile faults in a half-space, *Bulletin of the Seismological Society of America*, *75*(4), 1135–1154.

Pritchard, M. E., M. Simons, P. A. Rosen, S. Hensley, and F. H. Webb (2002), Co-seismic slip from the 1995 July 30 $M_w = 8.1$ Antofagasta, Chile earthquake as constrained by InSAR and GPS observations, *Geophysical Journal International*, *150*, 362–376, doi:10.1046/j.1365-246X.2002.01661.x.

Rawnsley, K. D., T. Rives, J.-P. Petit, S. R. Hencher, and A. C. Lumsden (1992), Joint development in perturbed stress fields near faults, *Journal of Structural Geology*, *14*(8/9), 939–951, doi:10.1016/0191-8141(92)90025-R.

Rech, J. A., J. Quade, and W. S. Hart (2003), Isotopic evidence for the source of Ca and S in soil gypsum, anhydrite and calcite in the Atacama Desert, Chile, *Geochimica et Cosmochimica Acta*, *67*(4), 575–586, doi:10.1016/S0016-7037(02)01175-4.

Rutland, R. W. R. (1971), Andean orogeny and ocean floor spreading, *Nature*, *233*(5317), 252–255.

Savalli, L., and T. Engelder (2005), Mechanisms controlling rupture shape during subcritical growth of joints in layered rocks, *Geological Society of America Bulletin*, *117*(3-4), 436–449, doi:10.1130/B25368.1.

Segall, P. (1984), Rate-dependent extensional deformation resulting from crack growth in rock, *Journal of Geophysical Research*, *89*(B6), 4185–4195.

Tichelaar, B. W., and L. J. Ruff (1991), Seismic coupling along the Chilean subduction zone, *Journal of Geophysical Research*, *96*(B7), 11,997–12,022.

Tucker, M. E. (1978), Gypsum crusts (gypcrete) and patterned ground from northern Iraq, *Zeitschrift für Geomorphologie*, *22*(1), 89–100.

von Huene, R., and C. R. Ranero (2003), Subduction erosion and basal friction along the sediment-starved convergent margin off Antofagasta, Chile, *Journal of Geophysical Research*, *108*(B2), 2079, doi:10.1029/2001JB001569.

von Huene, R., and D. W. Scholl (1991), Observations at convergent margins concerning sediment subduction, subduction erosion, and the growth of continental crust, *Reviews of Geophysics*, *29*(3), 279–316.

von Huene, R., W. Weinrebe, and F. Heeren (1999), Subduction erosion along the North Chile margin, *Journal of Geodynamics*, *27*, 345–358, doi:10.1016/S0264-3707(98)00002-7.

Yu, J. S., and B. L. Isacks (1999), Examination of the surface expression of the Atacama fault system in northern Chile from interferometrically derived (InSAR) topography, *EOS, Transactions AGU*, *80*(46), 1060.

CHAPTER 2

TECTONIC CRACK FORMATION IN THE SALAR GRANDE REGION, NORTHERN CHILE

2.1 Abstract

More than 37,000 surface cracks cut the surface of a 500 km^2 region west of Salar Grande in northern Chile (21°S latitude), providing new evidence for forearc extension. The cracks show a length-weighted mean strike of 347°, which is perpendicular to the azimuth of convergence between the subducting Nazca and overriding South American plates. The strong preferred orientation and distribution of cracks over a large region indicate that stress fields operating on a similar scale — namely those induced by the subduction zone earthquake cycle — are primarily responsible for crack formation. These stress fields drive the evolution of both the cracks and upper plate faults in the region. Cracks adjacent to fault scarps commonly show enhancement in their amount of opening, suggesting that upper plate faults concentrate the regional stress. We use boundary element modeling to examine the relationships between the faults and enhanced cracks. Our results show that the stress perturbations associated with normal slip on upper plate faults are generally consistent with the distribution of cracking, though in some cases reverse slip models also predict a compatible stress field. These results agree with recent studies of the neotectonics of the northern Chilean forearc, which suggest that structures in the region in general reflect east-west extension, with some faults showing shortening in the same direction. The opposite senses of deformation accumulated on structures with similar strikes mimic the complicated stress fields produced on decadal timescales by the subduction zone earthquake cycle.

2.2 Introduction

Coastal regions of the northern Chilean forearc (18–28°S) are characterized by structures demonstrating, in general, extension in the direction of convergence between the subducting Nazca and overriding South American plates. The dearth of precipitation in the hyperarid Atacama Desert allows for the conversion of bedrock to regolith at the surface, blanketing the area in a layer of gravel. Furthermore, induration of the gravel with gypsum cements this material, forming a brittle, competent crust that limits denudation of regolith during infrequent rainfall events. As a result of these climatic conditions, even subtle geologic structures are preserved throughout the forearc, most notably the meter-scale open cracks that we describe here and in Chapters 1 and 3.

West of the ∼200 km^2 Salar Grande (21°S) lies a region affected by pervasive open cracking of the surface (*Loveless et al.*, 2005). Using 1 m resolution imagery from the IKONOS satellite, we have compiled a database of ∼37,000 cracks within a 500 km^2 region (outlined in Figure 2.1). Statistical analysis of crack strikes shows a preferred orientation nearly parallel to the coastline and Nazca-South American plate boundary and perpendicular to the direction of plate convergence (Chapter 1, *Loveless et al.*, 2005). This consistency in strike over such a large region suggests that the evolution of cracks is governed by stress acting on a similar spatial scale, namely the subduction zone seismic cycle.

In this chapter, we explore the relationships between the deformation exhibited by the cracks and upper plate faults and the stress fields exerted on these features by interseismic and coseismic processes. While both types of structures are fundamentally driven by processes related to subduction, the cracks are further affected by local perturbations to the regional stress field caused by the presence

Figure 2.1: Topography of the Salar Grande region, as expressed in the SRTM 90 m digital elevation model. The region outlined by the black "jagged" line shows the extent of the IKONOS imagery used in our crack mapping. The large flat region immediately east of the imagery coverage is the Salar Grande proper. The smaller boxes show the focus regions described in the paper; IKONOS imagery of these regions is shown in Figures 2.8, 2.11, 2.13, and 2.15. Locations described in the text are labeled as follows: PL — Punta de Lobos fault, QP — Quebrada Pica, HM — Hombre Muerto fault, AB — Antena-Bahía Blanca faults, GG — gypsum "glaciers" region, GE — Geoglifos fault. The solid bold black lines show the faults used in the boundary element modeling, while the lighter-weight dashed lines show other prominent faults in the area. The east-west striking faults near the eastern extent of the map are part of the Chuculay system of reverse faults (*Allmendinger et al.*, 2005). Numerous cracks along the crests of the related fault scarps are discussed by *González et al.* (2007).

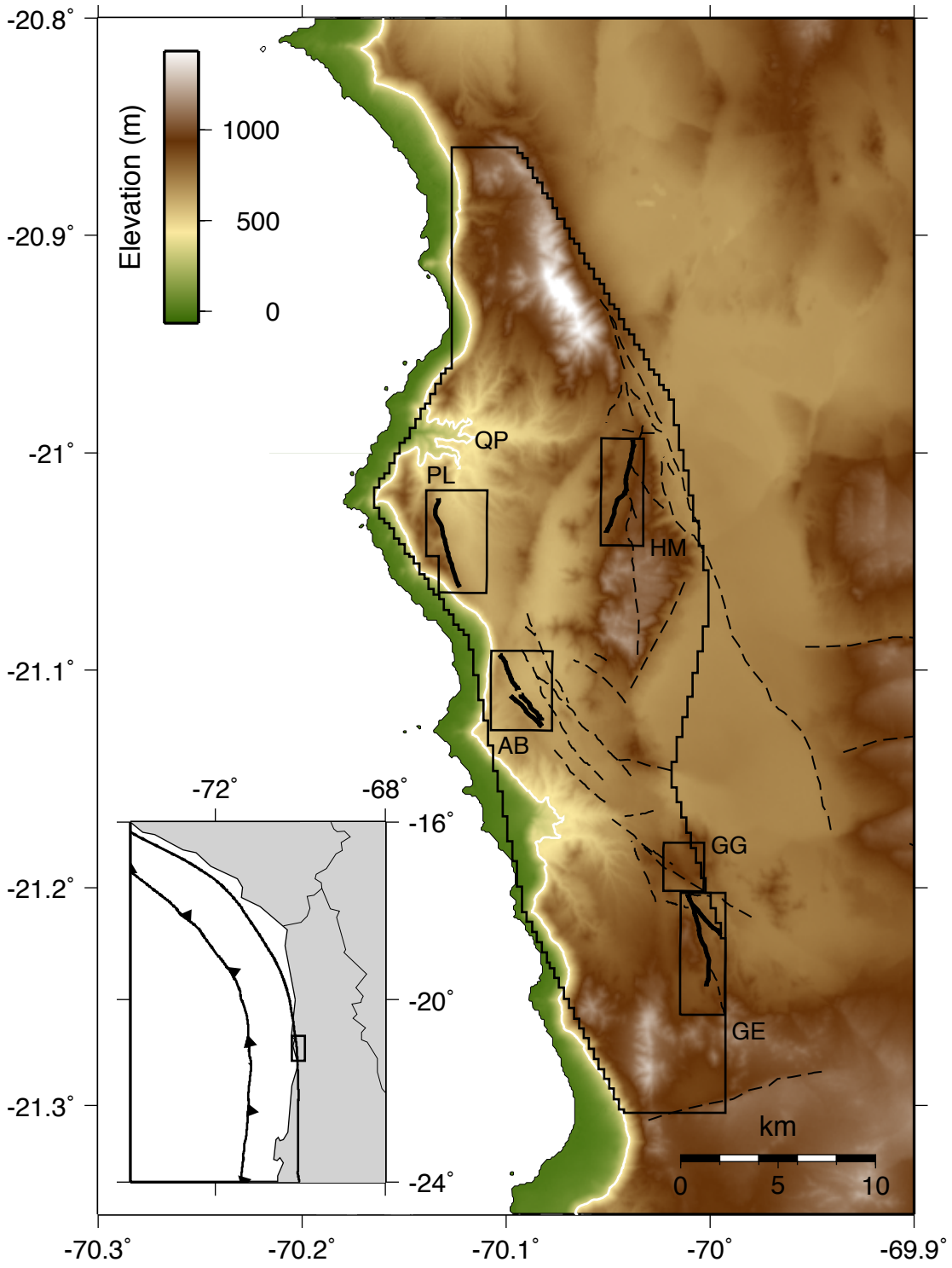
-20.8˚
-20.9˚
-21˚
-21.1˚
-21.2˚
-21.3˚
-70.3˚
-70.2˚
-70.1˚
-70˚
-69.9˚
Elevation (m)
1000
500
0
QP
PL
HM
AB
GG
GE
-72˚
-68˚
-16˚
-20˚
-24˚
km
0
5
10

of the faults. We use boundary element models to understand how faults and cracks respond to the earthquake cycle. We model several key faults in the Salar Grande region as discontinuities in an elastic medium, apply remote stress to simulate seismic cycle loading, and investigate the compatibility between the stress perturbations they introduce and the accentuation of cracks along their traces. In doing so, we evaluate whether or not the localized perturbations of the stress field around upper plate faults are capable of explaining the observed accentuation of cracking.

2.2.1 Geological setting

The principal structure of the northern Chilean forearc is the 1000 km long Atacama Fault System (AFS), which initially formed in the Mesozoic. The AFS, its splays, and other faults have accommodated vertical motions associated with the uplift of the Coastal Cordillera since the Miocene (*Riquelme et al.*, 2003) and show evidence of Quaternary to recent reactivation (*Delouis et al.*, 1998; *González et al.*, 2006). Morphological scarps striking approximately parallel to the coastline and plate boundary typify the AFS. Sparse fault kinematic data indicate dominantly dip-slip normal motion around the Antofagasta region (23–25°S latitude, *Delouis et al.*, 1998; *González et al.*, 2003) and dextral-normal oblique slip further north near Salar Grande (*González et al.*, 2003). However, *Carrizo et al.* (2007) describe the kinematics of the Salar Grande region as constrictional, with both margin-parallel and margin-perpendicular shortening accommodated by suites of faults striking north-south and east-west, respectively. Reverse motion has been well documented on the latter group of structures (*Allmendinger et al.*, 2005), which is restricted to latitudes between 19° and 21.6°S. Crests of fault-propagation folds

atop some of these structures — notably the Chuculay fault system, east of Salar Grande — show substantial cracking. The strikes of these cracks parallel that of the fault, and their formation has been attributed to surface flexure during growth of the fault-propagation folds (*González et al.*, 2007). The cracks we describe here differ in several regards from those associated with the east-west reverse faults: many cracks strike roughly parallel, not perpendicular, to the coastline, and there are many cracks spatially unrelated to larger-scale structures. However, cracks west of Salar Grande that are localized along fault scarps show enhancement adjacent to the fault trace, similar to the pattern seen along the Chuculay system.

2.2.2 Fault-related cracking

Several studies have recognized the association between faults and secondary deformation accommodated by open cracks or joints (e.g., *Bourne and Willemse*, 2001; *Hilley et al.*, 2001; *González et al.*, 2007). *Bourne and Willemse* (2001) analyzed tensile fracture patterns around a network of conjugate strike-slip faults at Nash Point, U.K., and found that the complex fracture trajectories can be explained by local perturbation of a regional stress field due to slip along the faults. This study revealed that cracks can be used as kinematic indicators, with the obliquity between faults and cracks placing constraint on the direction fault slip and regional stress field that drives both fault slip and crack propagation. *González et al.* (2007) found a relationship between the spatial extent of open cracks at the crest of the Chuculay reverse fault system and the height of the scarp, indicating that growth of fault-propagation folds above the fault system results in enhanced flexure of the scarp crest, driving the opening of cracks. *Hilley et al.* (2001) found that the interaction between surface-breaking tensile fractures and normal faults

can substantially modify the morphology of a fault scarp. When cracks are present above an active fault, extension is partitioned between fault slip and crack opening at the surface of the topographic scarp. Thus, a fault scarp forming in the presence of surface cracks will show subtler, more irregular topography than the sharper profile that forms in a region lacking cracks. The first two models (*Bourne and Willemse*, 2001; *González et al.*, 2007) are applicable to situations in which cracks evolve either in conjunction with or following fault activity. In the case of Nash Point, cracks propagate due to stress fields that are governed by properties of the fault (*Bourne and Willemse*, 2001), while cracks above the Chuculay faults grow as a response to flexure induced by fault propagation and slip (*González et al.*, 2007). Conversely, the model of *Hilley et al.* (2001) describes the variation in scarp morphology that results from fault slip in the presence of pre-existing cracks. Field observations suggest that many of the cracks we describe west of Salar Grande predate the most recent upper plate fault activity yet have been reactivated during subsequent episodes of fault slip and scarp construction. With these conceptual models in mind, we use boundary element models to compare the stress fields around the faults in the Salar Grande region with the extent and style of cracking observed.

2.3 Crack population characteristics

On a regional scale, we used 1 m resolution IKONOS satellite imagery to map meter-scale cracks throughout the Salar Grande area, hand tracing each in GIS software. Crack length is calculated by simply summing the lengths of segments. The strike of each crack is defined as the slope of a least squares linear fit through the vertex coordinates.

Crack aperture was only calculated for select transects across cracks in the Salar Grande region where we carried out appropriate field studies (Table 2.1). The true amount of tectonic opening of cracks that have either been filled by sediments eroded from their walls or deposited by aeolian processes is difficult to assess; in the case of such cracks, we estimated that one-half the distance between rounded edges represented the true extent of opening. For the most part, we focus on crack strike as opposed to aperture in our use of cracks as indicators of tectonic activity. Aperture is difficult to quantify on a regional scale due to the fact that the width of most cracks is less than the resolution of the imagery. Comparative field studies prove that cracks as narrow as 20 cm can be distinguished in the 1 m resolution imagery, but the actual aperture cannot be accurately measured.

We define crack density as the summed length of cracks per unit area. For ease of comparing crack density with topography from the SRTM digital elevation model, we calculate the crack density on a 90-m grid (Figure 2.2a). In each grid cell, we also calculate the length-weighted mean azimuth. For cracks that span more than one grid cell, we find the intersection of the crack with the cell wall so that only the portion of the crack lying within a particular cell contributes to that cell's crack density (*Bourke*, 1989). Our field observations indicate that cracks are best preserved in surface sediments that have been indurated with atmospherically-derived gypsum (documented in Chapter 3, *Rech et al.*, 2003), but because the surface cover is not uniform throughout the analyzed regions, crack density does not strictly reflect the magnitude or concentration of tectonic deformation; past deformation in non-cemented sediments may have occurred to the same degree as in the gypsum-indurated soil but may not be preserved due to the poor consolidation. Nevertheless, comparisons of the crack density with topography, slope, and

Table 2.1: Crack aperture transects (locations shown in Figures 2.4, 2.8, 2.11, and 2.13)

	Start		End		L		$\bar{a}$	Σa	ϵ
#	Long.	Lat.	Long.	Lat.	(m)[a]	N[b]	(m)[c]	(m)[d]	(%)[e]
Gypsum "glaciers" region (Figure 2.4):									
1	-70.0199	-21.1796	-70.0188	-21.1794	107.74	14	0.69	8.95	9.057
2	-70.0167	-21.1838	-70.0164	-21.1833	58.84	4	0.76	3.05	5.464
3	-70.0161	-21.1833	-70.0152	-21.1826	134.45	8	0.69	5.53	4.292
4	-70.0155	-21.1901	-70.0149	-21.1894	72.26	11	0.86	9.45	15.049
Southern Hombre Muerto fault (Figure 2.8):									
1	-70.0469	-21.0275	-70.0472	-21.0275	58.32	6	0.80	4.82	9.003
2	-70.0472	-21.0280	-70.0478	-21.0280	26.37	5	0.53	2.65	11.183
3	-70.0475	-21.0288	-70.0480	-21.0288	38.11	6	0.58	3.48	10.035
4	-70.0476	-21.0296	-70.0482	-21.0296	41.98	5	0.76	3.81	9.984
Punta de Lobos alluvial fan (Figure 2.11):									
1	-70.1272	-21.0384	-70.1202	-21.0364	757.32	67	0.14	18.38	2.490
2	-70.1269	-21.0388	-70.1194	-21.0381	785.21	67	0.13	16.81	2.190
3	-70.1273	-21.0393	-70.1232	-21.0397	421.01	46	0.14	13.11	3.210
Antena-Bahía Blanca faults (Figure 2.13):									
1	-70.0999	-21.0979	-70.0991	-21.0977	75.00	6	1.36	8.19	12.252
2	-70.1000	-21.0981	-70.0990	-21.0981	79.76	8	0.91	7.26	10.008
3	-70.0969	-21.1056	-70.0961	-21.1054	72.56	10	0.70	6.96	10.608
4	-70.0908	-21.1152	-70.0882	-21.1130	327.13	18	0.53	9.53	3.000

[a]Total transect length.
[b]Number of cracks along transect.
[c]Mean aperture.
[d]Total width of cracking.
[e]Elongation, defined as $\epsilon = \frac{\Sigma a}{L - \Sigma a} \times 100$.

Figure 2.2: A) Crack density in the Salar Grande region, defined as the total length of cracking per unit area, calculated on a 90 m grid. Cracks are concentrated along fault traces (black lines; solid, bold lines are the faults used in the boundary element modeling) but also show substantial populations spatially uncorrelated with faults. B) Map of length-weighted mean crack strike calculated on the same regularly-spaced grid as the crack density. Much of the map is colored light blue, indicating the strong preferred north-northwest strike of the cracks. On both plots, topographic contours are shown in gray lines at 100 m intervals, with 500 m intervals drawn in bolder lines. The "jagged" line shows the extent of IKONOS imagery coverage.

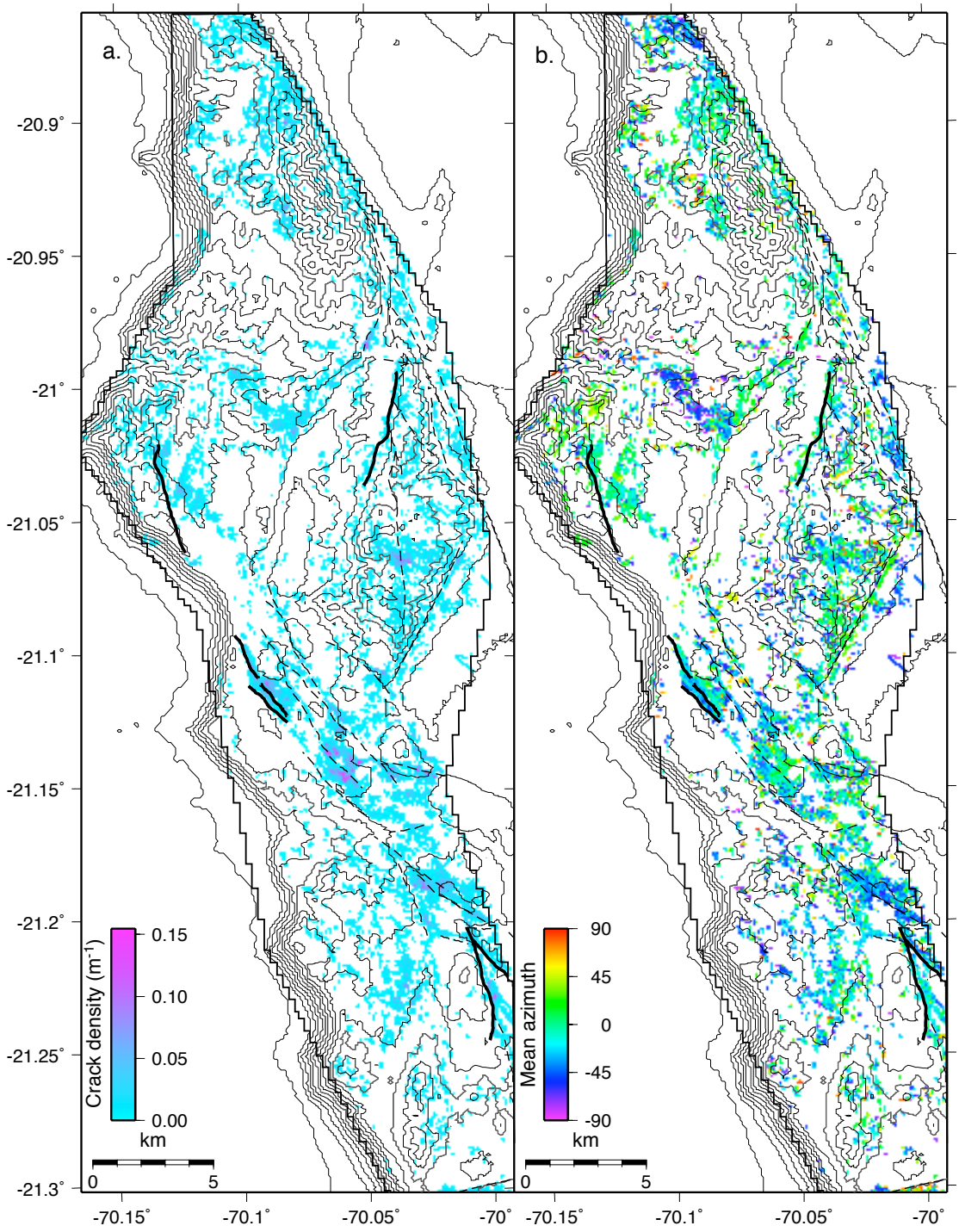
a.
b.
-20.9˚
-20.95˚
-21˚
-21.05˚
-21.1˚
-21.15˚
-21.2˚
-21.25˚
-21.3˚
-70.15˚
-70.1˚
-70.05˚
-70˚
Crack density (m-1)
0.15
0.10
0.05
0.00
km
0
5
Mean azimuth
90
45
0
-45
-90
km
0
5

proximity to larger-scale structures offer important insight into the generation and evolution of the cracks.

2.4 Crack observations in the Salar Grande region

In the Salar Grande region, we performed initial analysis of the structures using IKONOS imagery and used field studies to focus on measuring crack apertures, determining butting relationships, evaluating crack morphology, and comparing cracks to larger-scale structures. We distinguish subsets that have formed due to non-tectonic processes from the majority of cracks, which we interpret to be the result of tectonic stresses.

Cracks show a variety of cross-sectional morphologies, reflecting the material into which they cut, as well as their relative ages. The gypsum-indurated gravel is widespread but varies in thickness throughout the study area. Where bedrock is buried beneath just several centimeters of gravel, cracks show nearly vertical walls with sharp edges at the ground surface. Measurements of joint planes in bedrock (made in the Quebrada Pica, labeled "QP" on Figure 2.1) show a distribution of strikes similar to that of nearby cracks (Figure A.2), demonstrating a correspondence between bedrock weaknesses and surface cracking. Where the gypcrete layer is thicker, crack profiles show a variety of shapes, which we interpret to represent a range of relative ages. Younger cracks maintain vertical walls exposed up to 1 m deep and through time adopt a subtler, more rounded "V" shape indicating ongoing degradation of the crack edges.

The gypsum-indurated gravel creates a competent, brittle surface that exposes and preserves the meter-scale cracks. The hydrous nature of the gypsum in the sediment allows for shrinking and swelling of the sediment crust, which leads to

Figure 2.3: Field photos showing polygonal crack development in the gypsum-indurated sediments. Such cracks form through bulk shrinking and swelling of the saline soil, likely reflecting changes in moisture content (*Tucker*, 1978). Polygons develop at multiple scales, with diameters ranging from centimeter (bottom) to meter (top) scale, with bounding cracks showing apertures of millimeters to centimeters, respectively. For the most part, polygonal cracks cannot be identified in the IKONOS imagery and thus do not contribute to the regional-scale analysis of the cracks.

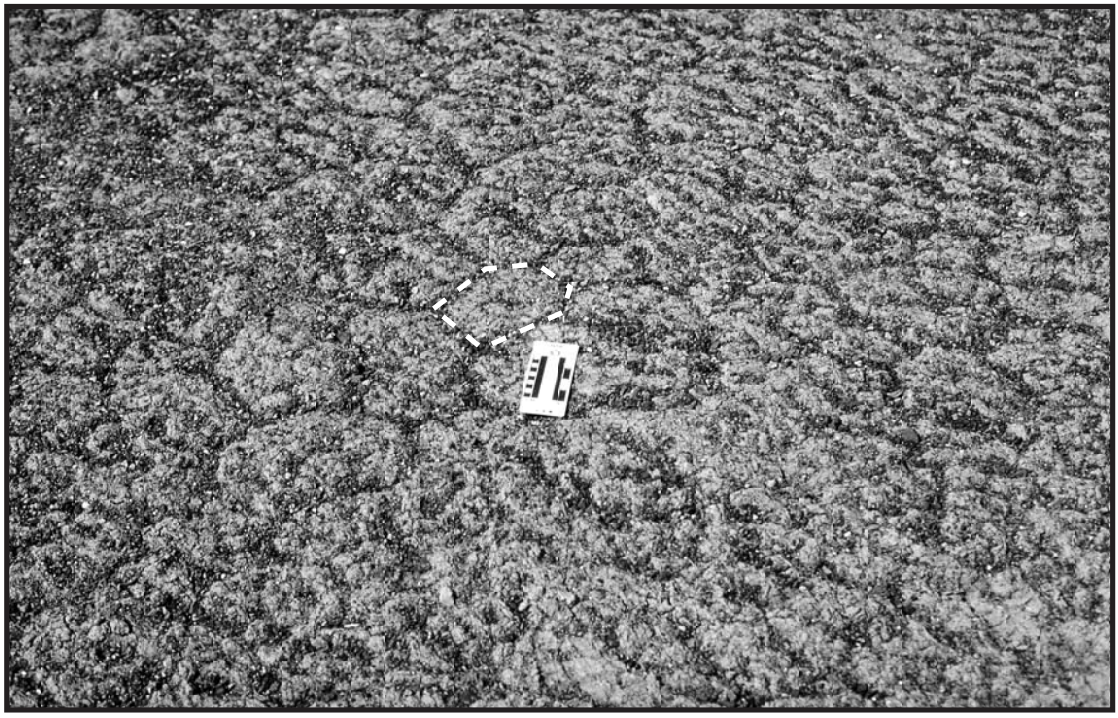

the formation of polygonal cracks through a process analogous to mud cracking (Figure 2.3, *Tucker*, 1978). The cracks that connect to form the polygons range in aperture from millimeter to centimeter scale and create polygons centimeters to meters in diameter. For the most part, these features too subtle to be observed in the remote sensing data, and therefore they are not considered in our regional-scale mapping and statistical analysis of the cracks.

An additional means of non-tectonic cracking is the movement of layers of gypsum-indurated gravel. On a gentle, northeast-facing slope along the southern segment of the Chomache fault ("GG" on Figure 2.1) are numerous cracks whose traces follow topographic contours (Figure 2.4, inset). Transects across these cracks (locations shown as numbered lines on Figure 2.4) yield elongation values ranging from 4–15% (Table 2.1). Midway down the slope, irregular lobe-like fronts of gypsum-indurated sediment (dotted lines on Figure 2.4) separate the cracked region upslope from an uncracked region downslope. In profile, the sediment front is characterized by an abrupt slope, similar in form to a fault scarp. We interpret the front as a layer of gypsum-indurated sediment that has slid downslope. In the process of moving as a relatively coherent sheet, the sediment layer has been pervasively fractured, not unlike crevasse formation in glaciers, or the bulging and landsliding mechanism of deep-seated gravitational slope deformation described by *Agliardi et al.* (2001). The sliding and cracking process could be triggered by shaking during earthquakes or episodic heavy precipitation events that mobilize the indurated sediment horizon. We observe similar cracks in a few other forearc localities and can distinguish them based on their strike parallel to topography, as well as the lobate fronts of sediment that are located downhill of the cracked area.

We interpret the majority of cracks to be of tectonic origin (Chapter 1, *Loveless*

et al., 2005). Microtopography on crack walls can be correlated across the fissure, suggesting a rapid opening process. In contrast to the polygonal cracks described above, most cracks have a linear trace, ranging in length from meters to 1 km. In some cases, the sides of adjacent polygonal cracks have been reactivated by a larger-scale forcing to form a continuous crack with a zigzag shape that closely approximates a linear trace, reflecting the direction of applied opening stress (Figure 2.5). Whereas the cracks that we attribute to downhill sliding show strikes that trace topographic contours, the linear tectonic cracks maintain a consistent strike that is independent of local slope (for example, the east-west striking crack in Figure 2.5). As discussed above, the aperture of cracks is difficult to define, as erosion of the once-sharp crack edges obscures the true magnitude of opening.

Cracks are filled with a variety of materials, and the nature of fill has implications for the crack evolution. We observe banded gypsum that has plated onto the nearly vertical crack walls (Figures 2.6, 3.2). Through time, the crack is sealed with gypsum from the walls inward to the center. Those that are open presently have either been completely sealed and subsequently reopened by a tectonic event, or they have been incompletely filled. In some filled cracks, gypsum and other salts are mixed with clastic material that is likely transported by wind and occasional precipitation events.

The crack density map (Figure 2.2a) shows that cracks are concentrated around faults, yet many other cracks are spatially uncorrelated with faults. Furthermore, no obvious relationships exist between crack density and topography or slope (Figure 2.2a); cracks are located on gentle to steep slopes, on flat-topped hills, and in broad valleys. The length-weighted mean crack strike throughout the entire study area is 347° (Chapter 1), and cracks show this preferred orientation throughout

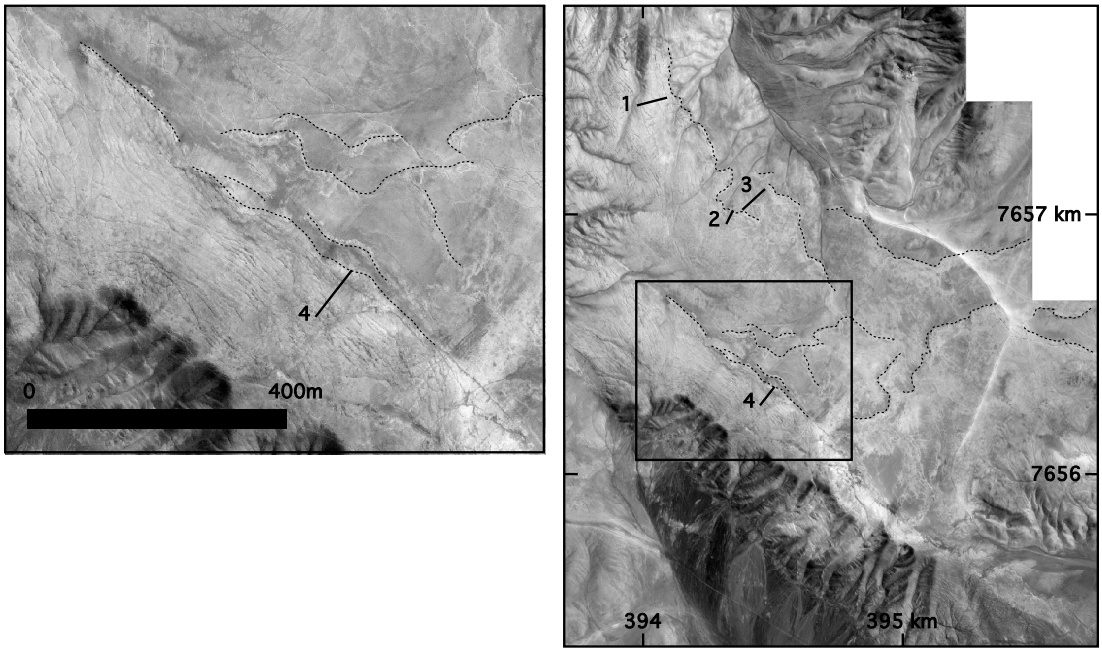

Figure 2.4: IKONOS image showing the "glaciers" region near the southern Chomache fault. The irregular black lines highlight the lobe-like fronts of sediment layers that have slid downhill, while the straight, solid lines show the positions of transects taken across the cracks. The inset zoom shows the arcuate cracks that parallel topographic contours, concentrated upslope from the main sediment front. Similar features with associated cracks are located southwest of this site, as well as in other locations in the forearc.

much of the region. Figure 2.2b shows the length-weighted mean crack strike calculated within each grid cell, with the same spacing as the crack density. The majority of the crack azimuth map is blue-green, showing the preferred north-northwest strike.

2.5 Boundary element modeling

The strong preferred orientation of cracks over a large area indicates that a stress field acting on a similar spatial scale is responsible for their formation. With the

Figure 2.5: Field photo showing an example of the reactivation of polygonal cracks to form through going, linear cracks. The trace of the north-south striking crack has a "zigzag" appearance, indicating that east-west tension reactivated adjacent polygonal cracks along a path of least resistance. Butting relationships in this area are, as in all locations, ambiguous, with some of the east-west striking cracks butting into the north-south feature and some continuing through it. We interpret these inconsistent butting relationships as indication that cracks evolve in a cyclic pattern, responding to episodic imposition of stress.

exception of body forces, the sole source of stress in the forearc region is the subduction zone seismic cycle. Therefore, the structures that we observe in the region — both cracks and faults — reflect deformation induced by subduction processes. The enhancement of cracks along fault traces suggests that the regional stress field is locally perturbed by the faults, resulting in a concentration of cracking. We seek to test this hypothesis through boundary element modeling.

As discontinuities in the Earth's crust, faults perturb the regional stress field. Using Poly3D, a three-dimensional boundary element code (*Thomas*, 1993), we

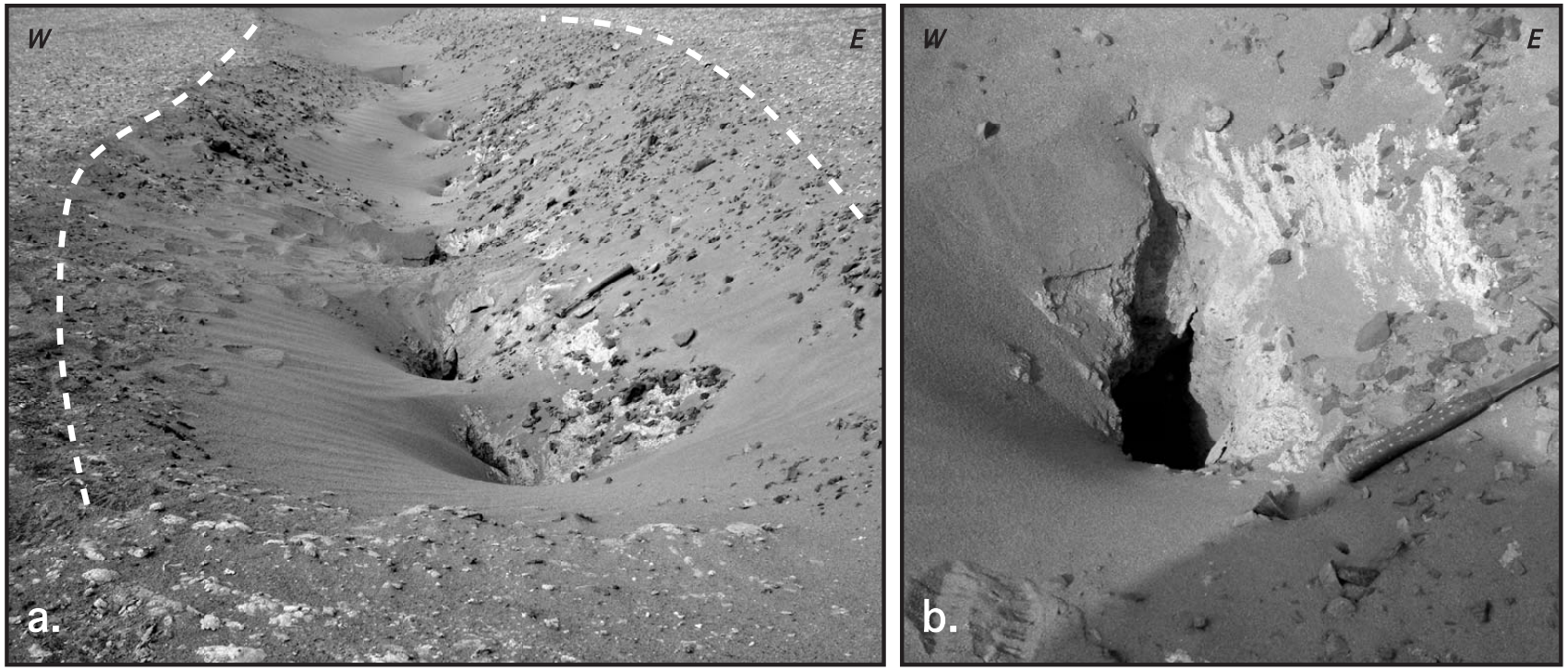

Figure 2.6: Field photo showing a crack filled by gypsum. a. The crack strikes in the view direction, with weathered walls delineated by the dashed white lines. Gypsum has filled the crack, but subsequent reactivation and/or dissolution of the gypsum fill has created discontinuous instances of reopening. b. Close-up of the gypsum fill, showing the vertical banding that we interpret to reflect the way in which gypsum accumulates on crack walls. Through time, gypsum precipitates onto the vertical crack walls, filling the crack from the outside in.

model the Hombre Muerto, Punta de Lobos, Antena-Bahía Blanca, and Geoglifos faults as frictionless discontinuities in an elastic half-space (with Young's modulus of $E = 3 \times 10^{10}$ Pa and Poisson's ratio of $\nu = 0.25$) and apply remote stress boundary conditions consistent with those induced by the subduction zone earthquake cycle. By considering the faults as frictionless surfaces, we model the maximum possible perturbation to the stress field that the discontinuities can induce within the elastic medium (e.g., *Crider and Pollard*, 1998). We compare the calculated stress fields around the faults to the distribution and orientations of adjacent, enhanced cracks. Based on the paucity of observed lateral offsets, we interpret the majority of cracks to be mode 1 fractures (Chapter 1), thus cracks should propagate parallel to the direction of maximum principal compression (σ_1) and open in the direction of minimum principal compression (σ_3, e.g., *Pollard and Segall*, 1987). However, once a crack is formed, it may be reactivated by a variety of stress fields so long as some component of the stress acting normal to its walls is tensional.

In all models, we define the geometry of the modeled discontinuities by projecting the surface trace to depth in an elliptical shape (Figure 2.7). In the accompanying material (Appendix D), we test several different fault dips, burial depths, and aspect ratios in order to investigate the general patterns of surface stress that result from varying fault geometries; we present only our preferred models in the present chapter. We define the fault length as L, the maximum downdip width of the fault as D, and the burial depth — representing the depth of the top of the fault — as B (Figure 2.7). In all cases presented here, we define both D and B to be some fraction of L.

The remote stress applied to all models is based on the calculated stress change

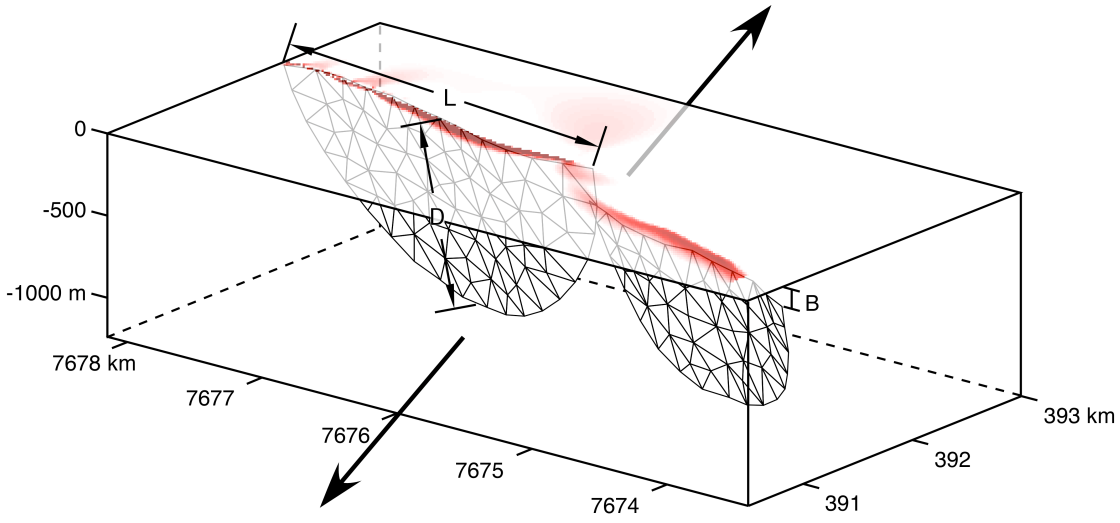

Figure 2.7: Diagram illustrating components of the boundary element models. Modeled faults are constructed by extrapolating the surface trace to depth in an elliptical shape. The burial depth B and the maximum downdip width of the fault D are defined as fractions of the total fault length L. The geometry is discretized using triangular elements on which various traction boundary conditions are imposed. The presence of such a discontinuity in the otherwise homogeneous elastic half-space introduces concentrations of stress, localized around the fault traces (example transparent color map), when subject to remote stress conditions, the direction of which is shown by the black arrows.

caused by a great underthrusting earthquake offshore Salar Grande, such as the 1877 event (Chapter 3, *Comte and Pardo*, 1991), and an accompanying interseismic period. During the earthquake, the Salar Grande region undergoes tension, which we specify to be of magnitude 2×10^6 Pa directed along an azimuth of 255°, parallel to the direction of plate convergence. During the interseismic period of the subduction cycle, we apply the opposite sense of stress: uniaxial compression directed 255°. Other remote stress conditions are explored in Appendix D.

Applying the equal and opposite senses of remote loading assumes that the stress changes induced at the surface are completely elastic. As shown in Chapters

4 and 5, the distribution of interseismic strain accumulation and coseismic slip on the plate interface affects the spatial patterns of stress induced at the surface. Therefore, it is also possible that forearc faults experience compression during subduction earthquakes (Chapter 4) and tension due to flexural effects during the interseismic period (Chapter 5), depending on the details of slip on the plate boundary. As shown in Chapter 5 (specifically in Figure 5.11), upper plate fault slip may take place exclusively when triggered by an interplate earthquake or during the interseismic period of the subduction cycle, depending on the loading history of that fault. In this paper, we investigate the more general, regional-scale patterns of loading that results from the seismic cycle, assuming that the coseismic period is characterized by tension directed along the plate convergence vector, while the interseismic period exerts compression in the same direction, at least in the Salar Grande region (Chapter 5).

In order to assess the compatibility between the modeled fault-perturbed stress fields and the crack observations, we plot the normal stress change resolved on vertical planes striking roughly parallel to the local mean crack strike (see rose diagrams in Figure 2.8, 2.11, 2.13, and 2.15). We define tensional normal stress as positive, encouraging opening along vertical planes. A plane of weakness that strikes parallel to the specified direction and lies in a zone of positive resolved normal stress is thus a candidate for (re)activation in response to the imposed stress and could form a surface crack. Varying the strike of the vertical plane onto which the normal stress is resolved by 10–20° does not substantially affect the patterns observed in the stress fields. For models in which uniaxial tension comprises the remote stress tensor, we subtract the remote tension resolved onto the specified vertical plane in order to isolate the stress field perturbation caused by the presence

of the faults. Those models subject to compression are not corrected in this way, as any tensional normal stress value must result solely from the perturbation induced by faulting. In the following sections, we present discussions of the compatibility between the normal stress fields and the spatially associated cracks.

In addition to presenting the modeled stress fields, we also examine patterns of vertical deformation induced by the remote stress boundary conditions. While the displacement fields predicted by the models may be reversed or relaxed by subsequent tectonic processes, they provide a first-order picture of how the ground surface is affected by fault processes which, through time, can form fault-related topography (*King et al.*, 1988). Because the modeling is carried out in a half-space, regional surface tilt and existing topography (namely mountain ranges) are not considered. Therefore, we restrict our comparisons between the models and the surface morphology to evaluation of the compatibility between the relative vertical displacements and the fault-related topography only. Given that the fault-related topography we discuss is relatively subtle, details are not well captured by available digital elevation models. Therefore, we instead discern the topographic features from the IKONOS imagery, which provides a detailed picture of the location of drainages and zones of relative subsidence given by where young alluvial materials accumulate.

2.6 Salar Grande region fault modeling

2.6.1 Hombre Muerto fault

The Hombre Muerto fault ("HM" on Figure 2.1) is a north-northeast striking fault that parallels a mountain range just west of the Salar Grande (Figure 2.8). The

east-side-down morphology of the scarp creates a pattern of topographic inversion in which the toe of the mountain front is elevated relative to the mountain front itself. Along much of the fault, the scarp is separated from the mountain front by a broad, flat-bottomed valley. The scarp shows variation in morphology along strike, which potentially suggests a segmented character. Atop the 7–8 m high scarp of the northern part of the fault trace, two orthogonal sets of cracks strike obliquely to the fault and show well-developed, V-shaped morphologies with measured apertures up to 2 m, depths up to 1.5 m, and vertical offset of up to 1 m (Figure 2.8a, 2.9). Cracks adjacent to the southern part of the Hombre Muerto fault, which is expressed as a subtle, 1–2 m scarp, also originated as two sets with different strikes, but they have been reactivated in a "zigzag" manner, with alternating N- and NE-striking cracks having been exploited to maintain an aggregated crack strike approximately parallel to the trace of the scarp (Figure 2.8c). The northern and southern traces of the fault are separated by a region in which a topographic scarp is not obvious, the width of the cracked region is greater than farther north and south, no valley separates the mountain front from fault-related topography, and drainages from the adjacent hills cut across the fault trace (Figure 2.8b), as opposed to the dammed drainage pattern evident along the northern fault trace (Figure 2.8a).

While the obliquity between the cracks and fault strike could be interpreted as indication of previous episodes of both sinistral and dextral motion on the fault, the lack of laterally-offset drainages across the scarp shows that cumulative transverse motion has been minimal (Figure 2.8a). Butting relationships between the scarp-top cracks are ambiguous, with no clear evidence that cracks of one orientation are younger than the other. The cracks may have evolved either simultaneously

Figure 2.8: IKONOS image of the Hombre Muerto fault region. Bold dashed line indicates the position of the fault scarp. The white segments show the surface traces of the two distinct segments used in the modeling, while the sum of the white segment plus the intervening black segment shows the single fault model geometry (Appendix D). A) Surface cracks exist at least 100 m from the fault trace (black arrows) but are enhanced within a 20–50 m wide zone near the crest of the scarp (zone of enhancement is shown by the dotted line). Two sets of cracks, one striking northeast and the other northwest, show inconsistent butting relationships. Westward-flowing drainages off of the mountain front are dammed or diverted by the topographic scarp. B) Zoom image of the transition zone between the northern and southern fault segments, showing the continuity of drainages from east to west in the absence of a topographic scarp. The zone of cracking is $\sim$400 m wide. C) Zoom image of the southern fault segment, which shows minimal topographic signature yet has enhanced surface cracks along its trace. Cracks show a "zigzag" pattern of reactivation, indicating that the two sets of cracks have been reactivated by fault processes following the path of least resistance to approximate a linear crack. Transects across the cracks, specifications of which are presented in Table 2.1, are shown as the numbered lines.

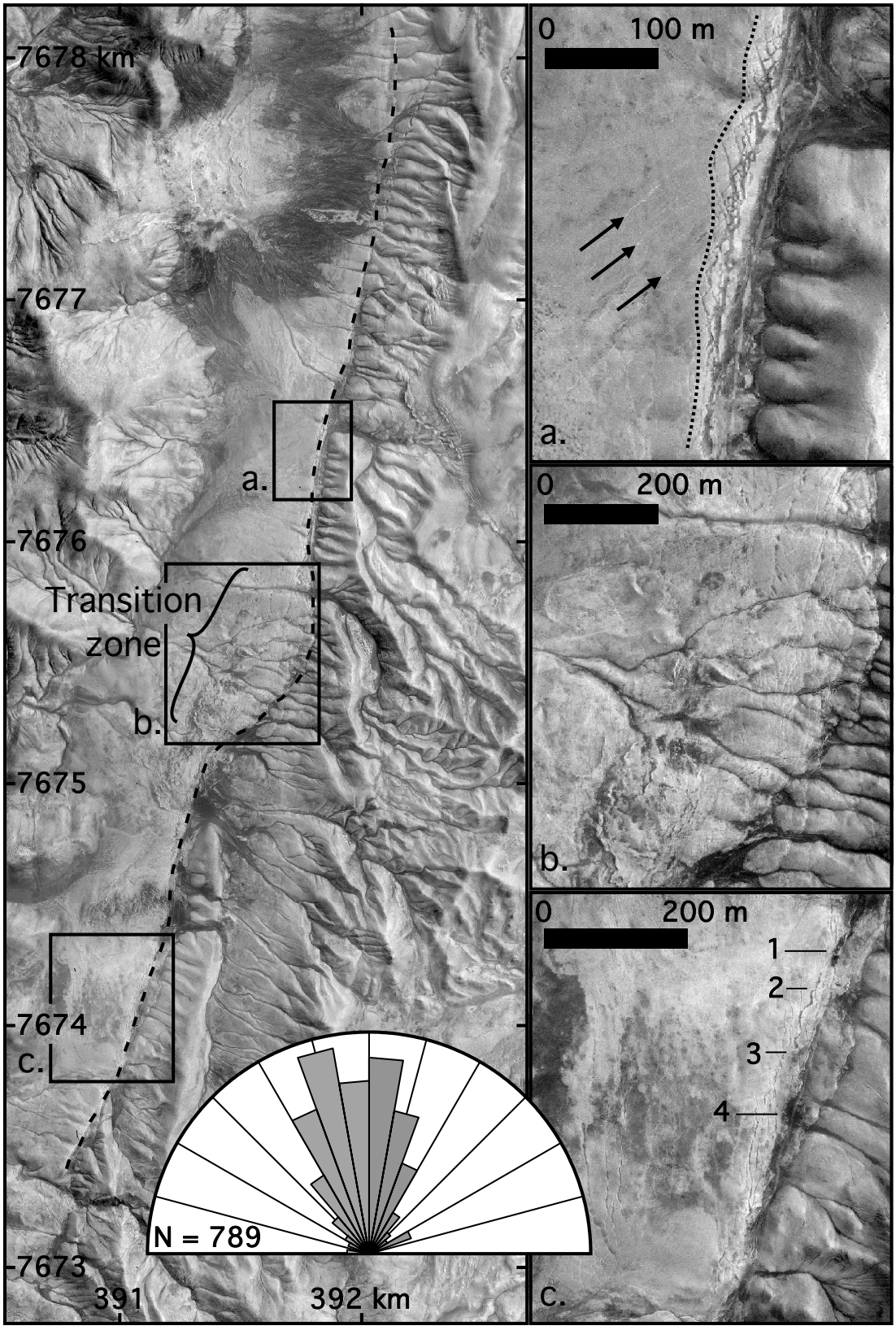
7678 km
7677
7676
7675
7674
7673
391
392 km
a.
b.
c.
Transition
zone
N = 789
0
100 m
a.
0
200 m
b.
0
200 m
1
2
3
4
c.

as conjugate sets or in a cyclic manner, with one set responding to a particular orientation of stress, followed by activity of the other set in a subsequent event. Cracks visible several hundred meters west of the fault scarp (arrows in Figure 2.8a) abruptly increase in aperture and depth within about 50 m from the scarp crest (Figure 2.9). There is a pronounced difference in aperture between cracks atop the scarp crest and those lying just 50 m west of the fault, indicating that the enhanced opening of cracks resulting from growth of the scarp is limited to the region immediately around the scarp crest. We suggest that, based on the sudden change in their morphology, cracks in this area predate formation of the modern topographic scarp, but not necessarily the underlying fault itself, and have been locally enhanced by the most recent instances of fault activity and scarp construction.

Trenching along the Hombre Muerto fault reveals a variety of fault plane dips, ranging from a shallowly- to steeply-inclined to the west (*Carrizo et al.*, 2007). Reverse faulting on structures oriented as such would produce a scarp geometry similar to that observed, and the enhancement of cracks at the scarp crest could be explained as the result of flexural folding above the fault. Because of the observed fault dip and east-side-down scarp geometry, our preferred model of the fault is that in which remote horizontal compression is applied to a west-dipping fault. Based on the distinct differences in scarp morphology along strike, from prominent and sharp in the north to subtle in the south, we model the fault as two fault segments, both of which terminate within the "transition zone" (Figure 2.8). Because the scarp of the southern fault segment is more subtle than that of the northern segment, we model different burial depths of each segment. The northern segment is modeled as nearly emergent ($B = L/200$), while the southern segment

is buried deeper ($B = L/20$). An alternative explanation for the difference in scarp morphology is that the southern segment has simply experienced less displacement and/or has been inactive for longer than the northern segment, thus the scarp has experienced a greater amount of degradation. The lack of cumulative lateral offset we observe along the fault is consistent with remote stress directed 075°, at a high angle to the fault strike.

Figure 2.10a shows the patterns of normal stress resolved onto vertical planes striking 000° that result from remote compression imposed on the modeled Hombre Muerto fault. The narrow zone of tension concentrated along the northern segment scarp crest is consistent with the enhanced cracking observed along the fault. Specifically, the narrow extent and abrupt nature of this anomalous stress mirrors the dramatic change in crack aperture within 50 m from the fault trace (Figure 2.9a). The model does not predict tensional stress around the transition zone, but it is possible that this region is characterized by a sequence of buried parallel fault segments, each of which introduces a perturbation to the surface stress field such that the cumulative result is a zone of diffuse tension without formation of obvious scarps. The modeled deeper burial of the southern segment of the Hombre Muerto fault significantly affects the extent of the tensional stress field at the surface (Figure 2.10a), shown by the fact that negligible tension is predicted along the scarp crest. It is possible that our interpretation of the subtler scarp topography representing a deeper buried fault is incorrect; indeed, a model in which the Hombre Muerto fault is simulated a single, shallowly buried fault ($B = L/200$) predicts tension along a greater proportion of its length (Figure D.3a–d), which is more consistent with the observations of crack aperture enhancement. A segmented fault model in which the burial depth of the southern segment is shallow

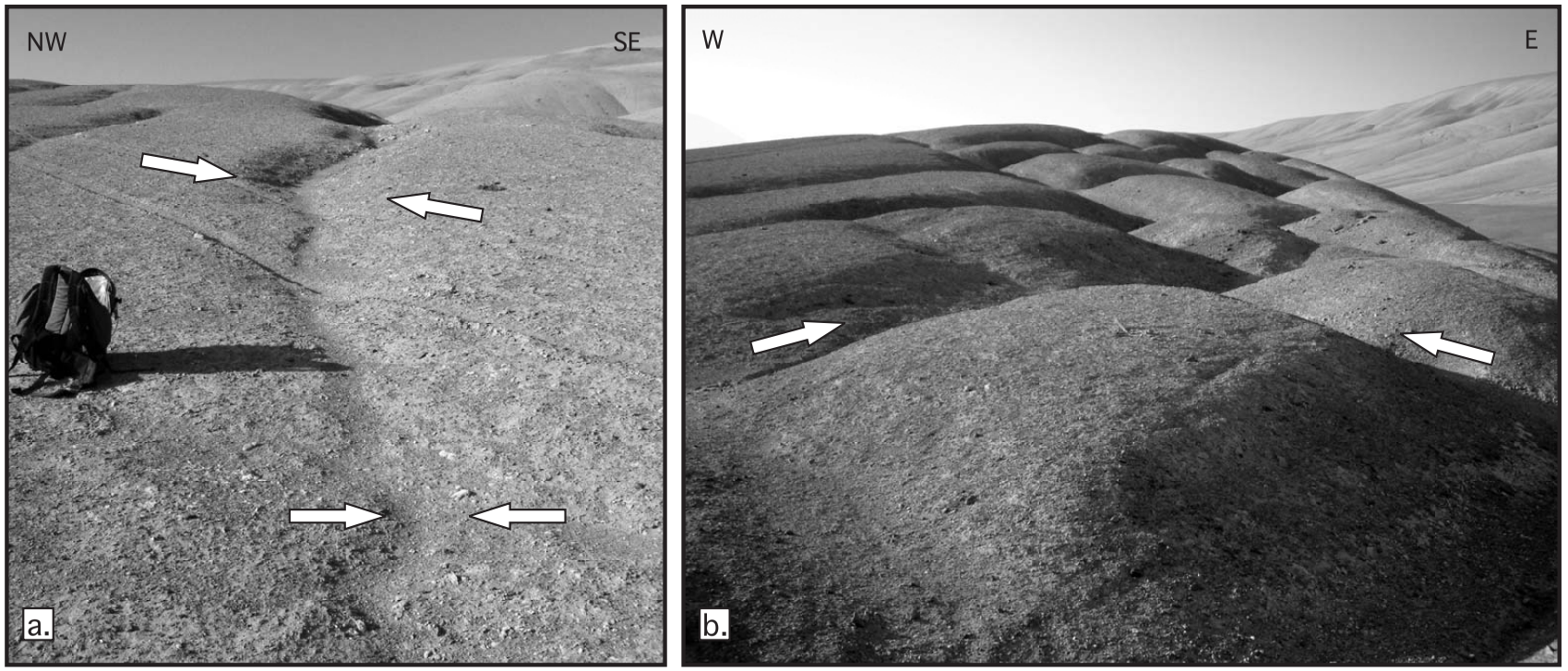

Figure 2.9: Field photos showing enhancement in the aperture of cracks near the Hombre Muerto fault, in the area shown in Figure 2.8a. a. The portion of the crack in the foreground increases abruptly in aperture and depth within ∼50 m from the scarp crest. b. Cracks along the crest of the scarp show well-developed "V" shaped profiles with apertures and depths greater than their continuations away from the scarp. Two sets of cracks, identified by the white arrows, both strike obliquely to the fault scarp, the trend of which is in the direction of view.

should also produce a zone of tension along the scarp crest.

The general patterns of predicted uplift and subsidence along the Hombre Muerto fault (Figure 2.10b) agree reasonably well with the observed fault-related topography, which can be discerned from the IKONOS image shown in Figure 2.8, indicating that repeated episodes of fault slip can explain the surficial expression. Because of the near-surface burial depth of the northern segment, the resulting fault scarp is higher and more abrupt than the subdued scarp of the deeper-buried southern segment. In the transition zone between segments, the gradient of the vertical displacement field is less than that along the fault segments, consistent with the continuous slope that is cut by continuous drainages in that area. Although the model is consistent with the topography and crack distribution along the northern segment, the disagreement between the model stress field and the crack distribution both within the transition zone and along the southern segment suggests that some process not considered by the simple simulations is responsible for the enhancement of crack apertures along the Hombre Muerto fault. We explore additional model parameters and results in Section D.3.1.

2.6.2 Punta de Lobos fault

The Punta de Lobos fault ("PL" on Figure 2.1, detailed image in Figure 2.11) marks the eastern mountain front of a ∼1000 m high range just east of the ∼400 m coastal escarpment. It demonstrates east-side-down normal slip on a fault with strike N10W and dip 82°E (exposure at white circle in Figure 2.11, *González et al.*, 2003), lowering the alluvial fan relative to the mountain front. Dating of an ash layer, vertically offset ∼1.5 m by the fault, yields an age of 3.5 Ma, placing an upper age limit on fault activity. Fresh-appearing fragmented blocks of gypsum-

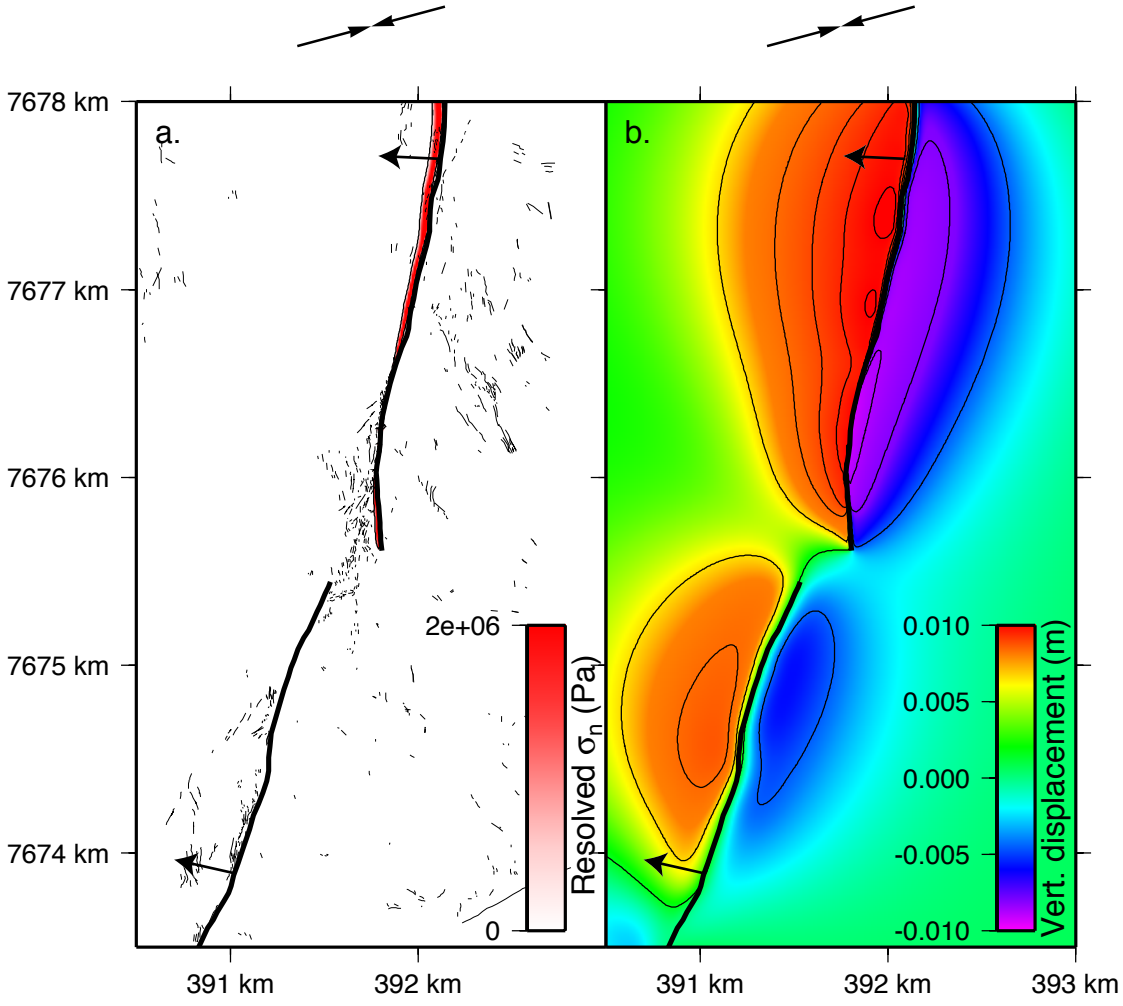

Figure 2.10: Results of modeling in which the Hombre Muerto fault is simulated as a structure dipping 75°W (dip direction denoted by arrows), broadly consistent with the trenching observations of *Carrizo et al.* (2007), and subject to compressional remote stress conditions directed 075° (black arrows above figures). The modeled fault segment traces are shown as bold black lines in both panels, while the thin black lines in a. show the mapped cracks. a. Tensional stress resolved onto planes striking 000°, which is the mean crack strike in this region (see rose diagram in Figure 2.8). b. Vertical displacement field. The linear patterns of uplift and subsidence along the fault traces mirror the fault-related topography as inferred from Figure 2.8, and the lack of relief across the transition zone between the two faults is also consistent with the observed topography. Additional stress field results using other model parameters are shown in Figure D.2 and D.3, while vertical displacement fields are shown in Figure D.4.

Figure 2.11: IKONOS image of the Punta de Lobos fault region. The dashed line shows the trace of the fault used to construct the boundary element model. The dotted line outlines the gypsum indurated alluvial fan sediments (lighter colored material) that are pervasively cut by surface cracks. Cracks also cut the darker, unconsolidated alluvium but are better expressed in the cemented sediments. Solid line segments on the alluvial fan show the position of crack aperture transects presented in Table 2.1. The intersection between the major NNE trending drainage and the fault trace (white circle) marks the location of the fault plane exposure reported by *González et al.* (2003). Many of the linear features on the fault scarp north of the exposure site are cracks that have been exploited as headwalls of landslides.

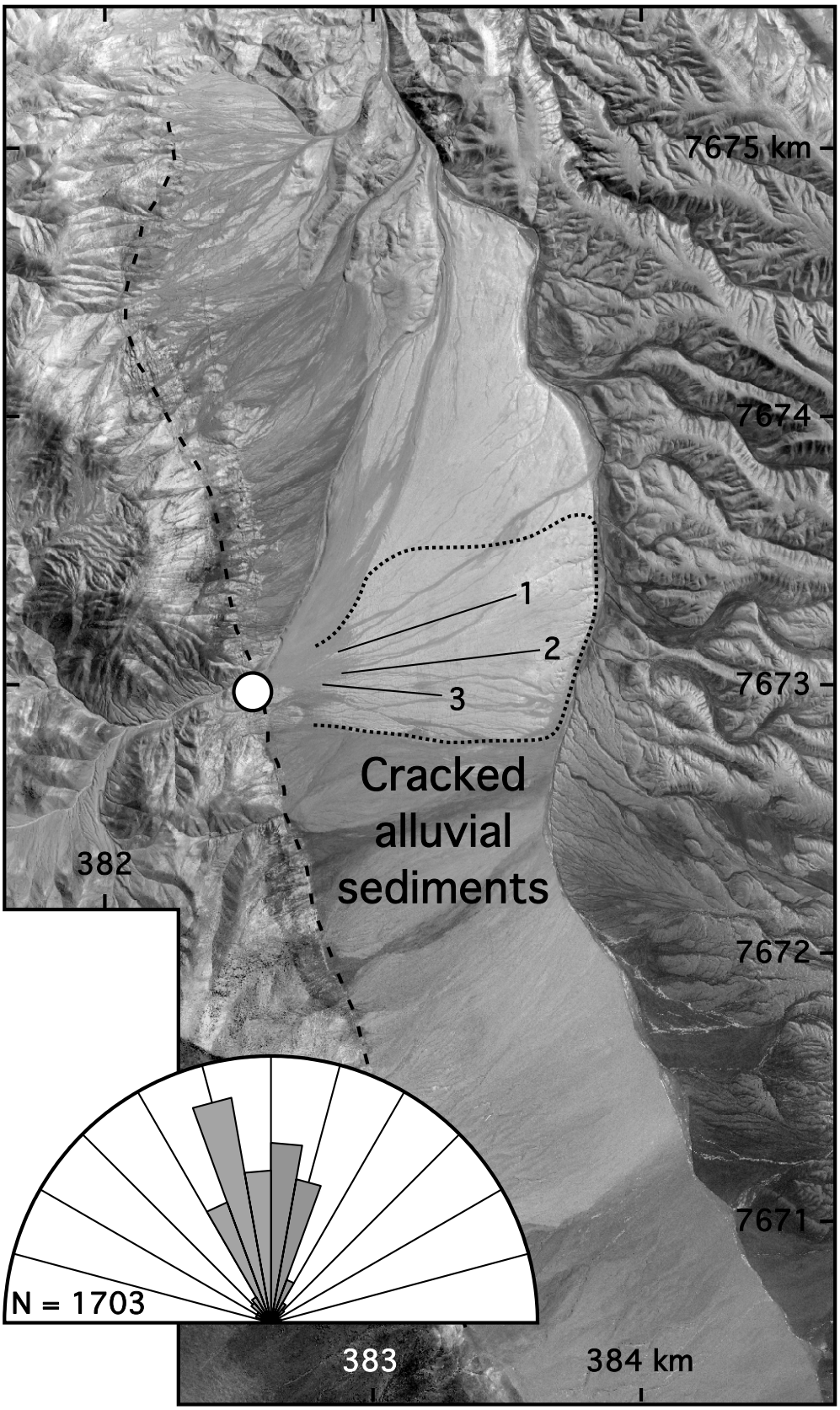
7675 km
7674
7673
7672
7671
382
383
384 km
1
2
3
Cracked
alluvial
sediments
N = 1703

indurated sediments on the footwall slopes (Figure 2.11) indicate recent landsliding, potentially triggered by seismic activity on the Punta de Lobos fault or a strong interplate earthquake. Bedrock outcrops in the footwall show jointing planes with strikes similar to the surface cracks. East of the fault exposure is a fan of alluvial sediments that have been cemented by gypsum. Numerous cracks cut the fan and show a strong preferred orientation parallel to the fault (rose diagram, Figure 2.11). The cracks affect a large expanse of the fan — up to 1 km away from the Punta de Lobos fault (dotted outline in Figure 2.11). Cracking is best preserved in the gypsum-indurated sediment, with less consolidated material showing cracks that are both less frequent and smoother in profile morphology. We measured several transects across the suite of cracks in the indurated fan to document to magnitude of extension that they represent (numbered lines on Figure 2.11). Summed opening of 13–18 m along transects 420–790 m long yield elongation values of 2–3% (Table 2.1).

Unlike the cracks along the Hombre Muerto fault, the cracks cutting the alluvial fan to the east of the Punta de Lobos fault do not indicate enhancement adjacent to the fault. Crack spacing and morphology remain relatively constant up to 1 km from the trace of the fault. Some cracks immediately to the east of the fault exposure are likely enhanced by faulting, but larger-scale stresses, such as those associated with interplate and not intraplate earthquakes, are a more plausible explanation for this pervasive cracking.

The normal kinematics of the Punta de Lobos fault are constrained by the surface exposure described by *González et al.* (2003), and so we model the fault only as planar fault dipping 80°E, consistent with the field observation, subject to remote tension applied along the plate convergence vector. Figure 2.12 shows the

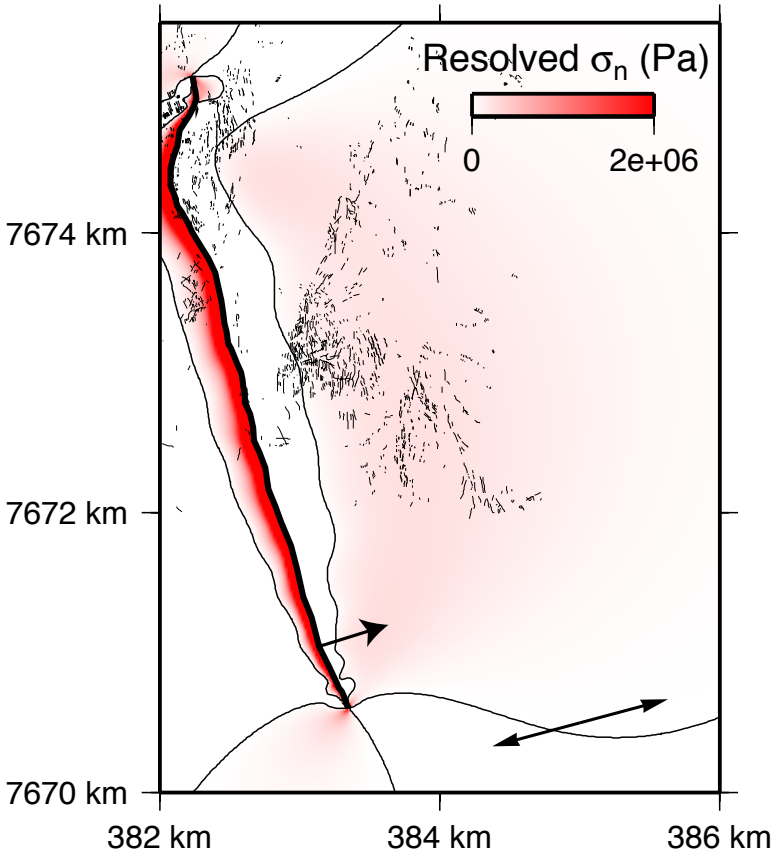

Figure 2.12: Tension resolved onto vertical planes striking 350° around the Punta de Lobos fault. The model is subject to 2×10^6 Pa of uniaxial tension directed 255°, causing normal slip on the fault. The planar fault dips 80°E (dip direction marked by the arrows), consistent with the observations of *González et al.* (2003), and has an aspect ratio of $D = L/2$.

stress perturbation resulting from the fault, represented as normal tension resolved onto vertical planes striking 350°. North of the fault plane exposure site (white circle in Figure 2.11), cracks located in the footwall lie within the zone of tension predicted by the model. A region of low-magnitude tension in the hangingwall extends eastward from a point several hundred meters from the fault trace. The zone of tension encompasses many of the cracks mapped in the hangingwall alluvial fan, but the small magnitude may not be capable of driving the evolution of these

cracks. Near the northern terminus of the modeled fault, the numerous cracks lie within a region where tension is not predicted. The actual trace of the fault in this area is difficult to identify, and it may terminate with branched ends rather than as a discrete plane, which could explain the wider extent of cracking observed.

2.6.3 Chomache fault system: Antena and Bahía Blanca segments

The Punta de Lobos fault marks the northernmost segment of the Chomache fault system (*Carrizo et al.*, 2007) and connects to the south with the NNW-striking Antena and Bahía Blanca segments ("AB" on Figure 2.1, detailed image in Figure 2.13). The Chomache system as a whole represents a segmented dextral fault system, with strike-slip kinematics well defined by geomorphic offsets (*González et al.*, 2003; *Carrizo et al.*, 2007). The scarp of the Antena Norte segment ("AN" on Figure 2.13) is characterized by a well preserved free face and numerous fault-parallel open cracks present in both the up- and downthrown blocks, suggesting that flexure of a fault-related fold is not exclusively responsible for the cracking. The linear trace of this segment argues for a steep dip, which is supported by recent trenching (*Carrizo et al.*, 2007) and an exposure on the coastal cliff showing a dip of 75°E (*González et al.*, 2003). Transects taken across cracks along the Antena Norte segment suggest a partitioning of deformation between tensile fracturing and fault slip: where the fault scarp is expressed as a vertical step, cracks are both narrower and less frequent than along stretches where the scarp morphology is poorly defined and cracks are wide and fresh (transects 1 and 2 on Figure 2.13a, Table 2.1). This variation in scarp morphology is consistent with the results of *Hilley et al.* (2001), who demonstrate the capabilities of surface cracks in modifying

Figure 2.13: IKONOS image showing the Antena-Bahía Blanca segments of the Chomache fault system. The black dashed lines show the surface traces of the fault segments, and the dashed oval outlines the region between the fault segments that is cut pervasively by surface cracks. A) Zoom image showing a portion of the Antena Norte segment ("AN") where a well-defined fault scarp (south) loses its clear topographic expression in a wide zone of giant cracks (north). We interpret this pattern as a variation in how deformation across the fault zone is partitioned: where the fault scarp is well-developed, deformation is accommodated primarily by fault slip, and where cracks are present in place of a single fault scarp, deformation is distributed between minor fault slip and opening of substantial surface cracks. B) Zoom image showing the cracked alluvial material in the eastern blocks of the Bahía Blanca ("BB") and Antena Sur ("AS") segments. Alluvial material transported east of the Bahía Blanca segment is dammed by the subtle topography related to the Antena Sur segment. The lighter colored material has been indurated by gypsum, while the darker regions are covered in younger, unconsolidated sediment. Cracks cut both types of material but are best preserved in the cemented sediments. The pull-apart basin at the releasing bend on the Bahía Blanca is one example of the large-scale geomorphic data that place constraint on the kinematics of the Chomache fault system. Sediments within the basin have washed off of the mountain range southwest of the fault and are dammed by the well-developed fault scarp. Numbered lines show the position of crack aperture transects.

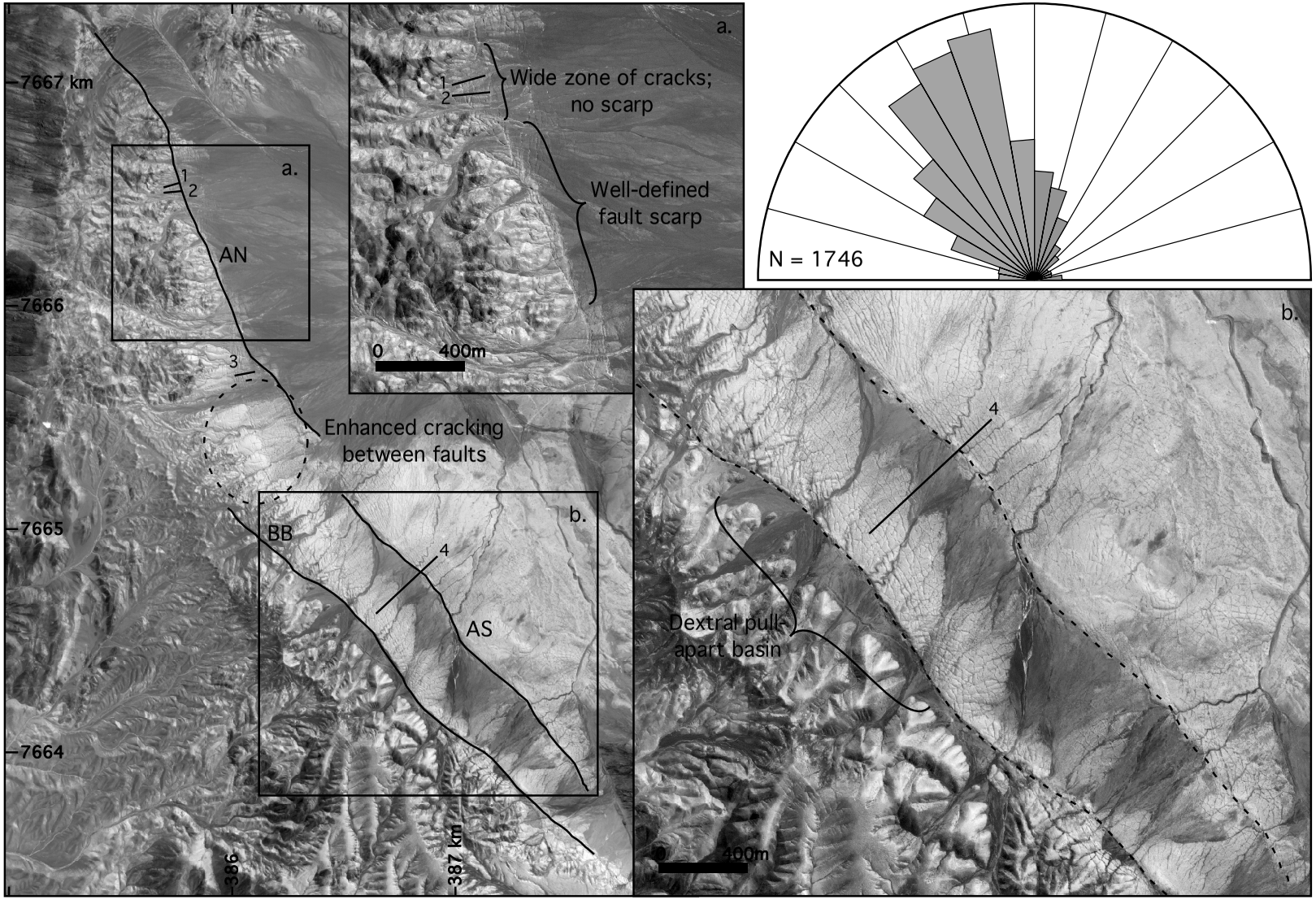
7667 km
7666
7665
7664
386
387 km
a.
1
2
AN
3
Enhanced cracking
between faults
b.
BB
4
AS
Wide zone of cracks;
no scarp
Well-defined
fault scarp
0
400m
N = 1746
Dextral pull-
apart basin

fault scarp profile shape by allowing partitioning of deformation among the two types of structures.

The Bahía Blanca segment ("BB" on Figure 2.13) is highlighted by a small pull-apart basin created by dextral slip across a releasing bend (Figure 2.13b). A small scarp 2–3 m high features a well-preserved free-face and west-side-down motion. This scarp creates a pattern of topographic inversion and mountain front slope interruption similar to that seen at the Hombre Muerto fault. East of the fault scarp numerous well developed open cracks cut a gypsum-indurated fan of sediments (transect 4 on Figure 2.13, Table 2.1). Morphological characteristics of some cracks, including oversteepened, caved-in walls and solution pits, suggest that they have been used as conduits by surface runoff and/or groundwater. As in the case of cracks adjacent to the Punta de Lobos fault, crack spacing and morphology remains roughly constant regardless of distance from the fault scarp (Figure 2.13b). Crack strikes in this region range from subparallel to oblique relative to the Bahía Blanca scarp. Around the northern extent of the fault segment, cracks strike about 345°, while the fault strikes around 315°. The 30° obliquity between cracks and fault is consistent with a stress field whose σ_1 trends 345°, driving opening of the observed cracks and oblique dextral slip on the fault.

Alluvial sediments transported eastward from the upthrown block of the Bahía Blanca segment are dammed by a small scarp here interpreted to represent the topographic expression of the Antena Sur fault segment ("AS" on Figure 2.13). The topography of this scarp is very subtle, yet its trace is parallel to that of the Bahía Blanca and Antena Norte segments, suggesting that it is a part of the same fault system. The west-side-down morphology of the scarp is similar to that of the Bahía Blanca segment but opposite the pattern generated by motion on

the Antena Norte segment, indicating a change in dip between the southern and northern faults. The eastern block of the Antena Sur segment is blanketed by gypsum-indurated sediments that have been thoroughly fractured (Figure 2.13b).

Between the northern ends of the Antena Sur and Bahía Blanca segments and the southern end of the Antena Norte segment is a region in which cracking is pervasive and individual cracks show substantial aperture (dashed oval in Figure 2.13, transect 3 of Table 2.1). The topographic scarps associated with the Antena Norte and Sur segments are subtle to nonexistent within this region, again suggesting that deformation may be partitioned between cracking and fault slip/scarp growth, or that the interaction between the fault segments produces an anomalous stress field. The enhanced cracking in this area is similar to the diffuse deformation seen in transition regions between other sets of overlapping, interacting faults (e.g., *Crider and Pollard*, 1998).

The reported 75°E dip for the Antena Norte segment (*González et al.*, 2003), in conjunction with the east-side-down morphology of the fault scarp, indicates that this fault experiences normal dip slip to accommodate extension in the direction of plate convergence. However, recent trenching and morphological analysis presented by *Carrizo et al.* (2007) suggests that two steeply-dipping faults with opposing vergence describe the southern extent of Antena Norte fault. The lack of continuously-exposed fault planes inhibits a conclusive kinematic analysis, but the exposures are interpreted to demonstrate both high-angle normal and reverse faulting (G. González, pers. comm., 2007). We know from the scarp morphology that there is a change in polarity between the northern and southern faults. In order to investigate the style of faulting most consistent with the associated cracks, we model faults with dips to both the east and west. To produce a scarp

geometry consistent with that observed in the field, the Antena Norte fault, when modeled with a west dip, is subject to remote compression directed 075°, resulting in east-side-down reverse fault scarps, while the east dipping fault models experience remote uniaxial tension in the same direction, which produces a normal fault scarp. The scarp geometries of the Antena Sur and Bahía Blanca segments imply that the underlying faults dip opposite the Antena Norte segment — to the west if they are normal faults (subject to remote tension) and to the east if reverse faults (subject to remote compression). For both the normal and reverse faulting cases, we model all faults as dipping 75°, with aspect ratios of $D = L/2$. Additional geometrical permutations are tested in Section D.3.3.

The scarp above the Antena Sur segment is subtle, yet it comprises a topographic anomaly sufficient to dam alluvial sediments transported from the west (Figure 2.13b). As in the case of the southern Hombre Muerto segment, the subtler topography of this segment as compared to the Antena Norte and Bahía Blanca scarps may suggest that the Antena Sur fault is inactive and has undergone substantial degradation, or that the fault is deeply buried, subduing its surface expression. In all cases, we model the fault assuming the latter characteristic, burying the Antena Sur fault to $B = L/20$ and the Antena Norte and Bahía Blanca to a nearly surface-breaking depth of $B = L/200$.

When modeled as a normal fault system, the Antena-Bahía Blanca faults introduce stress perturbations that are more consistent with the distribution of surface cracking than those predicted by the reverse fault simulation (compare Figures 2.14a and c). For both models in this region, we evaluate the results by plotting the tension resolved onto vertical planes striking 345° and comparing the stress fields with the extent of cracks. Uniaxial tension induces normal fault slip on all

faults, resulting in the west-side-down motion on the Bahía Blanca and Antena Sur segments, and east-side-down motion of the Antena Norte segment, shown by the vertical displacement field of Figure 2.14b. Some cracks lying to the east of each fault fall outside of the zone of induced tension (Figure 2.14a), suggesting that a process or parameter not considered by our simple models contributes to their formation. In the transition zone between the southern and northern fault segments, the broad region of tensional stress demonstrates the interaction between the faults. The wide region of cracking lies within the predicted zone of tension between the faults, supporting the hypothesis that the pervasive cracking represents diffuse deformation in a transfer zone between discrete fault segments.

In response to the applied uniaxial tension, oblique dextral-normal slip is induced on all faults, resulting in a vertical displacement field (Figure 2.14b) that closely resembles the topographic features of the fault system, which can be inferred from the satellite imagery in Figure 2.13. Even small details of the topography are reproduced by the model: the regions of lesser uplift along the concave-to-the-southwest portions of the Bahía Blanca and Antena Sur segments coincide with where drainages have broken through the scarp topography, suggesting that the barrier impeding incision is lower there (Figure 2.13). The slope of the vertical displacement field across the Antena Sur segment is far less than that across the Bahía Blanca segment, meaning that the scarp topography is subtler, as observed. In the transition zone between the two southern segments and the Antena Norte segment, negligible vertical displacement is predicted, consistent with the lack of a topographic scarp developed in this region. The pattern of uplift and subsidence along the Antena Norte segment mimic the linear trace of that fault, though the changes in scarp height that coincide with wide regions of cracking are not con-

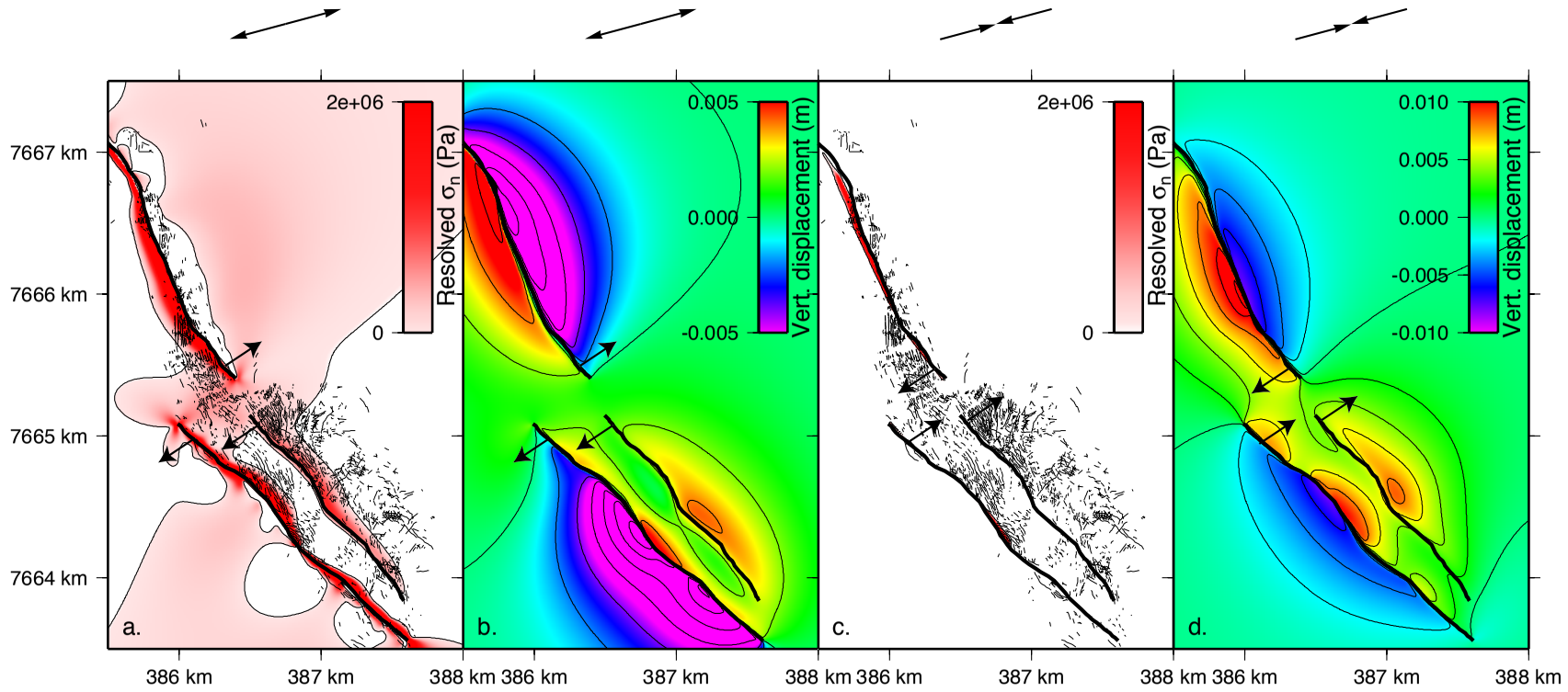

Figure 2.14: Stress (a, c) and vertical displacement (b, d) fields for the Antena-Bahá Blanca models. Stress fields are shown as tension resolved onto vertical planes striking 345°, representing the mean crack strike in the region. The normal faulting model, subject to 2×10^6 Pa of uniaxial tension oriented 075°, shows a perturbation to the stress field that is reasonably consistent with the distribution of cracking (a) and vertical displacement field that resembles the fault-related topography (b). The stress perturbation induced by the faults when subject to compression directed 075° is much more localized around the fault traces (c). The vertical displacement field, however, is also similar to the fault-related topography of the region (d).

sidered by the model and therefore are not expressed in the vertical displacement field.

When modeled as reverse faults, the Antena-Bahía Blanca faults produce perturbations to the regional stress field that are restricted to discontinuous bands on the hangingwall side of the faults that are far narrower than the extent of observed cracking (Figure 2.14c). The reverse fault model shows a vertical displacement field (Figure 2.14d) that approximates the fault-generated topography of the region, but not as well as the the normal fault model. Because both the stress and displacement fields of the normal fault model resemble the observed crack distribution and topography more closely than does the reverse fault model, we suggest that the Antena-Bahía Blanca system represents a normal-dextral oblique fault system.

2.6.4 Geoglifos fault

Branching off of the southern extent of the Chomache fault is the NNW-SSE striking Geoglifos fault ("GE" on Figure 2.1). The geometry of the linear fault scarp and the mountain front parallel to it is similar to that seen along the Hombre Muerto and Antena faults, with the scarp interrupting the slope of the mountain front (Figure 2.15). Cracks along the Geoglifos scarp generally strike parallel to the fault, although some show an arcuate geometry, concave towards the scarp crest (southern dashed oval in Figure 2.15a). There is a poor correlation between the scarp height and both the width of individual cracks and the extent of the cracked zone adjacent to the fault, indicating a more complicated relationship between the scarp growth and crack formation than is indicated by the cracks observed along the Chuculay system (*González et al.*, 2007). Some of this complication results

Figure 2.15: IKONOS image of the Geoglifos fault region. Dashed lines indicate the surface traces of faults. A) Zoom of the northern Geoglifos segment, demonstrating the zone of cracking localized around the intersection of the main Geoglifos fault with the northwest-striking structure (northern dashed oval) and the zone of wide cracks atop the tall, well-developed fault scarp (southern dashed oval). The small numbers along the scarp indicate the approximate scarp height in meters. B) Zoom image showing the southern array of northwest-striking open cracks. These cracks have an en echelon character suggesting dextral motion on a buried northwest-striking fault.

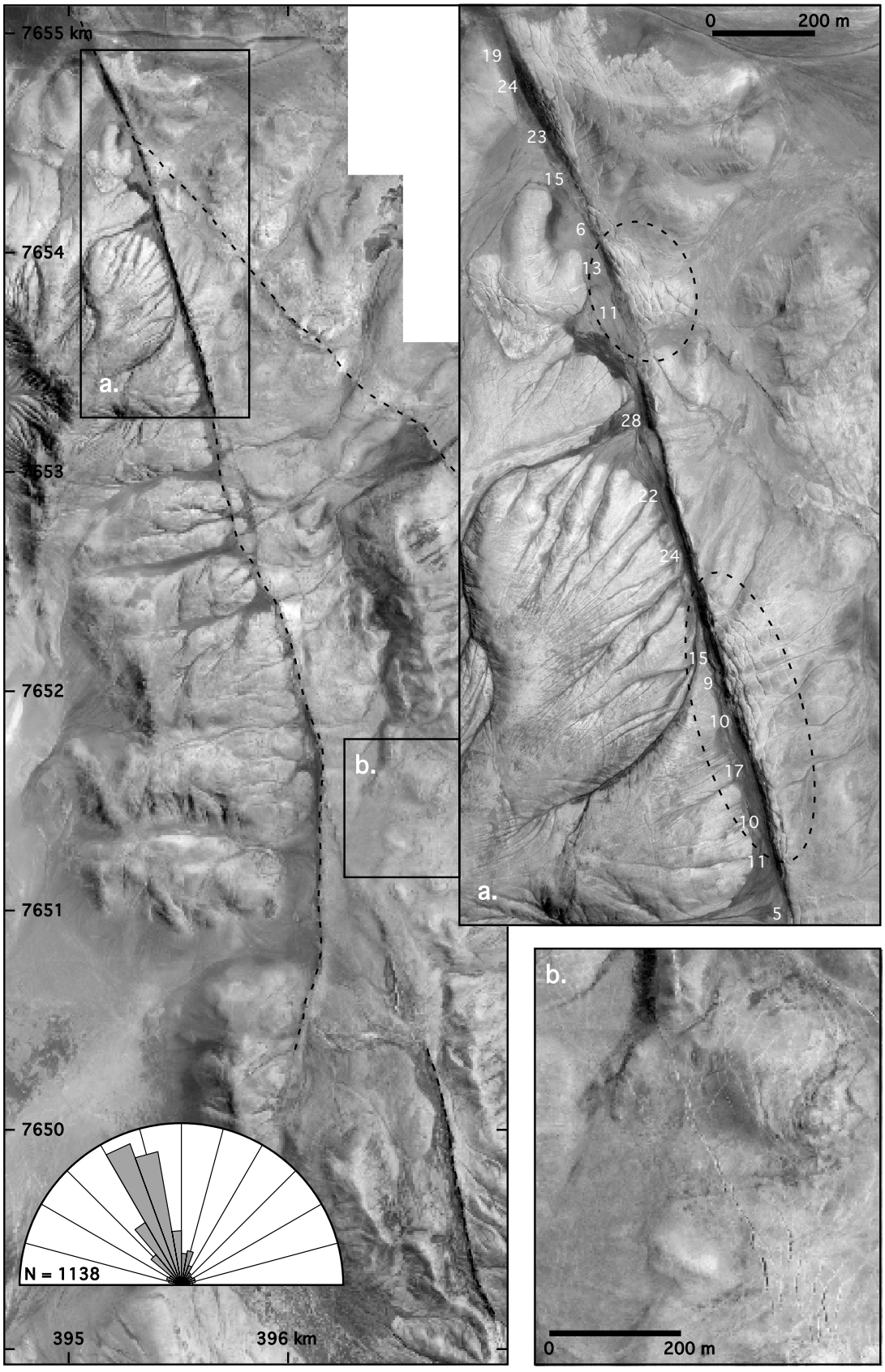
7655 km
7654
7653
7652
7651
7650
395
396 km
a.
b.
N = 1138
0
200 m
19
24
23
15
6
13
11
28
22
24
15
9
10
17
10
11
5
a.
b.
0
200 m

from the interaction between the Geoglifos fault and a more northwesterly-striking structure marked along its strike by a series of long open cracks (Figure 2.15a, northern dashed oval). However, even away from the intersection between these two structures, the extent of cracking at the scarp crest does not scale with the height of the Geoglifos scarp. For about 600 m south of the intersection between the Geoglifos and NW-striking fault, the 22–28 m high Geoglifos scarp is characterized by a sharp morphology and is separated from the adjacent mountain front by an incised valley with well-developed fill terraces. Along this portion of the fault, however, the scarp crest is devoid of surface cracks. South of this well-developed scarp, fault throw decreases abruptly and the scarp profile becomes less abrupt. Coincident with this change in scarp height and shape is a concentrated region of very large fractures with weathered apertures of up to 3 m and filled depths up to 1.5 m (within southern dashed oval of Figure 2.15a). At this location, the scarp crest is poorly defined as a result of the degree of cracking, which has modified the topography. This transition from a sharply-defined, tall scarp to a more subtle, rounded form pervasively cut by cracks is similar to the relationship seen along the Antena Norte fault, where deformation appears to be partitioned between fault slip and cracking.

Splaying off of the Geoglifos fault are two northwest striking arrays of open cracks. The northern array, mentioned above in the context of its interaction with the principal Geoglifos fault, shows subtle topographic features along strike (northwest striking dashed line in the main panel of Figure 2.15). We interpret this topography as the surface expression of a buried fault that has accommodated dominantly strike-slip deformation, but some oblique slip coincident with bends in the fault trace has resulted in minor uplift and subsidence. The southern crack

array is marked only by open fissures in the surface showing a distinct *en echelon* morphology (Figure 2.15b). The sense of deformation expressed by these cracks is of right-lateral slip, as the apertures of more northerly-striking crack segments are greater than the more northwesterly-striking segments (Figure 2.15b). These cracks suggest that buried, strike-slip faults are located beneath the arrays and splay off of the Geoglifos fault. Dextral slip on these secondary faults is kinematically consistent with that of the Chomache fault immediately north of the Geoglifos fault, and is indicative of a regional σ_1 axis oriented approximately north-south.

While focusing on the interaction between cracks and the Geoglifos fault, we also model the northernmost intersecting structure as a vertical frictionless discontinuity to examine its effects on the local stress field, particularly around the point of intersection. As in the case of the Antena-Bahía Blanca faults, no fault plane exposure exists, so we test both east and west dips for the main Geoglifos fault subject to tensional and compressional remote stress conditions, respectively, in order to explore a range of possible fault kinematics. Additional geometrical and boundary condition permutations appear in Section D.3.4. Furthermore, we examine the effects of the southern Geoglifos segment, which is exposed at the surface with reported dip of 78°E (*Carrizo et al.*, 2007).

Figure 2.16 shows the stress perturbations and vertical displacement fields caused by the Geoglifos fault (and splays from it) as a result of the tensional (Figure 2.16a, b) and compressional (Figure 2.16c, d) remote loading conditions. For these models, we present the tensional stress resolved on vertical planes striking 350°. Cracks along the fault scarp are restricted to a narrow band at the scarp crest, roughly coincident with the zone of tension predicted by the reverse faulting model (Figure 2.16c) and wholly within the region of tension surrounding

Figure 2.16: Stress (a, c) and vertical displacement (b, d) fields for the Geoglifos fault models. The normal fault model (a, b) simulates the main branch of the Geoglifos fault as dipping 75°W, the southern branch as dipping 78°E, and the northwest striking fault as a vertical plane. The reverse fault model (c, d) considers the main Geoglifos fault as dipping 75°E and uses the same geometry as the normal fault model for the southern and northwestern-striking faults. Dip directions are indicated by the arrows. Stress fields are shown as tension resolved onto vertical planes striking 350°, representing the mean crack strike in the region. The normal faulting model, subject to 2×10^6 Pa of uniaxial tension oriented 075°, shows a perturbation to the stress field that is reasonably consistent with the distribution of cracking (a) and vertical displacement field that resembles the fault-related topography (b), with the exception of the southernmost fault segment. The stress perturbation induced by the faults when subject to compression directed 075° is much more localized around the fault traces (c). The vertical displacement field is also similar to the fault-related topography of the region (d), except that the subtle topography related to bends in the strike of the northwest striking fault splay are not captured.

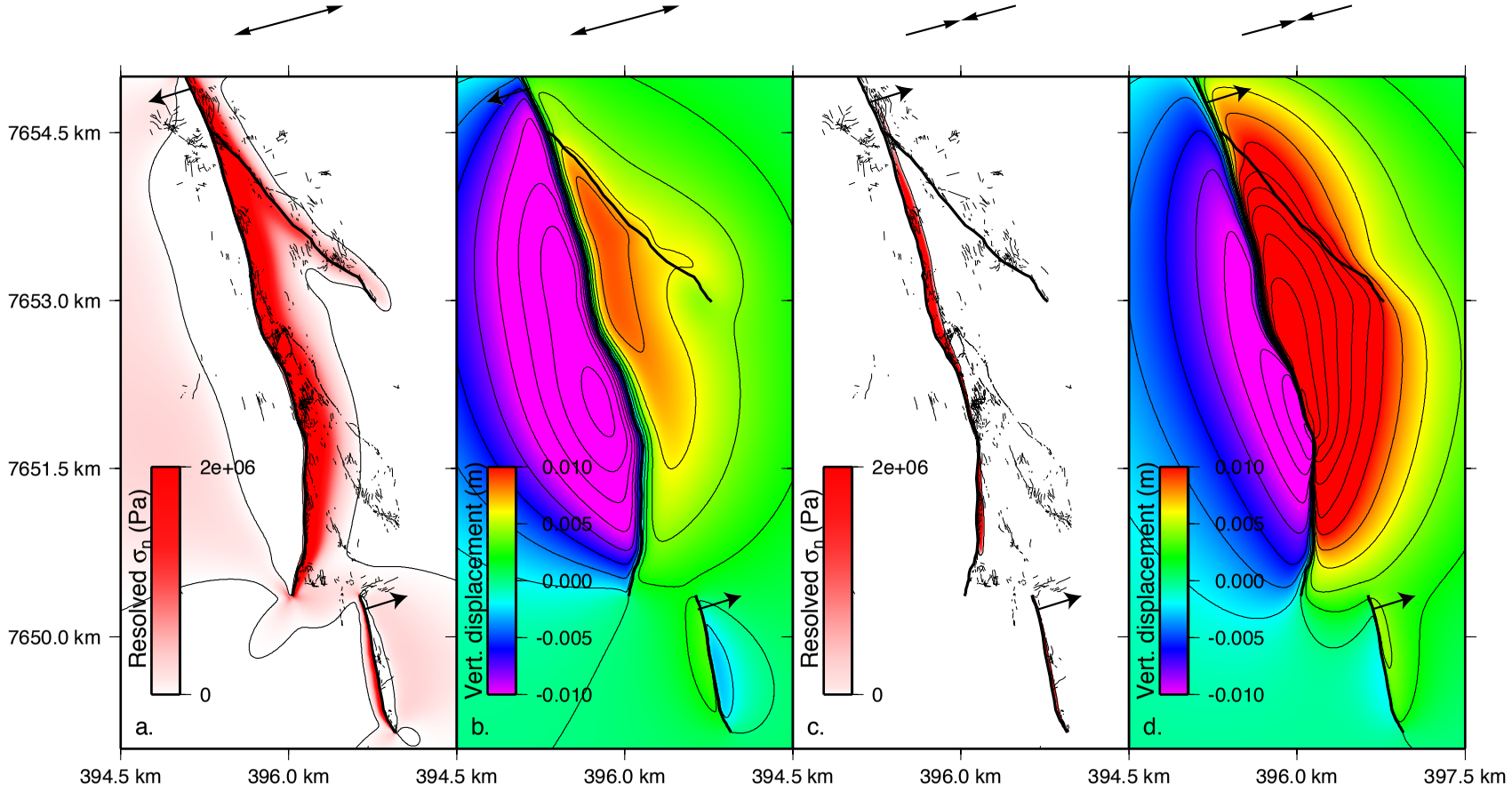
7654.5 km
7653.0 km
7651.5 km
7650.0 km
Resolved σn (Pa)
2e+06
0
Vert. displacement (m)
0.010
0.005
0.000
-0.005
-0.010
a.
b.
c.
d.
394.5 km
396.0 km
394.5 km
396.0 km
394.5 km
396.0 km
394.5 km
396.0 km
397.5 km

the normal fault models (Figure 2.16a). The dense concentration of cracks around 7652 km N (cluster of thin black lines on Figure 2.16a, c) is contained within the tensional stress predicted by the normal fault model, but the scarp-top tension predicted by the reverse fault model is anomalously thin at that location.

Interaction between the three modeled faults is evident from the distribution of tensional stress in the normal fault model (Figure 2.16a), which is more consistent with the distribution of cracking than is the reverse fault model, particularly in terms of the northwest striking array of cracks that splays off of the northern part of the Geoglifos fault. The reverse fault model also lacks a zone of tension near the interacting segments of the Geoglifos fault with its southern extension (Figure 2.16c), whereas the normal fault models show regions of low to moderate magnitude tensional stress within a "transition zone" between the two fault segments (Figure 2.16a), consistent with the diffuse cracking in that region.

We did not explicitly model the southernmost northwest-striking array of *en echelon* open cracks as a fault because it has no topographic expression along its trace. However, we expect that inclusion of a buried, vertical discontinuity similar to that which represents the northern array of northwest-striking open cracks would result in little change to the stress field of the reverse faulting model while perturbing the normal faulting model in a manner similar to that of the northern fault. This would make the extent of tensional stress of the normal fault model more consistent with the distribution of cracks, particularly in terms of the dense cluster located near the intersection of the northwest-striking array and the main Geoglifos fault.

The vertical deformation fields predicted by the Geoglifos fault models (Figure 2.16b, d) show patterns that mimic the fault related topography, namely in terms of

the elongated uplift and subsidence along the fault scarp. The normal fault model shows the opposite sense of vertical displacement than that observed across the southern fault segment, but shows gentle uplifts associated with slight changes in the strike of the modeled northwest striking splay, consistent with the topography (Figure 2.16b). Conversely, the reverse fault model displacement field predicts the correct sense of relative uplift across the southern fault segment but does not show any microtopography along the northwest striking scarp (Figure 2.16d).

2.7 Discussion

The boundary element models presented above demonstrate the localized perturbation to the regional stress field introduced by the presence of upper plate faults. These concentrations of tensile stress, restricted to near-fault regions, provide a mechanism for the enhancement of crack apertures along fault traces. Because the faults are modeled as frictionless discontinuities, fault slip in response to the imposed regional loading simulates a complete stress drop on the fault plane. Therefore, the results that we show here represent the maximum magnitude of stress perturbation resulting from fault slip in response to regional loading (*Crider and Pollard*, 1998). While the assumption of frictionless faults may not be correct, the boundary element results describe the end-member effects of upper plate faults on the stress field.

2.7.1 Model shortcomings

We find that, in general, the distribution of cracks along fault traces can be satisfactorily explained by the concentration of regional stress caused by the faults. As noted in the discussion of the individual fault models, there exist some discrepan-

cies between the crack distribution and modeled stress perturbations. We address some shortcomings of the model strategy to shed light on these discrepancies. As simple elastic boundary element models, our simulations do not consider several processes and parameters that undoubtedly also affect the evolution of cracking.

2.7.1.1 Lithologic heterogeneity

Having been affected by tectonic stressing since the Mesozoic, the bedrock of the Salar Grande region has sustained substantial damage. Where bedrock crops out, we observe several bedrock joint sets attesting to this deformation. If the bedrock surrounding regional-scale faults has been particularly damaged through time, it is more likely to respond to imposed stresses by pervasive brittle failure. Based on coseismic geodetic observations, it appears that the crust within zones up to 1 km wide surrounding strike-slip faults in southern California and Iran is characterized by a modulus of rigidity approximately half that of the "ambient" crust outside of the fault zone (*Fialko et al.*, 2002; *Fialko*, 2004; *Fialko et al.*, 2005). These weak regions show anomalously high strain in response to large earthquakes and are interpreted to reflect the degree of accumulated damage resulting from many episodes of fault slip.

In the case of the Punta de Lobos and Antena-Bahía Blanca faults, the spatial extent of enhanced cracking is greater than the modeled perturbation to the tensional stress field that faults induce, regardless of the fault geometry parameters that we used (see Appendix D). If the crust on both sides these faults is weaker than the "ambient" crust, the spatial extent and magnitude of deformation caused by the stress perturbation will likely be greater than that predicted by the homogeneous crust models. The Bahía Blanca and Antena Sur segments lie fewer than

500 m apart, so the crust between then has likely been damaged by activity on both faults, which could explain the cracking the persists throughout the intervening region. Such lithologic heterogeneity, not considered in our homogeneous half-space models, provides a plausible explanation for the width of the cracked region adjacent to some faults.

2.7.1.2 Dynamic stresses

Dynamic stress associated with an earthquake is capable of producing ground cracks (*Dalguer et al.*, 2003; *Dalguer and Ikikura*, 2003). Eyewitnesses of the great 1964 "Good Friday" earthquake in Alaska described cracks that opened at the peaks and closed in the troughs of passing surface waves (e.g., *Coulter and Migliaccio*, 1966). As surface waves propagate through weaker material surrounding fault zones, the velocity decreases as amplitude increases; such amplification can trigger fault slip (*Uenishi and Rossmanith*, 2000) and/or enhance damage around the fault (*Rovelli et al.*, 2002). *Segall* (1984) notes, however, that static deformation is more likely to induce brittle failure as compared to high magnitude, oscillatory strains to which a material responds elastically. As noted in Chapter 3, dynamic principal stress axes generated by a strong subduction zone earthquake vary more in magnitude than in direction, indicating that cracks of a given orientation formed or propagated by a static coseismic stress field may not be distinguishable from those opened by dynamic stress.

2.7.2 Regional implications

Our boundary element models suggest that when the Salar Grande region is subject to regional tension in the direction plate convergence, such as that imposed

by a strong interplate earthquake, stress concentrations around upper plate faults arise, which can explain the enhanced cracking we observe. This is consistent with the results of *González et al.* (2003), who suggest that the entire northern Chilean forearc demonstrates a structural signal of east-west extension and north-south shortening. Dextral slip on the northwest-striking Chomache fault is recorded by geomorphic offsets and is kinematically consistent with this strain regime. However, our models also indicate that reverse faulting on the Hombre Muerto and Geoglifos faults is capable of explaining many of the associated surface crack characteristics, and therefore these may structures represent deformation caused by a stress field different than that which drives slip on the other faults, namely compression directed parallel to plate convergence *Carrizo et al.* (e.g., 2007). Two segments of the Atacama Fault System, the Salar del Carmen and Paposo segments (23°–24°S), show evidence for minor reverse reactivation of faults that otherwise have experienced normal slip (Chapter 5). We interpret this reactivation as a result of fault-normal compression caused by a concentrated interplate slip distribution of a strong subduction zone earthquake (Chapters 4 and 5). In those cases, the topographic signature of the reverse faulting is a subtle decrease in slope on the normal fault scarp, forming a bench on which coarse sediment accumulates. The Hombre Muerto and Geoglifos faults may represent a similar pattern of reverse reactivation of otherwise normal faults, but to a greater extent than the faults farther south, forming prominent scarps rather than subtly modifying the slope. Given that there are fresh-appearing examples of both normal and reverse fault scarps along the northern Chilean forearc, the absolute level of stress within fault zones may be very low and thus faults slip in response to the opposite senses of relatively small magnitude imposed stresses, such as those induced on decadal time

scales by inter- and coseismic subduction zone processes.

Chapter 3 describes open cracks morphologically similar to those observed west of Salar Grande at 16 additional locations throughout the northern Chilean and southern Peruvian forearc. The clusters of cracks show strong preferred orientations that vary in direction as a function of position along the coastline. The pattern of mean crack strikes is consistent with the principal coseismic stress fields predicted for strong subduction zone earthquakes on distinct segments of the plate boundary. This consistency in crack orientation over a large area further promotes the argument that a regional-scale mechanism being responsible for their formation and reactivation. The results of the boundary element modeling shown here indicate that upper plate faults can localize these regional stresses to cause enhanced opening of cracks along their traces. Field surveys of the Taltal region (26°) following the 1966 Taltal subduction zone earthquake found surface cracking restricted to linear traces around mapped faults, which were interpreted to have opened due to "(fault) displacement of unknown character at depth (*Lemke et al.*, 1968)," and so it is logical that the cracks we observe in the Salar Grande region are similarly affected by large earthquakes. Both faults and cracks deform in response to the same stresses resulting from the subduction earthquake cycle. For the most part, the models subject to remote uniaxial tension, representing the principal stress induced by a strong subduction zone earthquake, are consistent with the zones of accentuated cracking, though in some cases the reverse faulting models are also capable of explaining this enhancement. The weaknesses introduced into the crust by the presence of faults, along with the damaged material within the fault zone, serve to concentrate stresses generated by the seismic cycle and enhance cracking in those regions.

BIBLIOGRAPHY

Agliardi, F., G. Crosta, and A. Zanchi (2001), Structural constraints on deep-seated slope deformation kinematics, *Engineering Geology*, *59*, 83–102, doi:10.1016/S0013-7952(00)00066-1.

Allmendinger, R. W., G. González, J. S. Yu, G. D. Hoke, and B. L. Isacks (2005), Trench-parallel shortening in the Northern Chilean forearc: Tectonic and climatic implications, *Bulletin of the Geological Society of America*, *117*(1/2), 89–104, doi:10.1130/B25505.1.

Bourke, P. (1989), Intersection point of two lines, `http://local.wasp.uwa.edu.au/~pbourke/geometry/lineline2d/`.

Bourne, S. J., and E. J. M. Willemse (2001), Elastic stress control on the pattern of tetnsile fracturing around a small fault network at Nash Point, UK, *Journal of Structural Geology*, *23*(11), 1753–1770, doi:10.1016/S0191-8141(01)00027-X.

Carrizo, D., G. González, and T. Dunai (2007), Constricción neógena en la cordillera de la costa norte de Chile: Neotectónica y datación de superficies con ^{21}Ne cosmogénico, *Revista Geológica de Chile*, *34*, in review.

Comte, D., and M. Pardo (1991), Reappraisal of great historical earthquakes in the northern Chile and southern Peru seismic gaps, *Natural Hazards*, *4*(1), 23–44, doi:10.1007/BF00126557.

Coulter, H. W., and R. R. Migliaccio (1966), Effects of the earthquake of March 27, 1964 at Valdez, Alaska, *U.S. Geological Survey Professional Paper 542-C*, p. 36.

Crider, J. G., and D. D. Pollard (1998), Fault linkage: Three-dimensional mechanical interaction between echelon normal faults, *Journal of Geophysical Research*, *103*(B10), 24,373–24,391.

Dalguer, L. A., and K. R. J. D. Ikikura (2003), Generation of new cracks accompanied by the dynamic shear rupture propagation of the 2000 Tottori (Japan) earthquake, *Bulletin of the Seismological Society of America*, *93*(5), 2236–2252.

Dalguer, L. A., K. Irikura, and J. D. Riera (2003), Simulation of tensile crack generation by three-dimensional dynamic shear rupture propagation during an earthquake, *Journal of Geophysical Research*, *108*(B3), 2144, doi:10.1029/2001JB001738.

Delouis, B., H. Philip, L. Dorbath, and A. Cisternas (1998), Recent crustal deformation in the Antofagasta region (northern Chile) and the subduction process, *Geophysical Journal International*, *132*, 302–338, doi:10.1046/j.1365-246x.1998.00439.x.

Fialko, Y. (2004), Probing the mechanical properties of seismically active crust with space geodesy: Study of the coseismic deformation due to the 1992 M_w 7.3 Landers (Southern California) earthquake, *Journal of Geophysical Research*, *109*, B03307, doi:10.1029/2003JB002756.

Fialko, Y., D. Sandwell, D. Agnew, M. Simons, P. Shearer, and B. Minster (2002), Deformation on nearby faults induced by the 1999 Hector Mine earthquake, *Science*, *297*(5588), 1858–1862, doi:10.1126/science.1074671.

Fialko, Y., D. Sandwell, M. Simons, and P. A. Rosen (2005), Three-dimensional deformation caused by the Bam, Iran, earthquake and the origin of shallow slip deficit, *Nature*, *435*(7040), 295–299, doi:10.1038/nature03425.

González, G., J. Cembrano, D. Carrizo, A. Macci, and H. Schneider (2003), The link between forearc tectonics and Pliocene-Quaternary deformation of the Coastal Cordillera, northern Chile, *Journal of South American Earth Sciences*, *16*, 321–342, doi:10.1016/S0895-9811(03)00100-7.

González, G., T. Dunai, D. Carrizo, and R. Allmendinger (2006), Young displacements on the Atacama Fault System, northern Chile from field observations and cosmogenic ^{21}Ne concentrations, *Tectonics*, *25*, TC3006, doi:10.1029/2005TC001846.

González, G., M. Gerbault, J. Martinod, J. Cembrano, D. Carrizo, R. Allmendinger, and J. Espina (2007), Crack formation above propagating reverse faults, Chuculay Fault System, Coastal Cordillera, northern Chile: Insight from IKONOS data and numerical modeling, *Journal of Structural Geology*, in review.

Hilley, G. E., J. R. Arrowsmith, and L. Amoroso (2001), Interaction between normal faults and fractures and fault scarp morphology, *Geophysical Research Letters*, *28*(19), 3777–3780, doi:10.1029/2001GL012876.

King, G. C., R. S. Stein, and J. B. Rundle (1988), The growth of geological structures by repeated earthquakes: 1. Conceptual framework, *Journal of Geophysical Research*, *93*(B11), 13,307–13,318.

Lemke, R. W., E. Dobrovolny, L. Alvarez S., and F. Ortiz O. (1968), Geologic and related effects of the Taltal earthquake, Chile, of December 28, 1966, *Bulletin of the Seismological Society of America*, *58*(3), 851–859.

Loveless, J. P., G. D. Hoke, R. W. Allmendinger, G. González, B. L. Isacks, and D. A. Carrizo (2005), Pervasive cracking of the northern Chilean Coastal Cordillera: New evidence for forearc extension, *Geology*, *33*(12), 973–976, doi:10.1130/G22004.1.

Pollard, D. D., and P. Segall (1987), Theoretical displacements and stresses near fractures in rock: With applications to faults, joints, veins, dikes, and solution

surface, in *Fracture Mechanics of Rock*, edited by B. K. Atkinson, pp. 277–349, Academic Press, London.

Rech, J. A., J. Quade, and W. S. Hart (2003), Isotopic evidence for the source of Ca and S in soil gypsum, anhydrite and calcite in the Atacama Desert, Chile, *Geochimica et Cosmochimica Acta*, *67*(4), 575–586, doi:10.1016/S0016-7037(02)01175-4.

Riquelme, R., J. Martinod, G. Herail, J. Darrozes, and R. Charrier (2003), A geomorphological approach to determining the Neogene to Recent tectonic deformation in the Coastal Cordillera of northern Chile (Atacama), *Tectonophysics*, *361*(3-4), 255–275, doi:10.1016/S0040-1951(02)00649-2.

Rovelli, A., A. Caserta, F. Marra, and V. Ruggiero (2002), Can seismic waves be trapped inside an inactive fault zone? The case study of Nocera Umbra, central Italy, *Bulletin of the Seismological Society of America*, *92*(6), 2217–2232.

Segall, P. (1984), Formation and growth of extensional fracture sets, *Geological Society of America Bulletin*, *95*(4), 454–462.

Thomas, A. L. (1993), Poly3D: A three-dimensional, polygonal element, displacement discontinuity boundary element computer program with applications to fractures, faults, and cavities in the Earth's crust, M.S. thesis, Stanford University, Stanford, CA.

Tucker, M. E. (1978), Gypsum crusts (gypcrete) and patterned ground from northern Iraq, *Zeitschrift für Geomorphologie*, *22*(1), 89–100.

Uenishi, K., and H.-P. Rossmanith (2000), Dynamic triggering of fault slip, in *Aspects of Tectonic Faulting*, edited by F. K. Lehner and J. L. Urai, pp. 185–192, Springer, Berlin, Germany.

CHAPTER 3

SURFACE CRACKS RECORD SEISMIC SEGMENTATION OF THE ANDEAN PLATE BOUNDARY

3.1 Abstract

Concentrations of meter-scale surface cracks in the northern Chile and southern Peru forearc provide a long-term record of deformation related to plate boundary seismicity. These cracks, which have been observed to form during and/or shortly after strong subduction earthquakes, are preserved throughout the hyperarid Atacama Desert and show changes in orientation as a function of position along the margin. The variable opening direction of cracks is consistent with the dynamic and static coseismic stress fields that we calculate for earthquakes on several segments of the plate boundary; stress axis orientations vary spatially based on the earthquake rupture extent and slip distribution. Some cracks form and/or are enhanced by localized structural and topographic processes, but the strong preferred orientation over large regions indicates that the cracks are dominantly formed by plate boundary-scale stresses, namely earthquakes. Regions in which cracks show a bimodal strike distribution are located primarily at earthquake segment boundaries. In these localities, one population of cracks is activated during an earthquake on one segment, and the orthogonal set of cracks is affected by an event on the adjacent segment. Field observations of the cracks indicate that they have undergone multiple episodes of opening. Because they represent deformation caused by many earthquakes, we suggest that these meter-scale structures are a permanent record of subduction zone seismicity and can be used to map the segmentation of the plate boundary that persists over at least several earthquake cycles.

3.2 Introduction

Several studies of historical seismicity along the Andean margin suggest that great earthquakes often rupture the plate boundary in distinct segments (*Nishenko*, 1985; *Dorbath et al.*, 1990; *Comte and Pardo*, 1991). Delineating the boundaries of the segments or asperities is difficult, as the data used to estimate the rupture extent are commonly qualitative and sparsely distributed. Furthermore, the longevity of asperities is uncertain, complicating the long-term understanding of plate boundary behavior. To understand better the segmentation of the plate boundary and its implications for modern seismicity, we seek data that constrain the distribution of coseismic slip during past earthquakes.

Numerous regions containing meter-scale surface cracks that penetrate coastal regions of the northern Chile and southern Peru forearc (17°–25°S) provide such insight into the long-term nature of plate boundary seismicity. Cracks open as a result of tension applied in a certain direction, thereby providing a permanent record of a past stress field. By constructing a regional map of crack strikes, we effectively map the orientations of the principal stress axes responsible for their formation. We know from field observations that populations of cracks were generated by the 1995 M_w 8.1 Antofagasta, Chile (*Ruegg et al.*, 1996; *González et al.*, 2003) earthquake and were reported to have opened as a result of the 2001 M_w 8.5 Arequipa, Peru event (*Wartman et al.*, 2003; *Keefer and Moseley*, 2004), indicating that strong subduction earthquakes serve as one source of stress for crack formation. We use elastic dislocation models to explore how earthquakes on several segments of the margin have exerted stress on the forearc, comparing the orientations of modeled principal stress axes to the finite strain demonstrated by the surface cracks, and we use our results to evaluate the ability of the cracks to

serve as long-term records of interplate seismicity.

3.3 Tectonic setting

Great earthquakes rupture distinct segments of the Andean subduction zone every 100–150 years (*Dorbath et al.*, 1990; *Comte and Pardo*, 1991). The Coastal Cordillera of the forearc of northern Chile and southern Peru directly overlies the downdip extent of the seismogenic portion of the plate interface where these large events originate. Therefore, permanent upper plate deformation related to subduction zone earthquakes can be directly observed in the field and in remote sensing data. Hyperaridity in the region, which has persisted for at least the last 6 Myr (*Hartley and Chong*, 2002), if not since before 16–18 Ma (*Dunai et al.*, 2005; *Rech et al.*, 2006), allows for long-term preservation of surficial features. Furthermore, the gypsum-indurated soil that covers much of the forearc of northern Chile and southernmost Peru provides a durable surface crust that further enhances preservation of small-scale features.

Historical and modern records place constraints on the size, epicentral location, and approximate rupture extent of the most recent great earthquakes on four segments of the plate boundary between 16°S and 25°S (Figure 3.1). Two historical events in 1868 and 1877 respectively represent the last great earthquakes to rupture the southernmost Peru and Iquique (Chile) segments of the margin (*Nishenko*, 1985; *Comte and Pardo*, 1991; *Delouis et al.*, 1997). The inferred boundary between the rupture zones of these events coincides approximately with the large bend in the coastline near the Peru-Chile border (*Kausel*, 1986; *Comte and Pardo*, 1991). The 1995 M_w 8.1 Antofagasta earthquake ruptured southward from the Mejillones Peninsula, which is thought to represent a physical barrier that marks

Figure 3.1: Seismotectonic map of the northern Chile and southern Peru forearc regions. Ovals indicate the approximate rupture segments of the most recent earthquakes on four segments of the plate boundary, while large dots represent the inferred epicenters. Inverted triangles show the positions of crack clusters along the forearc, and the corresponding rose diagrams show the length-weighted distribution of crack strikes, with the black vector denoting the mean strike. The dark gray region onshore shows the area lying between 300 m and 1200 m elevation, delineating the bounds within which gypsum precipitates from the dense coastal fog (*Rech et al.*, 2003).

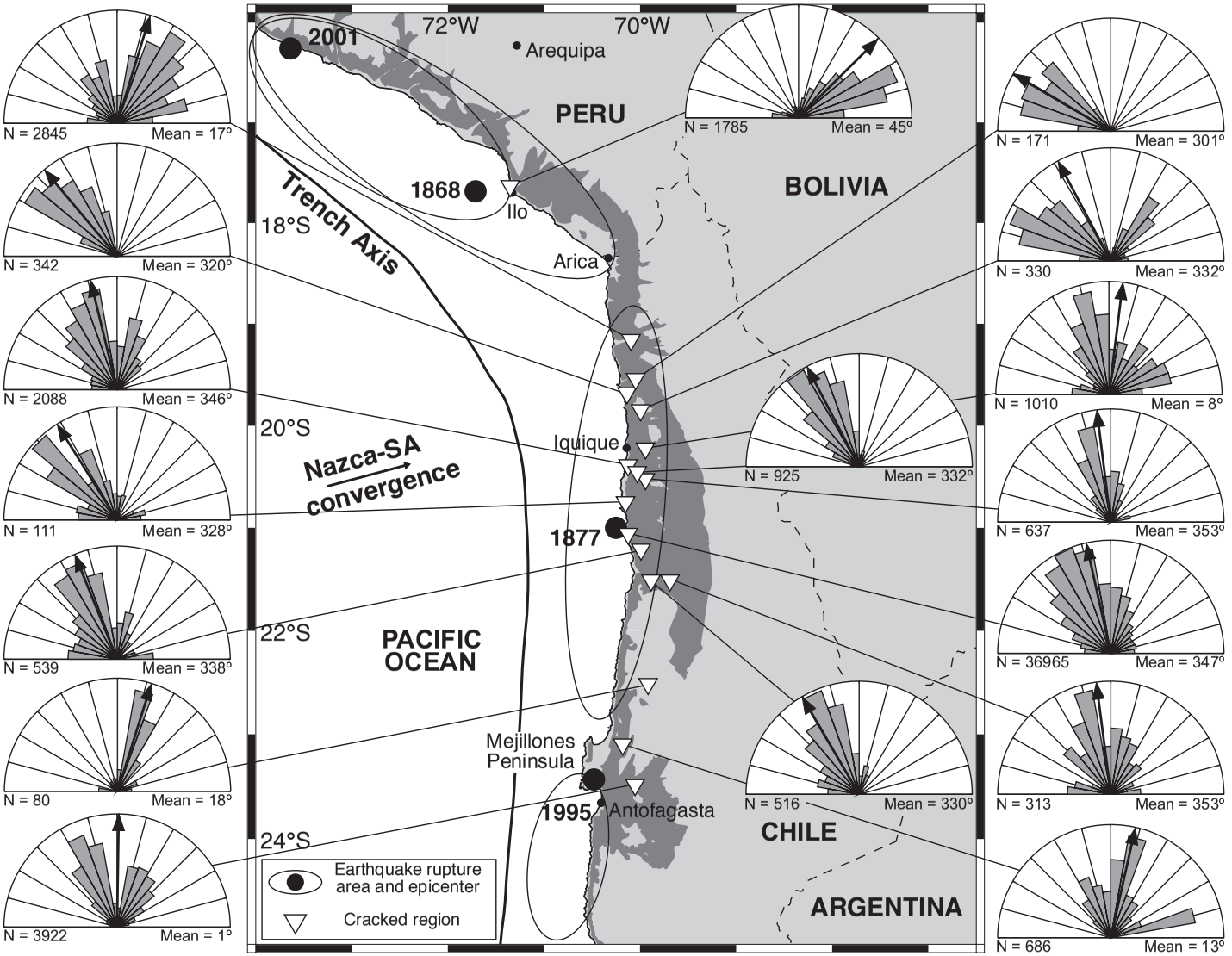
72°W
70°W
2001
Arequipa
PERU
BOLIVIA
1868
Ilo
Trench Axis
18°S
Arica
20°S
Iquique
Nazca-SA
convergence
1877
22°S
PACIFIC
OCEAN
Mejillones
Peninsula
1995
Antofagasta
CHILE
ARGENTINA
24°S
Earthquake rupture
area and epicenter
Cracked region
N = 2845 Mean = 17°
N = 342 Mean = 320°
N = 2088 Mean = 346°
N = 111 Mean = 328°
N = 539 Mean = 338°
N = 80 Mean = 18°
N = 3922 Mean = 1°
N = 1785 Mean = 45°
N = 925 Mean = 332°
N = 516 Mean = 330°
N = 171 Mean = 301°
N = 330 Mean = 332°
N = 1010 Mean = 8°
N = 637 Mean = 353°
N = 36965 Mean = 347°
N = 313 Mean = 353°
N = 686 Mean = 13°

the boundary between the Antofagasta and Iquique segments of the margin (*Delouis et al.*, 1997). The 2001 M_w 8.2–8.5 Arequipa, Peru earthquake partially re-ruptured the 1868 segment (e.g., *Ruegg et al.*, 2001), but left the southernmost extreme unbroken (Figure 3.1).

In Chapter 1, we used 1-m resolution IKONOS satellite imagery to document a large cluster of meter-scale open cracks cutting the surface of the Salar Grande region (21°S latitude) of the northern Chilean forearc. Our fundamental conclusion was that the preferred orientation of cracks over a 500 km^2 region indicated a genetic relationship between plate boundary-scale processes and the surface structures. We attributed their formation as a response to static stresses resulting from strong subduction zone earthquakes with some contribution from interseismic flexure, subduction erosion effects, and dynamic stress changes during earthquakes. The cracks show similar morphologies to those described near Antofagasta, Chile (*González et al.*, 2003) and Ilo, Peru (*Keefer and Moseley*, 2004), which have been described as coseismic features related to the great 1995 and 2001 earthquakes, respectively. Previously, our analysis of cracks was limited to the local survey near Salar Grande because costly, high-resolution satellite imagery is required to comprehensively sample the meter-scale features.

3.4 Regional crack mapping

In this study, we use Google Earth software, which provides free access to 2.5-m resolution imagery from the Quickbird satellite, to map concentrations of cracks throughout a segment of the Andean forearc between 17.5°S and 23.5°S. Examination of regions outside these latitudinal bounds yields only sparse examples of cracking. We identify 17 regions, ranging in area from ∼0.5 to 900 km^2, within

which we have mapped between 171 and 36965 cracks (Figure 3.1). In total, we have cataloged the location, length, and mean strike of more than 50,000 cracks. Using these data, we calculate a length-weighted mean strike for cracks in all populations; the strike distributions and average directions are shown in the rose diagrams of Figure 3.1. For the most part, cracks in all clusters show a preferred orientation, and the mean strike of cracks varies as a function of position along the coastline. In general, mean crack rotates from NW to NNE between 19° and 23°S. East of the Mejillones Peninsula and near the Peru-Chile border, there are several populations of cracks that show a bimodal distribution in strike, with one set of cracks striking NE and the other striking NW. Cracks near Ilo, Peru strike at a high angle to the coastline and plate boundary, approximately parallel to the direction of plate convergence.

Our imagery-based, regional-scale analysis is limited to two dimensions, but our complementary field work provides information about crack width and depth. Field observations of subsets of the cracks indicate that crack apertures range from tens of cm to more than 1 m; these cracks can be mapped using the imagery, but we can not quantitatively define their apertures. Although many cracks are best preserved in the aforementioned gypsum-indurated regolith that blankets the study area, there are numerous fissures penetrating as much as 12 m into bedrock. There exist some examples of lateral offset along cracks but our field observations (*Loveless et al.*, 2005) indicate that most are pure mode 1 fractures (as defined by *Pollard and Segall*, 1987). The lateral offsets, as well as vertical offsets of up to a few meters across some cracks indicate some mixed-mode (mode 1 and 2) fracturing.

The morphologies of surface cracks indicate variation in age of formation and

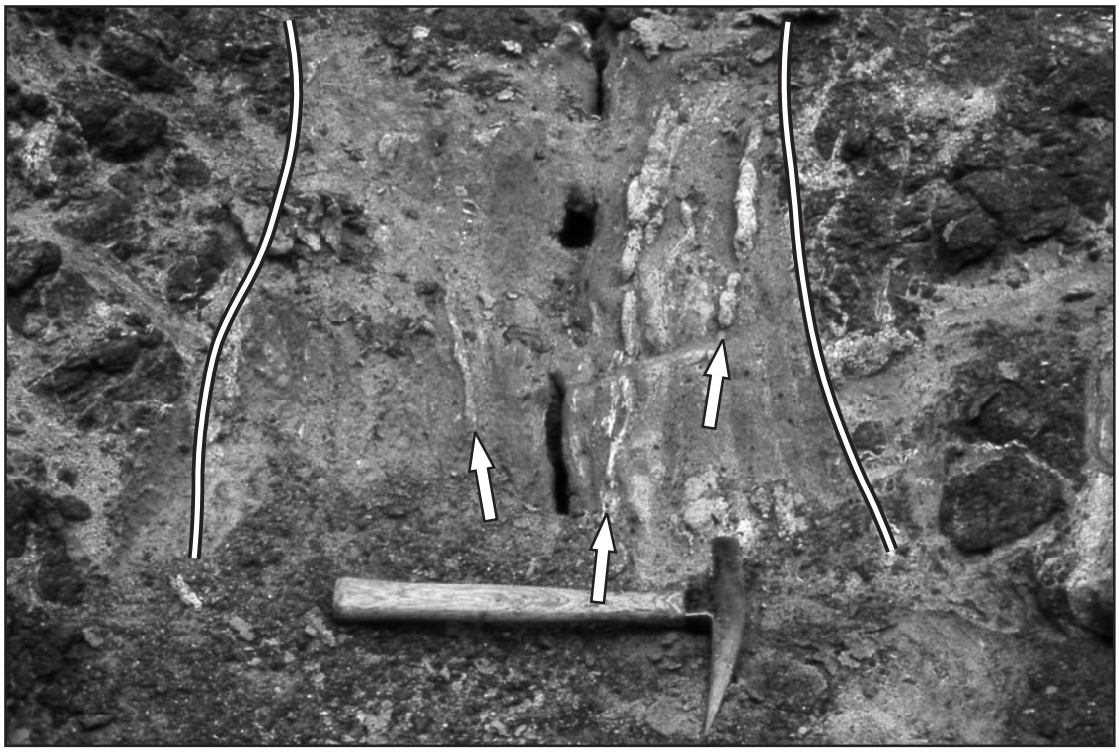

Figure 3.2: Field photo showing crack filled with vertical-banded gypsum (highlighted by white arrows). The white lines indicate the approximate position of the bedrock/fill contact, marking the extent of tectonic opening.

degree of degradation of the walls. Within the cracks, vertically-banded gypsum and gypsum-indurated sediment indicates that material is plated onto the exposed crack walls, sealing the crack from the outside in (Figure 3.2). We interpret the numerous layers of gypsum as indication of repeated episodes of sealing and reopening during several seismic cycles. The mechanism by which gypsum accumulates within cracks is likely a combination of precipitation directly out of the coastal fog, if the fog can penetrate the narrow, deep structures, and transport into the cracks by occasional rainfall. The rate of accumulation is also unknown, limiting the information that the gypsum sealant can provide about the age and evolution of cracks. However, several tangential pieces of evidence place loose bounds on the age

of cracking in the forearc: 1) Northeast of Antofagasta, *González et al.* (2006) used cosmogenic ^{21}Ne dating to define the upper bounds on the age of young faulting on the Salar del Carmen segment of the Atacama Fault System to be 424±151 ka. The fault scarp has a youthful morphology, and so fresh structures in the Coastal Cordillera, such as the small-scale surface cracks, may represent Quaternary but not necessarily recent deformation. 2) *Carrizo et al.* (2007) present ^{21}Ne ages of morphological surfaces, alluvial fans, and paleodrainages, and an ^{40}Ar/^{39}Ar age of faulting near Salar Grande. From these data, they conclude that the paleosurfaces cut by neotectonic faults are 24–18 Ma, while the fault activity itself spans 15 Ma–300 ka. 3) Two instances of recent cracking accompanying the 1995 and 2001 earthquakes show different characteristics. The small suite of cracks that formed during or shortly after the 1995 Antofagasta earthquake cut poorly consolidated sediments and have degraded substantially since formation. Conversely, the cracks near Ilo, Peru that were observed shortly after the 2001 Arequipa earthquake and are interpreted to have formed as a result of that event (*Keefer and Moseley*, 2004) cut cemented sediments similar in appearance to those that we note in the Salar Grande region and other crack localities. The old ages of structural features with youthful morphologies indicates the preservation potential of the hyperarid environment. This in turn suggests that the surficial cracks that we describe, despite being meter-scale features, are likely capable of preserving a record of deformation over several subduction earthquake cycles, if not several hundred thousand years.

Our examination of a large part of the forearc leads to several conclusions regarding the conditions required to preserve cracking. The features are best expressed in the gypsum-indurated regolith, which is generally identified by regions of high albedo in the available satellite imagery. Isotopic evidence indicates that

the gypsum precipitates from coastal fog that invades regions between ∼300 and 1200 m elevation (*Rech et al.*, 2003), leaving higher parts of the forearc devoid of substantial gypsum. The steep coastal escarpment, which lines much of the northern Chilean forearc, places the 300 m contour close to the shoreline. With one exception around 22.5°S, all of the cracked regions lie within these elevation limits (darker gray area on Figure 3.1). Immediately north of Arica (18°S), the trace of the 300 m contour indicates a wide coastal plain, which may place higher topography too far inland to experience the marine fog. The few cracks we observe in that region appear to cut poorly consolidated beach sands and are restricted to a small seaside cliff. To the north and south of Antofagasta, high topography of the Coastal Cordillera, indicated by the position of the 1200 m contour very near the coastline, impedes inland development of the gypsum-indurated crust and therefore negligible cracking is preserved. Furthermore, loss of atmospherically-derived salts through weathering and leaching increases south of Antofagasta (*Ewing et al.*, 2006), leaving the surface there less cemented than the more arid corridor between Antofagasta and Arica.

3.4.1 Structural and topographic effects on crack evolution

In addition to spatial variations in the degree of presevations, our observations of the cracks are also subject to the effects of topographic and/or structural features, which can locally perturb the propagation path of the crack. Such cracks are not appropriate for use in constraining the regional stress field. We note several examples of cracks that are spatially correlated with fault scarps and other large topographic gradients such as the giant canyon systems that mark the northernmost Chilean forearc (*Hoke et al.*, 2004). East of the Salar Grande region (21°S),

González et al. (2007) describe a suite of cracks atop east-west striking reverse fault scarps up to 300 m high and ascribe their evolution to ongoing fault-propagation folding above the underlying structures. These cracks are concentrated at the scarp crests and show strikes parallel to the fault, indicating that cracks propagate as a result of the tension induced by the anticlinal flexure. Cracks on smaller fault scarps also show a genetic relationship to the underlying, larger-scale structures. In some instances, cracks predate the fault activity but have been enhanced by faulting close to the scarp (Chapters 1, 2). We have excluded some populations of cracks because of obvious spatial correlation with large topographic features. In other populations, variability in orientation seen in the rose diagrams can be explained in part by local topographic and/or structural effects.

A further source of complication in using the cracks as a record of past interplate seismicity is the effect of other, intraplate earthquakes in both the upper plate and subducting slab. *Marquardt et al.* (2006) observed cracks that opened as a result of the 13 June 2005 Tarapacá earthquake, a $M_w = 7.9$ event located 115 km NE of Iquique at 115 km depth, within the Nazca Plate. The occurrence of cracking was minor but widespread, stretching from regions near the epicenter to the coastline near Iquique. In general, the cracks formed parallel to topographic contours of debris slopes and at slope breaks along hillsides (*Marquardt et al.*, 2006). The cracks observed both by *Marquardt et al.* (2006) and during our own field campaigns following this event were small compared to those that we have mapped using remote sensing: up to 20 m length with apertures less than 5 cm. Close to the epicenter, numerous buildings experienced substantial damage, which *Marquardt et al.* (2006) attribute to site effects related to the construction of towns on unconsolidated gravels. Though this deep intraplate earthquake caused some

cracking at the surface, the features are small and are tied to local attributes. Nonetheless, it is important to take into account such alternative means of crack formation when addressing the tectonic significance of these features.

3.5 Coseismic stress modeling

3.5.1 Forward model parameters

Based on the strong preferred orientation over large areas and similarity of the cracks we have mapped to those interpreted to have formed during or shortly after the 1995 and 2001 earthquakes (*González et al.*, 2003; *Keefer and Moseley*, 2004), we suggest that these features dominantly result from stress induced by strong earthquakes occurring on the subduction interface. Because we interpret the majority of the cracks to be mode 1 fractures, crack strike can be used to infer characteristics of the stress field that drives the opening. According to linear elastic fracture mechanics, a mode 1 crack opens in the direction the least compressional principal stress direction (σ_3) and therefore strikes parallel to σ_1 (e.g., *Pollard and Segall*, 1987). In order to explore the relationships between the surface cracks and plate boundary earthquakes, we simulate the coseismic stress fields related to great earthquakes on four segments of the Andean subduction zone. We use dislocation models carried out in an elastic half-space using the boundary element code Poly3D (*Thomas*, 1993) to calculate the principal axes of stress induced at the surface by the earthquakes and compare these instantaneous stress fields to the directions of permanent strain recorded by the crack populations. Because these models consider small magnitude deformation, the principal stress axes should be parallel to the principal strain axes. In other words, the cracks represent permanent strain

Table 3.1: Earthquake forward modeling parameters

Event	Moment (N-m)[a]	M_w	Dimensions (km)[b]	Mean slip (m)	Max. slip (m)	Mean rake[c]
1868	6.6×10^{21}	8.5	625×125	3.18	9.98	54
1877	4.2×10^{21}	8.3	530×135	1.90	9.85	105
1995	1.2×10^{21}	8.0	210×160	0.94	6.58	105
2001	4.0×10^{21}	8.3	320×210	2.19	12.80	69

[a]Moment is defined as the modulus of rigidity (3×10^{10} N/m^2) times the sum of the slip times area of all fault patches.

[b]Rupture dimensions, shown as along-strike $\times$ down-dip dimension.

[c]Mean of rake on all fault patches, weighted by slip magnitude. 0° = left-lateral slip, 90° = reverse slip, ±180° = right-lateral slip, -90° = normal slip.

markers that formed in response to an imposed stress. In the case of the 1995 Antofagasta and 2001 Arequipa earthquakes, we use slip distributions constrained by a joint inversion of seismic and geodetic data (*Pritchard et al.*, 2006, 2007) to calculate the principal coseismic surface stress axes (Figures 3.3 and 3.6). For the 1868 and 1877 events, we assume a simple Gaussian slip distribution with maximum slip located at the inferred epicenter of the earthquake (*Comte and Pardo*, 1991), smoothly tapering to zero slip at the rupture terminations, with maximum slip magnitude and overall moment magnitude similar to that estimated from historical data (Figures 3.4 and 3.5, *Nishenko*, 1985; *Comte and Pardo*, 1991). In the historical models, the rake of the slip vector on each modeled fault element is such that the azimuth of the surficial projection of slip is 255°, opposite the plate convergence vector. Details of the forward model parameters are shown in Table 3.1.

3.5.2 Forward model results

Figures 3.3–3.6 illustrate the relationships between the forward models of coseismic static stress fields and the permanent strain demonstrated by the surface cracks. At each crack locality, we show the length-weighted mean crack orientation (solid black bar) and the predicted strike direction of a mode 1 crack that would form in response to the local stress field — parallel to σ_1 and perpendicular to σ_3 (open bar). the overall stress field is shown by the gray bars, which indicate the orientation of the σ_1 axis throughout the affected region. We describe the effects of the earthquakes from south to north, noting the degree to which the observed mean crack strike agrees with the predicted σ_1 direction.

The model for the 1995 earthquake, which propagated southward from the Mejillones Peninsula (*Delouis et al.*, 1997; *Ihmlé and Ruegg*, 1997; *Pritchard et al.*, 2002; *Sobiesiak*, 2004; *Pritchard et al.*, 2006), shows predicted opening directions (open bars in Figure 3.3) reasonably consistent (20°–30° of obliquity) with the NW striking subsets of cracks (black bars in Figure 3.3) in the two populations that lie east of the Mejillones Peninsula. We do not have conclusive evidence that indicates whether or not cracks in either of these regions were reactivated during the earthquake. In both of clusters, we also observe a concentration of cracks striking NE (Figure 3.1), oblique to the crack strikes predicted by the coseismic model. We suggest that the NW striking cracks can be reactivated by earthquakes on the Antofagasta segment of the plate boundary, while the NE striking features could be affected by an earthquake on the Iquique segment, which lies directly to the north. We propose an alternative hypothesis for the evolution of the bimodal crack populations in the discussion of dynamic stress effects.

The NE striking cracks near Antofagasta are consistent with the stress field

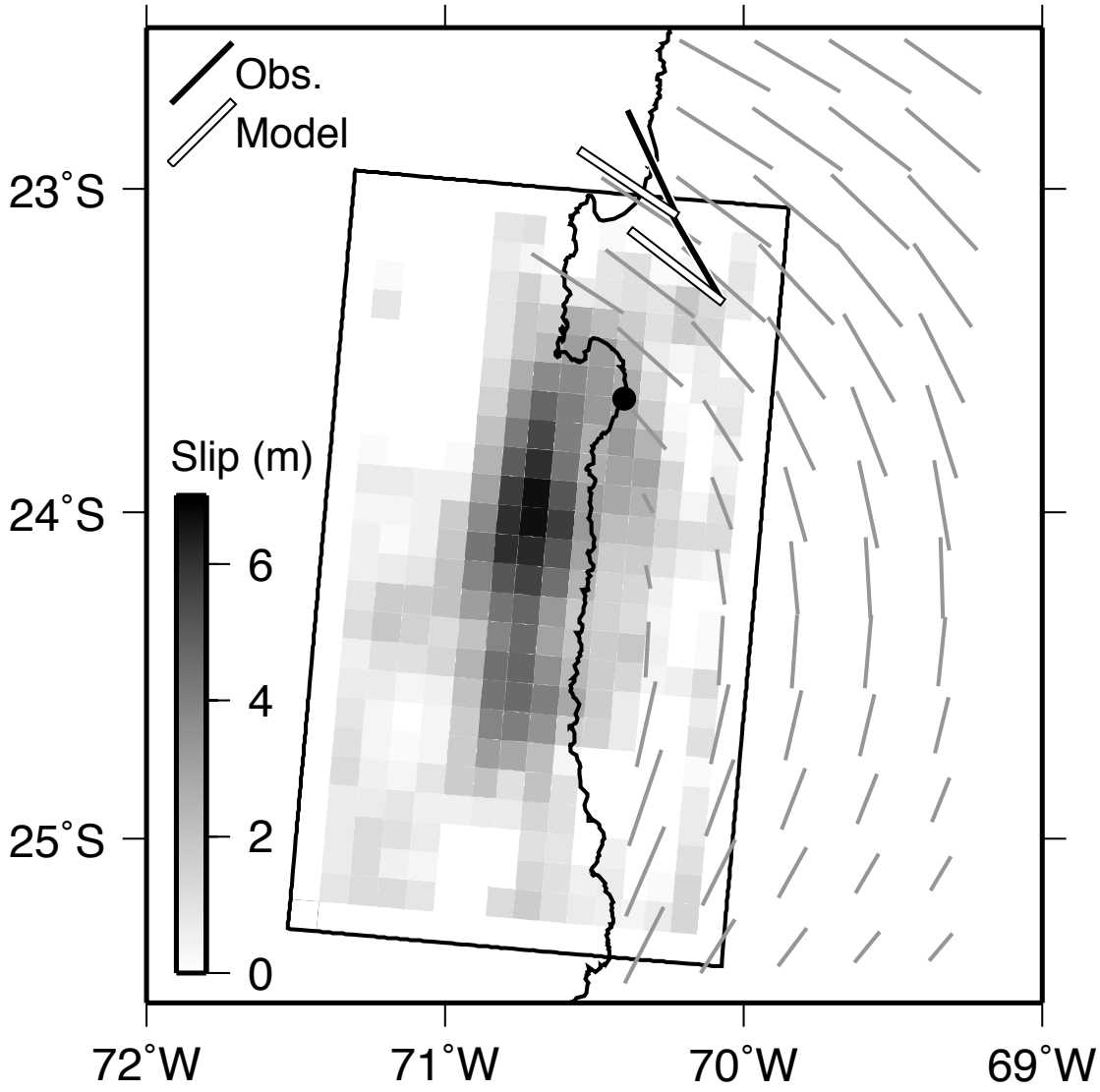

Figure 3.3: Static principal coseismic stress axes resulting from the 1995 M_w 8.1 Antofagasta earthquake on the Andean subduction interface. The distribution of slip is based on a joint inversion of seismic, GPS, and InSAR data (*Pritchard et al.*, 2006). The gray lines show the most compressional principal stress axes (σ_1); the least compressional (σ_3) axes are omitted for clarity but are oriented perpendicular to σ_1. The solid black bars show the mean strike of cracks within a particular cluster. In this case, the bimodal crack distributions were filtered and the orientation shown represents the mean of only the northwest-striking cracks. The open bars show the model-predicted orientation of σ_1 at the locality of the crack populations, which represents the strike of a crack that would theoretically open in response to the coseismic stress field.

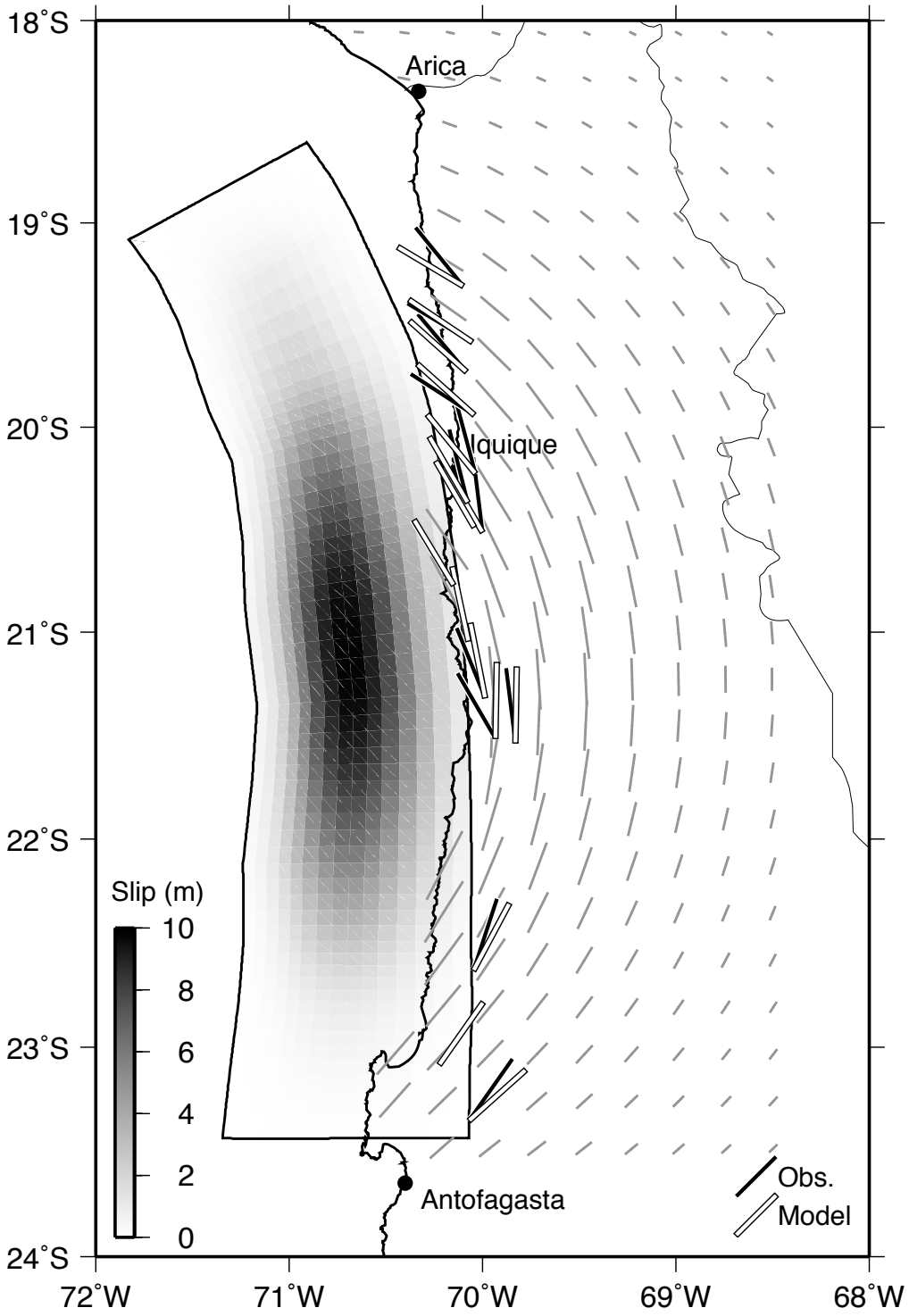

Figure 3.4: Static stress model for the 1877 M∼8.5 Iquique earthquake. The slip distribution is approximated based on the event description in *Comte and Pardo* (1991). All symbols are as described in Figure 3.3.

predicted for the simulated 1877 Iquique earthquake, which is inferred to have ruptured the plate boundary between the Arica bend to the Mejillones Peninsula (Figure 3.4). The boundaries of the Iquique segment encompass 16 of the 17 mapped crack populations, and the stress field induced by the simple Gaussian approximation of the coseismic slip distribution for the great 1877 event shows remarkable consistency with the orientations of cracks occurring along the entire length of rupture. Near the inferred epicenter (*Comte and Pardo*, 1991) and locus of maximum modeled slip, cracks strike nearly parallel to the coastline and coseismic σ_1 trend nearly parallel to the coast. Near 21.5°S, where a population of cracks strike dominantly NNE, the predicted principal stress axes show a consistent clockwise rotation relative to their orientations nearer the epicenter. The four northernmost crack populations affected by seismicity on the Iquique segment show a concentration of NW strikes, consistent with the opening direction predicted by the model. However, two of the regions show bimodal strike distributions, with a second concentration of NE strikes. As in the case of the cracks near the Mejillones Peninsula, the NW striking cracks may be activated by Iquique segment seismicity, while activity on the adjacent segment to the north may dominantly drive the evolution of the NE striking features.

The 1868 earthquake ruptured a large segment of the southernmost Peru margin, with a southeastern termination estimated to coincide approximately with the large bend in the plate boundary and coastline (Figure 3.5, *Comte and Pardo*, 1991). The rupture area of the 1604 great earthquake is estimated to be very similar to that of the 1868 event (*Dorbath et al.*, 1990; *Comte and Pardo*, 1991). As postulated above, the σ_1 axes induced by the 1868 earthquake in northernmost Chile trend NE-SW, consistent with the NE striking cracks that we observe in two

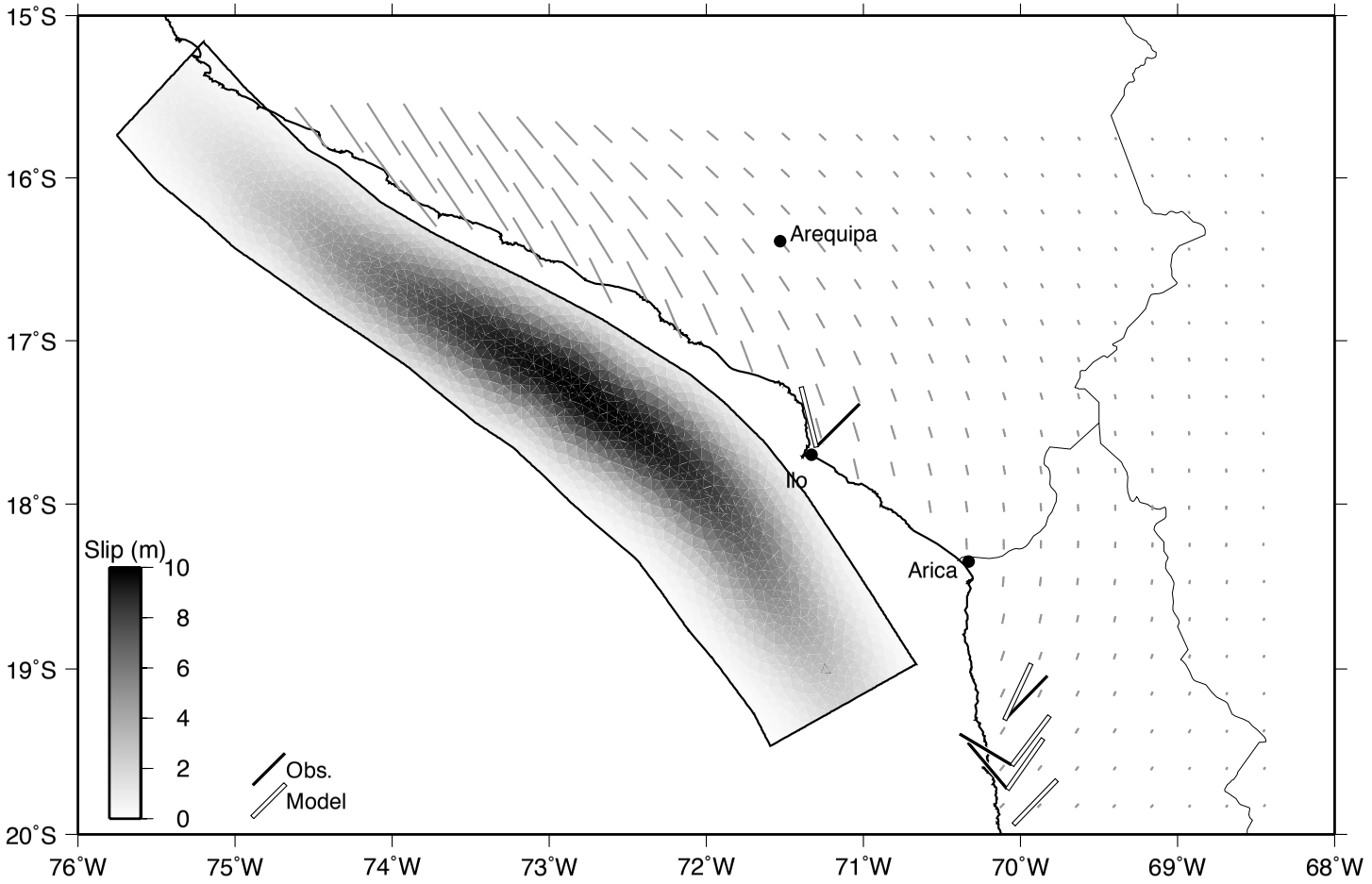

Figure 3.5: Static stress model for the 1868 M∼8.5 earthquake in southern Peru. The slip distribution is approximated based on the rupture extent and magnitude estimates (*Dorbath et al.*, 1990; *Comte and Pardo*, 1991). All symbols are as described in Figure 3.3. The northernmost and southernmost crack populations in Chile show bimodal strike distributions (Figure 3.1), while the others show unimodal strikes.

populations in that region. The NW striking cracks in the northernmost Chile clusters are not strongly influenced by the static stress related to the 1868 and 1604 earthquakes. The cracks mapped near the city of Ilo, Peru lie near the center of the estimated rupture zone and strike nearly perpendicular to the σ_1 orientation predicted by the 1868 model, indicating that these cracks are also minimally affected by the static stress caused by earthquakes on this segment.

The Ilo cracks are presumed to encompass those described by *Keefer and Moseley* (2004) that are suggested to have formed either during or shortly after the 2001 Arequipa earthquake. The σ_1 predicted from the coseismic model is rotated $\sim$45° counterclockwise from observed strike (Figure 3.6), thus the static stress induced by the 2001 earthquake was not ideally oriented for generating mode 1 cracks of the observed orientation. These features are interpreted to be reactivated structures initially formed during the 1604 earthquake (*Keefer and Moseley*, 2004) but, as described above, static stress caused by the 1604 event is unlikely to have been oriented favorably for opening mode 1 cracks with the mapped strikes. There are several minor upper-plate fault scarps within the cracked region and so the cracks may be related primarily to localized deformation around these features. *En echelon* map patterns of cracks suggest accommodation of WSW-directed left-lateral shear in addition to opening, consistent with the kinematics reported for nearby faults (*Audin et al.*, 2006). This suggests that the cracks near Ilo are mixed-mode (1 and 2) cracks and thus we expect that σ_1 for the stress field that created them should be oblique to the crack strike and oriented approximately as predicted by our elastic model.

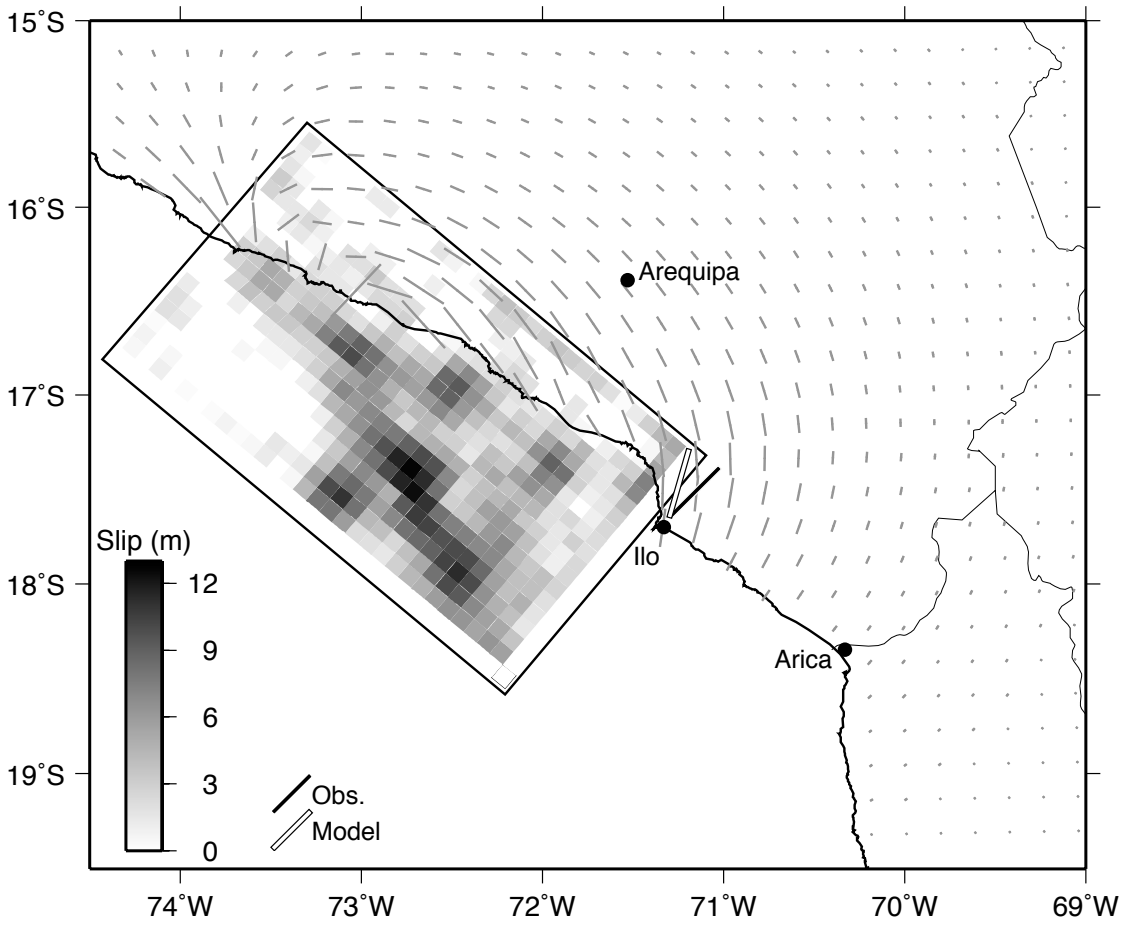

Figure 3.6: Static stress model for the 2001 M_w 8.3 8.5 Arequipa, Peru earthquake. The slip distribution is based on a joint inversion of seismic, GPS, and InSAR data (*Pritchard et al.*, 2007). The symbols are as described in Figure 3.3.

3.5.3 Inverse model parameters

The forward modeling described above allows for comparison between the earthquake stress fields, which are a function of the coseismic interplate slip distribution, and the patterns of strain demonstrated by the cracks. In the case of the 1995 and 2001 earthquakes, geodetic and seismic data provide constraints on the details of slip distributions. For the historical earthquakes, however, no such quantitative information is available, leaving the slip distributions poorly constrained.

Because the inferred rupture limit of the 1877 earthquake encompasses 16 of the 17 cracked regions (Figure 3.1), we use the cracks to explore plausible slip distributions related to that event, or a sum of events occurring on the segment. In doing so, we make the assumption that cracks within a given cluster open exclusively due to earthquakes on this segment and that the observed latitudinal variation in strike is related to heterogeneity in the coseismic slip distributions.

We use Poly3DInv (*Maerten et al.*, 2005) to invert the strain fields demonstrated by the surface cracks for the slip on the subduction thrust. This boundary element program allows use of strain tensor data to constrain the distribution of slip on the subduction interface. We assign a principal strain tensor to each of the 16 crack populations within the bounds of the 1877 earthquake segment, with the principal axis orientations reflecting the mean strike of cracks in the cluster and the principal strain magnitudes representing the amount of finite strain exhibited by cracks. Where cracks show a bimodal distribution in strike, we selectively filter the crack population such that the mean strike used in the inversion reflects only the set more favorably oriented for opening according to the predictions of the simple Gaussian slip forward model. In some models, we define the strain magnitude by calculating the mean crack density (total length of cracking per unit area) in each population, while in others, we assign a uniform strain magnitude to all crack clusters. Further discussion of the inversion strategy is found in Appendix E.

3.5.4 Inverse model results

Though there are angular discrepancies between the mean crack strikes and the orientations predicted by the forward models, there is generally good agreement between the modeled stress and observed strain. The results of our preferred inver-

sion of the crack distributions for slip along the Iquique segment of the margin are shown in Figure 3.7. While the preferred solution for coseismic slip is non-unique and sensitive to the choice of parameters governing the inversion (see Appendix E), several robust features of the slip distribution are noted. The majority of interplate slip constrained by the crack distributions is concentrated around 35 km depth offshore Iquique (20.25°S), about 1 degree north of the inferred epicenter of the 1877 earthquake (*Comte and Pardo*, 1991). Smaller loci of moment release are located around 21.75°S and 23.5°S. These southern patches are disconnected from the region of greatest slip near Iquique, suggesting that they may reflect slip associated with separate earthquakes or widely-spaced asperities that rupture during a single event. Alternatively, we suspect that the discontinuity between these slip patches may result from the lack of constraining data between ∼21.5° and 22.75°S. Because of the lack of temporal information contained in the dataset, the crack-based strain field cannot distinguish a single earthquake with a heterogeneous slip distribution from several smaller earthquakes.

The surface stress field resulting from the preferred inverse model (Figure 3.7) is more chaotic than that of the Gaussian forward model (Figure 3.4), reflecting the heterogeneity of slip in the inversion. Figure 3.7 shows the mean strike observed in each crack population as well as the predicted strike of cracks resulting from the modeled stress field. The mean difference between the observed crack strike and the modeled σ_1 direction is 9.0° and at only one of the 16 crack distributions is the discrepancy greater than 15°, indicating a good statistical fit.

Figure 3.7: Preferred inverse model of the 1877 Iquique earthquake, or a combination of several strong earthquakes on this segment of the plate boundary. The slip distribution was calculated by inverting the strain field represented by the populations of surface cracks for slip on the subduction interface. The symbols are as described for Figure 3.3. Additional discussion and models appear in Appendix E.

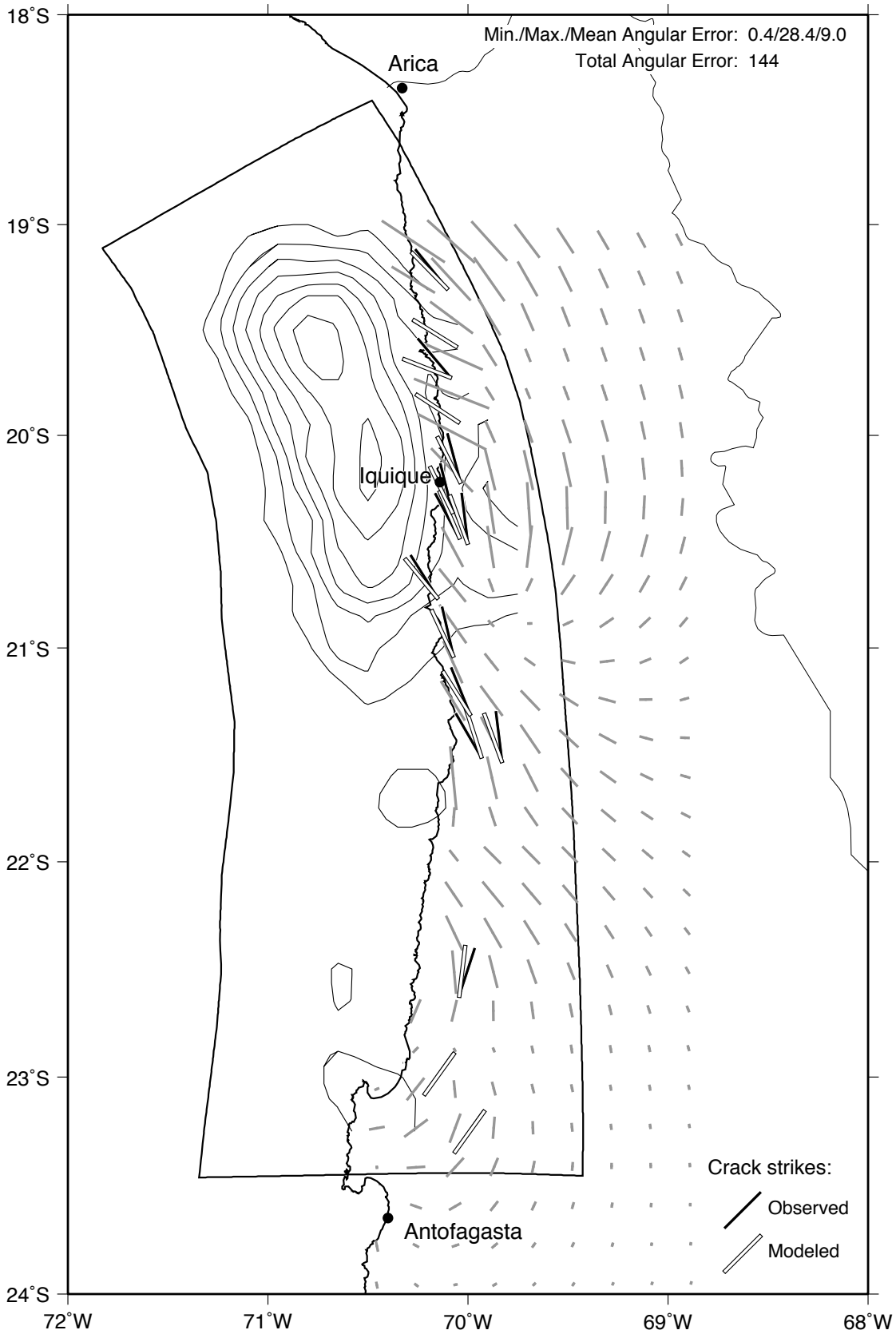
Min./Max./Mean Angular Error: 0.4/28.4/9.0
Total Angular Error: 144
Arica
Iquique
Antofagasta
Crack strikes:
Observed
Modeled
18˚S
19˚S
20˚S
21˚S
22˚S
23˚S
24˚S
72˚W
71˚W
70˚W
69˚W
68˚W

3.5.5 Dynamic stress parameters

The simulations described above allow for comparison between the observed distribution and orientation of cracks and the static coseismic stress. *Dalguer et al.* (2003) indicate that dynamic stresses, associated with the passage of seismic waves, can also cause mode 1 cracking of the surface. To address the possibility that such a process could be responsible for the cracks we observe, we use the method of *Cotton and Coutant* (1997) to calculate the temporal evolution of stress induced at the surface for the 1995 and 2001 earthquakes and compare the orientation of the time-varying principal stress axes to the static stress fields for the same events. For these models, we use the spatiotemporal slip distributions presented by *Pritchard et al.* (2006, 2007) and the crustal velocity model of *Husen et al.* (1999) as model parameters.

3.5.6 Dynamic stress results

Our simulations of the 1995 and 2001 earthquakes show that the static stress axes calculated from the simple dislocation models are reasonably similar in orientation to the dynamic principal stresses (Figures 3.8, 3.9 and associated electronic material). This indicates that our regional-scale mapping of macroscopic cracks places constraints on the extent and distribution of slip associated with plate boundary earthquakes, regardless of whether static or dynamic coseismic stress is the primary driver of crack evolution.

A notable characteristic of the dynamic stress fields is the occurrence of locations where both principal axes have the same sign. Where and when both horizontal principal stresses axes are tensional, it is possible that surface cracks could open in directions orthogonal to each other. Therefore, the dynamic stress

fields provide a mechanism for the bimodal strike distributions of crack populations near earthquake rupture segments. Furthermore, the cracks near Ilo with orientations highly oblique to the strike predicted by the static model for the 1868 (and therefore 1604) and 2001 earthquakes, may open and propagate as a result of this type of dynamic phenomenon. The same explanation could apply to the cracks east of the Mejillones Peninsula. The slip distribution in the static inverse model shows only minor moment release on the southern portion of the modeled Iquique segment (Figure 3.7), which may not be sufficient to activate cracks at the surface. Rather than being activated by the static stress field related to earthquakes on the Iquique and Antofagasta segments of the plate boundary, the evolution of these cracks may be controlled primarily by the larger-magnitude dynamic stresses.

3.6 Discussion

3.6.1 Plausibility of the inversion slip distribution

Several characteristics of the inverse slip distribution (Figure 3.7) warrant comparison with previous studies of subduction zone seismicity and properties of the plate interface. We solved for slip on a portion of the plate boundary that is larger, both in along-strike and down-dip extent, than the inferred rupture limits of the 1877 earthquake (*Comte and Pardo*, 1991). The preferred inversion resolves a region of substantial moment release offshore Iquique, with maximum slip located near 35 km depth and smoothly decreasing in all directions (Figure 3.7). Previous studies of the depth limits of the seismogenic zone (e.g., *Tichelaar and Ruff*, 1991) suggest that most plate boundary earthquakes occur on a portion of the interface between 20 and 50 km depth. Below 50 km, the plate interface is thought to be

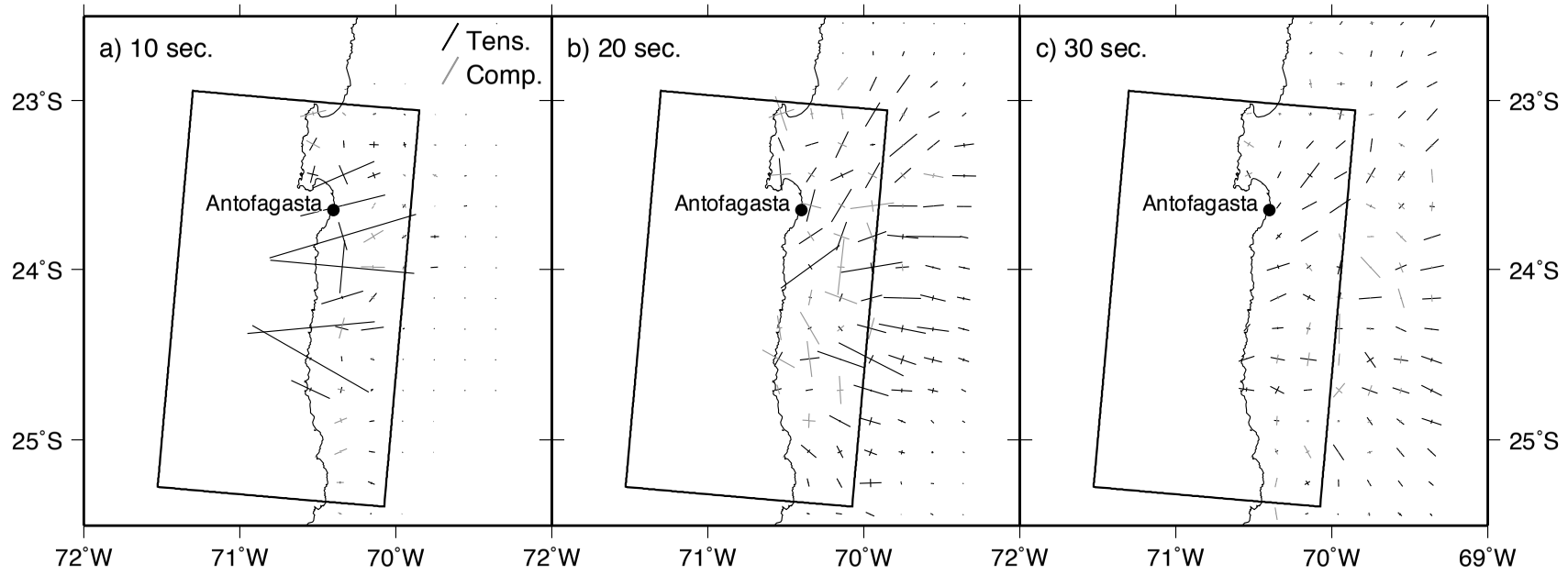

Figure 3.8: Temporal evolution of the coseismic stress field of the 1995 Antofagasta earthquake. We chose time snapshots at 10 (a), 20 (b), and 30 (c) seconds after the beginning of the rupture to show the variation in the dynamic stress field. In general, the magnitude and sign of stress axes change more so than the orientation, indicating that the static principal stress axes shown in Figure 3.3 describe reasonably well the potential impact of coseismic stress on crack formation. The time series of principal stress axes were calculated using the algorithms of *Cotton and Coutant* (1997) and the spatiotemporal slip distribution of *Pritchard et al.* (2006).

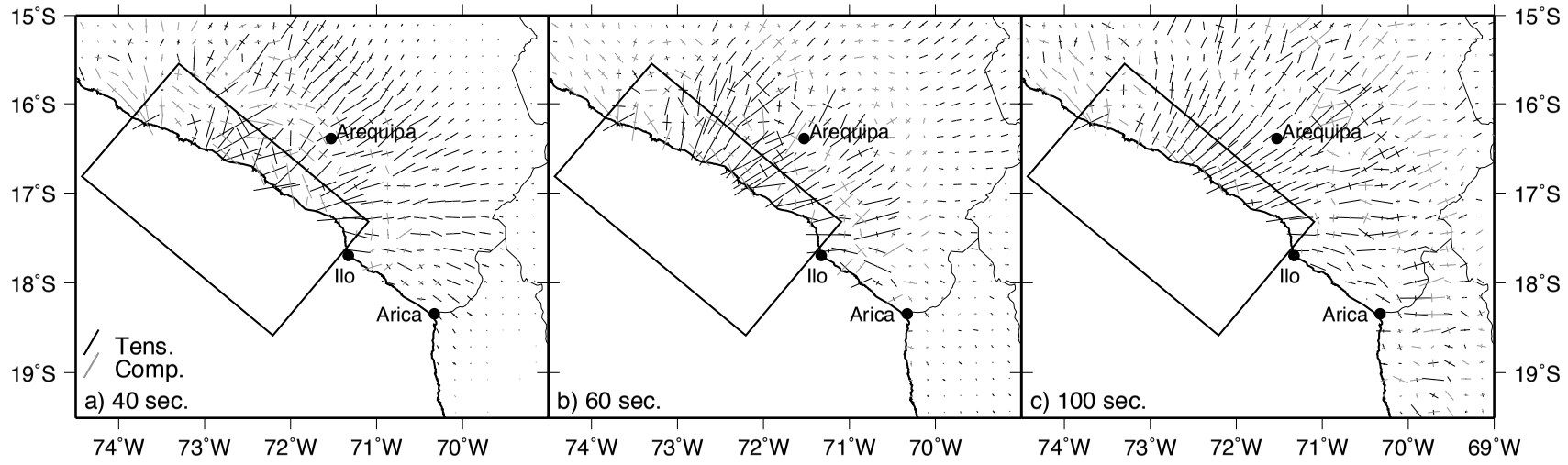

Figure 3.9: Temporal evolution of the stress field related to the 2001 Arequipa earthquake, shown as snapshots taken at 40, 60, and 100 seconds after rupture initiation. The distribution of slip is from *Pritchard et al.* (2007) and all symbols are as described in the caption for Figure 3.8.

characterized by a transition zone (e.g., *Oleskevich et al.*, 1999) within which seismic rupture may propagate but not initiate. Therefore, a physically reasonable interpretation of the slip resolved by the inversion is that the rupture initiated northwest of Iquique around 35 km depth and propagated down-dip and to the southeast. The disconnect between the patches of slip towards the south end of the model geometry relative to the zone near Iquique suggests that the southern rupture patches may reflect a small sub-event triggered by the primary moment release. It is unclear whether or not the sub-event alone would be capable of producing stress of sufficient magnitude to cause cracking at the surface.

Because the inversion of crack-based strain data for slip on the fault relies on an assumption that cracking results primarily from strong subduction earthquakes, we seek an independent constraint on the resolved slip distribution. The resolved 35 km depth of maximum slip is consistent with the concentration of slip during the Antofagasta earthquake (Figure 3.3, *Pritchard et al.*, 2006), indicating that this basic characteristic of the inversion result is plausible given regional seismogenic behavior.

Two independent studies (*Song and Simons*, 2003; *Wells et al.*, 2003) examined gravity anomalies along subduction zones worldwide and presented a correlation between the gravity field and coseismic slip magnitude. *Wells et al.* (2003) presented a spatial correlation between large magnitudes of slip during great underthrusting earthquakes and negative anomalies in the gravity field. *Song and Simons* (2003) subtracted the mean trench-perpendicular profile from the gravity anomaly field in each subduction zone to create a map of the trench-parallel gravity anomaly (TPGA), which effectively highlights short-wavelength features of the anomaly field. They found that the regions experiencing the largest magnitude

Figure 3.10: Trench-parallel gravity anomaly (TPGA) constructed for the Iquique segment of the Andean plate boundary. The construction is based on the gravity anomaly data of *Sandwell and Smith* (1997) and the method of *Song and Simons* (2003). The thin dashed black line shows the inland extent of the TPGA calculation. The position of the trench is indicated by the barbed line. The black polygon shows the outline of the crack inversion subduction thrust geometry and the gray contours show the slip distribution of our preferred inverse model (1 m slip contour interval).

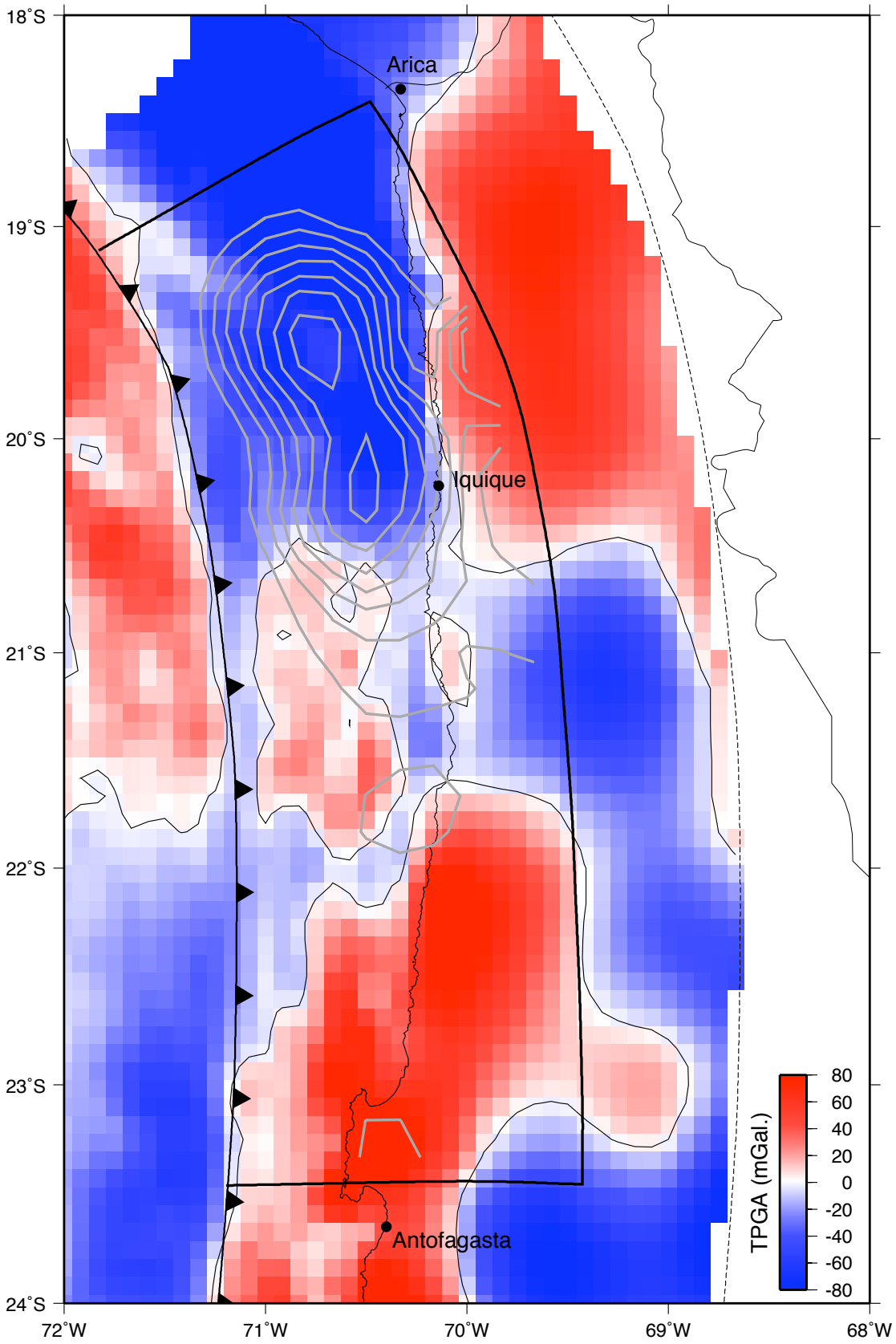
18°S
19°S
20°S
21°S
22°S
23°S
24°S
72°W
71°W
70°W
69°W
68°W
Arica
Iquique
Antofagasta
TPGA (mGal.)
80
60
40
20
0
-20
-40
-60
-80

of coseismic slip are also characterized by negative TPGA. We use the gravity anomaly field of *Sandwell and Smith* (1997) and the method of *Song and Simons* (2003) to construct a TPGA field for the Iquique segment to compare with the slip distribution resolved from inversion of the crack-based strain data (Figure 3.10). The region in which resolved slip is greatest coincides with an area of strongly-negative TPGA. The lack of resolved slip at shallow depths south of 21°S is consistent with the prevalence of positive TPGA, which predicts slip of lower magnitude. While not a perfect correlation, the spatial coincidence between coseismic slip and negative TPGA provides some independent support for the plausibility of the slip distribution determined by inverting the crack-based strain data.

3.6.2 Effects of multiple subduction earthquakes

Our field observations of the cracks indicate that they record extension associated with more than a single event. However, the scarcity of dateable materials cut by the cracks limits the temporal information they provide. The favorable comparisons between the coseismic stress fields and the strain represented by the cracks demonstrates the influence that strong subduction zone earthquakes have on the development of small-scale surface features. However, the single earthquakes considered in our analyses can not explain the repeated opening indicated by the crack morphologies. Once formed, a crack can be reactivated by a stress tensor with principal axes oriented differently than those that initiated the crack. Therefore, the cracks we observe in the Andean forearc could possibly represent a compound response to principal stresses of varying orientations induced by earthquakes with varying slip distributions. However, the aforementioned paucity of lateral offset implies that, for the most part, reactivation of cracks is accomplished by stresses

oriented favorably for mode 1 fracture, requiring a similar rupture extent for each great earthquake along a particular segment.

As the inversion of the cracks affected by seismicity on the Iquique segment indicates, deformation resulting from a heterogeneous slip distribution provides the best statistical fit to the crack patterns. A single earthquake may be characterized by a smoothly varying rupture pattern, such as the Gaussian approximation we use in modeling the historical earthquakes (Figures 3.4 and 3.5), or slip may be concentrated in distinct patches (asperities) surrounded by velocity-strengthening material (e.g., *Bilek and Lay*, 2002), as seen in the slip maps of the recent earthquakes (Figures 3.3 and 3.6) and the inversion of crack strikes for slip on the Iquique segment (Figure 3.7; see also Appendix E). The results of the forward and inverse modeling indicates that, when examined on a regional scale, the stress field induced at the surface by subduction earthquakes is more sensitive to the extent of coseismic slip rather than the details of its distribution. This suggests that earthquakes on a given segment of the plate boundary may vary in their distribution of slip, but the accumulated strain exhibited by the suites of surface cracks indicates that the dimensions of rupture remain relatively constant. The obliquity between cracks strike and the plate boundary and the concentration of bimodal strike distributions at inferred segment boundaries is consistent with longevity of the rupture limits. If the location of segment boundaries varied substantially though time, we would expect cracks to show a range of strikes rather than one or two preferred orientations.

3.7 Conclusions

According to our models, stresses caused by strong subduction zone earthquakes are oriented favorably for reactivation of the many surface cracks that cut coastal regions of northern Chile and southern Peru. Our modeling indicates that the spatial patterns of principal stress axes depend more strongly on the extent of rupture than on the details of the slip distribution. Despite the fact that numerous subduction zone earthquakes on a particular segment — each of which may have a unique rupture pattern — are required to explain the extent and style of cracking observed, the dimensions of rupture play the dominant role in determining crack orientation. The meter-scale surface cracks represent a permanent record of subduction zone seismicity and, more specifically, can be used to map the extent of plate boundary segments that persist for at least several seismic cycles if not several hundred thousand years.

BIBLIOGRAPHY

Audin, L., P. Lacan, H. Tavera, and S. Carretier (2006), The Chololo Fault System and geomorphic evidences of recent faulting activity in the Coastal Cordillera, southern Peru, in *XI Congreso Geológico Chileno*, vol. 2, pp. 371–374, Antofagasta, Chile.

Bilek, S. L., and T. Lay (2002), Tsunami earthquakes possibly widespread manifestations of frictional conditional stability, *Geophysical Research Letters*, *29*(14), 1673, doi:10.1029/2002GL015215.

Carrizo, D., G. González, and T. Dunai (2007), Constricción neógena en la cordillera de la costa norte de Chile: Neotectónica y datación de superficies con ^{21}Ne cosmogénico, *Revista Geológica de Chile*, *34*, in review.

Comte, D., and M. Pardo (1991), Reappraisal of great historical earthquakes in the northern Chile and southern Peru seismic gaps, *Natural Hazards*, *4*(1), 23–44, doi:10.1007/BF00126557.

Cotton, F., and O. Coutant (1997), Dynamic stress variations due to shear faults in a plane-layered medium, *Geophysical Journal International*, *128*, 676–688, doi:10.1111/j.1365-246X.1997.tb05328.x.

Dalguer, L. A., K. Irikura, and J. D. Riera (2003), Simulation of tensile crack generation by three-dimensional dynamic shear rupture propagation during an earthquake, *Journal of Geophysical Research*, *108*(B3), 2144, doi:10.1029/2001JB001738.

Delouis, B., T. Monfret, L. Dorbath, M. Pardo, L. Rivera, D. Comte, H. Haessler, J. P. Caminade, L. Ponce, E. Kausel, and A. Cisternas (1997), The M_W = 8.0 Antofagasta (Northern Chile) earthquake of 30 July 1995: A precursor to the end of the large 1877 gap, *Bulletin of the Seismological Society of America*, *87*(2), 427–445.

Dorbath, L., A. Cisternas, and C. Dorbath (1990), Quantitative assessment of great earthquakes in Peru, *Bulletin of the Seismological Society of America*, *80*, 551–576.

Dunai, T. J., G. A. González L., and J. Juez-Larré (2005), Oligocene–Miocene age of aridity in the Atacama Desert revealed by exposure dating of erosion-sensitive landforms, *Geology*, *33*(4), 321–324, doi:10.1130/G21184.1.

Ewing, S., B. Sutter, J. Owen, K. Nishiizumi, W. Sharp, S. S. Cliff, K. Perry, W. Dietrich, C. P. McKay, and R. Amundson (2006), A threshold in soil formation at Earth's arid–hyperarid transition, *Geochimica et Cosmochimica Acta*, *70*, 5293–5322, doi:10.1016/j.gca.2006.08.020.

González, G., J. Cembrano, D. Carrizo, A. Macci, and H. Schneider (2003), The link between forearc tectonics and Pliocene-Quaternary deformation of the Coastal Cordillera, northern Chile, *Journal of South American Earth Sciences*, *16*, 321–342, doi:10.1016/S0895-9811(03)00100-7.

González, G., T. Dunai, D. Carrizo, and R. Allmendinger (2006), Young displacements on the Atacama Fault System, northern Chile from field observations and cosmogenic ^{21}Ne concentrations, *Tectonics*, *25*, TC3006, doi:10.1029/2005TC001846.

González, G., M. Gerbault, J. Martinod, J. Cembrano, D. Carrizo, R. Allmendinger, and J. Espina (2007), Crack formation above propagating reverse faults, Chuculay Fault System, Coastal Cordillera, northern Chile: Insight from IKONOS data and numerical modeling, *Journal of Structural Geology*, in review.

Hartley, A. J., and G. Chong (2002), Late Pliocene age for the Atacama Desert: Implications for the desertification of western South America, *Geology*, *30*(1), 43–46, doi:10.1130/0091-7613(2002)030<0043:LPAFTA>2.0.CO;2.

Hoke, G. D., B. L. Isacks, T. E. Jordan, and J. S. Yu (2004), Groundwater-sapping origin for the giant quebradas of northern Chile, *Geology*, *32*(7), 605–608, doi:10.1130/G20601.1.

Husen, S., E. Kissling, E. Flueh, and G. Asch (1999), Accurate hypocentre determination in the seismogenic zone of the subducting Nazca Plate in northern Chile using a combined on-/offshore network, *Geophysical Journal International*, *138*(3), 687–701, doi:10.1046/j.1365-246x.1999.00893.x.

Ihmlé, P. F., and J. Ruegg (1997), Source tomography by simulated annealing using broad-band surface waves and geodetic data: Application to the $M_w = 8.1$ Chile 1995 event, *Geophysical Journal International*, *131*, 146–158.

Kausel, E. (1986), Los terremotos de agosto de 1868 y mayo de 1877 que afectaron el sur del Perú y norte de Chile, *Boletín Academia Chilena de Ciencias*, *3*, 8–13.

Keefer, D. K., and M. E. Moseley (2004), Southern Peru desert shattered by the great 2001 earthquake: Implications for paleoseismic and paleo-El Niño-Southern Oscillation records, *Proceedings of the National Academy of Sciences*, *101*, 10,878–10,883, doi:10.1073/pnas.0404320101.

Loveless, J. P., G. D. Hoke, R. W. Allmendinger, G. González, B. L. Isacks, and D. A. Carrizo (2005), Pervasive cracking of the northern Chilean Coastal Cordillera: New evidence for forearc extension, *Geology*, *33*(12), 973–976, doi:10.1130/G22004.1.

Maerten, F., P. Resor, D. D. Pollard, and L. Maerten (2005), Inverting for slip on three-dimensional fault surfaces using angular dislocations, *Bulletin of the Seismological Society of America*, *95*(5), 1654–1665, doi:10.1785/0120030181.

Marquardt, C., J. A. Naranjo, and A. Lavenu (2006), Efectos geológicos del sismo del 13 de junio 2005, Región de Tarapacá, in *XI Congreso Geológico Chileno*, vol. 2, pp. 435–438, Antofagasta, Chile.

Nishenko, S. P. (1985), Seismic potential for large and great interplate earthquakes along the Chilean and southern Peruvian margins of South America: A quantitative reappraisal, *Journal of Geophysical Research*, *90*(B5), 3589–3615.

Oleskevich, D. A., R. D. Hyndman, and K. Wang (1999), The updip and downdip limits to great subduction earthquakes: Thermal and structural models of Cascadia, south Alaska, SW Japan, and Chile, *Journal of Geophysical Research*, *104*(B7), 14,965–14,991, doi:10.1029/1999JB900060.

Pollard, D. D., and P. Segall (1987), Theoretical displacements and stresses near fractures in rock: With applications to faults, joints, veins, dikes, and solution surface, in *Fracture Mechanics of Rock*, edited by B. K. Atkinson, pp. 277–349, Academic Press, London.

Pritchard, M. E., M. Simons, P. A. Rosen, S. Hensley, and F. H. Webb (2002), Coseismic slip from the 1995 July 30 $M_w = 8.1$ Antofagasta, Chile earthquake as constrained by InSAR and GPS observations, *Geophysical Journal International*, *150*, 362–376, doi:10.1046/j.1365-246X.2002.01661.x.

Pritchard, M. E., C. Ji, and M. Simons (2006), Distribution of slip from 11 $M_w > 6$ earthquakes in the northern Chile subduction zone, *Journal of Geophysical Research*, *111*, B10302, doi:10.1029/2005JB004013.

Pritchard, M. E., E. O. Norabuena, C. Ji, R. Boroschek, D. Comte, M. Simons, T. Dixon, and P. A. Rosen (2007), Geodetic, teleseismic, and strong motion constraints on slip from recent southern Peru subduction zone earthquakes, *Journal of Geophysical Research*, *112*, B03307, doi:10.1029/2006JB004294.

Rech, J. A., J. Quade, and W. S. Hart (2003), Isotopic evidence for the source of Ca and S in soil gypsum, anhydrite and calcite in the Atacama Desert, Chile, *Geochimica et Cosmochimica Acta*, *67*(4), 575–586, doi:10.1016/S0016-7037(02)01175-4.

Rech, J. A., B. S. Currie, G. Michalski, and A. M. Cowan (2006), Neogene climate change and uplift in the Atacama Desert, Chile, *Geology*, *34*(9), 761–764, doi:10.1130/G22444.1.

Ruegg, J., J. Campos, R. Armijo, S. Barrientos, P. Briole, R. Thiele, M. Arancibia, J. Cañuta, T. Duquesnoy, M. Chang, D. Lazo, H. Lyon-Caen, L. Ortlieb, J. Rossignol, and L. Serruier (1996), The $M_w = 8.1$ Antofagasta (North Chile) Earthquake of July 30, 1995: First results from teleseismic and geodetic data, *Geophysical Research Letters*, *23*(9), 917–920.

Ruegg, J., M. Olcay, and D. Lazo (2001), Co-, post- and pre-seismic displacements associated with the M_w 8.4 southern Peru earthquake of 23 June 2001 from continuous GPS measurements, *Seismological Research Letters*, *72*(6), 673–678.

Sandwell, D. T., and W. H. F. Smith (1997), Marine gravity anomaly from Geosat and ERS-1 satellite altimetry, *Journal of Geophysical Research*, *102*(B5), 10,039–10,054, doi:10.1029/96JB03223.

Sobiesiak, M. M. (2004), Fault Plane Structure of the 1995 Antofagasta Earthquake (Chile) Derived From Local Seismological Parameters, PhD. thesis, Universität Potsdam, Potsdam, Germany.

Song, T.-R. A., and M. Simons (2003), Large trench-parallel gravity variations predict seismogenic behavior in subduction zones, *Science*, *301*(5633), 630–633, doi:10.1126/science.1085557.

Thomas, A. L. (1993), Poly3D: A three-dimensional, polygonal element, displacement discontinuity boundary element computer program with applications to fractures, faults, and cavities in the Earth's crust, M.S. thesis, Stanford University, Stanford, CA.

Tichelaar, B. W., and L. J. Ruff (1991), Seismic coupling along the Chilean subduction zone, *Journal of Geophysical Research*, *96*(B7), 11,997–12,022.

Wartman, J., A. Rodriguez-Marek, P. C. Reperro, and D. K. Keefer (2003), Ground failure, in *Southern Peru Earthquake of 23 June 2001 Reconnaissance Report*, edited by A. Rodriguez-Marek and C. Edwards, Earthquake Spectra, Supplement to v. 19, pp. 35–56.

Wells, R. E., R. J. Blakely, Y. Sugiyama, D. W. Scholl, and P. A. Dinterman (2003), Basin-centered asperities in great subduction zone earthquakes: A link between slip, subsidence, and subduction erosion?, *Journal of Geophysical Research*, *108*(B10), 2507, doi:10.1029/2002JB002072.

CHAPTER 4

VARIATION IN UPPER PLATE COULOMB STRESS CHANGES DUE TO THE 1995 ANTOFAGASTA (CHILE) EARTHQUAKE

4.1 Abstract

The Atacama Fault System (AFS), a 1000 km long fault that has accommodated dominantly normal neotectonic motion, is the dominant structure of the northern Chilean forearc. Several important questions exist regarding its behavior, including its capability to produce shallow earthquakes, the recurrence interval of slip events, and its interaction with the Andean subduction seismic cycle. We use two approaches, theoretical and observational, to evaluate how coseismic stress induced by the 1995 M_w=8.1 subduction earthquake near the city of Antofagasta affected the AFS and other upper plate faults in the forearc. Using seven published slip maps constrained by geodetic and/or seismic data, we calculate Coulomb stress change (CSC) on faults in the Antofagasta region. The CSC field varies between models and depends on the distribution of coseismic interplate slip. Some simulations predict positive CSC (encouraging failure) at shallow depths on normal faults south of Antofagasta, while other models constrained by multiple data sets show zero change or stress decrease on these faults. Negative CSC on faults on the Mejillones Peninsula and east of Antofagasta is predicted by all models and may provide a mechanism for the reverse reactivation of some normal faults that we observe in the field. Field reports of coseismically-triggered normal motion on the Paposo segment of the AFS, south of the city, are consistent with the positive CSC calculated using some models but incompatible with the negligible to negative shallow CSC predicted by the models constrained by all available data. In addi-

tion to stress modeling, we use synthetic aperture radar interferometry (InSAR) to search for small-scale deformation on individual faults triggered by the subduction zone earthquake. The InSAR data are ambiguous, as some images show apparent offset consistent with coseismic faulting on the Paposo segment and others lack such signal. The fact that we do not observe the fault-like displacement in all coseismic interferograms suggests that atmospheric contamination across steep fault scarps, and not tectonic deformation, is responsible for the signal. Abrupt, localized changes in radar phase delay are induced by propagation through water vapor in the troposphere and require consideration in InSAR-based observations of small-scale deformation, particularly in areas of high relief.

4.2 Introduction

The Atacama Fault System (AFS) and other upper plate faults throughout the northern Chilean forearc have been the target of several structural studies (e.g., *Arabasz*, 1971; *Armijo and Thiele*, 1990; *Niemeyer et al.*, 1996; *Delouis et al.*, 1998; *González et al.*, 2003). However, several important questions remain regarding the neotectonic behavior of these structures, including their connection with the subduction earthquake cycle, the recurrence interval of slip events, and their seismogenic potential. For the most part, faults in the Antofagasta region (Figure 4.1) demonstrate finite extension in the direction of plate convergence (*Arabasz*, 1971; *Delouis et al.*, 1998; *González et al.*, 2003). Several mechanisms have been proposed to explain the presence of these extensional structures in a convergent margin setting, including earthquake-cycle processes of interseismic flexure (Chapters 1, 5; *González et al.*, 2003) and coseismic elastic rebound (Chapters 1, 5; *Delouis et al.*, 1998; *González et al.*, 2003), and longer-term effects associated with

subduction erosion (*Niemeyer et al.*, 1996; *Delouis et al.*, 1998; *von Huene and Ranero*, 2003; *Sallàres and Ranero*, 2005). While the dominant deformation signal on these structures is of east-west extension, minor reverse movement is superimposed on some faults (Chapter 5) and in at least one case represents the most recent episode of fault motion. Despite numerous examples of fresh-appearing surface faulting, inferred to reflect Quaternary deformation (*Delouis et al.*, 1998; *González et al.*, 2003; *González and Carrizo*, 2003), there exists only one definitive date on young fault activity, which constrains motion on one segment of the AFS to be younger than 424±151 kyr (*González et al.*, 2006). Three local seismic surveys found little upper plate seismicity distinctly correlated with mapped faults (*Arabasz*, 1971; *Comte et al.*, 1994; *Delouis et al.*, 1996), leaving the seismogenic capability of the AFS poorly understood.

We use the 30 July 1995 M_w= 8.1 Antofagasta, Chile earthquake as a test case for examining the relationships between the Atacama Fault System (AFS) and subduction zone processes. Studies of this event have benefitted from the availability of geodetic, seismic, and geological data sets that captured various aspects of the co- and postseismic deformation. Collection of GPS (*Ruegg et al.*, 1996; *Klotz et al.*, 1999; *Chlieh et al.*, 2004), InSAR (*Pritchard et al.*, 2002; *Xia et al.*, 2003; *Chlieh et al.*, 2004; *Pritchard et al.*, 2006a), and geological data (*Ortlieb et al.*, 1996; *Delouis et al.*, 1997, 1998; *Klotz et al.*, 1999; *González et al.*, 2003) before and after the event, and seismic data during the earthquake and its aftershock sequence (*Ruegg et al.*, 1996; *Delouis et al.*, 1997; *Husen et al.*, 1999) have provided a comprehensive suite of information that has been used to model characteristics and effects of the rupture. In particular, *Delouis et al.* (1997); *Ihmlé and Ruegg* (1997); *Klotz et al.* (1999); *Pritchard et al.* (2002); *Xia et al.* (2003) and *Pritchard*

et al. (2006a) use these data to constrain the distribution of coseismic slip on the subduction thrust.

In this paper, we use seven published slip maps to calculate Coulomb stress change (CSC) on the AFS and other upper plate faults in order to explore the capacity of the earthquake for triggering slip on forearc structures. The neotectonic observations of normal and reverse motion indicate that upper plate faults slip in response to both compressional and tensional stress fields. Given the low magnitude of CSC induced by the subduction earthquake cycle, the level of stress on forearc fault zones must be very low, thus allowing slip in response to these minor stress perturbations (e.g., *Fialko et al.*, 2002; *Fialko*, 2004; *Fialko et al.*, 2005).

Field observations made shortly after the 1995 Antofagasta earthquake report ∼20 cm of east-side-down normal fault motion on the Paposo segment of the AFS (*Delouis et al.*, 1997, 1998; *Klotz et al.*, 1999) and 30 cm of normal offset near the Uribe rail station along the Salar del Carmen segment of the AFS (*Klotz et al.*, 1999, locations shown in Figure 4.1). However, other studies found no coseismically-triggered faulting (*Campos et al.*, 1995; *Ortlieb et al.*, 1996; *Ruegg et al.*, 1996) and only minor surface rupture in the form of small surface cracks located near the Salar del Carmen segment as noted by *González et al.* (2003); these features have been attributed to deep slip on that fault related to small aftershocks (*Ruegg et al.*, 1996; *González and Carrizo*, 2003). *Husen et al.* (1999) found several aftershocks potentially correlated with slip on the AFS but could not confirm a relationship to mapped fault traces.

To image the normal faulting reportedly triggered by the 1995 earthquake, we use InSAR observations, which should be capable of detecting the small-scale verti-

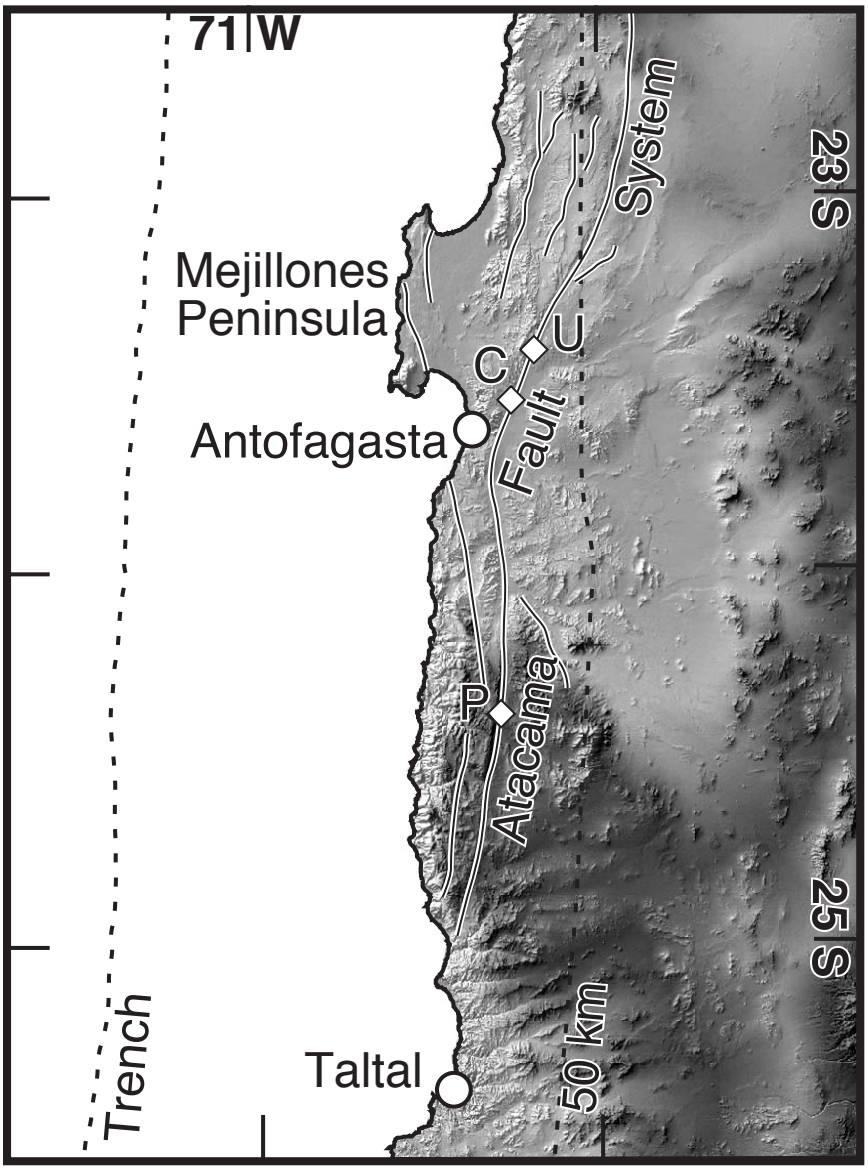

Figure 4.1: Location map of the Antofagasta region, showing the trace of the Atacama Fault System and other scarps (thin black lines with white outline). The dashed lines indicate the surface projections of the subduction trench and 50 km contour to the Wadati-Benioff zone (*Cahill and Isacks*, 1992). Diamonds indicate the approximate positions of the field reports of surface rupture triggered by the earthquake: P marks the Paposo rupture (*Delouis et al.*, 1997, 1998; *Klotz et al.*, 1999), U marks the Uribe rail station rupture (*Klotz et al.*, 1999), and C marks the surface cracking along the Salar del Carmen segment (*González et al.*, 2003; *González and Carrizo*, 2003).

cal offsets proposed by *Delouis et al.* (1997, 1998) and *Klotz et al.* (1999). However, because the putative slip occurred along a ∼200 m high fault scarp, InSAR observations are complicated by the presence of atmospheric water vapor, which shows a spatial correlation with the underlying topography. The radar signal is delayed by moisture as it propagates through the troposphere (e.g., *Hanssen*, 2001), introducing signals resembling fault offset into the interferograms. We analyze the atmospheric water vapor measured by the satellite-based MODIS sensor and consider the patterns of spatial and temporal variability in moisture content in our interpretation of the InSAR observations.

4.3 Modeling Coulomb stress change

To investigate the upper plate deformation induced in the Antofagasta region by the 1995 earthquake, we use seven published maps of coseismic slip on the subduction thrust (*Delouis et al.*, 1997; *Ihmlé and Ruegg*, 1997; *Klotz et al.*, 1999; *Pritchard et al.*, 2002; *Xia et al.*, 2003; *Pritchard et al.*, 2006a) to calculate upper-plate Coulomb stress change (CSC) fields. The CSC resulting from a tectonic perturbation is defined as

$$CSC = \Delta\tau - \mu'\Delta\sigma_n \tag{4.1}$$

where $\Delta\tau$ is the change in shear stress on a surface of prescribed orientation, μ' is the effective coefficient of friction, and $\Delta\sigma_n$ is the change in normal stress across the defined surface (*King et al.*, 1994; *Toda and Stein*, 2002). The maps of CSC presented in Figure 4.2 represent the changes in Coulomb stress resolved onto fault planes striking N10°E, approximately parallel to the northern Chilean coastline, dipping 80° E with a slip vector of rake -100° (positive counterclockwise from the strike direction). This orientation and slip sense are broadly consistent

Figure 4.2: a. Location map of region affected by the 1995 Antofagasta earthquake. Select upper plate faults (Papo: Paposo, Colo: Coloso, SdC: Salar del Carmen, Fort: Fortuna, Mj: Mejillones, Hr: Caleta Herradura) considered in the boundary element models are shown as black lines in all figures. Focal mechanism is from Harvard CMT catalog. b–h. Results of the Coulomb stress modeling. Models 1, 3, and 5, for which the slip distribution was digitized from the referenced publications, show outlines of the fault patches used in the calculation of Coulomb stress. For model 2, only the outline of the entire fault is shown, though it was modeled using individual patches. For model 4, the actual slip distribution from (*Pritchard et al.*, 2002) was used and the fault patches are shown here. Contours of slip magnitude are shown for models 6 and 7 (contour interval is 1 m).

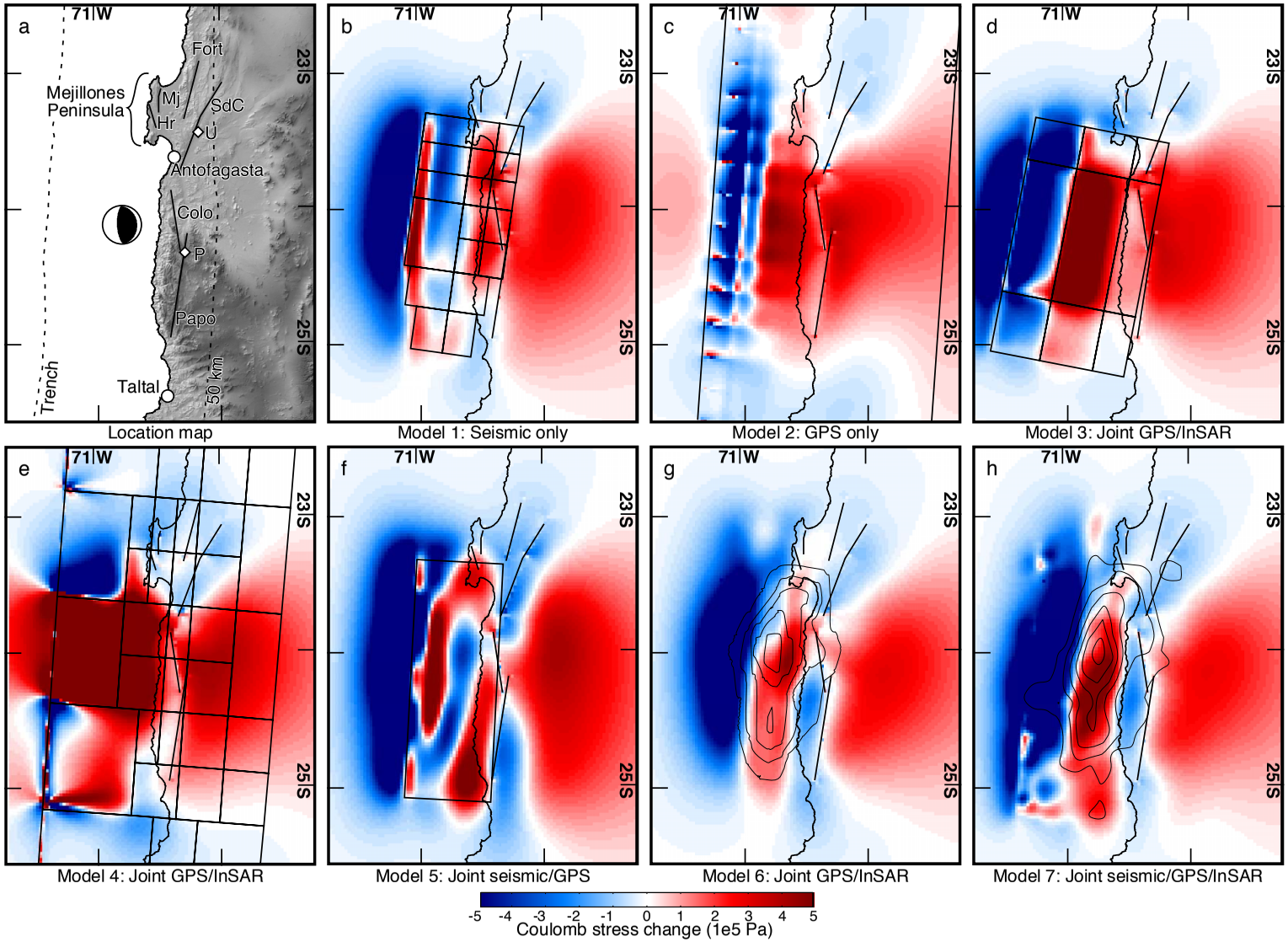
a
71|W
23|S
25|S
Fort
Mejillones
Peninsula
Mj
SdC
Hr
U
Antofagasta
Colo
P
Papo
Taltal
Trench
50 km
Location map
b
Model 1: Seismic only
c
Model 2: GPS only
d
Model 3: Joint GPS/InSAR
e
Model 4: Joint GPS/InSAR
f
Model 5: Joint seismic/GPS
g
Model 6: Joint GPS/InSAR
h
Model 7: Joint seismic/GPS/InSAR
-5 -4 -3 -2 -1 0 1 2 3 4 5
Coulomb stress change (1e5 Pa)

with fault kinematic data collected in the Antofagasta region (*Delouis et al.*, 1998; *González et al.*, 2003). We calculate the coseismic stress tensor using a three-dimensional boundary element code (Poly3D, *Thomas*, 1993) incorporating discontinuities within a homogenous elastic half-space in order to examine the effects of the stress perturbation resulting from the subduction zone earthquake on upper plate faults. We then convert the stress tensor into values of CSC by rotating the tensor into a coordinate system whose three axes are parallel to the slip vector and fault plane, perpendicular to the slip vector and parallel to the fault plane, and normal to the specified fault plane. All CSC calculations were carried out at a depth of 1 km, with μ'=0.4, following previous studies of static CSC (*King et al.*, 1994; *Toda et al.*, 1998; *Toda and Stein*, 2002; *Lin and Stein*, 2004). Slight changes in the depth ($0 \leq z \leq 3$ km), μ' value ($0 \leq \mu' \leq 0.6$), or receiver fault geometry (-10° $\leq$ strike $\leq$ 30°, 65° $\leq$ dip $\leq$ 85°E) and rake (-110° $\leq$ rake $\leq$ -90°) used in the calculation do not substantially affect the overall patterns of CSC. Additionally, calculations made in a layered elastic half-space based on the velocity model of *Husen et al.* (1999) do not differ substantially from those in the homogenous half-space; the results using the latter are presented here.

The sign convention adopted is such that positive CSC increases the likelihood of failure in the direction of the specified rake. Conversely, a negative CSC decreases the chances of normal rupture on these faults and may even encourage movement in a direction opposite the specified vector if the existing stress level on the fault is sufficiently low. Several studies (e.g., *Toda et al.*, 1998; *Toda and Stein*, 2002; *Lin and Stein*, 2004) have demonstrated that earthquake aftershocks generally are concentrated in regions in which the coseismic Coulomb stress is increased, while the rate of seismicity tends to decrease in stress shadows (areas of negative

CSC) generated by a large event. No aftershocks of the Antofagasta earthquake have been definitively correlated with the reported rupture on the Paposo or Salar del Carmen segments (*Delouis et al.*, 1998; *Husen et al.*, 1999; *Sobiesiak*, 2004), but we assume that any coseismic normal surface rupture should lie within a region in which positive CSC is predicted at shallow depths.

4.3.1 Slip distribution parameters

We generated seven maps of CSC (Figure 4.2b–h), each based on a different distribution of slip on the subduction thrust interface. The slip maps vary significantly in geometry and slip distribution (Table 4.1, Figure 4.3). In models 1, 3, and 5, we relied on digitization of published slip maps, and for models 2, 4, 6, and 7 we used the exact published slip distributions in the calculations. Interpolating the irregularly-spaced slip maps (models 1, 3, and 4) onto regularly-spaced grids of smaller fault patches, as shown in Figure 4.3, results in variation in the CSC predictions, but similar smoothing of the already regularly-spaced slip distributions (models 2, 5, 6, and 7) does not have a substantial impact on the CSC. Though the interpolated slip maps produce a smoother distribution of CSC, we consider only the original, published slip maps, as they represent the models that best fit the data used as constraint.

4.4 Modeling results

Figure 4.2 shows the results of the CSC modeling. Models 1–4 show increases in Coulomb stress along the Paposo segment of the AFS (labeled "Papo" in Figure 4.2a) and models 5–7 show zero or negative CSC along this fault, where *Delouis et al.* (1997, 1998) suggest 20 cm of coseismic normal faulting. The Coloso fault

Table 4.1: Coulomb stress change modeling parameters

Model[a]	Data Used	Length (km)	Width (km)	ΔZ (km)[b]	N[c]	Mean Dip[d]	Mean Rake[d]	Moment (m^3)[e]
1	Body-wave	193	81	15–41	18	18.1°	102°	3.29×10^{10}
2	GPS	400	200	0–72	150	21.1°	107°	4.74×10^{10}
3	InSAR, GPS	195	115	9–42	9	16.9°	117°	4.10×10^{10}
4	InSAR, GPS	647	212	0–79	41	21.4°	119°	7.28×10^{10}
5	Surface wave, GPS	195	75	12–39	65	21.3°	102°	4.91×10^{10}
6	InSAR, GPS	260	160	5–59	416	20.3°	107°	3.75×10^{10}
7	InSAR, GPS, Body-wave	260	160	5–59	416	20.3°	105°	3.92×10^{10}

[a]Model references: 1. *Delouis et al.* (1998), 2. *Klotz et al.* (1999), 3. *Xia et al.* (2003), 4. *Pritchard et al.* (2002), 5. *Ihmlé and Ruegg* (1997), 6. & 7. *Pritchard et al.* (2006a).

[b]Depth range

[c]Number of fault patches

[d]Mean values are weighted by slip magnitude.

[e]Geometric moment (sum of fault patch areas times slips) is reported.

Figure 4.3: a. Location map of region affected by the 1995 Antofagasta earthquake as in Figure 4.2a. b–h. Slip distributions used as input for the Coulomb stress modeling. Slip distributions for models 1, 3, and 5 were digitized from the publications referenced in Table 4.1, while exact slip distributions were used for models 2, 4, 6, and 7. All slip maps shown here have been interpolated on a 10×10 km grid, but the original slip distributions were used in the Coulomb stress calculations. Lines on land show positions of faults, as identified in (a). Position of trench (west) and 50 km Wadati-Benioff zone contour (east) from *Cahill and Isacks* (1992) are shown as dashed lines and vary to different degrees from the subduction zone geometry assumed in each of the models.

a
Location map
23°S
25°S
71°W
Trench
Meijillones Peninsula
Fort
Mj
SdC
Hr
U
Antofagasta
Colo
P
Papo
Taltal
50 km
b
Model 1: Seismic only
c
Model 2: GPS only
d
Model 3: Joint GPS/InSAR
e
Model 4: Joint GPS/InSAR
f
Model 5: Joint seismic/GPS
g
Model 6: Joint GPS/InSAR
h
Model 7: Joint seismic/GPS/InSAR

(Colo), located just north of the Paposo segment, experienced positive CSC according to models 1–5, but was affected by negative CSC in models 6 and 7. Most if not all of the Mejillones Peninsula, on which several normal faults are located, experienced a Coulomb stress decrease according to all models. Likewise, all models predict negative CSC along the Fortuna (Fort) fault and Salar del Carmen segment (SdC) of the AFS, although the southern extreme of this segment lies within a region of Coulomb stress increase in models 1–3.

In addition to performing a calculation of CSC on fault planes of the specified orientation with the specified slip vector, which is meant to approximate the fault slip data collected in the field, we also calculated the rake on the specific faults identified in Figure 4.2a that maximizes the increase in Coulomb stress. That is, we solved for the direction of slip most likely induced due only to the coseismic forcing. At the northern end of the Paposo segment (diamond marked "P" in Figure 4.2a), where pure normal rupture was reported by *Delouis et al.* (1997, 1998), only model 2 predicts normal motion as the optimal slip direction (rake of -82°, Table 4.2). Normal/left-lateral motion is suggested by models 1, 4, and 5, while models 3 and 5–7 predict left-lateral to reverse motion as the most-likely sense of slip (Table 4.2), which is inconsistent with the field reports. At the Uribe rail station ("U" in Figure 4.2a), where *Klotz et al.* (1999) reported 30 cm of normal fault offset, left-lateral motion, with a small component of reverse faulting, is predicted as the optimal type of failure by all models (Table 4.2).

4.5 InSAR observations

In order to investigate further any small-scale deformation caused by the Antofagasta earthquake, we examine 6 coseismic and 19 postseismic interferograms con-

Table 4.2: Calculated optimal slip directions on upper plate faults with reported coseismic rupture.

			Slip direction[a] predicted by model:						
Fault[b]	Strike	Dip	1	2	3	4	5	6	7
P	009	75 E	-65.3	-82.2	-14.1	-57.1	-34.6	47.4	26.5
U	020	75 E	6.6	11.6	3.7	9.3	18.9	23.6	33.0

[a]Rake is measured counterclockwise from strike, i.e. 0° : left-lateral, 90° : reverse, ±180° : right-lateral, -90° : normal.

[b]See Figure 4.2a for rupture locations.

structed from scenes collected along ERS track 96 (Table 4.3). We processed the data using the publicly-available Caltech/JPL ROI_PAC (*Rosen et al.*, 2004) software and a digital elevation model (DEM) from the Shuttle Radar Topography Mission, interpolated from 90 m per pixel resolution to 30 m resolution (*Pritchard et al.*, 2006b), to remove the topographic contribution to the radar-imaged displacement field. We used the "Snaphu" algorithm of *Chen and Zebker* (2001) to unwrap the interferograms and analyzed the line-of-sight (LOS) displacement field at 30-m resolution. We focus on the Paposo segment of the AFS, where field evidence for coseismically-triggered normal faulting was reported (*Delouis et al.*, 1997, 1998; *Klotz et al.*, 1999). We take profiles across the fault scarp in several locations along strike to detect abrupt variations in the LOS displacement that could mark an instance of coseismic surface rupture. The steep incidence angle of the ERS satellites (24° off nadir at the Paposo fault site) means that vertical motion dominates the displacement field, making InSAR an appropriate technique for examining dip-slip displacement on steeply-inclined faults.

Delouis et al. (1997, 1998) noted that the Paposo segment surface rupture they observed 3 weeks after the Antofagasta earthquake was not present in April

1995, implying that the rupture was generated as a response to the mainshock. Therefore, at least 5 of the 6 coseismic interferograms that we analyze should contain a signal of the surface rupture. The post-earthquake SAR scene used in the first coseismic interferogram listed in Table 4.3 was acquired about 8 hours after the mainshock. Given that the field observations can only constrain the time of formation of the surface break to be before mid-August when the field survey was carried out, this interferogram does not necessarily span the scarp formation. For all other coseismic interferograms, we expect abrupt gradients in the LOS displacement across the scarp to include effects of the reported 20 cm vertical surface offset. We expect negligible tectonic signal to be present in profiles taken across the scarp in all of the postseismic interferograms, except possibly those which are calculated using the 30 July 1995 scene, which may contain a tectonic signal depending on the actual time of surface rupture.

4.5.1 MODIS Data Analysis

As the SAR signal propagates through the troposphere, precipitable water vapor (PWV) causes delay of the signal phase (e.g., *Hanssen*, 2001). Though the Antofagasta region lies within the hyperarid Atacama Desert, PWV, primarily in the form of coastal fog, can introduce errors into interferograms. PWV is frequently correlated with topography, as fog is typically concentrated in valleys more so than on hilltops, thus examination of line-of-sight displacements across variable topography requires consideration of the radar signal delay due to tropospheric effects. In order to investigate tropospheric contamination of the InSAR signal, we examine all available PWV data from the MODerate-resolution Imaging Spectroradiometer (MODIS-Terra) for the region between 2000 and early 2007. Two characteristics

Table 4.3: InSAR data used in this study (all images from ERS track 96).

Image 1	Image 2	$B_\perp$, m[a]
Coseismic:		
16 Apr 1995	30 Jul 1995	200
16 Apr 1995	8 Oct 1995	120
8 May 1992	9 Oct 1995	50
19 Nov 1993	1 Apr 1996	240
16 Apr 1995	13 Oct 1997	20
19 Nov 1993	17 Nov 1997	90
Postseismic:		
12 Oct 1997	30 Jul 1995	60
31 Mar 1996	2 Dec 1996	60
1 Apr 1996	2 Dec 1996	60
31 Mar 1996	21 Apr 1997	90
1 Apr 1996	21 Apr 1997	100
2 Dec 1996	21 Apr 1997	40
30 Jul 1995	13 Oct 1997	240
8 Oct 1995	13 Oct 1997	80
12 Oct 1997	17 Nov 1997	460
30 Jul 1995	7 Dec 1998	230
17 Nov 1997	7 Dec 1998	310
30 Jul 1995	31 May 1999	310
8 Oct 1995	31 May 1999	10
13 Oct 1997	31 May 1999	80
30 Jul 1995	6 Mar 2000	290
1 Apr 1996	6 Mar 2000	160
13 Oct 1997	6 Mar 2000	520
17 Nov 1997	6 Mar 2000	250
7 Dec 1998	6 Mar 2000	70

[a] $B_\perp$ is the perpendicular baseline between the two images used to create each interferogram.

of these data limit their direct applicability to our InSAR analyses. First, the MODIS and SAR data collections do not coincide temporally. Ideally, the PWV content of the troposphere should be measured concurrently with acquisition of SAR data. With the exception of one SAR scene (6 March 2000), all of our interferometric data were collected before launch of the Terra satellite, which carries the MODIS sensor. Therefore, we use MODIS data to examine the daily and seasonal fluctuations in PWV and extrapolate these patterns backwards in time to explore the potential contamination of the InSAR data by PWV. All MODIS and ERS data were collected around the same time of day (between 14:00 and 16:00 UTC), which is serendipitous considering the significant variability in the density of fog throughout a given day. A second shortcoming of the MODIS data is that the spatial resolution of the measurements (1 km pixel spacing) is far lower than that of the derived interferogram (30 m spacing). This hinders our ability to directly correlate small-scale gradients in the LOS displacement field with abrupt changes in the PWV content. The resolution of the MODIS data is, however, sufficient to detect changes in PWV across scarps of the AFS, and so despite the temporal and spatial limitations, we use the MODIS data to place some constraints on the potential PWV contamination of small-scale signals in the SAR interferograms.

Because we are interested in using InSAR to detect whether or not upper plate faults experienced slip triggered by the Antofagasta earthquake, we examine profiles of PWV signal delay across of the Paposo fault scarp. We extract the PWV content along the profiles for all MODIS data collected within the 15 day window centered on the day-of-year of each SAR acquisition used in the interferometry to constrain the seasonality of the PWV content. For example, MODIS data collected between 23 July and 6 August in 2000–2006 are used to approximate the PWV

distribution at the time of acquisition of the 30 July 1995 SAR image. We elected to use a 15 day window to capture the seasonal variability in the PWV signal, and also the intra-period variability. Figure 4.4 shows the mean and standard deviation of the difference in PWV (ΔPWV) across the Paposo scarp for periods of 7, 15, and 30 days throughout the year. The sign convention of ΔPWV is such that positive values of ΔPWV indicate PWV content greater in the valley adjacent to the scarp than above the scarp itself. We calculated ΔPWV across the scarp for all MODIS acquisitions for all days within a given time period. The weekly periods were calculated for the 4^{th}, 11^{th}, 18^{th}, and 25^{th} day of each month, plus and minus 3 days. The 15 day (twice monthly) windows were calculated on the 7^{th} and 21^{st} day of each month, plus and minus 7 days, while the monthly values were extracted on the 15^{th} day of each month, plus and minus 15 days. The weekly periods show short-wavelength fluctuations in both the means and standard deviations (Figure 4.4a). The 15 day periods capture much of the inter-period variability (Figure 4.4b), but are not subject to as much noise as the weekly time windows. The monthly periods (Figure 4.4c) show only a smoothly-varying seasonal trend in ΔPWV that does not reflect some of the shorter-wavelength changes shown by the weekly and twice monthly calculations. In all cases, the standard deviations are large compared to the magnitude of ΔPWV, demonstrating the significant daily variation of moisture content.

For each interferometric pair, we calculate a histogram showing the frequency of phase delay magnitudes (Figure 4.5). These histograms indicate the likelihood that an observed offset in LOS displacement across a fault scarp can be explained solely by the phase delay resulting from propagation of the radar signal through the PWV in the troposphere. To prepare these histograms, we converted the MODIS-

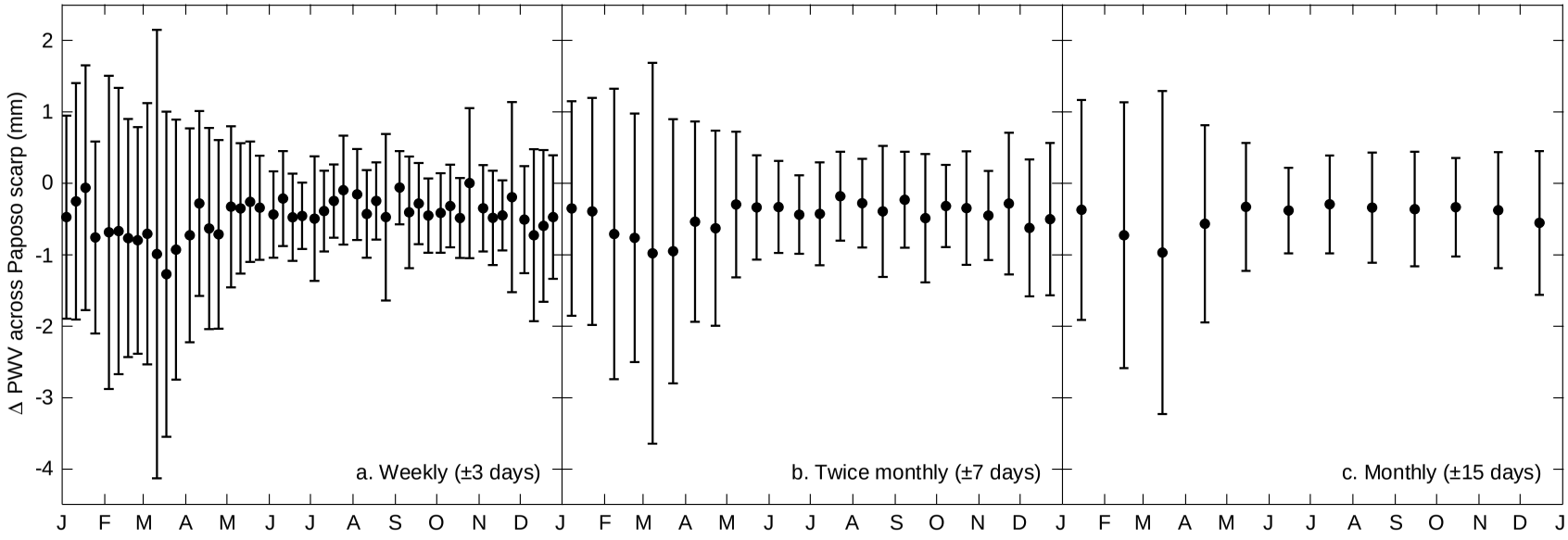

Figure 4.4: Annual variability in the PWV content across the Paposo fault. We extracted profiles across the scarp and calculated the maximum difference in the PWV content on either side of the scarp slope (ΔPWV). Note that this is not the same quantity as the LOS delay shown in Figure 4.5. Shown on all plots are the mean and standard deviation for time windows of MODIS acquisitions throughout the years 2000–2007. For the weekly calculations (a), we calculated the mean and standard deviation of all ΔPWV values collected on the 4^{th}, 11^{th}, 18^{th}, and 25^{th} days of all months, plus and minus 3 days (7 day window), in 2000–2007. The twice monthly time windows (b) were defined as the 7^{th} and 21^{st} day of each month, with a 7 day window on either side, for a total of a 15 day window. The monthly calcuations (c) were made using windows centered on the 15^{th} day of each month, plus and minus 15 days. The weekly time windows (a) show substantial inter-period variability, while the twice monthly windows (b) demonstrate much of that variability. The monthly window calculations (c) show only a smoothly-varying seasonal trend in PWV.

measured PWV to magnitude of LOS radar phase delay using the equation (e.g., *Hanssen*, 2001; *Pavez et al.*, 2006)

$$\phi_v = \frac{\Pi^{-1}\mathrm{PWV} * 4\pi}{\lambda \cos\theta_i}, \tag{4.2}$$

where ϕ_v is the phase delay induced by 1 mm of PWV in the troposphere, Π is a constant ($\sim$0.15, *Bevis et al.*, 1996), λ is the radar wavelength (56.56 mm for ERS-1 and -2 data), and θ_i is the radar incidence angle in degrees from vertical (24° for ERS-1 and -2 data at the Paposo scarp). Each ϕ_v profile within the 15 day window encompassing the first SAR image in a interferometric pair is subtracted from the ϕ_v profiles taken across the data collected within the 15 day window of the second SAR image, resulting in a differenced profile of $\Delta\phi_v$ values. The frequency distribution of the maximum range of $\Delta\phi_v$ values in each differenced profile (converted from radians to cm to facilitate comparison with the LOS measurements) is represented by the histograms (Figure 4.5), with positive range values indicating $\Delta\phi_v$ that are greater in the east than in the west of the profile.

4.6 InSAR and MODIS interpretation

Based on our analyses of the co- and postseismic InSAR data, we conclude that the reported normal fault offset at the Paposo segment of the AFS is not imageable using satellite geodesy. Figures 4.6 and 4.7 show example interferograms in the Paposo region demonstrating key conclusions of our observations. Figure 4.8 summarizes the LOS offsets observed across the Paposo segment in all InSAR data, measured from swath profiles taken at four different locations along the strike of the scarp. We use the mean LOS values within the profile swath immediately west and east of the fault scarp to define the offsets. In some cases, the offsets are not

Figure 4.5: Histograms showing the frequency distribution of delay of the InSAR phase by propagation through precipitable water vapor (PWV) in the troposphere. The first column shows the contamination by PWV of the 6 coseismic interferograms, while the remaining columns indicate the effect of PWV on the postseismic data. Histograms are constructed by taking a swath profile across the Paposo fault of PWV measured by the MODIS satellite within one week of each SAR acquisition, differencing the profiles for SAR image 1 from those for SAR image 2, then finding the maximum range of PWV within each differenced profile and converting the range to the LOS delay using Equation 4.2. The mean ("M") and standard deviation ("SD") are given in the upper right corner of each histogram. See Section 4.5.1 for details.

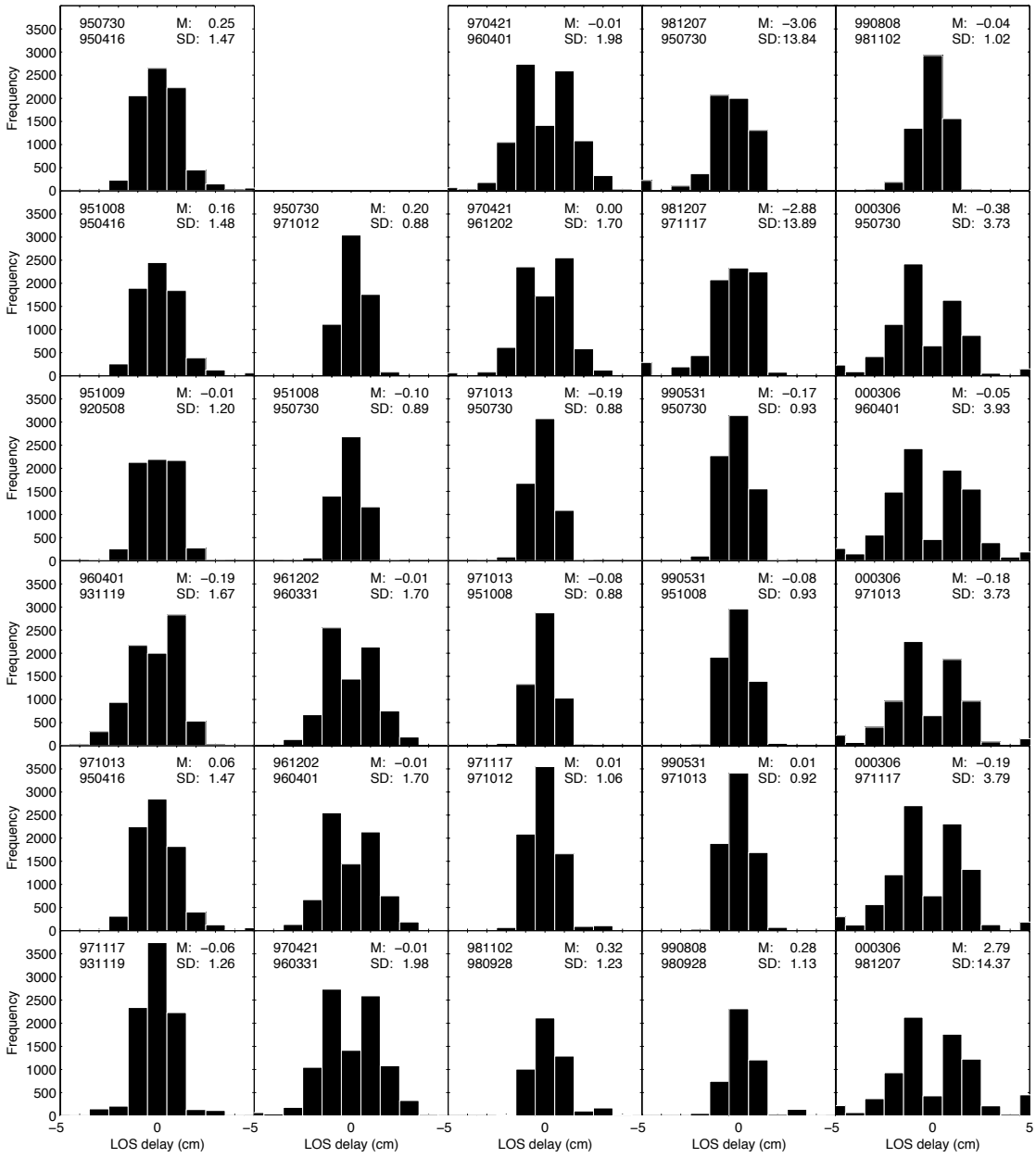
950730 M: 0.25
950416 SD: 1.47
970421 M: −0.01
960401 SD: 1.98
981207 M: −3.06
950730 SD:13.84
990808 M: −0.04
981102 SD: 1.02
951008 M: 0.16
950416 SD: 1.48
950730 M: 0.20
971012 SD: 0.88
970421 M: 0.00
961202 SD: 1.70
981207 M: −2.88
971117 SD:13.89
000306 M: −0.38
950730 SD: 3.73
951009 M: −0.01
920508 SD: 1.20
951008 M: −0.10
950730 SD: 0.89
971013 M: −0.19
950730 SD: 0.88
990531 M: −0.17
950730 SD: 0.93
000306 M: −0.05
960401 SD: 3.93
960401 M: −0.19
931119 SD: 1.67
961202 M: −0.01
960331 SD: 1.70
971013 M: −0.08
951008 SD: 0.88
990531 M: −0.08
951008 SD: 0.93
000306 M: −0.18
971013 SD: 3.73
971013 M: 0.06
950416 SD: 1.47
961202 M: −0.01
960401 SD: 1.70
971117 M: 0.01
971012 SD: 1.06
990531 M: 0.01
971013 SD: 0.92
000306 M: −0.19
971117 SD: 3.79
971117 M: −0.06
931119 SD: 1.26
970421 M: −0.01
960331 SD: 1.98
981102 M: 0.32
980928 SD: 1.23
990808 M: 0.28
980928 SD: 1.13
000306 M: 2.79
981207 SD:14.37
Frequency
0
500
1000
1500
2000
2500
3000
3500
−5
0
5
LOS delay (cm)

Figure 4.6: a) Wrapped coseismic interferogram using SAR acquisitions on 8 Oct 1995 and 16 Apr 1995. Arrows show position of abrupt phase offset at the Paposo fault scarp. b) Unwrapped interferogram. Parallel black lines show the locations of profiles. c) Profile data taken across the Paposo scarp on the unwrapped interferogram. Red, blue, and green lines represent the maximum, mean, and minimum LOS displacement values encountered along the profile lines. The abrupt LOS offset located at the fault scarp has an east-side-up appearance and is of magnitude 0.7 cm. d) Wrapped coseismic interferograms using scenes collected on 13 July 1997 and 16 April 1995. Arrows show position of the Paposo scarp, yet fringes are not offset. e) Unwrapped interferogram, confirming the lack of distinct LOS offset across the scarp. f) Profiles taken across the Paposo scarp at the same location as those in c). There is not a pronounced LOS offset across the scarp.

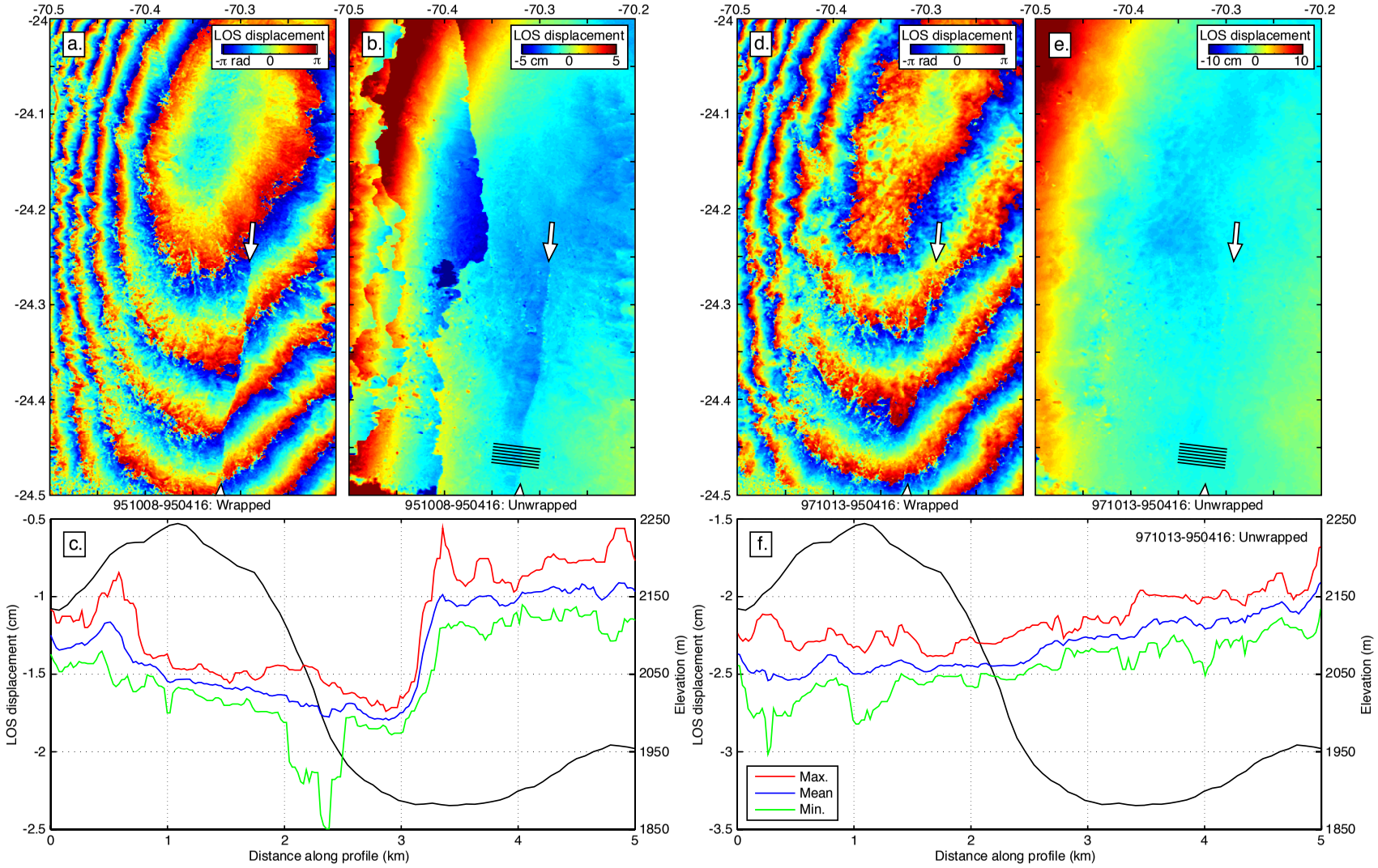
a.
b.
d.
e.
c.
f.
LOS displacement
-π rad 0 π
-5 cm 0 5
-10 cm 0 10
951008-950416: Wrapped
951008-950416: Unwrapped
971013-950416: Wrapped
971013-950416: Unwrapped
LOS displacement (cm)
Elevation (m)
Distance along profile (km)
Max.
Mean
Min.

Figure 4.7: a) Unwrapped postseismic interferogram constructed using SAR data acquired on 31 May 1999 and 8 October 1995. Black lines show the positions of scarp profiles shown in (c). (b) Unwrapped postseismic interferogram calculated using SAR data collected on 2 Dec 1996 and 1 Apr 1996. Black lines show the positions of scarp profiles in (d). (c) Profile data across the Paposo scarp, showing LOS positively correlated with topography. Even the subtle topographic high and low at the west end of the profile are mirrored by the LOS signal. (d) Postseismic profile data showing negative correlation with topography and an abrupt LOS offset similar to that seen in the coseismic profile of Figure 4.6c. The fact that some postseismic data show LOS gradients similar to those seen in the coseismic image indicates that any coseismic deformation triggered by the subduction zone earthquake is not imageable using currently-available interferograms.

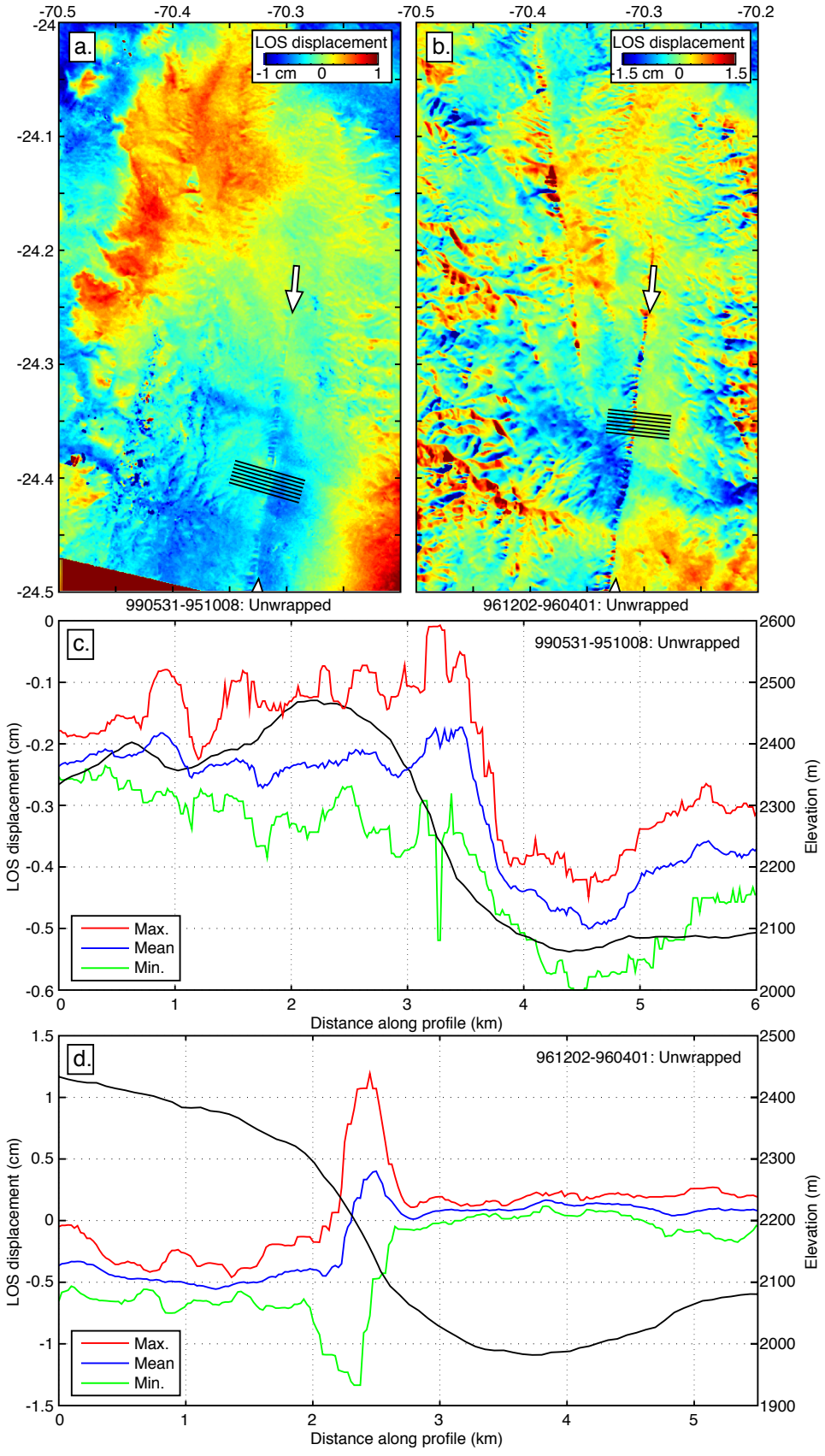
a.
LOS displacement
-1 cm 0 1
b.
LOS displacement
-1.5 cm 0 1.5
990531-951008: Unwrapped
961202-960401: Unwrapped
c.
990531-951008: Unwrapped
LOS displacement (cm)
Elevation (m)
Distance along profile (km)
Max.
Mean
Min.
d.
961202-960401: Unwrapped
LOS displacement (cm)
Elevation (m)
Distance along profile (km)
Max.
Mean
Min.

abrupt and show a gradient similar to that of the topography (e.g., Figure 4.7b).

Although some coseismic interferograms show an apparent offset across the fault (Figure 4.6a–c), several lines of evidence led us to conclude that the signal is more likely to result from errors in the interferogram than from tectonic deformation: 1) The apparent offset signal is not present in all coseismic interferograms (i.e., Figure 4.6d–f and low magnitude signals in Figure 4.8). Furthermore, some postseismic interferograms, which we expect to contain no signal of upper plate faulting, show a LOS displacement gradients across the scarp that are both positively and negatively correlated with topography (Figure 4.7b, d; 4.8). 2) The apparent offset in LOS occurs along more than 20 km of the fault scarp (Figure 4.6a, b), whereas the field reports indicate that the putative coseismic scarp was only several hundred meters long (*Delouis et al.*, 1997, 1998). The extent of the surface rupture does not necessarily reflect the region affected by upper plate faulting: buried (non-surface breaking) slip on the Paposo segment may have produced cm-scale deflections of the surface for several km along strike on either side of the surface scarp bounds. However, if this were the case, we would expect the InSAR data to show an approximately elliptical along strike distance-displacement profile (e.g., *Dawers et al.*, 1993), presumably centered about the reported 20 cm vertical offset. Profiles taken across the scarp show approximately the same magnitude of phase offset regardless of position along strike. 3) The magnitude of the LOS displacement offset is on the order of 1–3 cm (Figures 4.8), which can be explained solely by the variation in PWV content across the scarp (Figure 4.5). 4) The symmetry of the PWV histograms indicates that positive and negative correlation between PWV-influenced LOS displacement and topography are more or less equally likely to occur, which can explain both the apparent west-side-up

Figure 4.8: Date vs. offset plots for profiles P1–P4 taken at different locations perpendicular to the strike of the Paposo segment of the AFS. Offset is defined as the LOS displacement measured on the unwrapped interferograms on the east side of the scarp minus the LOS displacement on the west side. The vertical line on 30 July 1995 marks the date of the earthquake, and the SAR data acquired that day were collected after the mainshock. The largest magnitude of postseismic offset is 5–6 cm, similar to the 5.6 cm wavelength of the radar signal, indicating that this offset likely results from an unwrapping error.

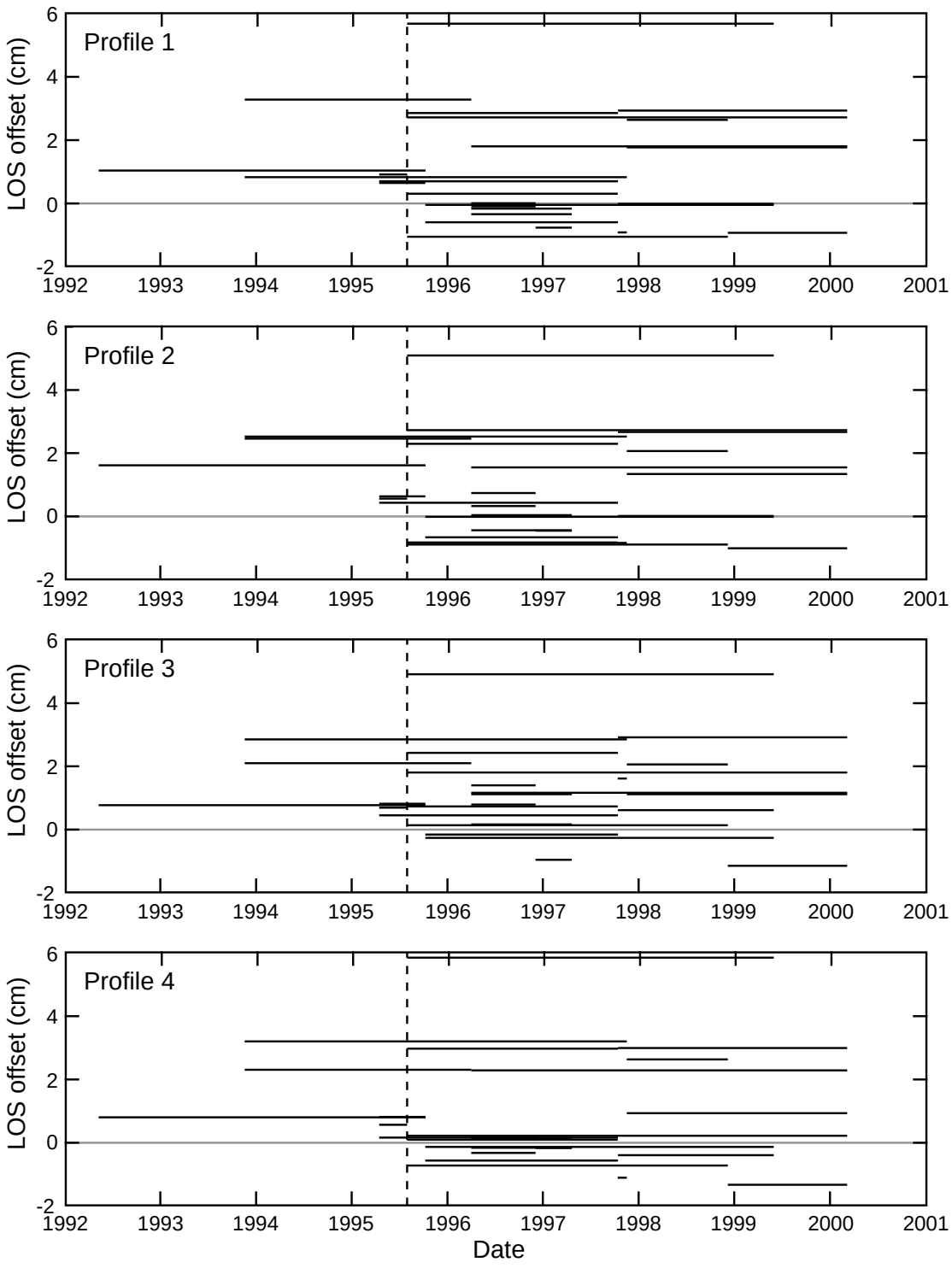
Profile 1
Profile 2
Profile 3
Profile 4
LOS offset (cm)
6
4
2
0
-2
1992
1993
1994
1995
1996
1997
1998
1999
2000
2001
Date

and east-side-up patterns of displacement across the scarp seen in the postseismic images (Figures 4.7, 4.8). Negligible displacement gradients across the scarp (e.g., Figure 4.6d–f and small magnitude offsets of Figure 4.8) indicate more spatially homogeneous tropospheric conditions at the times of both SAR scene acquisitions. Unwrapping errors (evident as the very sharp LOS gradients in the western half of Figure 4.6b), which result from phase unwrapping across noisy portions of the interferograms (compare Figures 4.6a and b) also produce abrupt offsets in the LOS profiles (most notably the highest magnitude offset seen in Figure 4.8), but even images without unwrapping errors show a similar style of offset.

Simons et al. (2002) and *Fielding et al.* (2005) used maps of interferometric correlation to map surface ruptures associated with the 1999 Hector Mine, California and 2003 Bam, Iran earthquakes. In regions of low relief, correlation can be used to determine the extent to which the reflecting properties of the surface have changed between the SAR scene acquisitions as a result of tectonic and other disturbances (e.g., *Zebker and Villasenor*, 1992; *Fielding et al.*, 2005). In the regions affected by the Hector Mine and Bam earthquakes, linear traces of decorrelated pixels in the interferograms coincide with mapped surface ruptures, thereby providing a spatially-complete view of the extent of ground deformation caused by the events (*Simons et al.*, 2002; *Fielding et al.*, 2005). In areas of high relief, the viewing geometries between the satellite and ground surface are slightly different in each SAR scene, which can contribute a baseline-dependent geometric decrease in correlation (e.g., *Zebker and Villasenor*, 1992; *Fielding et al.*, 2005). The fault scarps of the Antofagasta region are characterized by steep topographic slopes, which in most of the co- and postseismic interferograms are highlighted by linear traces of low correlation. The fact that this pattern is more obvious in interfero-

grams with longer perpendicular baselines suggests that the low correlation results from a geometric effect rather than a change in the radar scattering properties through time. More widespread decorrelation in the mountainous region south of Antofagasta, where the Paposo fault is located, likely stems from the effects of imaging steep topography combined with the associated variability in atmospheric moisture. Such decorrelation is evident even in the interferograms with baselines 40 m or less (Table 4.3). Because the reported surface rupture associated with the Antofagasta earthquake lies along the Paposo fault scarp (*Delouis et al.*, 1997, 1998), any decorrelation caused by the rupture itself may be masked by the larger field of decorrelation resulting from the steep topography.

4.7 Discussion

4.7.1 Effects of slip distribution

Differences between models in the predicted upper-plate CSC result from the data used as constraint, as well as the modeling strategy employed to find the best-fitting slip distribution. Models 1–4 show broadly distributed slip of low to moderate magnitude (maximum 3–4 m), whereas models 5–7 show a concentration of greater magnitude slip (6–7 m) near the center of their model fault (Figure 4.3). The groups of models, 1–4 and 5–7, differ in their predicted CSC fields in that the former shows a continuous zone of positive CSC from regions offshore eastward into the inner forearc, whereas the latter group is characterized by a zone of zero to negative CSC in the coastal area near where upper plate normal faults are concentrated. The slip maps differ not only in the magnitude and distribution of coseismic slip, but also in the rake. Each fault patch of models 1, 2, 4, 6, and 7 is

Figure 4.9: Perspective view demonstrating the Gaussian surface fitting described in Section 4.7.1. All plots show the spatial distribution of coseismic slip on the subduction thrust, with the x- and y-axes representing the downdip and along-strike position, respectively, of a given fault element, and the z-axis showing the slip magnitude. (a) Original slip map of model 6. (b) Best-fit Gaussian slipmap for parent model 6. (c) Gaussian slipmap that produces continuous, positive CSC throughout the coastal region. (d) Synthetic model with reduced curvature as compared to (b), yet still produces a zone of negative CSC near the coast. Parameters for (b), (c), and (d) are given in Table 4.4 (models S4–6). The color scale applies to all diagrams. See text for more details about the procedure.

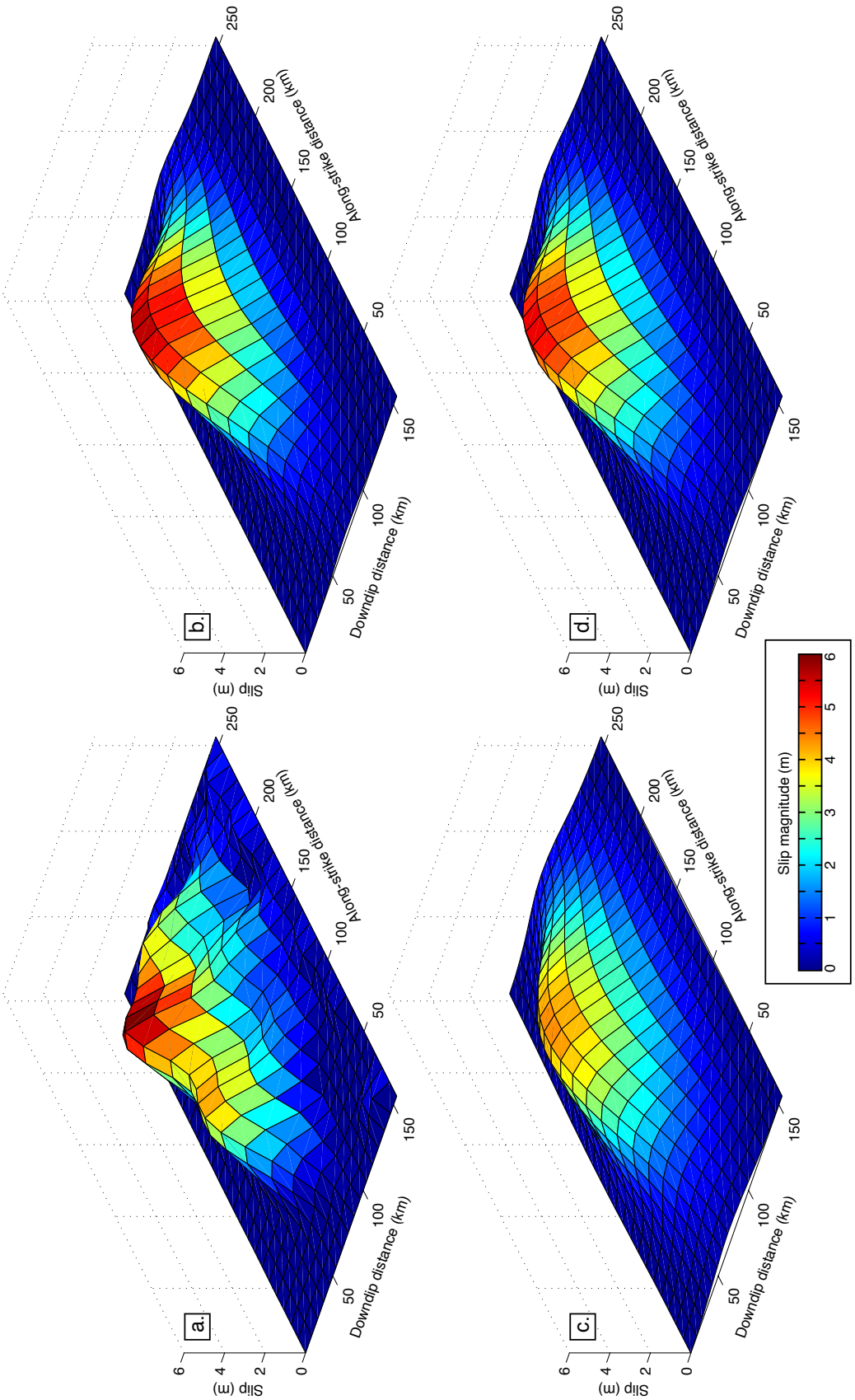
a.
b.
c.
d.
Slip (m)
Downdip distance (km)
Along-strike distance (km)
Slip magnitude (m)

characterized by slip with a unique rake, whereas models 3 and 5 use a constant rake for every fault element.

Because of the clear difference in both the spatial distribution of coseismic slip and CSC patterns between the two groups of models, we explore further the link between the concentration of slip and the resulting near-surface stress field. To do so, we create synthetic slip maps that approximate the slip distribution of one model from each of the two groups (models 2 and 6). These two models were qualitatively judged to feature the smoothest varying slip distributions, which we approximate with a Gaussian surface (Figure 4.9). By defining the synthetic slip maps with a mathematical function, we can explore which of its properties most strongly affect the stress field. We define the Gaussian slip distribution using the equation

$$u = a \exp\left(-\frac{(x-b_x)^2}{2c_x^2} - \frac{(y-b_y)^2}{2c_y^2}\right) \tag{4.3}$$

where u is the synthetic slip magnitude, x and y are the along-strike and down-dip center coordinates of fault patches, a is the maximum slip magnitude of the parent model, b_i $(i = x, y)$ are the coordinate locations of the maximum slip value (relative to the southwest corner of the slipmap), and c_i describe the curvature of the Gaussian surface. We first use a grid search to solve for the best-fitting parameters, then vary c_i in order to examine the effects of the slip gradient on the resulting map of CSC and calculate the total curvature for each slip map. For all synthetic slip maps, we use the average rake of the corresponding parent model (Table 4.1) for every fault element and hold constant the location b_i of the element with maximum slip. We adjust the magnitude of maximum slip a in order to minimize the difference between the moment of the synthetic and parent models.

The differences present between the CSC maps of Figure 4.10 result from the

varied curvature of the Gaussian surface describing the slip distribution. It is important to note that, despite the adjustments made to a, moment is not conserved in these perturbed Gaussian models (Table 4.4). The variations in curvature serve to demonstrate the difference in resulting near-surface CSC, but the slip models themselves are not meant to accurately fit the constraining data of the parent model.

The aforementioned effect of the qualitative differences in slip distribution in models 1–4 and 5–7 on the CSC maps (Figures 4.2, 4.3) is confirmed by the Gaussian surface synthetic slip maps. For each parent model, three Gaussian slipmap approximations are shown in Figure 4.10: a statistical best-fit model (Figure 4.10a, d), a model with c_i values that produce a continuous region of positive CSC from the coast towards the arc (Figure 4.10c, f), and a model whose slip distribution results in a zone of negative CSC in the coastal zone south of Antofagasta (Figure 4.10c, f). Reducing the overall curvature of the Gaussian surface fit to parent model 6 — in other words, smoothing the transition from zero to a by increasing c_i — eliminates the coastal region of negative CSC that appears in the parent model and the best-fitting Gaussian slip distribution (Figures 4.2g; 4.10e; Table 4.4). Conversely, increasing the slip gradient of the Gaussian approximation of model 2 (by decreasing c_i) introduces a zone of negative CSC similar to that seen in models 5–7 (Figure 4.10c, Table 4.4).

The original inversions of geodetic and seismic data for slip on the subduction thrust incorporate smoothing algorithms to reduce the oscillatory nature of a statistically best-fitting slip map. That is, the slip distribution that best fits the constraining data in a purely statistical sense may show a physically unreasonable pattern, where spatial variations in slip magnitude and direction are abrupt. Inver-

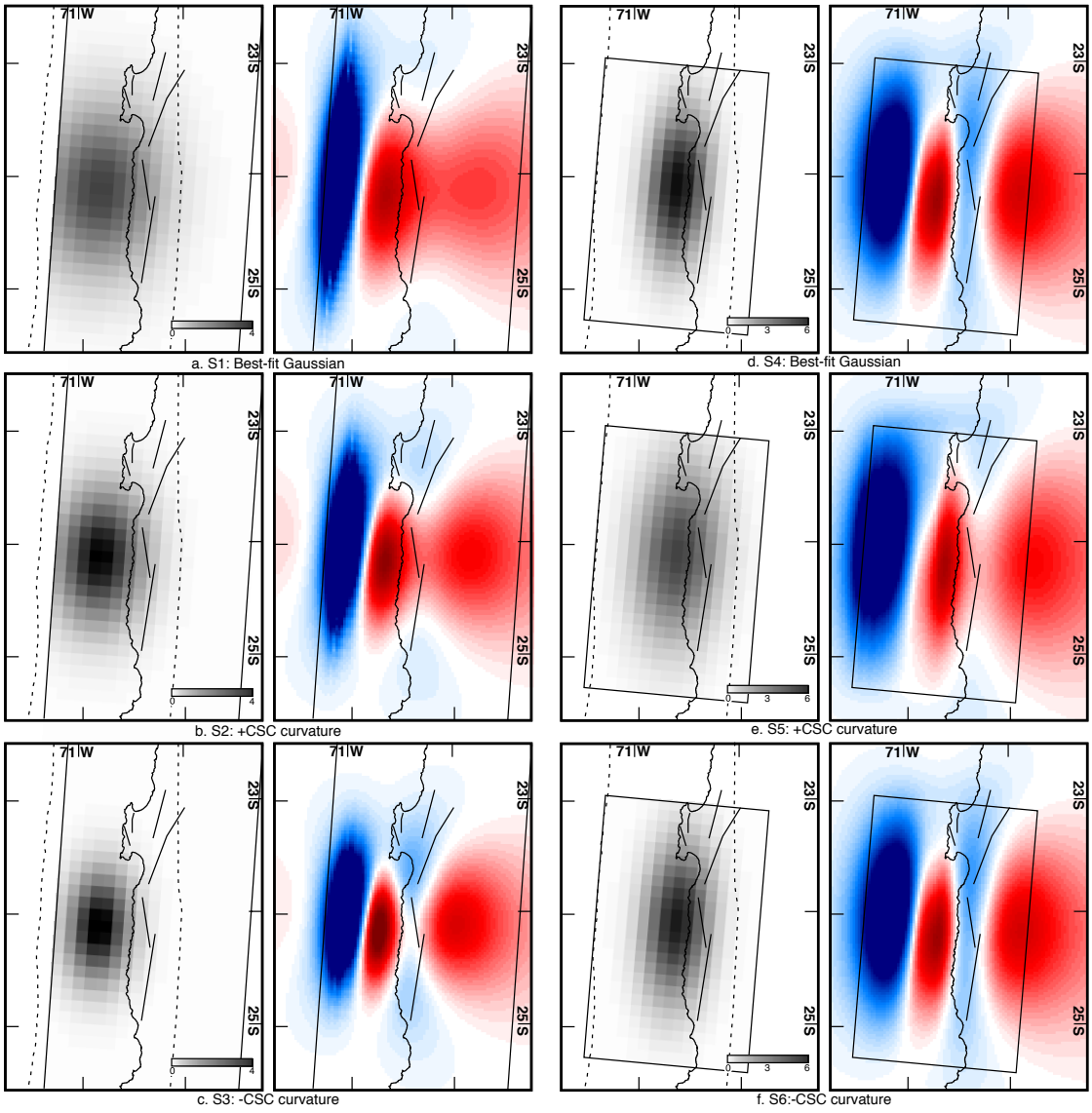

Figure 4.10: Gaussian surface approximations of slip distributions and resulting CSC maps. a–c. Gaussian distribution of slip based on parent model 2. d–f. Gaussian distribution of slip based on model 6. For each parent model, the Gaussian distribution that best fits the actual slip magnitude distribution is shown (a, d) along with adjusted Gaussian distributions that produce all positive CSC region near the coast (b, e) and a zone of negative CSC along the coast (c, f). Table 4.4 shows parameters used in the Gaussian surface fitting of slip distribution. Moment is not conserved in all models: the difference in Gaussian fitting parameters demonstrates only that the concentration of coseismic slip affects the near-surface distribution of CSC.

Table 4.4: Gaussian surface parameters for synthetic slip maps (see Equation 4.3).

Synthetic model	Parent model[a]	a[b]	b_x[c]	b_y	c_x	c_y	Synthetic curvature[d]	Parent curvature	Synthetic Moment (10^{10} m^3)[e]	Parent Moment (10^{10} m^3)	Result[f]
S1	2	3.19	59	175	39	54	0.0624	0.0943	3.77	4.74	B-P
S2	2	3.92	59	175	29	44	0.0880	0.0943	3.00	4.74	P
S3	2	4.65	59	175	21	36	0.1266	0.0943	2.19	4.74	N
S4	6	5.65	76	139	20	49	0.2039	0.4911	3.45	3.75	B-N
S5	6	4.38	76	139	28	57	0.1283	0.4911	4.27	3.75	P
S6	6	5.30	76	139	22	51	0.1809	0.4911	3.69	3.75	N

[a]Original slip map interpolated to a 10×10 km grid.

[b]Parameter a is equivalent to maximum slip of parent model in meters.

[c]Values of b_i are presented in km relative to the SW corner of the parent model fault.

[d]Curvature is calculated by summing the absolute value of the discrete Laplacian of slip calculated at each fault element.

[e]Geometric moment, as in Table 4.1.

[f]B = Model which best fits the parent model. P = Continuous zone of positive Coulomb stress change. N = Coastal zone of negative Coulomb stress change.

sion strategies seek to minimize both the error between data and model prediction as well as the roughness of the solution (*Menke*, 1984). The fact that the smoothness or curvature of the solution affects the distribution of CSC demonstrates that care must be taken in choosing a smoothing operator for the initial data inversion. The geometric moment (defined as $\Sigma A_n u_n$, where A_n is the area of fault patch n and u_n is the slip magnitude on the patch and the sum is taken over all patches) of both parent models used for the Gaussian fitting study are very similar (3.79×10^{10} m^3 for model 2 and 3.64×10^{10} m^3 for model 7, see Table 4.1), but the maximum slip magnitude and curvature of the slip are very different, indicating that it is the distribution of coseismic displacement on the subduction thrust that governs the stress change patterns imposed in the forearc.

Sobiesiak (2004) used the distribution of aftershocks from the 1995 earthquake to compute a b-value map for the event. Correlation between peak b-values and isostatic residuals led *Sobiesiak* (2004) to propose that Jurassic batholiths in the Antofagasta region, exert anomalously high normal stress on the subduction interface, resulting in asperities on the fault plane. While the correlation between the regions of highest b-values, where mainshock moment release was greatest, do not coincide exactly with the maximum slip of model 7 (Figure 4.11), the b-value mapping shows distinct concentrations of high values, similar to the slip distributions of models 5–7 and the Gaussian surface models that employ steep slip gradients. This provides further suggestion that the concentrated high-magnitude slip distributions of models 5–7 more accurately portray the rupture pattern of the 1995 earthquake.

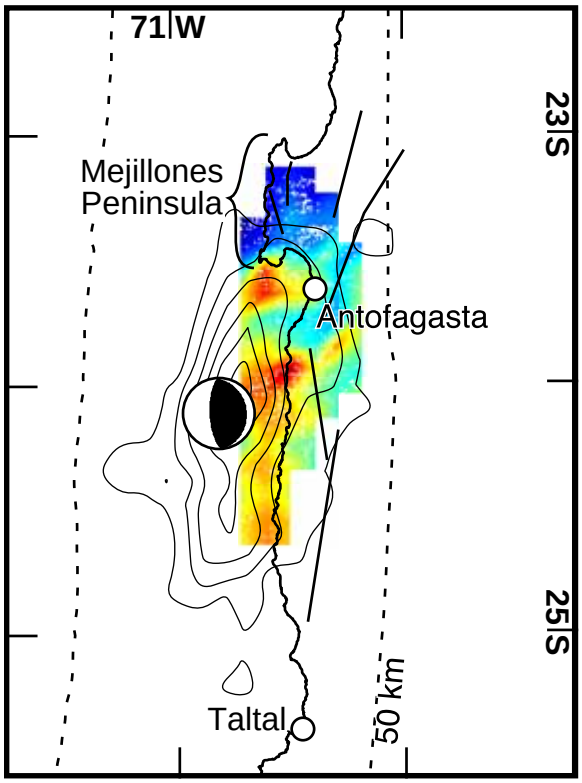

Figure 4.11: 1 m contours of coseismic slip from model 7 (*Pritchard et al.*, 2006a) overlain on a color plot of the spatial distribution of b-value from *Sobiesiak* (2004).

4.7.2 Role of dynamic Coulomb stress changes

Dynamic Coulomb stress changes (DCSC) describe the change in Coulomb stress as a function of time. As noted by *Kilb et al.* (2002), DCSC depend on both the spatial and temporal evolution of the earthquake rupture and thus show different patterns as compared to static CSC. We calculate DCSC using the method of *Cotton and Coutant* (1997), the coseismic slip map based on the joint inversion of *Pritchard et al.* (2006a) (model 7), and the layered elastic 1-D velocity model of *Husen et al.* (1999). We calculate the stress tensor at 1 second intervals for 200 seconds, then rotate the stress tensor components to determine DCSC. We use the same depth, friction, and receiver fault parameters as those presented in Section

4.3 for the DCSC calculations. Figure 4.12a shows the peak DCSC, calculated by taking the mean of the ten greatest-magnitude values of DCSC through the time series. This approach was taken to smooth the plot of DCSC; the unsmoothed version using the true maximum DCSC shows a similar albeit rougher distribution of peak DCSC with magnitude up to 27 bars (compared to the maximum of 14 bars for the averaged version). Figure 4.12b shows the approximate static CSC, calculated by taking the mean DCSC value over seconds 120-200 of the DCSC record. The distribution of static CSC calculated in this way is reasonably similar to that shown in Figure 4.2h.

Because the dynamic Coulomb stress change is a transient forcing carried by the passing seismic waves, it does not affect the final state of stress on a particular fault. Rather, dynamically triggered slip results from a change in the physical properties of the fault and/or its surroundings (*Kilb et al.*, 2002). The locality where coseismic surface cracks formed nearly parallel to the Salar del Carmen segment of the AFS (*González et al.*, 2003) is anomalous in that vegetation is relatively dense and the water table is nearer the surface than it is throughout much of the Antofagasta region (D. Carrizo, pers. comm., 2004). Therefore, dynamic stress waves through this region may have exploited the unique physical properties of the soil and/or caused fluctuations in pore fluid pressure to cause open cracking. The strike of cracks parallel to the local orientation of the AFS suggests that the fault influenced crack formation by defining a preexisting weak zone and/or guiding stress waves along a trajectory appropriate for opening surface cracks, though this effect is not considered in our dynamic stress model.

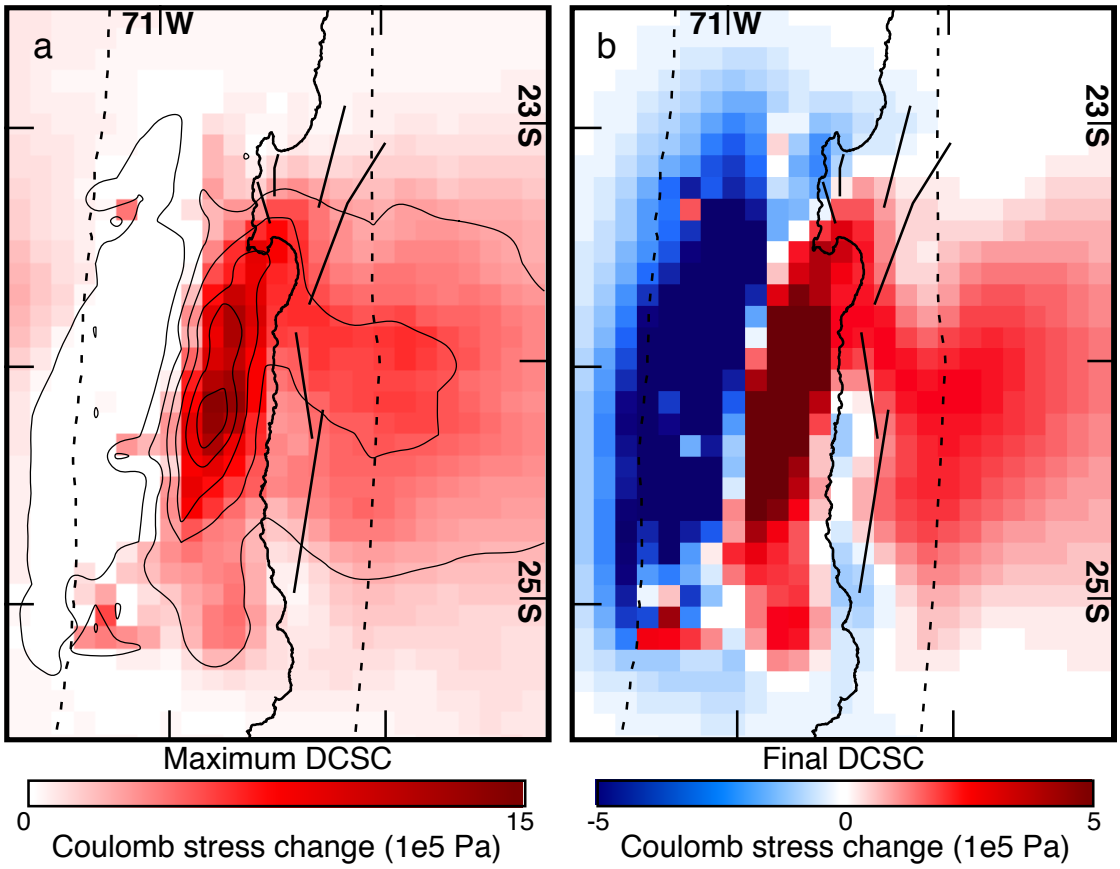

Figure 4.12: Dynamic Coulomb stress change (DCSC) calculations. a. Maximum DCSC calculated at 1 km depth using the method of *Cotton and Coutant* (1997). b. Final DCSC calculated using the mean DCSC from seconds 120-200 of the synthetic stress-gram.

4.7.3 End-member interpretations of InSAR observations

The lines of evidence presented in Section 4.6 indicate that the offsets seen in the LOS profiles of the co- and postseismic InSAR data result from atmospheric contamination of the radar signal, not tectonic surface deformation. The symmetry of the PWV range histograms (Figure 4.5, Section 4.6) shows that the phase delay caused by tropospheric PWV is equally likely to produce an east-side-up offset of the SAR signal across topography as a west-side-up signal. Therefore, it is possible

that the inconsistency we observe in the sense and magnitude of any LOS offset in the interferograms could result from a convolution of true surface offset and the effects of PWV. In other words, all apparent offsets seen in the coseismic InSAR data may represent the combined effects of surface faulting and PWV delay, and the lack of LOS offset in some coseismic interferograms, such as that shown in Figure 4.6d-f, may result from a tectonic signal being "erased" by the appropriate opposite PWV delay pattern.

The maximum LOS offset across the Paposo fault that we observe in any coseismic interferogram is ∼3 cm (Figure 4.8), while *Delouis et al.* (1997, 1998) report 20 cm of vertical displacement. The disparate measurements are not necessarily contradictory: the field observations were presumably made at the location of the scarp, while InSAR measures offsets over a length scale of one or more pixels (i.e., 30 m). Assuming that the surface displacement field associated with the scarp decays from 20 cm to 3 cm over a distance of 1–3 pixels (30–90 m), we can place constraint on the depth to which the fault experienced triggered slip. To do so, we use a simple 2-dimensional elastic dislocation model to calculate the vertical displacement field resulting from 20 cm of slip on a surface-breaking fault dipping 70°E. Vertical offset is ∼20 cm at the fault and decays smoothly with distance from the fault (Figure 4.13). We hold the fault dip and applied slip constant and vary the downdip extent of faulting. We calculate the maximum vertical offset at distances 30, 60, and 90 m from the fault, corresponding to the difference in LOS at spacing 1, 2, and 3 pixels apart. In order to agree with both the end-member interpretation of the InSAR observations and the field reports, the line-of-sight displacement must be 3 cm at a distance of a few pixels away from the fault. We find that the required downdip extent of faulting is just 25–50 m, which results in

offset of 7–12, 2–7, and 0.7–3.7 cm at distances 30, 60, and 90 m from the fault (Figure 4.13). If taken at face value, this end-member interpretation of the InSAR data suggests that recent surface ruptures on forearc faults reflect deformation restricted to very shallow levels. However, as discussed in Section 4.6, we instead interpret the lack of consistent sign and magnitude of offset signal across the fault in the co- and postseismic interferograms as indication that no surface rupture can be imaged using the currently-available data.

4.7.4 Implications for normal fault evolution

The lack of consistency between the static CSC predicted by the best-constrained models (5–7), the InSAR observations, and the reported examples of coseismic fault slip indicates that the static stress changes associated with the 1995 Antofagasta earthquake can not explain the putative surface faulting attributed to the event. Peak DCSC is everywhere positive and is thus a plausible mechanism for triggering normal slip. There appears no clear relationship between the distribution of DCSC and the localities of reported coseismic faulting, implying that the preexisting state of stress on the fault segments that experienced triggered slip was such that the DCSC was sufficient to cause rupture.

The majority of young normal fault scarps in the coastal region of northern Chile lie within the negligible to negative CSC predicted by the models of slip distribution that are constructed by inversion of multiple constraints from seismic and/or geodetic data (models 5–7 and the negative CSC Gaussian variants). Furthermore, models that predict positive CSC (models 1–4, positive CSC Gaussian variants, and peak DCSC) for the coastal region south of Antofagasta show a "saddle" pattern of Coulomb stress increase: areas just offshore and in the eastern

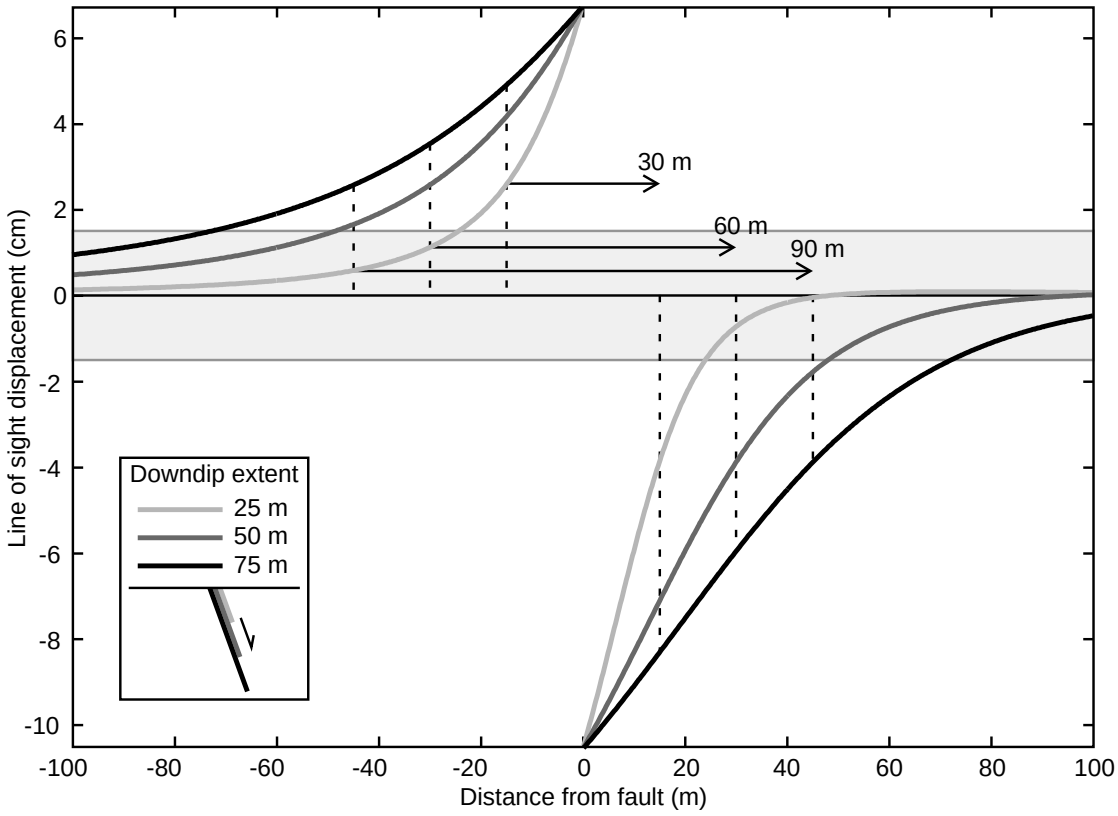

Figure 4.13: Simple two-dimensional dislocation model of the displacement field surrounding the Paposo segment of the Atacama Fault System. In order for the displacement field to agree with both the field reports and the end-member interpretation of the InSAR data (Section 4.7.3), vertical offset must be ∼20 cm at the fault and just 3 cm at a distance of a few pixels away from the fault. 20 cm of slip is applied uniformly to a surface-breaking fault dipping 70°E with a downdip extent of 25, 50, or 75 m. Light gray box defines a 3 cm offset, centered about zero displacement.

part of the Coastal Cordillera lie within zones of CSC of greater magnitude than the changes predicted for the coastal region where faults are mapped. Numerous north-south striking normal faults have been imaged offshore and are thought to result from gravitational instability caused by tectonic erosion at the subduction trench (*von Huene and Ranero*, 2003; *Sallàres and Ranero*, 2005). However, models resolving the coseismic CSC onto planes dipping 30°W, consistent with the low-angle nature of these faults as seen in seismic reflection data (*von Huene and Ranero*, 2003; *Sallàres and Ranero*, 2005), also show a maximum increase in Coulomb stress in offshore regions at ∼23.75–24.5° S latitude, suggesting that coseismic stress may be superimposed on the long term gravitational stress field to induce movement on these structures.

The fact that the majority of onshore normal faults around Antofagasta lie within regions of near zero to negative CSC (models 5–7), or in the low magnitude part of the "saddle" of Coulomb stress increases (models 1–4) argues against coseismic static stress change being the sole cause of extensional failure. *Delouis et al.* (1998) present a model in which Coulomb stress on normal faults is reduced by interseismic contraction and increased by subduction earthquakes, and when a Coulomb failure stress is reached following several subduction earthquake cycles, rupture will occur. Models of interseismic deformation (Chapter 5) indicate that Coulomb stress is increased due to flexural stresses, while the coseismic models presented here indicate that stress may then be increased or decreased during a subduction earthquake depending on the distribution of coseismic slip (Section 5.7.3, Figure 5.11). Thus, normal fault slip may occur during the interseismic period of the subduction earthquake cycle or exclusively when triggered by coseismic increases in Coulomb stress.

Reverse slip may be encouraged on faults lying within a zone of negative CSC. Minor reverse slip has occurred on the Salar del Carmen and Paposo segments (Sections 5.4.1, 5.4.2), and the CSC models presented here provide a mechanism for this style of deformation. For a fault to reverse its long-term sense of motion in response to the low-magnitude stress change induced by a subduction zone earthquake, the level of existing stress on the fault must be minute. This may indicate that the slipping zone is weak, characterized by a low coefficient of friction, high fluid pressure, and/or reduced rigidity of the fault zone (*Fialko et al.*, 2002; *Fialko*, 2004; *Fialko et al.*, 2005). Distributed failure within complaint fault zones 1–2 km wide with a modulus of rigidity about half that of the surrounding crust is found to be the mechanism most consistent with small-scale deformation triggered by the 1992 Landers (*Fialko*, 2004) and 1999 Hector Mine (*Fialko et al.*, 2002) strike-slip earthquakes in southern California. The width of the compliant zone is inferred from the lateral extent of detectable LOS displacement in InSAR data. If the offset signals we observe in the InSAR data spanning the Antofagasta earthquake indeed represent tectonic deformation (Section 4.7.3), the width of the deforming zone around the Paposo fault is on the order of 100-200 m — an order of magnitude smaller than that suggested for the southern California faults (*Fialko et al.*, 2002; *Fialko*, 2004). Therefore, the slip on the AFS and other forearc faults that results in surface rupture seems restricted to a narrow and shallow zone immediately surrounding the fault.

The apparent restriction of surface-rupturing motion on the AFS and other forearc faults to shallow depths leaves open the question of the seismogenic capacity of these structures. Models of co- and interseismic CSC calculated at a depth of 10 km — a depth more typical of seismogenesis in well-developed fault zones

(e.g., *Scholz*, 2002) — show more homogeneous stress fields, lacking the short-wavelength anomalies of the near-surface models (Figures 4.2, 5.9). Specifically, at this depth, interseismic convergence induces negative CSC on normal faults, while the elastic rebound of the deep crust during subduction zone earthquakes increases the Coulomb stress on the forearc faults. Stress changes at 10 km depth are also less sensitive to the slip distribution on the plate interface than those at 1 km depth. As a result, the stress exerted by an earthquake on upper plate faults at 10 km depth may completely cancel the stress applied by the preceding interseismic period. Regions nearer the surface, which are more sensitive to the details of the earthquake rupture, may experience co- and interseismic CSC that do not cancel each other. This allows stress to accumulate from one seismic cycle to the next, eventually resulting in an episode of deformation that could either be triggered by a subduction zone earthquake or occur during the interseismic period.

BIBLIOGRAPHY

Arabasz, W. J. (1971), Geological and geophysical studies of the Atacama fault zone, in northern Chile, PhD. thesis, California Institute of Technology, Pasadena, CA.

Armijo, R., and R. Thiele (1990), Active faulting in northern Chile: Ramp stacking and lateral decoupling along a subduction plate boundary?, *Earth and Planetary Science Letters*, *98*(1), 40–61.

Bevis, M., S. Chiswell, S. Businger, T. Herring, and Y. Bock (1996), Estimating wet delay using numerical weather analysis and predictions, *Radio Sciences*, *31*(3), 447–487.

Cahill, T. A., and B. L. Isacks (1992), Seismicity and shape of the subducted Nazca Plate, *Journal of Geophysical Research*, *97*(B12), 17,503–17,529.

Campos, J., L. Ponce, S. Barrientos, A. Lavenue, J. Naranjo, J.-P. Caminade, B. Delouis, T. Monfret, M. Pardo, L. Rivera, J. Thomas, J.-C. Ruegg, J.-C. Roissignol, and E. Kausel (1995), *Estudio del Terremoto de Antofagasta del 30 de Julio de 1995*, vol. 3733, 42 pp., Universidad de Chile, Departamento de Geofísica, report prepared for the Ministry of Public Works (in Spanish).

Chen, C. W., and H. A. Zebker (2001), Two-dimensional phase unwrapping with use of statistical models for cost functions in nonlinear optimization, *Journal of the Optical Society of America A.*, *18*(2), 338–351.

Chlieh, M., J. B. de Chabalier, R. J. C., R. Armijo, R. Dmowska, J. Campos, and K. Feigl (2004), Crustal deformation and fault slip during the seismic cycle in the North Chile subduction zone, from GPS and InSAR observations, *Geophysical Journal International*, *158*(2), 695–711, doi: 10.1111-j.1365-246X.2004.02326.x.

Comte, D., M. Pardo, L. Dorbath, C. Dorbath, H. Haessler, L. Rivera, A. Cisternas, and L. Ponce (1994), Determination of seismogenic interplate contact zone and crustal seismicity around Antofagasta, northern Chile using local data, *Geophysical Journal International*, *116*(3), 553–561, doi:10.1111/j.1365-246X.1994.tb03279.x.

Cotton, F., and O. Coutant (1997), Dynamic stress variations due to shear faults in a plane-layered medium, *Geophysical Journal International*, *128*, 676–688, doi: 10.1111/j.1365-246X.1997.tb05328.x.

Dawers, N. H., M. H. Anders, and C. H. Scholz (1993), Growth of normal faults: Displacement-length scaling, *Geology*, *21*(12), 1107–1110, doi: 10.1130/0091-7613(1993)021<1107:GONFDL>2.3.CO;2.

Delouis, B., A. Cisternas, L. Dorbath, L. Rivera, and E. Kausel (1996), The Andean subduction zone between 22 and 25°S (northern Chile): Precise geometry and state of stress, *Tectonophysics*, *259*, 81–100.

Delouis, B., T. Monfret, L. Dorbath, M. Pardo, L. Rivera, D. Comte, H. Haessler, J. P. Caminade, L. Ponce, E. Kausel, and A. Cisternas (1997), The M_W = 8.0 Antofagasta (Northern Chile) earthquake of 30 July 1995: A precursor to the end of the large 1877 gap, *Bulletin of the Seismological Society of America*, *87*(2), 427–445.

Delouis, B., H. Philip, L. Dorbath, and A. Cisternas (1998), Recent crustal deformation in the Antofagasta region (northern Chile) and the subduction process, *Geophysical Journal International*, *132*, 302–338, doi: 10.1046/j.1365-246x.1998.00439.x.

Fialko, Y. (2004), Probing the mechanical properties of seismically active crust with space geodesy: Study of the coseismic deformation due to the 1992 M_w 7.3 Landers (Southern California) earthquake, *Journal of Geophysical Research*, *109*, B03307, doi:10.1029/2003JB002756.

Fialko, Y., D. Sandwell, D. Agnew, M. Simons, P. Shearer, and B. Minster (2002), Deformation on nearby faults induced by the 1999 Hector Mine earthquake, *Science*, *297*(5588), 1858–1862, doi: 10.1126/science.1074671.

Fialko, Y., D. Sandwell, M. Simons, and P. A. Rosen (2005), Three-dimensional deformation caused by the Bam, Iran, earthquake and the origin of shallow slip deficit, *Nature*, *435*(7040), 295–299, doi:10.1038/nature03425.

Fielding, E. J., M. Talebian, P. A. Rosen, H. Nazari, J. A. Jackson, M. Ghorashi, and R. Walker (2005), Surface rupture and building damage of the 2003 Bam, Iran earthquake mapped by satellite synthetic aperture radar interferometric correlation, *Journal of Geophysical Research*, *110*, B03302, doi: 10.1029/2004JB003299.

González, G., and D. Carrizo (2003), Segmentación, cinemática y chronología relativa de la deformación tardía de la Falla Salar del Carmen, Sistema de Fallas Atacama, (23°40′S), norte de Chile, *Revista Geológica de Chile*, *30*(2), 223–244.

González, G., J. Cembrano, D. Carrizo, A. Macci, and H. Schneider (2003), The link between forearc tectonics and Pliocene-Quaternary deformation of the Coastal Cordillera, northern Chile, *Journal of South American Earth Sciences*, *16*, 321–342, doi: 10.1016/S0895-9811(03)00100-7.

González, G., T. Dunai, D. Carrizo, and R. Allmendinger (2006), Young displacements on the Atacama Fault System, northern Chile from field observations and cosmogenic ^{21}Ne concentrations, *Tectonics*, *25*, TC3006, doi: 10.1029/2005TC001846.

Hanssen, R. F. (2001), *Radar interferometry: Data interpretation and error analysis*, Kluwer Academic, Boston.

Husen, S., E. Kissling, E. Flueh, and G. Asch (1999), Accurate hypocentre determination in the seismogenic zone of the subducting Nazca Plate in northern Chile using a combined on-/offshore network, *Geophysical Journal International*, *138*(3), 687–701, doi: 10.1046/j.1365-246x.1999.00893.x.

Ihmlé, P. F., and J. Ruegg (1997), Source tomography by simulated annealing using broad-band surface waves and geodetic data: Application to the $M_w = 8.1$ Chile 1995 event, *Geophysical Journal International*, *131*, 146–158.

Kilb, D., J. Gomberg, and P. Bodin (2002), Aftershock triggering by complete Coulomb stress changes, *Journal Of Geophysical Research*, *107*(B4), 2060, doi: 10.1029/2001JB000202.

King, G. C., R. S. Stein, and J. Lin (1994), Static stress changes and the triggering of earthquakes, *Bulletin of the Seismological Society of America*, *84*(3), 935–953.

Klotz, J., D. Angermann, G. W. Michel, R. Porth, C. Reigber, J. Reinking, J. Viramonte, R. Perdomo, V. H. Rios, S. Barrientos, R. Barriga, and O. Cifuentes (1999), GPS-derived deformation of the Central Andes including the 1995 Antofagasta $M_w = 8.0$ earthquake, *Pure and Applied Geophysics*, *154*, 709–730, doi: 10.1007/s000240050249.

Lin, J., and R. S. Stein (2004), Stress triggering in thrust and subduction earthquakes and stress interaction between the southern San Andreas and nearby thrust and strike-slip faults, *Journal of Geophysical Research*, *109*(B2), B02303, doi: 10.1029/2003JB002607.

Menke, W. (1984), *Geophysical Data Analysis: Discrete Inverse Theory*, 285 pp., Academic Press, New York.

Niemeyer, H., G. González, and E. Martinez-de los Ríos (1996), Evolución tectónica cenozoica del margen continental activo de Antofagasta, norte de Chile, *Revista Geológica de Chile*, *23*(2), 165–186.

Ortlieb, L., S. Barrientos, and N. Guzman (1996), Coseismic coastal uplift and coralline algae record in northern Chile: the 1995 Antofagasta earthquake case, *Quaternary Science Reviews*, *15*(8-9), 949–960.

Pavez, A., D. Remy, S. Bonvalot, M. Diament, G. Gabalda, J. L. Froger, P. Julien, D. Legrand, and D. Moisset (2006), Insight into ground deformations at Lascar volcano (Chile) from SAR interferometry, photogrammetry and GPS data: Implications on volcano dynamics and future space monitoring, *Remote Sensing of Environment*, *100*(3), 307–320, doi:10.1016/j.rse.2005.10.013.

Pritchard, M. E., M. Simons, P. A. Rosen, S. Hensley, and F. H. Webb (2002), Coseismic slip from the 1995 July 30 $M_w = 8.1$ Antofagasta, Chile earthquake as constrained by InSAR and GPS observations, *Geophysical Journal International*, *150*, 362–376, doi: 10.1046/j.1365-246X.2002.01661.x.

Pritchard, M. E., C. Ji, and M. Simons (2006a), Distribution of slip from 11 $M_w > 6$ earthquakes in the northern Chile subduction zone, *Journal of Geophysical Research*, *111*, B10302, doi: 10.1029/2005JB004013.

Pritchard, M. E., L. M. Tumia, and E. M. Trautmann (2006b), InSAR monitoring of volcanoes at the highest resolution: Creation and analysis of 30 meter/pixel topographic maps with interferograms from Andean volcanoes, *EOS Transactions, AGU*, *87*(52), Fall Meeting Supplement, Abstract G43C-03.

Rosen, P. A., S. Hensley, G. Peltzer, and M. Simons (2004), Updated Repeat Orbit Interferometry Package released, *EOS Transactions, AGU*, *85*(5), 47.

Ruegg, J., J. Campos, R. Armijo, S. Barrientos, P. Briole, R. Thiele, M. Arancibia, J. Cañuta, T. Duquesnoy, M. Chang, D. Lazo, H. Lyon-Caen, L. Ortlieb, J. Rossignol, and L. Serruier (1996), The $M_w = 8.1$ Antofagasta (North Chile) Earthquake of July 30, 1995: First results from teleseismic and geodetic data, *Geophysical Research Letters*, *23*(9), 917–920.

Sallàres, V., and C. R. Ranero (2005), Structure and tectonics of the erosional convergent margin off Antofagasta, north Chile (23°30′S), *Journal of Geophysical Research*, *110*, B06101, doi:10.1029/2004JB003418.

Scholz, C. H. (2002), *The Mechanics of Earthquakes and Faulting*, 2 ed., 471 pp., Cambridge University Press, Cambridge.

Simons, M., Y. Fialko, and L. Rivera (2002), Coseismic deformation from the 1999 m_w 7.1 Hector Mine, California, earthquake as inferred from InSAR and GPS observations, *Bulletin of the Seismological Society of America*, *92*(4), 1390–1402, doi: 10.1785/0120000933.

Sobiesiak, M. M. (2004), Fault Plane Structure of the 1995 Antofagasta Earthquake (Chile) Derived From Local Seismological Parameters, PhD. thesis, Universität Potsdam, Potsdam, Germany.

Thomas, A. L. (1993), Poly3D: A three-dimensional, polygonal element, displacement discontinuity boundary element computer program with applications to fractures, faults, and cavities in the Earth's crust, M.S. thesis, Stanford University, Stanford, CA.

Toda, S., and R. S. Stein (2002), Response of the San Andreas fault to the 1983 Coalinga-Nunez earthquakes: An application of interaction-based probabilities for Parkfield, *Journal of Geophysical Research*, *107*, 2126, doi:10.1029/2001JB000172.

Toda, S., R. S. Stein, P. A. Reasenberg, J. H. Dieterich, and A. Yoshida (1998), Stress transferred by the 1995 $M_w = 6.9$ Kobe, Japan shock: Effect on aftershocks and future earthquake probabilities, *Journal of Geophysical Research*, *103*(B10), 24,543–24,565.

von Huene, R., and C. R. Ranero (2003), Subduction erosion and basal friction along the sediment-starved convergent margin off Antofagasta, Chile, *Journal of Geophysical Research*, *108*(B2), 2079, doi:10.1029/2001JB001569.

Xia, Y., G. Michel, C. Reigber, J. Klotz, and H. Kaufmann (2003), Seismic unloading and loading in northern central Chile as observed by differential Synthetic Aperture Radar Interferometry (D-INSAR) and GPS, *International Journal of Remote Sensing*, *24*(22), 4375–4391.

Zebker, H. A., and J. Villasenor (1992), Decorrelation in interferometric radar echoes, *IEEE Transactions on Geoscience and Remote Sensing*, *33*(5), 950–959, doi: 10.1109/36.175330.

CHAPTER 5

RELATIONSHIPS BETWEEN UPPER-PLATE STRUCTURES AND THE SUBDUCTION ZONE EARTHQUAKE CYCLE IN THE NORTHERN CHILEAN FOREARC

5.1 Abstract

Despite its location in a convergent tectonic setting, the Coastal Cordillera of the northern Chilean forearc between 18° and 25°S is dominated by structures demonstrating extension in the direction of plate convergence. In some locations, however, normal faults have been reactivated as reverse faults, complicating the long-term strain patterns. Here we combine new structural observations and models of Coulomb stress changes associated with the Andean subduction zone earthquake cycle in order to investigate the influence of plate boundary processes on upper plate deformation. Models of strain accumulation on the subduction interface predict positive Coulomb stress changes on mapped upper plate normal faults during the interseismic period. These increases in stress bring structures closer to the point of failure, which may occur as a result of triggering by elastic rebound due to interplate earthquakes, or as seismic or aseismic motion that takes place within the interseismic period of the subduction earthquake cycle. Seismic hazard analysis for northern Chile requires consideration not only of the major plate boundary earthquake cycle, but also an intraplate cycle that may or may not coincide with the interplate seismic pattern. A latitudinally-varying maximum depth of interplate coupling along the northern Chilean plate boundary, based on previous seismic and geodetic studies, predicts a distribution of interseismic Coulomb stress change that is consistent with the distribution of normal faults. North of the

Mejillones Peninsula (∼23°S latitude), the Andean margin is modeled as locked (zero slip condition) between 20 and 50 km depth, while locking south of the peninsula is restricted to between 20 and 38 km depth. Strong subduction earthquakes, such as the 1995 M_w=8.1 Antofagasta event, produce coseismic stress fields that, while complex, provide a mechanism for the small amounts of reverse motion we observe on some faults. Though the relationships between permanent strain and deformation calculated using elastic models remain unclear, the compatibility of stress fields predicted by these models with the distribution of faulting in the forearc indicates that interseismic strain accumulation and coseismic deformation both play significant roles in determining faulting patterns within the forearc.

5.2 Introduction

The Central Andes have long been considered the type example of a non-collisional orogen (*Allmendinger et al.*, 1997). The crustal shortening and thickening that results from coupling between the subducting Nazca and overriding South American plates is well documented by both geologic and geodetic measurements. The Altiplano-Puna plateau, the second largest continental plateau on Earth, and foreland fold-and-thrust belts provide evidence of long-term thickening and shortening of the crust (e.g., *Isacks*, 1988; *Allmendinger et al.*, 1997), while GPS surveys of the central Andes capture the modern strain field, which also demonstrates shortening on the scale of the orogen during interseismic periods (Figure 5.1; *Norabuena et al.*, 1998; *Bevis et al.*, 2001; *Klotz et al.*, 2001; *Brooks et al.*, 2003).

Deformation in the Andean forearc of northern Chile, however, is marked by structures indicating extension in the direction of plate convergence. Numerous normal faults and open cracks striking approximately north-south occur both on-

Figure 5.1: Seismotectonic setting of the northern Chilean forearc. Interseismic shortening on the scale of the orogen is demonstrated by the eastward decrease in GPS velocity (black vectors, length scale labeled "I"), while elastic rebound during the 1995 Antofagasta earthquake is shown by the westward increase in coseismic GPS displacement (gray arrows, length scale labeled "C"). Interseismic data north of Antofagasta is from *Kendrick et al.* (2001) and from *Brooks et al.* (2003) to the south. Interseismic data is contaminated by the co- and postseismic signal of the 1995 earthquake. Coseismic data are from *Klotz et al.* (1999). Nazca-South America convergence vector shows approximate direction but not magnitude of relative plate motion. Dashed ovals show approximate rupture areas of several prominent underthrusting earthquakes, while the circles mark the actual or inferred epicenters (Data from *Kelleher*, 1972; *Comte and Pardo*, 1991; *Ruegg et al.*, 1996).

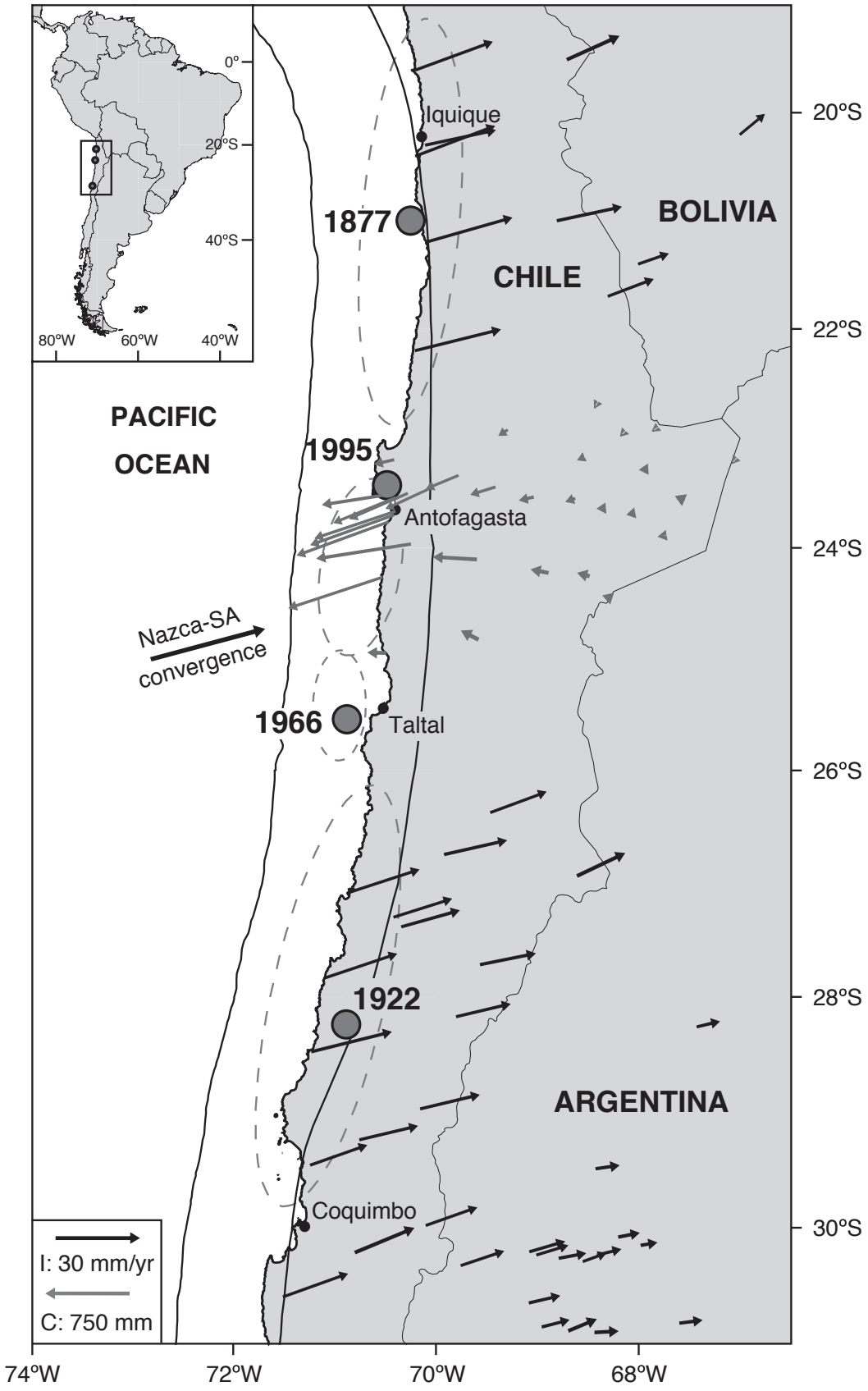
0°
20°S
40°S
80°W
60°W
40°W
Iquique
1877
BOLIVIA
CHILE
PACIFIC
OCEAN
1995
Antofagasta
Nazca-SA
convergence
1966
Taltal
1922
ARGENTINA
Coquimbo
I: 30 mm/yr
C: 750 mm
20°S
22°S
24°S
26°S
28°S
30°S
74°W
72°W
70°W
68°W

and offshore (*Arabasz*, 1971; *Delouis et al.*, 1998; *González et al.*, 2003; *von Huene and Ranero*, 2003; *Loveless et al.*, 2005). Several hypotheses have been put forth to explain the observed extension within a tectonic setting otherwise characterized by shortening: (1) extension and uplift associated with subduction erosion (*Armijo and Thiele*, 1990; *Niemeyer et al.*, 1996; *Delouis et al.*, 1998; *von Huene et al.*, 1999; *Sallàres and Ranero*, 2005); (2) coseismic release of strain accumulated during interseismic periods (*Delouis et al.*, 1998; *Loveless et al.*, 2005); and (3) strains associated with the interseismic convergence (*Delouis et al.*, 1998; *González et al.*, 2003; *Loveless et al.*, 2005).

Insight into the latter two proposed mechanisms for upper plate faulting can be gained using elastic models of stress changes induced by the subduction zone earthquake cycle. We present models showing that the interseismic period plays an important role in the evolution of extensional structures in the northern Chilean forearc, while complicated coseismic deformation fields have implications for the apparently contradictory senses of motion on some of these faults. We focus on the region near the city of Antofagasta (23.5°S), where numerous well-developed fault scarps and some exposed fault planes provide information about the kinematics of permanent deformation. The patterns of deformation associated with the subduction zone earthquake cycle are similar to those demonstrated by geological structures, indicating a relationship between the short- and long-term deformation fields. The seismic cycle and permanent surface deformation are fundamentally driven by the same stress field (*Allmendinger et al.*, 2005, 2007), which implies their interdependence. Numerous previous studies in the Andean forearc have used elastic modeling of geodetic data to extract information about subduction processes (e.g., *Klotz et al.*, 1999; *Bevis et al.*, 2001; *Pritchard et al.*, 2002; *Khaz-*

aradze and Klotz, 2003; *Pritchard et al.*, 2006), and we suggest here that geological data also offer insight into the properties of the plate boundary interface. Unlike the geodetic measurements which record only a snapshot of the tectonics, the permanent deformation fields reflect plate boundary strain accumulated over many earthquake cycles.

5.3 Tectonic and geological setting

For the past 25 Ma, convergence across the strongly-coupled plate interface between the Nazca and South American plates has resulted in significant crustal thickening and shortening. Presently, motion of the Nazca Plate relative to stable South America is described by a vector with velocity ∼65 mm yr^{-1} directed ∼075° along the northern Chilean coastline (Figure 5.1; *Kendrick et al.*, 2001). Elastic dislocation modeling of interseismic GPS data indicates that the Nazca-South American plate interface is fully locked between depths of 20 and 35–50 km (*Bevis et al.*, 2001; *Khazaradze and Klotz*, 2003), which is broadly consistent with the extent of the seismogenic zone as determined by inversion of teleseismic waveforms (*Tichelaar and Ruff*, 1991). GPS data capture shortening in the direction of plate convergence on the scale of the orogen during the interseismic period (*Kendrick et al.*, 2001; *Bevis et al.*, 2001; *Brooks et al.*, 2003; *Chlieh et al.*, 2004) and extension of the forearc in the same direction during subduction earthquakes (Figure 5.1; *Ruegg et al.*, 1996; *Klotz et al.*, 1999). Much of the strain that accumulates across the locked plate boundary during the interseismic period is relieved during strong subduction earthquakes, the recurrence interval of which is estimated to be 100-150 years (*Comte and Pardo*, 1991) in northern Chile.

This paper focuses on the Coastal Cordillera of the northern Chile forearc,

which represents a relic of the Mesozoic Andean arc and comprises dominantly Late Jurassic and Cretaceous plutonic and volcanic rocks. Bedrock exposure is generally poor as the surface is blanketed with gypsum-indurated regolith (*Rech et al.*, 2003, 2006). The hyperarid climate of the Atacama Desert, which has persisted since at least 6 Ma (*Hartley and Chong*, 2002) if not 19–13 Ma (*Rech et al.*, 2006), allows for long-term preservation of surface features. The principal structure of the northern Chilean forearc is the Atacama Fault System (AFS, Figure 5.1), which originated in the Mesozoic as a major strike-slip structure governing the tectonics of the arc (*Arabasz*, 1971; *Naranjo*, 1987; *Scheuber and Andriessen*, 1990). Lithologic relationships, steep dips, and traces that are linear over great distances indicate the previous kinematics of the AFS and splays from it (*Arabasz*, 1971; *Scheuber and Andriessen*, 1990; *Scheuber and González*, 1999; *Delouis et al.*, 1998; *González et al.*, 2003).

5.3.1 Neotectonics of the Antofagasta Region

While numerous margin-parallel faults in the Coastal Cordillera are of suspected Mesozoic strike-slip origin, field studies indicate that they have experienced strike- and/or dip-slip neotectonic reactivation (*Arabasz*, 1971; *Armijo and Thiele*, 1990; *Delouis et al.*, 1998; *Riquelme et al.*, 2003; *González et al.*, 2003, 2006). Compilations of slip data from the Mejillones Peninsula and the Salar del Carmen segment of the AFS show fault plane solutions consistent with normal faulting due to east-west extension (*Delouis et al.*, 1998; *González et al.*, 2003). Dextral slip indicators on northwest-striking faults in the Salar Grande region (21°S) and the Barazarte fault, southeast of Antofagasta, are kinematically consistent with regional east-west extension. The activity level and recurrence interval of faults are poorly

constrained, primarily due to the lack of dateable organic material within faulted sediments and complications brought about by the hyperarid climate. *González et al.* (2006) present cosmogenic dating of alluvial fan surface which date the most recent motion of the Salar del Carmen segment of the AFS to 424±151 ka. Scarp morphology dating suggests scarp ages ranging between 16 and 400 ka; the large range reflects uncertainty in the diffusion constant used in the dating (*González and Carrizo*, 2003). The hyperaridity of the region is capable of preserving structures for long periods of time; even ruptures with a fresh appearance may reflect deformation that occurred thousands of years ago (*González and Carrizo*, 2003; *González et al.*, 2006). Vertical offset of 15-20 cm along the Paposo segment of the AFS, located south of Antofagasta around 25°S latitude (*Delouis et al.*, 1997, 1998; *Klotz et al.*, 1999), and near the Uribe railway station along the Salar del Carmen segment (*Klotz et al.*, 1999), are reported to have accompanied the 1995 M_w=8.1 subduction zone earthquake, which occurred offshore Antofagasta.

5.4 New Structural Observations

New field observations at several key localities in the Antofagasta region augment the neotectonic database described above. Along the northern part of the Salar del Carmen segment of the AFS (labeled "SC" on Figure 5.2), we observe reverse fault reactivation of the normal fault that has accommodated the displacement responsible for the large topographic scarp. At a site along the Paposo segment of the AFS ("P" on Figure 5.2), we see morphological characteristics similar to those present at the Salar del Carmen site and thus infer the same style of fault reactivation.

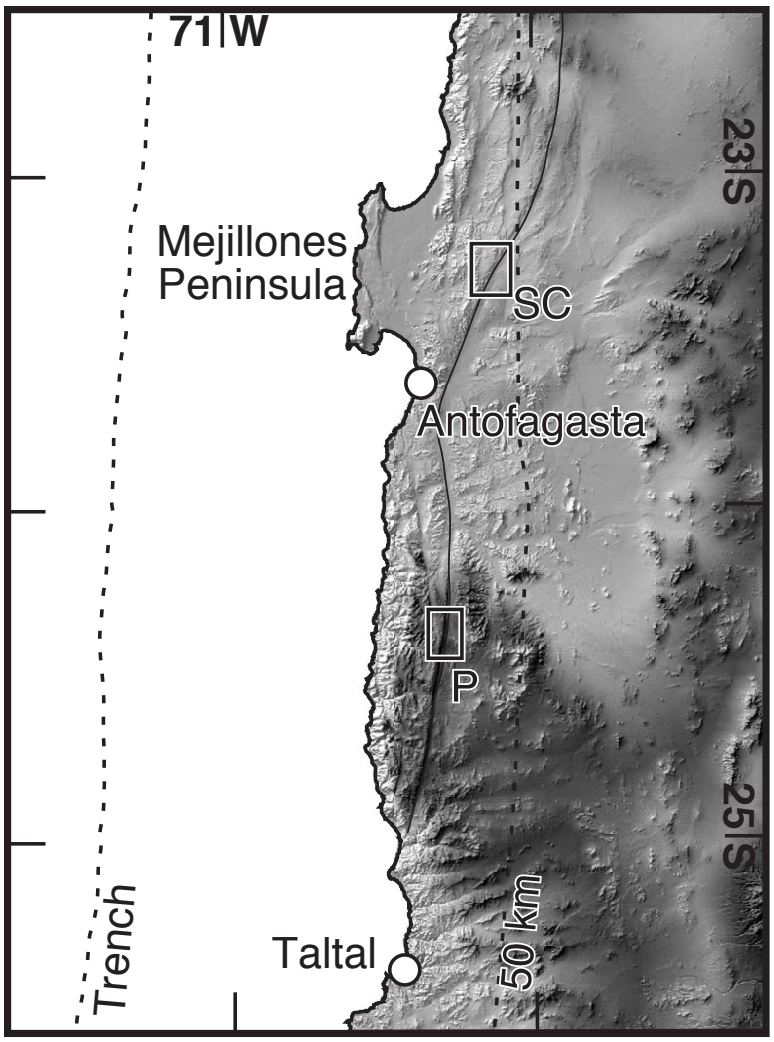

Figure 5.2: Shaded-relief topography location map showing key localities in the Antofagasta region. Black dashed lines show surface projections of subduction trench and 50 km Wadati-Benioff zone contour (*Cahill and Isacks*, 1992). Thin black line marks the trace of the Atacama Fault System (AFS), while other prominent topographic scarps mark subsidiary faults. Field sites discussed in Section 5.4 are labeled as "SC" (Salar del Carmen segment of the AFS, Section 5.4.1) and "P" (Paposo segment, Section 5.4.2).

5.4.1 Northern Salar del Carmen segment of the AFS

About 65 km northeast of Antofagasta at the northern end of the Salar del Carmen segment of the AFS (23.15°S, 70.06°W), we observe structural and morphological characteristics indicating that the basin at the foot of the scarp has moved up relative to the fault-bounded mountain front. In map view (Figure 5.3), the SE-facing topographic scarp, which we interpret to have been constructed by normal slip on a SE-dipping fault, features a narrow yet prominent dark band midway up the slope. The band marks a subtle topographic bench on the scarp, where a gentler slope has allowed for accumulation of coarse alluvium. Channels incising the scarp provide structural and morphological lines of evidence for reverse fault reactivation of the Salar del Carmen segment. Channels that are sufficiently deeply incised expose a basement wedge in the hanging wall is upthrust against footwall alluvium (Figure 5.4a). Measurement of the magnitude of slip is complicated by discontinuity of offset marker horizons but is estimated to be on the order of 1–2 m. Uplift of this basement wedge has resulted in folding of salt-indurated alluvial material (Figure 5.4a, inset) immediately above it, and broad-scale uplift and gentle warping of the modern surface, producing the topographic bench. The uplift of the hanging wall relative to the footwall is indicated by the change in incision style of scarp-perpendicular channels that occurs at the level of the reverse faulting. Above this height, channels show a gentler morphology, whereas below the topographic bench, incision into the hanging-wall alluvium is more pronounced (Figure 5.4b). Other anomalies in the scarp topography, as can be seen above the main topographic bench in Figure 5.4b, may represent minor amounts of normal or reverse faulting on other fault splays, or they may represent slumping of alluvium unrelated to faulting.

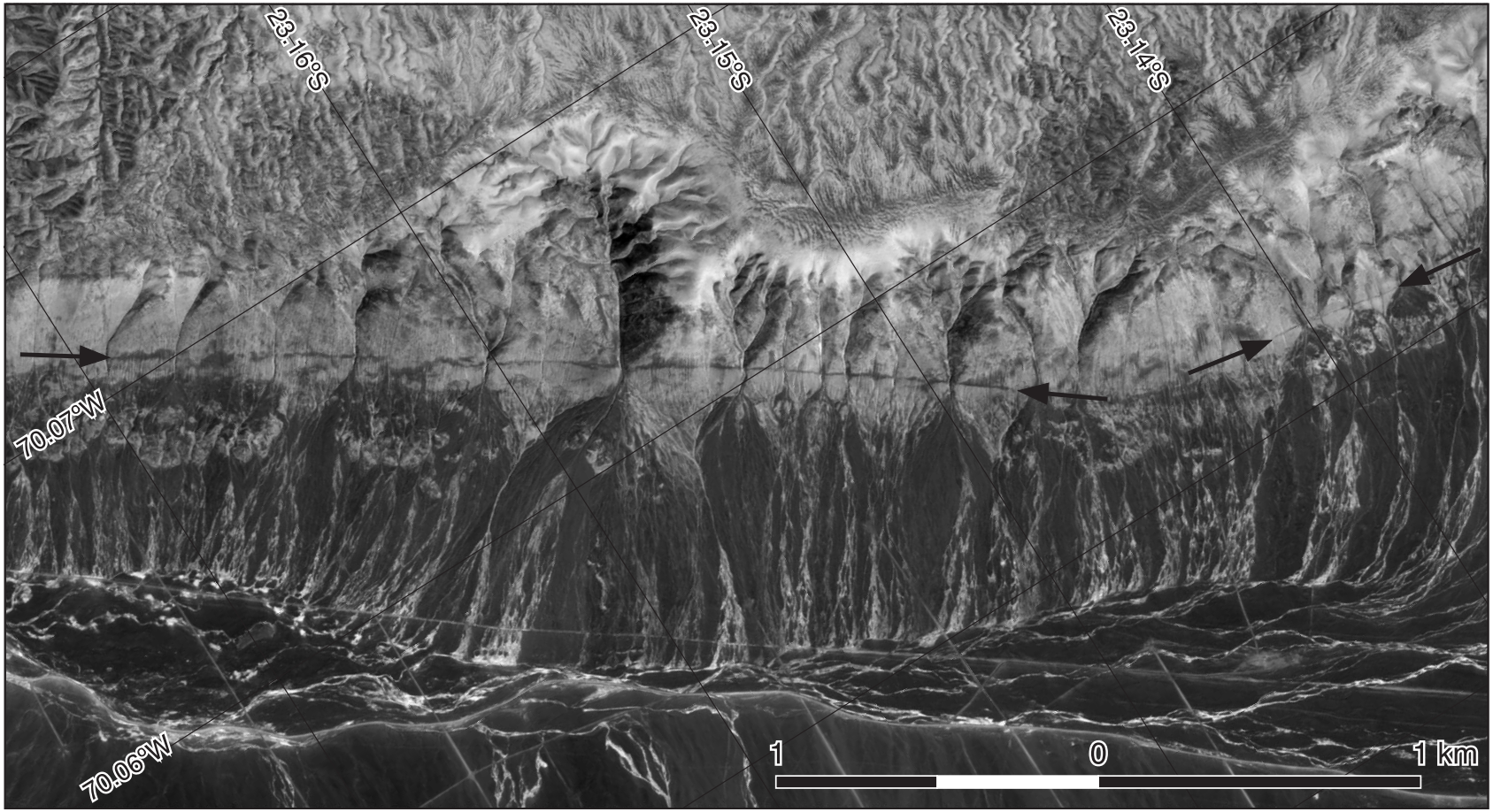

Figure 5.3: QuickBird satellite image of the site of reverse fault reactivation of the northern Salar del Carmen segment of the Atacama Fault System. Locality is shown as box labeled "SC" in Figure 5.2. The topographic bench is highlighted by the arrows.

Figure 5.4: a) Field photo showing exposure of reverse faulting in a scarp-perpendicular channel with topographic bench overlying the fault. Black arrows on the scarp surface mark the topographic bench on which darker cobbles have accumulated. Dashed white arrow shows approximate location of fault. Geologist for scale. Zoom photo demonstrates salt-cemented alluvial material folded by the reverse faulting. Dashed white line represents the approximate axial plane of the fault-related fold. b) Field photo, taken facing scarp, showing the change in incision style coincident with the topographic bench (marked by black dashed line), from shallowly-incised above the bench to more sharp below the bench.

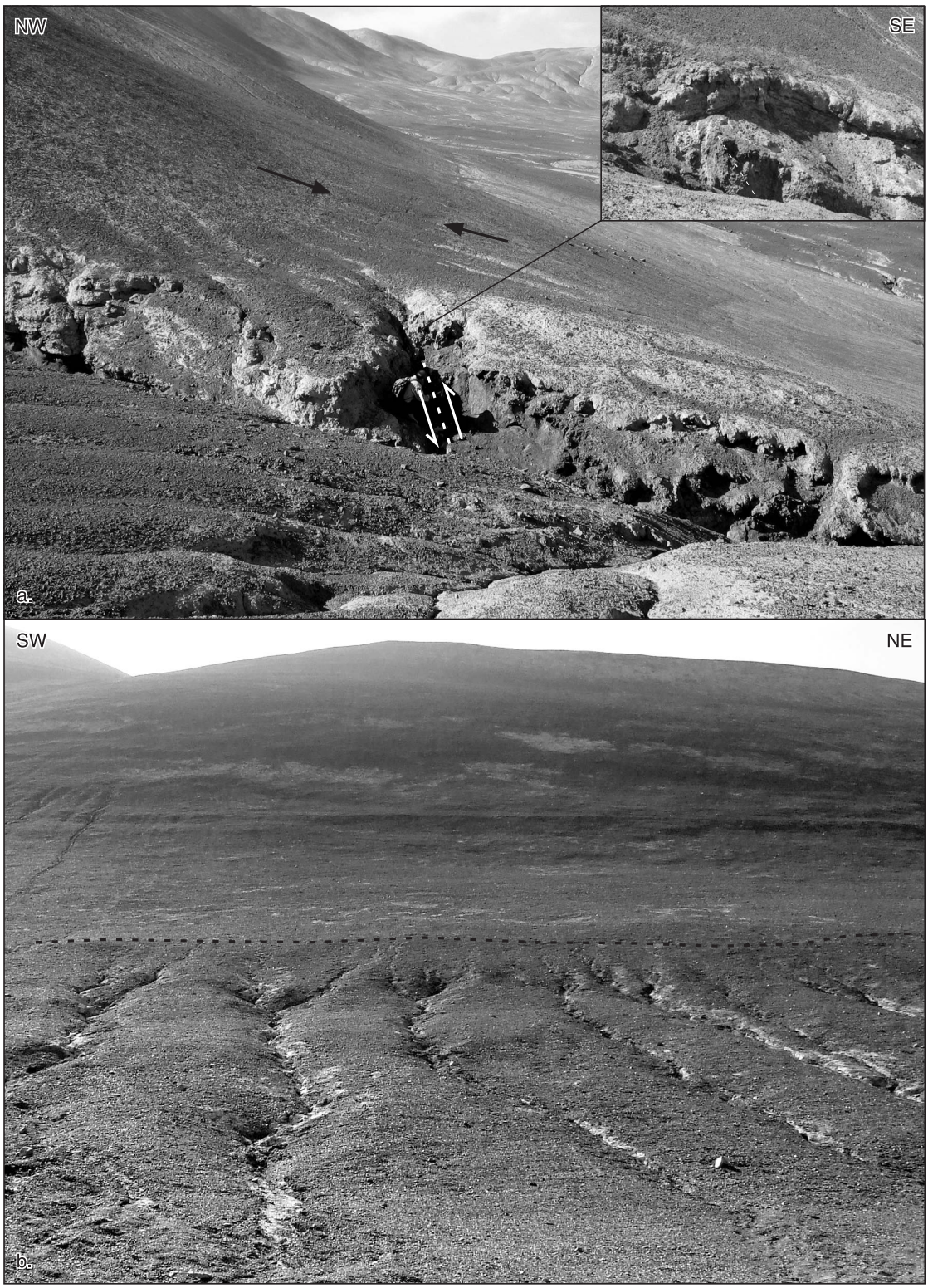
NW
SE
a.
SW
NE
b.

The correlation between the reverse faulting and the overlying topographic bench allows the bench to be used as an indicator of the along-strike extent of reverse fault reactivation. Along the Salar del Carmen segment, the bench extends for about 2 km (Figure 5.3). The width of the bench (as expressed in satellite imagery and as defined by the extent of anomalously dark surface cobble accumulation) is a function of the degree of surface curvature. That is, the bench is narrower where the surface is more abruptly curved by the reverse faulting beneath, and wider where the bench is more subtle. Given the relationships between the subsurface faulting and development of the topographic bench, as seen in and above the deepest-incised channels, the topographic bench width and curvature depends primarily on the burial depth of the reverse fault. A narrow, more abrupt bench correlates with a shallowly-buried fault, while the wider, subtler bench indicates a more deeply-buried fault.

5.4.2 Northern Paposo segment of the AFS

Morphological characteristics similar to those seen at the northern Salar del Carmen segment site are observed along a 3.5 km-long stretch of the scarp of the Paposo segment of the AFS (73 km south of Antofagasta; 24.32°S, 70.31°S, box "B" on Figure 5.2). In this case, a topographic bench on the scarp is highlighted by alluvial material lighter in color than that covering other parts of the slope (Figure 5.5a). No channels cross-cut the scarp sufficiently to expose bedrock, but some shallow drainages do show a change in incision style at the height of the topographic bench, similar to those at the Salar del Carmen site. This change in channel morphology, from gently incised above the bench to more sharply incised below, in conjunction with the relative uplift of the hanging-wall alluvial fan

Figure 5.5: Site of inferred reverse fault reactivation of the northern Paposo segment of the Atacama Fault System. Locality is shown as a diamond along the fault labeled "P" in Figure 5.2. a) Field photo looking obliquely at the scarp. The white arrows highlight the topographic bench, which is marked by an accumulation of alluvium lighter in color than that covering other parts of the slope. b) Profile view of the scarp indicating the uplift of the hanging-wall alluvial fan relative to the footwall. Offset is on the order of 1–2 m.

N
S
a
E
W
b

as seen in profile (Figure 5.5b), indicates about 1 m of reverse fault reactivation. About 70 km along strike to the south (at 24.94°S, 70.43°W), an exposure of the master normal fault in a pronounced canyon indicates a steep east dip, consistent with the morphology of the cumulative normal fault scarp and suggestive of east-side-up reverse faulting as the cause of the relative uplift of the alluvial fan surface.

5.5 Modeling seismic cycle deformation

The new field observations demonstrate complexity in the permanent strain field of the forearc. Whereas previous studies of the neotectonics of the Antofagasta region have found fault kinematic indicators consistent with east-west extension, the northern Salar del Carmen and Paposo faults show signals of deformation indicative of east-west shortening. To explore the consistency between these complicated permanent strain patterns and the stress fields generated by the subduction zone earthquake cycle, we use elastic dislocation modeling to calculate the influence of the seismic cycle on upper plate structures.

Elastic dislocation algorithms (*Savage*, 1983; *Okada*, 1985, 1992) have been widely used to model surface displacement and velocity fields determined through geodetic measurements. Such data lend themselves to this type of modeling, as they are interpreted to reflect primarily signals of elastic strain accumulation and release resulting from fault processes. We use these models to generate a first-order view of the stress fields that are induced by the inter- and coseismic periods and compare these stress fields to the deformation patterns exhibited by structures in the forearc.

5.5.1 Interseismic modeling

In the case of a subduction zone, interseismic strain accumulation is commonly simulated using the "backslip" model proposed by *Savage* (1983), which prescribes artificial normal fault slip at the plate convergence rate on a locked (not slipping) portion of the plate interface and zero slip on the stably sliding parts of the fault. This construction is kinematically equivalent to thrust-type interseismic strain accumulation across a locked plate boundary. The application of the dislocation only on the locked portion of the plate boundary is justified by the assumption that significant strain accumulation takes place only on this portion of the interface (*Savage*, 1983). We use this model as the foundation for our interseismic simulations.

5.5.1.1 Model parameters

We model the effects of interseismic strain accumulation on the plate boundary interface using Poly3D, a three-dimensional boundary element program (*Thomas*, 1993). The plate boundary is discretized into triangular elements, allowing the curvature of the interface to be accurately modeled. We define the plate boundary geometry by first taking a series of profiles perpendicular to the local strike of the plate boundary from 20°–31°S, determining the latitude and longitude of the trench and 50 km and 100 km depths of the Wadati-Benioff zone (*Cahill and Isacks*, 1992), then finding the parameters of the arcs defined by the latitude, longitude, and depth triplets. We then interpolate the resulting geometry to define the triangular slip elements used in the modeling (Figure 5.6a). The backslip distribution is calculated using the program DISL3D (*Wang et al.*, 2003), which determines the magnitude and rake of slip on each element based on its position with respect to the

Euler pole of relative plate motion as defined by *Kendrick et al.* (2001). Because the modeling is carried out in an elastic half-space, we correct the plate boundary geometry for topography and bathymetry (Figure 5.6b, *Flück et al.*, 1997). The plate boundary is divided into three regions: the seaward transition zone, which extends from the trench to approximately 20 km depth; the locked portion of the interface, between 20 and 32–45 km depth; and the downdip transition zone, which extends 15 km deeper than the bottom of the locked zone.

5.5.1.2 Slip distribution

We apply backslip equal to the plate convergence rate to the locked portion of the subduction fault in order to mimic interseismic strain accumulation. Within the transition zones, up- and downdip of the locked zone, the applied backslip magnitude lies between zero and the convergence rate. With increasing depth, subducted material lying at the plate interface within updip (seaward) transition zone is progressively dewatered, allowing for the transition from stable to unstable interplate sliding (*Oleskevich et al.*, 1999). Downdip of the locked zone, the interface behavior experiences a transition from stick-slip to thermally-activated stable sliding (*Oleskevich et al.*, 1999). Smoothly tapering the slip within the transition zones serves as a kinematic approximation for the gradual changes in physical behavior (e.g., *Wang et al.*, 2003; *Chlieh et al.*, 2004). We use a Gaussian function, shown schematically in Figure 5.6c, that minimizes abrupt changes in slip magnitude which could produce concentrations of near-surface strain (Figure 5.6c, e.g., *Savage*, 1983). The slip magnitude on each element within the transition zone is described as

$$u' = u \exp\left(\frac{-s^2}{2c^2}\right) \tag{5.1}$$

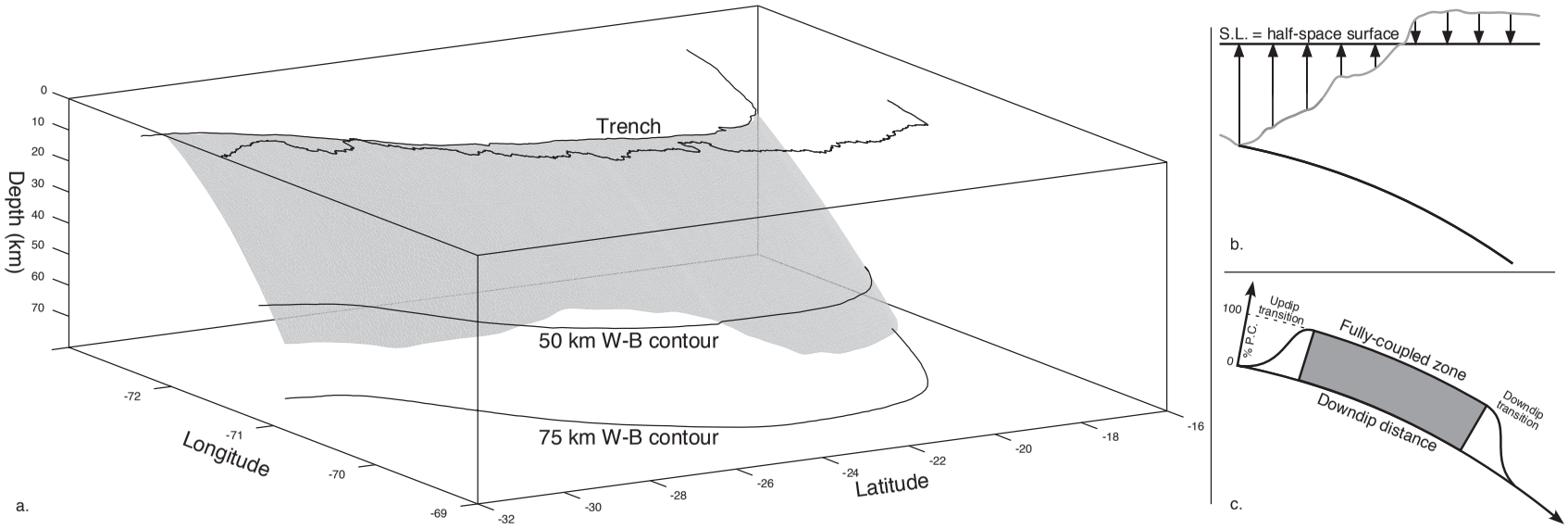

Figure 5.6: Construction of the boundary element model for interseismic strain accumulation. a) The model geometry is based on the shape of the Wadati-Benioff zone as defined by *Cahill and Isacks* (1992). The modeled plate interface is discretized into triangular elements in order to accurately capture the curved geometry. b) Because the modeling is carried out in an elastic half-space, we modify the plate boundary geometry based on the overlying topography, using the method of *Flück et al.* (1997). The resulting distance between the adjusted plate boundary and the half-space surface is equivalent to the distance between the original plate boundary model and the overlying topography. c) We use a Gaussian function (Equation 5.1) to smoothly taper the backslip magnitude from its maximum value to zero across the transition zones, thereby minimizing abrupt changes in slip magnitude between adjacent elements.

where u' is the corrected slip magnitude within the transition zone, u is the slip magnitude of the locked element nearest the particular transition zone element, s is the along-arc position of the transition zone element relative to the updip extent of that zone, and c is a shape factor governing the Gaussian curvature or gradient of the slip transition.

The maximum depth of interplate locking has been addressed by several studies in northern Chile (*Tichelaar and Ruff*, 1991; *Comte et al.*, 1994; *Delouis et al.*, 1996; *Bevis et al.*, 2001; *Khazaradze and Klotz*, 2003), which we considered when choosing our model parameters. Ambiguities in the definition of the term "plate coupling" have been discussed previously (*Wang and Dixon*, 2004a) and we here present the concepts relevant to our models. Variation in the nature of the interface between the subducting and overriding plates in a subduction zone can be characterized using frictional or kinematic boundary conditions. The frictional conditions on the interface vary from those that allow stable sliding to those consistent with unstable or stick-slip interaction (e.g., *Pacheco et al.*, 1993). Kinematic boundary conditions describe relative motion between the plates ranging from slipping at the rate of plate convergence to not slipping. Equivalence between the frictional and kinematic descriptions of interplate behavior is not clearly established (*Wang et al.*, 2003; *Wang and Dixon*, 2004a; *Lay and Schwartz*, 2004; *Wang and Dixon*, 2004b). We note that the 20–50 km depth extent of kinematic locking (i.e., no relative motion) that accurately predicts surface GPS velocities (*Bevis et al.*, 2001) agrees with the observed depth range of underthrusting earthquakes (*Tichelaar and Ruff*, 1991), indicating that, to a first-order, the zone of kinematic interplate locking and the seismogenic zone coincide. In our modeling of the seismic cycle, we use information regarding the extent of locking used to model GPS data (e.g.,

Bevis et al., 2001; *Khazaradze and Klotz*, 2003) as well as the depth range of the seismogenic zone (e.g., *Tichelaar and Ruff*, 1991; *Comte et al.*, 1994; *Delouis et al.*, 1996).

Tichelaar and Ruff (1991) used seismic waveform inversion to deduce that the maximum seismogenic depth is at least 45–48 km for northern Chile (18°–24°S), no deeper than 36–41 km for the Taltal region (24°–27°S), and at least 48–53 km in the Copiapó region (27°–30°S). Thus, transitions between deeper and shallower coupling take place around the latitudes of Antofagasta and Copiapó. In their local seismic study of the Antofagasta region, *Delouis et al.* (1996) note a "reduced" number of earthquakes occurring between 35 and 50 km depth and indicate that these events are more consistent with reverse faulting than underthrusting. *Khazaradze and Klotz* (2003) show a change in extent of coupling from 50 km to 35 km depth around the latitude of the Mejillones Peninsula based on elastic modeling of GPS data. Their modeling is complicated in the region of the transition by post-seismic deformation associated with the 1995 Antofagasta earthquake and the low density of stations from 25°–30°S. *Comte et al.* (1994) suggest that the maximum depth of the coupled interplate zone is 47 km throughout the Antofagasta region based on locations of thrust-type earthquakes. By inverting geodetic and seismic data, *Pritchard and Simons* (2006) determined the slip distributions for 11 $M_w > 6$ earthquakes in the Antofagasta region. The largest earthquake studied — the 1995 event — ruptured the plate boundary to a depth of ∼40 km, while 4 smaller earthquakes occured farther downdip. *Pritchard and Simons* (2006) propose that the interface between 40–50 km depth may be characterized by discontinuous patches within which the smaller earthquakes can nucleate, but surrounded by stably-sliding regions. The kinematic definition of the transition

zone serves as a gross approximation for such heterogeneity: because only isolated portions of the interface slip seismically, it is likely that interseismic strain accumulation occurs on these patches, with lesser accumulated strain in the intervening, stably-sliding regions.

We model a change in the maximum depth of full interplate locking around the latitude of the Mejillones Peninsula (23.5°S), based the observations of the seismogenic zone described above. North of this latitude, the locked portion of the plate interface extends from 20–45 km, with transitional slip to 60 km. This extent of locking is consistent with the elastic modeling of interseismic GPS data in northern Chile and southern Peru (*Bevis et al.*, 2001). Near Antofagasta, we model locking between 20–32 km, with transitional slip to 45 km. We follow the geometry described *Tichelaar and Ruff* (1991) for the Copiapó region and smoothly increase the width of the coupled zone around 27°S (Figure 5.7).

5.5.1.3 Asperity model of interseismic strain accumulation

The prescription of distributed slip described above assumes that interseismic strain accumulation occurs in a broadly distributed manner subject to the geometrical constraints along strike and within the transition zones. However, detailed studies of the 1995 Antofagasta earthquake (e.g., *Ihmlé and Ruegg*, 1997; *Sobiesiak*, 2004; *Pritchard et al.*, 2006) indicate a spatially-variable distribution of slip with several concentrations of enhanced moment release. Additionally, *Song and Simons* (2003) and *Wells et al.* (2003) demonstrate a correlation between regions of substantial seismic moment release and negative gravity anomalies in several subduction zones worldwide. *Bürgmann et al.* (2005) show that GPS data recording interseismic deformation can be modeled using either a broad slip distribution

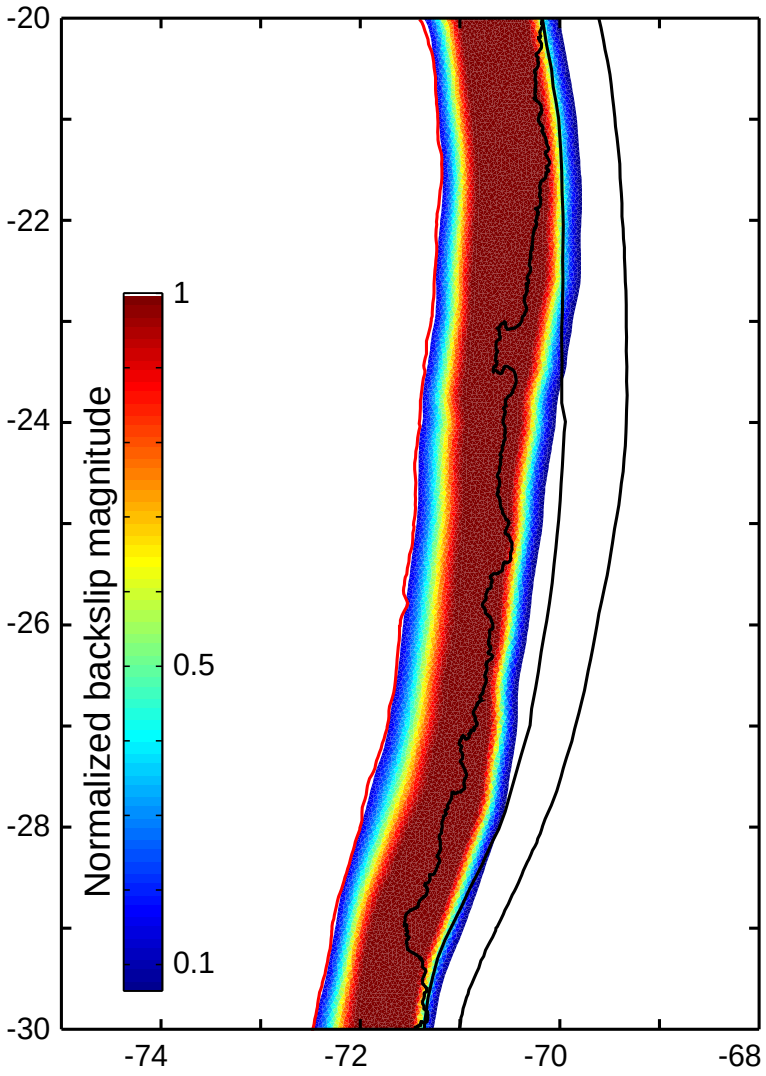

Figure 5.7: Slip distribution of the boundary element model, shown as the backslip magnitude normalized to the maximum slip. The slip values are calculated using the method of *Wang et al.* (2003) and the Euler pole of relative plate convergence of *Kendrick et al.* (2001). The extent of full interplate coupling lies between 20 and 50 km depth in northernmost Chile and decreases to between 20 and 38 km around the latitude of the Mejillones Peninsula. Updip and downdip of this zone are transition zones within which the backslip magnitude decreases smoothly from the maximum value to zero. See Section 5.5.1.2 for more details.

or a more concentrated distribution consistent with regions of large-magnitude coseismic slip, which correlate with measured negative gravity anomalies. To explore the effects of irregularly-distributed interseismic strain accumulation on the northern Chilean subduction zone, governed by gravity anomalies as measured by *Sandwell and Smith* (1997), we follow the approach of *Song and Simons* (2003) and calculate the trench-parallel gravity anomaly (TPGA) along the northern Chilean forearc (Figure 5.8a). The TPGA is determined by subtracting the average trench-normal free-air gravity anomaly from the gravity field, which serves to highlight short-wavelength variations in gravity. We scale the backslip magnitude on the subduction thrust (calculated as described in Section 5.5.1.2) by the TPGA, defining regions of full coupling (backslip at the plate convergence rate) as those that correlate with most negative TPGA. Within the regions where positive TPGA reaches a maximum values, backslip magnitude is scaled by 50% of its value as defined in Section 5.5.1.2 and shown in Figure 5.7. The resulting adjusted slip distribution is shown in Figure 5.8b.

5.6 Modeling results

Models of interseismic loading in the Antofagasta region show patterns of deformation consistent with the distribution of normal faults. We use the calculated stress tensor to determine the Coulomb stress change ($\Delta\sigma_c$), which provides a single, convenient quantity used to evaluate how the subduction zone processes influence the upper plate structures. $\Delta\sigma_c$ is defined as

$$\Delta\sigma_c = \Delta\tau - \mu'\Delta\sigma_n, \tag{5.2}$$

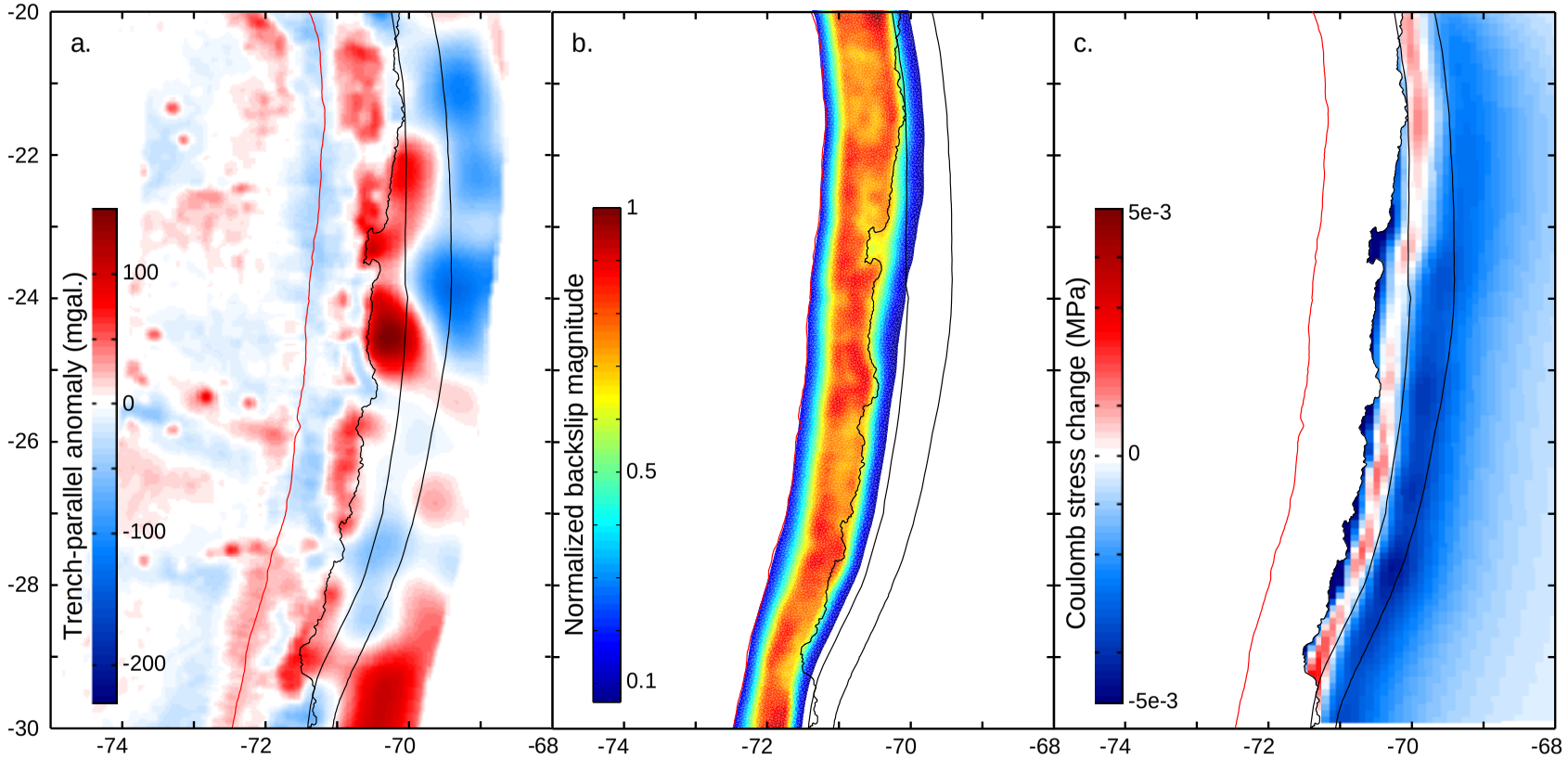

Figure 5.8: Gravity field, slip distribution, and CSC results of the asperity model. a) The trench parallel gravity anomaly ("TPGA," *Song and Simons*, 2003) highlights short-wavelength features of the forearc gravity anomaly field, which could indicate variation in the nature of interseismic coupling (*Bürgmann et al.*, 2005). b) We scale the interseismic backslip distribution by the TPGA, with regions of most negative TPGA retaining their full value and those coincident with the most positive TPGA reduced to 50% their value as defined in Figure 5.7. c) The resulting CSC is calculated using the same parameters as in Figure 5.9.

where $\Delta\tau$ is the change in shear stress in a particular direction (rake), μ' is the effective coefficient of friction (accounting for pore fluid pressure), and $\Delta\sigma_n$ is the change in stress acting normal to the fault plane. All quantities represent conditions on fault planes of a specified orientation with a slip vector of specified rake. We calculate $\Delta\sigma_c$ resolved on planes striking 010° and dipping 75°E, with $\mu' = 0.4$ and a slip vector of rake -110° (i.e., normal fault slip). These values are broadly consistent with the fault geometries and kinematic indicators observed around Antofagasta (*Delouis et al.*, 1998; *González et al.*, 2003), and variation of any angular parameter by ±10° does not substantially affect the distribution of $\Delta\sigma_c$. Faults lying within zones of positive $\Delta\sigma_c$ are moved closer to failure by interseismic convergence, whereas normal faulting is discouraged on faults lying within regions of negative $\Delta\sigma_c$. The quantity $\Delta\sigma_c$ encompasses changes in either or both shear and normal stresses on a fault plane, plus a possible change in the frictional coefficient. Thus, a negative $\Delta\sigma_c$ also indicates encouragement towards failure in a direction opposite the specified rake, i.e., reverse faulting according to our convention. We do not explicitly model a regional stress field. Rather, the distribution of $\Delta\sigma_c$ represents solely the effect of interseismic convergence on the state of stress on upper plate faults.

Figure 5.9a shows the distribution of $\Delta\sigma_c$ resulting from one year of interseismic convergence, calculated at 1 km depth. Positive $\Delta\sigma_c$ is predicted within a narrow region of the Coastal Cordillera and shows a spatial correlation with the downdip extent of the coupled plate interface. The distribution of positive $\Delta\sigma_c$, reflecting the geometry of the locked plate boundary, is consistent with the change in trace of the AFS along the Salar del Carmen segment (Figure 5.9a). Figure 5.9b indicates that the shear stress change $\Delta\tau$ is also positive within a narrow zone near the

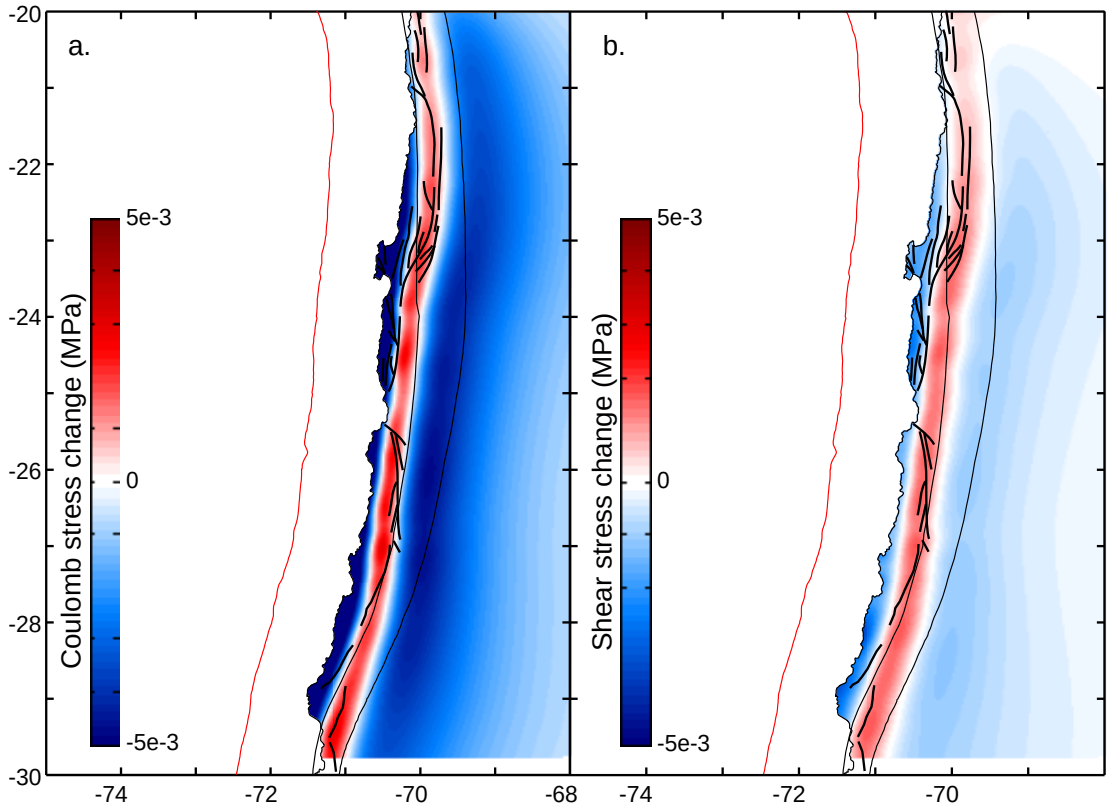

Figure 5.9: a) Coulomb stress change calculated using the slip distribution shown in Figure 5.7. The Coulomb stress change is resolved on planes striking 010°, dipping 80°, with a slip vector of -110° and is calculated at a depth of 1 km assuming an effective coefficient of friction of $\mu' = 0.4$. Red line offshore shows the position of the trench, while nearly parallel black lines onshore show the 50 km (west) and 75 km (east) contours of the Wadati-Benioff zone. Bold, discontinuous lines in forearc show prominent fault traces. b) Shear stress resolved on planes with same orientation and rake described in a.

coastline, demonstrating that interseismic convergence increases downdip shear stress on the normal fault planes. Stress acting normal to the specified fault planes (not shown) is distributed similarly to $\Delta\sigma_c$, which means that the AFS and nearby are unclamped due to convergence. The Paposo segment of the AFS lies on the edge of the region of positive $\Delta\sigma_c$, and some faults immediately west of it lie within the zone of negative $\Delta\sigma_c$. *Naranjo* (1987) suggested that these faults have been dominantly inactive since 10 Ma, but the reported normal faulting triggered by the 1995 Antofagasta earthquake (*Delouis et al.*, 1997, 1998), as well as the reverse faulting we describe in Section 5.4.2 suggest otherwise. The numerous examples of recent normal faulting on Mejillones Peninsula show poor correlation with the pattern of interseismic $\Delta\sigma_c$; we address some potential explanations for this discrepancy in the discussion. Introducing the gravity-based variability in interplate locking (Section 5.5.1.3) serves to segment the near-surface stress change (Figure 5.8c), but the overall pattern is similar to that shown in the homogeneously distributed model (Figure 5.9). Zone of greater Coulomb stress increases (darker red on Figure 5.8c) coincide with the positions of negative TPGA (blue on Figure 5.8a).

5.6.1 Effects of subduction zone earthquakes

Chapter 4 and Figure 5.10 show that forearc faults could experience either an increase or decrease in Coulomb stress during a strong subduction earthquake, depending on the position of the fault relative to the coseismic slip distribution. Therefore, a subduction zone earthquake has the potential to trigger either normal or reverse faulting, depending on the existing state of stress on a particular upper plate fault. The near-surface stress field shown in Figure 5.10 is complicated but

provides a mechanism for the apparently contradictory normal and reverse faulting on the Salar del Carmen and Paposo segments of the AFS (Section 5.4), and potentially other forearc faults. It is interesting to note that the narrow zone of negative $\Delta\sigma_c$ mimics the region of positive $\Delta\sigma_c$ of the interseismic model, emphasizing that the short-wavelength patterns of the stress field need to be considered in each period of the seismic cycle.

5.7 Discussion

5.7.1 Effects of dislocation geometry on surface stress

Elastic models are limited by unrealistic rheological assumptions. These models do, however, allow for a simple analysis of the subduction zone seismic cycle, providing some insight into the plate-scale processes that drive surface deformation. The surface strain field predicted by a dislocation model is dependent on the geometry of the applied dislocation. As noted by *Savage* (1983), surface strain in a modeled subduction zone is concentrated above the downdip extent of the locked part of the plate boundary. We note that the zone of positive interseismic $\Delta\sigma_c$ in the Coastal Cordillera coincides roughly, but not exactly, with the downdip extent of the modeled plate boundary. Increasing the width of the fully-coupled and/or downdip transitional region a) decreases the magnitude of the $\Delta\sigma_c$ anomaly and b) increases the width of this anomalous zone. If backslip is applied to a sufficiently wide portion of the plate boundary, the sign of $\Delta\sigma_c$ in the coastal regions changes from positive to negative. However, the width of the backslipping zone required to cause this reduction of $\Delta\sigma_c$ to below zero is inconsistent with the bounds placed on the coupled zone from seismic and geodetic studies (*Tichelaar and Ruff*, 1991;

Bevis et al., 2001; *Klotz et al.*, 2001; *Khazaradze and Klotz*, 2003). In central and southern Chile (i.e., south of 34°S), the width of the coupled zone is greater than in northern Chile due to differences in the geometry of the subducting plate (*Khazaradze and Klotz*, 2003). This greater width of interplate locking would result in a deformation field lacking the positive $\Delta\sigma_c$ anomaly seen in our models of northern Chile.

Savage (1983) showed that the zone of extensional trench-normal strain (analogous to our zone of positive $\Delta\sigma_c$) above the lower extent of the subduction thrust could be eliminated by smoothly tapering the backslip from its maximum rate to zero over a finite distance. In our models, we apply a smoothing function within the transition zones in order to minimize abrupt changes in backslip magnitude that could lead to stress singularities within the elastic half-space. Despite these considerations, the zone of positive $\Delta\sigma_c$ persists near the coast. Numerous studies correlating the distribution of aftershocks to the $\Delta\sigma_c$ resulting from a strong earthquake show concentrations of aftershocks within the regions of elevated $\Delta\sigma_c$ near the mainshock fault plane terminations, suggesting that the stress concentrations near fault tips do exert influence on the deformation fields of the material surrounding them (e.g., *King et al.*, 1994; *Toda et al.*, 1998; *Toda and Stein*, 2002; *Kilb et al.*, 2002; *Lin and Stein*, 2004). Furthermore, the positive $\Delta\sigma_c$ near the coast is coincident with the region of interseismic uplift, and so the positive $\Delta\sigma_c$ is consistent with the stresses induced along the outer surface of an upward-flexed body. *Riquelme et al.* (2003) demonstrated that Neogene uplift of the Coastal Cordillera relative to the Central Depression, just to its east, is accommodated by vertical motion on the Atacama Fault System, providing a link between the regions of uplift and normal faulting.

Bevis et al. (2001) and *Khazaradze and Klotz* (2003) interpreted differences between GPS-measured velocities and those modeled using elastic dislocations as representative of permanent strain not predicted by the purely elastic theory. In both cases, permanent deformation is inferred to take place in regions of the Andean backarc. Additionally, *Khazaradze and Klotz* (2003) calculate statistically significant east-west extension based on residual GPS velocities, defined as the difference between the actual velocities and those calculated in their preferred model, in the forearc between 29°S and 34°S, coinciding with N-S striking normal faulting observed between 30°S and 31°S (*Heinze*, 2003). We suggest that the interseismic stress field predicted by our elastic modeling is itself responsible for the permanent strain exhibited by forearc structures, as it is eventually manifested as permanent deformation through slip on upper plate faults (i.e., *Pollitz*, 2003; *Allmendinger et al.*, 2005, 2007). At present, GPS stations in the Central Andes are too coarsely spaced to place constraints on the abruptness of the slip gradient within the downdip transition zones. Future studies using interferometric radar, which provides a spatially-complete image of interseismic surface deformation, could potentially resolve this parameter. Our suggestion that the interseismic deformation drives forearc normal faulting implies that geological data can be used to complement geodetic data in defining the nature of interplate strain accumulation, assuming a genetic relationship between the earthquake cycle and forearc structural evolution.

5.7.2 Spatial implications

The $\Delta\sigma_c$ map (Figure 5.9) shows that modeling a change in the extent of interplate locking around the latitude of the Mejillones Peninsula predicts a stress field

consistent with distribution of faulting around Antofagasta. Similar correlations between the distribution of interplate coupling and permanent deformation exist elsewhere in the forearc. Near the city of Iquique, around 20.5°S, the 50 km Wadati-Benioff zone contour line (*Cahill and Isacks*, 1992) and zone of positive $\Delta\sigma_c$ trend offshore, consistent with the distribution of faults. South of Antofagasta, normal faults also project offshore following the trend of the downdip extent of the locked plate boundary (Figures 5.7, 5.9) and coincident zone of positive $\Delta\sigma_c$.

The Mejillones Peninsula itself lies entirely within a zone of negative $\Delta\sigma_c$, yet it features several examples of recent normal faulting (*Delouis et al.*, 1998; *González et al.*, 2003). We suggest several potential reasons for the discrepancy between the deformation fields. The peninsula is a first-order anomaly of northern Chile: it protrudes prominently from the otherwise linear coastline, is located at the same latitude as the Salar de Atacama, which interrupts the linear trend of Andean volcanoes along the arc, and is characterized by a positive gravity anomaly (Figure 5.8a). The peninsula has been recognized as a boundary between earthquake rupture segments on the plate boundary (*Delouis et al.*, 1997). An earthquake along the northernmost Chile segment of the margin in 1877 is interpreted to have terminated rupture at the peninsula (*Comte and Pardo*, 1991; *Delouis et al.*, 1997), while the 1995 Antofagasta earthquake initiated beneath the southern edge of the peninsula and propagated southward (*Delouis et al.*, 1997; *Ihmlé and Ruegg*, 1997; *Sobiesiak*, 2004). The physical properties that allow the Mejillones Peninsula to serve as a barrier to rupture may affect the nature of interseismic coupling beneath it. Postseismic afterslip following the 1995 earthquake occurs at a rate faster than plate convergence beneath the peninsula (e.g., *Chlieh et al.*, 2004; *Pritchard and Simons*, 2006), suggesting that the plate interface there may not be fully

locked (*Pritchard and Simons*, 2006). Abrupt, small-scale changes in the degree of interplate locking (not considered by our interseismic models) would introduce heterogeneity in the upper plate stress field that may encourage normal faulting observed on the peninsula.

Elevations on the west coast of the Mejillones Peninsula reach nearly 1000 m and lie 75 km from the 7000 m deep trench, resulting in a steep continental slope. *Wang and He* (1999) describe a gravitational trenchward "stretching" force brought about by the presence of forearc topography, and the magnitude of this force is positively correlated with the gradient of the continental slope. Bathymetric data reveal numerous slump faults on the continental slope; these and the faults onshore are attributed to gravitational trenchward extension (*von Huene and Ranero*, 2003; *von Huene et al.*, 2004; *Sallàres and Ranero*, 2005). Subduction erosion processes remove material from the upper plate at the subduction trench, allowing the continental slope to "spread" toward the trench (*von Huene and Ranero*, 2003; *von Huene et al.*, 2004; *Sallàres and Ranero*, 2005). The consequences of subduction erosion, including subsidence of the continental slope, development of a $\sim$1 km thick "subduction channel" on the plate interface, and incorporation of forearc material into arc magma, have thus far been measured on million year time scales (e.g., *von Huene and Ranero*, 2003; *Kay et al.*, 2005), yet its effects on decadal time scales are poorly understood. We consider the extension induced by gravity as a long-term, static effect that is modulated by stress changes related to the seismic cycle.

5.7.3 Conceptual models for Coulomb stress evolution

Delouis et al. (1998) suggest that subduction erosion processes place forearc in

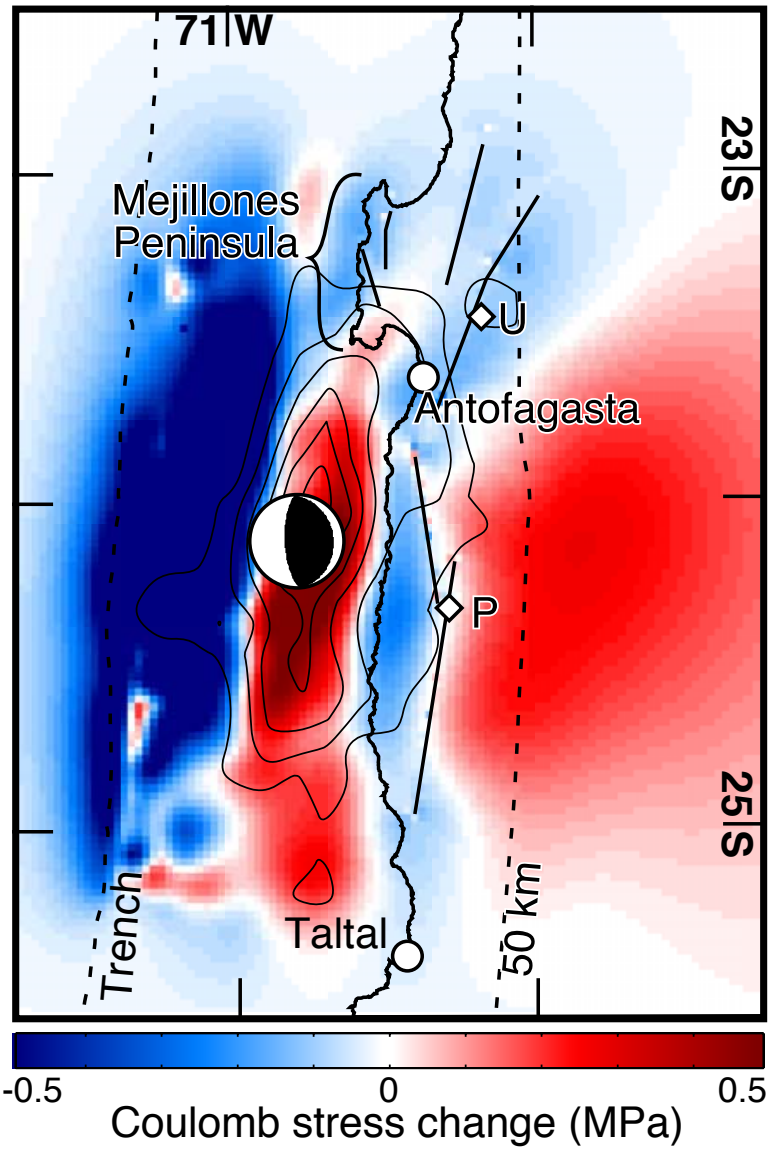

Figure 5.10: Preferred model of coseismic upper plate $\Delta\sigma_c$ induced by the 1995 M_w=8.1 Antofagasta earthquake (see Chapter 4 for more details). $\Delta\sigma_c$ is calculated using the slip distribution of *Pritchard et al.* (2006) and the same parameters as those used for Figure 5.9. Thin black lines show the surface projection of 1 m contours of coseismic slip on the subduction interface, bold black lines show the surface traces of prominent forearc faults, and black dashed lines show the positions of the trench and 50 km contour to the Wadati-Benioff zone.

Figure 5.11: Conceptual models of the state of Coulomb stress (σ_c) on upper plate faults induced by the seismic cycle. Here, positive σ_c refers to the stress encouraging normal failure on the upper plate faults, while negative σ_c favors reverse failure. Gray vertical lines are quasi-periodic and mark the occurrence of major subduction zone earthquakes. Interseismic $\Delta\sigma_c$ is shown as accumulating linearly with time and ignores the effects of postseismic deformation. σ_c^n refers to the critical value of σ_c at which the fault slips in a normal sense, σ_c^r denotes the value at which the fault slips in a reverse sense, and A represents a background or ambient level of stress favoring neither normal nor reverse failure. a. Simple model of σ_c evolution presented by *Delouis et al.* (1998). During the interseismic period (sloping lines), faults are brought further away from normal failure, while strong subduction earthquakes increase σ_c. b. Revised model of σ_c evolution induced by the seismic cycle, based on the simulations presented in this paper. During the interseismic period, faults are brought closer to normal failure. Depending on the location of a particular upper plate fault relative to the distribution of coseismic slip on the subduction interface, great earthquakes may either increase (1 and 4) or reduce (2 and 3) σ_c. c. Model illustrating the effect of the existing state of stress on the fault response to the seismic cycle. Because of the state of stress on the fault, different behaviors are possible, including normal fault rupture during the interseismic period of the subduction zone earthquake cycle, and reverse faulting driven by a subduction zone earthquake. See Section 5.7.3 for further discussion.

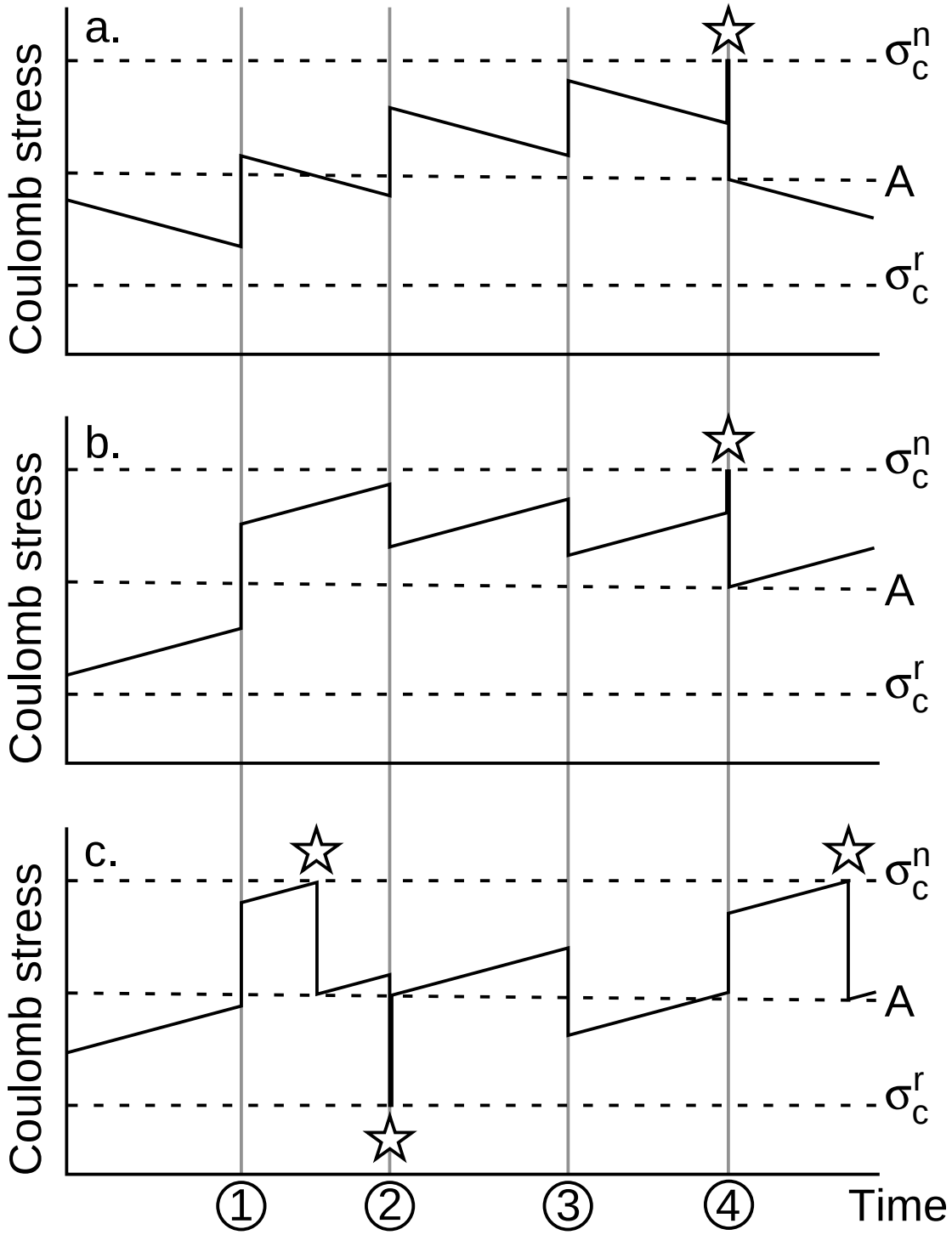

② Interplate earthquake

☆ Upper plate fault rupture

σ_c^n Upper plate fault strength (normal)

σ_c^r Upper plate fault strength (reverse)

A "Ambient" fault stress (favors neither sense of slip)

an extensional tectonic regime and the observed normal faulting occurs due to coseismic enhancement of this extension. *González et al.* (2003) agree, noting that the restriction of faulting to the Mejillones Peninsula and coastal regions is consistent with the location of maximum coseismic extension accompanying the 1995 Antofagasta earthquake. The models of interseismic deformation presented here complement these results, providing a mechanism for the extensional tectonic regime of *Delouis et al.* (1998), restricted to a narrow longitudinal zone encompassing the Coastal Cordillera. These models are also provide some quantification of the suggestion of *González et al.* (2003) that extensional faulting may result from upward flexure driven by plate convergence.

Based on the results of our inter- and coseismic simulations, we present three conceptual models for the evolution of the state of stress on upper plate faults in response to the subduction zone earthquake cycle in Figure 5.11. All models show the changes in stress during 5 interseismic periods separated by 4 quasi-periodic earthquakes, the occurrences of which are shown as vertical gray lines. The interseismic stress change is linear with time and is the same in all seismic cycles. Postseismic deformation is neglected in this model. The coseismic stress change magnitude is slightly different for each earthquake, reflecting spatial heterogeneity in the deformation induced by the event, which depends on the exact distribution of coseismic slip (Chapter 4). More importantly, the sign of the coseismic stress change can be either positive or negative, based on the location of the upper plate fault with respect to the rupture zone.

Figure 5.11a shows the model of *Delouis et al.* (1998). In this model, upper plate faults are brought away from normal faulting during the interseismic period. This reflects the larger-scale pattern of interseismic stress change and neglects the

narrow zone of positive $\Delta\sigma_c$ where faults are concentrated. The elastic rebound effect of strong subduction zone earthquakes induces positive stress change on upper plate faults, encouraging normal failure. Assuming that the coseismic increase and interseismic decrease in stress do not completely cancel each other, stress on upper plate faults accumulates over several seismic cycles. Eventually, a subduction zone earthquake increases the Coulomb failure stress on a fault to its critical level for normal faulting, σ_c^n. This slip reduces the magnitude of stress on the fault to a level favoring neither normal nor reverse failure (labeled "A"). On the scale of the orogen, interseismic strain is characterized by shortening in the direction of convergence, which would serve to decrease the likelihood of normal faulting (and indeed encourages thrust faulting in the Andean foreland). However, as we have shown in Figure 5.9, prominent forearc normal faults experience an increase in Coulomb stress as a result of interseismic convergence and either an increase or decrease in stress due to strong subduction earthquakes (Section 5.7.1).

A modified conceptual model for fault stress evolution throughout the seismic cycle incorporates these considerations. Figure 5.11b is meant to represent the stress evolution on a single forearc fault. The fault experiences an increase in stress, bringing it closer to normal failure, during the interseismic period of the subduction earthquake cycle. Earthquake 1 abruptly increases the stress on the fault and the subsequent interseismic period further pushes the fault towards normal faulting. Due to a different slip distribution, earthquake 2 decreases the magnitude of stress on the fault, as does earthquake 3, reducing the likelihood of normal failure. The slip distribution of earthquake 4, however, is such that stress on the fault is increased to σ_c^n. This normal failure of the fault reduces the stress magnitude to the background level A.

Figure 5.11c represents the evolution of stress on a fault other than that shown in Figure 5.11b and addresses the structural observations presented in Section 5.4. In this model, the fault is pushed towards normal failure during the first interseismic period and as a result of earthquake 1. During the subsequent interseismic period, stress again increases gradually, and because of the stress that had previously accumulated on the fault, normal failure occurs in the middle of the interseismic period. This drops the stress on the fault to the background magnitude A, and stress resumes accumulation due to interseismic flexure. Earthquake 2 induces a decrease in stress and, because the state of stress was near its background level due to the recent failure, causes a reduction of the stress on the fault to the level required for reverse faulting, σ_c^r. The act of reverse faulting brings the stress back to the background level, and the interseismic period then gradually increases the level of stress. Earthquakes 3 and 4 cause abrupt changes to the stress state, but it is not until the middle of the interseismic period following earthquake 4 that the conditions on the fault are again appropriate for failure. This model allows for two key phenomena: reverse fault rupture on forearc faults, and rupture of faults during the interseismic period of the subduction zone earthquake cycle.

If interseismic strain accumulation on the plate boundary, and therefore the forces transmitted to the upper plate, is heterogeneously distributed, the rate of interseismic stress change may vary with time. For a particular forearc fault, we expect the variability in rate of interseismic stress change to be less than the variability in the coseismic stress change. If the distribution of plate coupling is governed by gravity anomalies (Section 5.5.1.3, *Song and Simons*, 2003; *Wells et al.*, 2003; *Bürgmann et al.*, 2005), the distribution likely remains the same for long periods of time, as the composition and morphology of the forearc, both

of which long-lived characteristics relative to the span of a single seismic cycle, contribute to the gravity field.

5.7.4 Mechanical implications of new structural data

The AFS shows a long history of reactivation. *Scheuber and González* (1999) propose that the AFS originated ∼125 Ma, following three stages of deformation within the Jurassic-Early Cretaceous volcanic arc. Therefore, the development of the AFS proper likely involved reactivation of older weaknesses in the crust. We suggest that the damage sustained to the AFS throughout both the Mesozoic and Cenozoic plays an important role in dictating its response to the acting stress field. Our structural observations indicate that minor amounts of reverse faulting are superimposed on dominantly normal faults. Though the ages of fault slip of any sense are poorly constrained, morphological evidence indicates that both normal and reverse slip has occurred during the Quaternary along various parts of the AFS. At the reverse fault localities on both the Paposo and Salar del Carmen segments, stream incision patterns are used as indicators of reverse faulting, demonstrating that the reverse faulting occurred between the most recent and penultimate episodes of substantial fluvial downcutting. Our suggestion that the seismic cycle is the primary cause of both normal and reverse faulting implies that the two modes of faulting are contemporaneous; the "active" mode is dictated by the mechanical conditions of the fault zone as well as the sense of acting stress field.

The maximum magnitude of near-surface stress change induced by one 100–150 yr interseismic period (*Comte and Pardo*, 1991) or one strong subduction earthquake is on the order of 0.5 MPa — about 50 times smaller than the lithostatic

stress at even 1 km depth (25 MPa, given a crustal density of 2600 kg/m^3). For such low magnitude stresses to overcome the lithostatic conditions to drive fault slip, the absolute stress within the deforming part of the fault zones themselves must be very low. This in turn could imply that the fault zones are very weak, indicating a low coefficient of friction, elevated pore fluid pressure, and a reduced modulus of rigidity within the fault zone as compared to the surrounding rock (e.g., *Fialko et al.*, 2002, 2005). The concept that forearc fault zones are weak is consistent with the fact that they have sustained substantial damage by persistent faulting since ∼125 Ma. The Coulomb failure stresses σ_c^n and σ_c^r (defined in Section 5.7.3 and Figure 5.11) are thus likely to be low, allowing the small magnitude $\Delta\sigma_c$ induced by the seismic cycle to drive either reverse or normal faulting. *González et al.* (2006) suggest that at least three discrete episodes of fault slip since 424±151 ka have constructed a suite of alluvial terraces found along the Salar del Carmen segment of the AFS. In the extreme case where only three events have constructed the modern geometry, the mean repeat time is 141±50 ka. Incorporating the fault mechanics and recurrence interval into the model presented in Figure 5.11c involves reducing the slope of the interseismic $\Delta\sigma_c$ and the magnitude of the coseismic $\Delta\sigma_c$ relative to σ_c^n and σ_c^r. This serves to decrease the frequency of upper plate ruptures, from one rupture every few seismic cycles (i.e., several hundred years), as shown in Figure 5.11c, to one rupture every thousand seismic cycles (∼150 kyr). As noted in Section 5.4.1, the burial depth of fault slip impacts its surficial expression, thus the alluvial fan geometry described by *González et al.* (2006) may have been constructed at least in part by multiple episodes of buried slip.

5.8 Conclusions

Our elastic modeling predicts that convergence across the Andean plate boundary interface produces stress within a narrow longitudinal zone that is consistent with the normal faulting on north-south striking structures. The complicated interseismic stress field is mimicked by coseismic stress fields, which show a narrow zone along the coastline in which reverse faulting is encouraged on the observed faults, providing a mechanism for the opposite senses of slip that we observe. The elastic rebound model (*Reid*, 1910; *Savage*, 1983) suggests that all interseismic deformation is released by subduction zone earthquakes, but our field observations and modeling results suggest that some seismic cycle stress is "used" to drive the evolution of structures in the Coastal Cordillera. Seismic hazard analysis for northern Chile therefore requires consideration not only of the major plate boundary earthquake cycle, but also an intraplate cycle that may or may not coincide with the interplate seismic pattern; upper plate seismic fault slip may be triggered exclusively by subduction zone earthquakes, or it could take place during the interseismic period of the subduction cycle. The pervasive damage sustained by the region since the Mesozoic allows low magnitudes of stress to cause permanent strain, and the hyperarid climate of the Atacama Desert preserves evidence of this deformation over long periods of time.

BIBLIOGRAPHY

Allmendinger, R. W., T. E. Jordan, S. M. Kay, and B. L. Isacks (1997), The evolution of the Altiplano-Puna Plateau of the Central Andes, *Annual Review of Earth and Planetary Sciences*, *25*, 139–174.

Allmendinger, R. W., R. Smalley Jr., M. Bevis, H. Caprio, and B. Brooks (2005), Bending the Bolivian orocline in real time, *Geology*, *33*(11), 905–908, doi:10.1130/G21779.1.

Allmendinger, R. W., R. Reilinger, and J. Loveless (2007), Strain and rotation rate from GPS in Tibet, Anatolia, and the Altiplano, *Tectonics*, *26*, TC3013, doi:10.1029/2006TC002030.

Arabasz, W. J. (1971), Geological and geophysical studies of the Atacama fault zone, in northern Chile, PhD. thesis, California Institute of Technology, Pasadena, CA.

Armijo, R., and R. Thiele (1990), Active faulting in northern Chile: Ramp stacking and lateral decoupling along a subduction plate boundary?, *Earth and Planetary Science Letters*, *98*(1), 40–61.

Bevis, M., E. Kendrick, R. Smalley Jr., B. Brooks, R. W. Allmendinger, and B. L. Isacks (2001), On the strength of interplate coupling and the rate of back arc convergence in the central Andes: An analysis of the interseismic velocity field, *Geochemistry, Geophysics, Geosystems*, *2*, doi:10.1029/2001GC000198.

Brooks, B. A., M. Bevis, R. Smalley Jr., E. Kendrick, R. Manceda, E. Lauria, R. Maturana, and M. Araujo (2003), Crustal motion in the Southern Andes (26°—36°S): Do the Andes behave like a microplate?, *Geochemistry, Geophysics, Geosystems*, *4*(10), 1085, doi:10.1029/2003GC000505.

Bürgmann, R., M. G. Kogan, G. M. Steblov, G. Hilley, V. E. Levin, and E. Apel (2005), Interseismic coupling and asperity distribution along the Kamchatka subduction zone, *Journal of Geophysical Research*, *110*, B07405, doi:10.1029/2005JB003648.

Cahill, T. A., and B. L. Isacks (1992), Seismicity and shape of the subducted Nazca Plate, *Journal of Geophysical Research*, *97*(B12), 17,503–17,529.

Chlieh, M., J. B. de Chabalier, R. J. C., R. Armijo, R. Dmowska, J. Campos, and K. Feigl (2004), Crustal deformation and fault slip during the seismic cycle in the North Chile subduction zone, from GPS and InSAR observations, *Geophysical Journal International*, *158*(2), 695–711, doi:10.1111-j.1365-246X.2004.02326.x.

Comte, D., and M. Pardo (1991), Reappraisal of great historical earthquakes in the northern Chile and southern Peru seismic gaps, *Natural Hazards*, *4*(1), 23–44, doi:10.1007/BF00126557.

Comte, D., M. Pardo, L. Dorbath, C. Dorbath, H. Haessler, L. Rivera, A. Cisternas, and L. Ponce (1994), Determination of seismogenic interplate contact zone and crustal seismicity around Antofagasta, northern Chile using local data, *Geophysical Journal International*, *116*(3), 553–561, doi:10.1111/j.1365-246X.1994.tb03279.x.

Delouis, B., A. Cisternas, L. Dorbath, L. Rivera, and E. Kausel (1996), The Andean subduction zone between 22 and 25°S (northern Chile): Precise geometry and state of stress, *Tectonophysics*, *259*, 81–100.

Delouis, B., T. Monfret, L. Dorbath, M. Pardo, L. Rivera, D. Comte, H. Haessler, J. P. Caminade, L. Ponce, E. Kausel, and A. Cisternas (1997), The M_W = 8.0 Antofagasta (Northern Chile) earthquake of 30 July 1995: A precursor to the end of the large 1877 gap, *Bulletin of the Seismological Society of America*, *87*(2), 427–445.

Delouis, B., H. Philip, L. Dorbath, and A. Cisternas (1998), Recent crustal deformation in the Antofagasta region (northern Chile) and the subduction process, *Geophysical Journal International*, *132*, 302–338, doi:10.1046/j.1365-246x.1998.00439.x.

Fialko, Y., D. Sandwell, D. Agnew, M. Simons, P. Shearer, and B. Minster (2002), Deformation on nearby faults induced by the 1999 Hector Mine earthquake, *Science*, *297*(5588), 1858–1862, doi:10.1126/science.1074671.

Fialko, Y., D. Sandwell, M. Simons, and P. A. Rosen (2005), Three-dimensional deformation caused by the Bam, Iran, earthquake and the origin of shallow slip deficit, *Nature*, *435*(7040), 295–299, doi:10.1038/nature03425.

Flück, P., R. D. Hyndman, and K. Wang (1997), Three-dimensional dislocation model for great earthquakes of the Cascadia subduction zone, *Journal of Geophysical Research*, *102*(B9), 20,539–20,550.

González, G., and D. Carrizo (2003), Segmentación, cinemática y chronología relativa de la deformación tardía de la Falla Salar del Carmen, Sistema de Fallas Atacama, (23°40′S), norte de Chile, *Revista Geológica de Chile*, *30*(2), 223–244.

González, G., J. Cembrano, D. Carrizo, A. Macci, and H. Schneider (2003), The link between forearc tectonics and Pliocene-Quaternary deformation of the Coastal Cordillera, northern Chile, *Journal of South American Earth Sciences*, *16*, 321–342, doi:10.1016/S0895-9811(03)00100-7.

González, G., T. Dunai, D. Carrizo, and R. Allmendinger (2006), Young displacements on the Atacama Fault System, northern Chile from field observations and cosmogenic ^{21}Ne concentrations, *Tectonics*, *25*, TC3006, doi:10.1029/2005TC001846.

Hartley, A. J., and G. Chong (2002), Late Pliocene age for the Atacama Desert: Implications for the desertification of western South America, *Geology*, *30*(1), 43–46, doi:10.1130/0091-7613(2002)030<0043:LPAFTA>2.0.CO;2.

Heinze, B. (2003), Active intraplate faulting in the forearc of north central Chile (30°–31°S): Implications from neotectonic field studies, GPS data, and elastic dislocation modeling, PhD. thesis, Freie Universität Berlin, Berlin, Germany.

Ihmlé, P. F., and J. Ruegg (1997), Source tomography by simulated annealing using broad-band surface waves and geodetic data: Application to the $M_w = 8.1$ Chile 1995 event, *Geophysical Journal International*, *131*, 146–158.

Isacks, B. L. (1988), Uplift of the Central Andean Plateau and bending of the Bolivian Orocline, *Journal of Geophysical Research*, *93*(4), 3211–3231.

Kay, S. M., E. Godoy, and A. Kurtz (2005), Episodic arc migration, crustal thickening, subduction erosion, and magmatism in the south-central Andes, *Bulletin of the Geological Society of America*, *117*(1-2), 67–88, doi:10.1130/B25431.1.

Kelleher, J. A. (1972), Rupture zones of large South American earthquakes and some predictions, *Journal of Geophysical Research*, *77*(11), 2087–2103.

Kendrick, E., M. Bevis, R. Smalley Jr., and B. Brooks (2001), An integrated crustal velocity field for the Central Andes, *Geochemistry, Geophysics, Geosystems*, *2*, doi:10.1029/2001GC000191.

Khazaradze, G., and J. Klotz (2003), Short- and long-term effects of GPS measured crustal deformation rates along the south central Andes, *Journal of Geophysical Research*, *108*(B6), 2289, doi:10.1029/2002JB001879.

Kilb, D., J. Gomberg, and P. Bodin (2002), Aftershock triggering by complete Coulomb stress changes, *Journal Of Geophysical Research*, *107*(B4), 2060, doi: 10.1029/2001JB000202.

King, G. C., R. S. Stein, and J. Lin (1994), Static stress changes and the triggering of earthquakes, *Bulletin of the Seismological Society of America*, *84*(3), 935–953.

Klotz, J., D. Angermann, G. W. Michel, R. Porth, C. Reigber, J. Reinking, J. Viramonte, R. Perdomo, V. H. Rios, S. Barrientos, R. Barriga, and O. Cifuentes (1999), GPS-derived deformation of the Central Andes including the 1995 Antofagasta $M_w = 8.0$ earthquake, *Pure and Applied Geophysics*, *154*, 709–730, doi:10.1007/s000240050249.

Klotz, J., G. Khazaradze, D. Angermann, C. Reigber, R. Perdomo, and O. Cifuentes (2001), Earthquake cycle dominates contemporary crustal deformation in Central and Southern Andes, *Earth and Planetary Science Letters*, *193*(3-4), 437–446, doi:10.1016/S0012-821X(01)00532-5.

Lay, T., and S. Y. Schwartz (2004), "Coupling" semantics and science in earthquake research: Comment, *EOS Transactions, AGU*, *85*(36), 339–340.

Lin, J., and R. S. Stein (2004), Stress triggering in thrust and subduction earthquakes and stress interaction between the southern San Andreas and nearby thrust and strike-slip faults, *Journal of Geophysical Research*, *109*(B2), B02303, doi:10.1029/2003JB002607.

Loveless, J. P., G. D. Hoke, R. W. Allmendinger, G. González, B. L. Isacks, and D. A. Carrizo (2005), Pervasive cracking of the northern Chilean Coastal Cordillera: New evidence for forearc extension, *Geology*, *33*(12), 973–976, doi:10.1130/G22004.1.

Naranjo, J. A. (1987), Interpretación de la actividad cenozoica superior a lo largo de la zona de Falla de Atacama, norte de Chile, *Revista Geológica de Chile*, *31*, 43–55.

Niemeyer, H., G. González, and E. Martinez-de los Ríos (1996), Evolución tectónica cenozoica del margen continental activo de Antofagasta, norte de Chile, *Revista Geológica de Chile*, *23*(2), 165–186.

Norabuena, E., L. Leffler-Griffin, A. Mao, T. Dixon, S. Stein, I. S. Sacks, L. Ocola, and M. Ellis (1998), Space geodetic observations of Nazca-South America convergence across the Central Andes, *Science*, *279*(5349), 358–362.

Okada, Y. (1985), Surface deformation due to shear and tensile faults in a half-space, *Bulletin of the Seismological Society of America*, *75*(4), 1135–1154.

Okada, Y. (1992), Internal deformation due to shear and tensile faults in a half-space, *Bulletin of the Seismological Society of America*, *82*(2), 1018–1040.

Oleskevich, D. A., R. D. Hyndman, and K. Wang (1999), The updip and downdip limits to great subduction earthquakes: Thermal and structural models of Cascadia, south Alaska, SW Japan, and Chile, *Journal of Geophysical Research*, *104*(B7), 14,965–14,991, doi:10.1029/1999JB900060.

Pacheco, J. F., L. R. Sykes, and C. H. Scholz (1993), Nature of seismic coupling along simple plate boundaries of the subduction type, *Journal of Geophysical Research*, *98*, 14,133–14,159.

Pollitz, F. F. (2003), The relationship between the instantaneous velocity field and the rate of moment release in the lithosphere, *Geophysical Journal International*, *153*, 595–608, doi:10.1046/j.1365-246X.2003.01924.x.

Pritchard, M. E., and M. Simons (2006), An aseismic slip pulse in northern Chile and along-strike variations in seismogenic behavior, *Journal of Geophysical Research*, *111*, b08405, doi:10.1029/2006JB004258.

Pritchard, M. E., M. Simons, P. A. Rosen, S. Hensley, and F. H. Webb (2002), Coseismic slip from the 1995 July 30 $M_w = 8.1$ Antofagasta, Chile earthquake as constrained by InSAR and GPS observations, *Geophysical Journal International*, *150*, 362–376, doi:10.1046/j.1365-246X.2002.01661.x.

Pritchard, M. E., C. Ji, and M. Simons (2006), Distribution of slip from 11 $M_w > 6$ earthquakes in the northern Chile subduction zone, *Journal of Geophysical Research*, *111*, B10302, doi:10.1029/2005JB004013.

Rech, J. A., J. Quade, and W. S. Hart (2003), Isotopic evidence for the source of Ca and S in soil gypsum, anhydrite and calcite in the Atacama Desert, Chile, *Geochimica et Cosmochimica Acta*, *67*(4), 575–586, doi:10.1016/S0016-7037(02)01175-4.

Rech, J. A., B. S. Currie, G. Michalski, and A. M. Cowan (2006), Neogene climate change and uplift in the Atacama Desert, Chile, *Geology*, *34*(9), 761–764, doi:10.1130/G22444.1.

Reid, H. F. (1910), The mechanics of the earthquake, in *The California earthquake of April 18, 1906*, vol. 2, p. 192, Carnegie Institute of Washington, Washington, D.C.

Riquelme, R., J. Martinod, G. Herail, J. Darrozes, and R. Charrier (2003), A geomorphological approach to determining the Neogene to Recent tectonic deformation in the Coastal Cordillera of northern Chile (Atacama), *Tectonophysics*, *361*(3-4), 255–275, doi:10.1016/S0040-1951(02)00649-2.

Ruegg, J., J. Campos, R. Armijo, S. Barrientos, P. Briole, R. Thiele, M. Arancibia, J. Cañuta, T. Duquesnoy, M. Chang, D. Lazo, H. Lyon-Caen, L. Ortlieb, J. Rossignol, and L. Serruier (1996), The $M_w = 8.1$ Antofagasta (North Chile) Earthquake of July 30, 1995: First results from teleseismic and geodetic data, *Geophysical Research Letters*, *23*(9), 917–920.

Sallàres, V., and C. R. Ranero (2005), Structure and tectonics of the erosional convergent margin off Antofagasta, north Chile (23°30′S), *Journal of Geophysical Research*, *110*, B06101, doi:10.1029/2004JB003418.

Sandwell, D. T., and W. H. F. Smith (1997), Marine gravity anomaly from Geosat and ERS-1 satellite altimetry, *Journal of Geophysical Research*, *102*(B5), 10,039–10,054, doi:10.1029/96JB03223.

Savage, J. C. (1983), A dislocation model of strain accumulation and release at a subduction zone, *Journal of Geophysical Research*, *88*(B6), 4984–4996.

Scheuber, E., and P. A. M. Andriessen (1990), The kinematic and geodynamic significance of the Atacama fault zone, northern Chile, *Journal of Structural Geology*, *12*(2), 243–257.

Scheuber, E., and G. González (1999), Tectonics of the Jurassic-Early Cretaceous magmatic arc of the North Chilean Coastal Cordillera (22°–26°S): A story of crustal deformation along a convergent plate boundary, *Tectonics*, *18*(5), 895–910.

Sobiesiak, M. M. (2004), Fault Plane Structure of the 1995 Antofagasta Earthquake (Chile) Derived From Local Seismological Parameters, PhD. thesis, Universität Potsdam, Potsdam, Germany.

Song, T.-R. A., and M. Simons (2003), Large trench-parallel gravity variations predict seismogenic behavior in subduction zones, *Science*, *301*(5633), 630–633, doi:10.1126/science.1085557.

Thomas, A. L. (1993), Poly3D: A three-dimensional, polygonal element, displacement discontinuity boundary element computer program with applications to fractures, faults, and cavities in the Earth's crust, M.S. thesis, Stanford University, Stanford, CA.

Tichelaar, B. W., and L. J. Ruff (1991), Seismic coupling along the Chilean subduction zone, *Journal of Geophysical Research*, *96*(B7), 11,997–12,022.

Toda, S., and R. S. Stein (2002), Response of the San Andreas fault to the 1983 Coalinga-Nunez earthquakes: An application of interaction-based probabilities for Parkfield, *Journal of Geophysical Research*, *107*, 2126, doi:10.1029/2001JB000172.

Toda, S., R. S. Stein, P. A. Reasenberg, J. H. Dieterich, and A. Yoshida (1998), Stress transferred by the 1995 $M_w = 6.9$ Kobe, Japan shock: Effect on aftershocks and future earthquake probabilities, *Journal of Geophysical Research*, *103*(B10), 24,543–24,565.

von Huene, R., and C. R. Ranero (2003), Subduction erosion and basal friction along the sediment-starved convergent margin off Antofagasta, Chile, *Journal of Geophysical Research*, *108*(B2), 2079, doi:10.1029/2001JB001569.

von Huene, R., W. Weinrebe, and F. Heeren (1999), Subduction erosion along the North Chile margin, *Journal of Geodynamics*, *27*, 345–358, doi:10.1016/S0264-3707(98)00002-7.

von Huene, R., C. R. Ranero, and P. Vannucchi (2004), Generic model of subduction erosion, *Geology*, *32*(10), 913–916, doi:10.1130/G20563.1.

Wang, K., and T. Dixon (2004a), "Coupling" semantics and science in earthquake research, *EOS Transactions, AGU*, *85*(18), 180–181.

Wang, K., and T. Dixon (2004b), "Coupling" semantics and science in earthquake research: Reply, *EOS Transactions, AGU*, *85*(36), 340.

Wang, K., and J. He (1999), Mechanics of low-stress forearcs: Nankai and Cascadia, *Journal of Geophysical Research*, *104*(B7), 15,191–15,205.

Wang, K., R. Wells, S. Mazzotti, R. D. Hyndman, and T. Sagiya (2003), A revised dislocation model of interseismic deformation of the Cascadia subduction zone, *Journal of Geophysical Research*, *108*(B1), 2026, doi:10.1029/2001JB001227.

Wells, R. E., R. J. Blakely, Y. Sugiyama, D. W. Scholl, and P. A. Dinterman (2003), Basin-centered asperities in great subduction zone earthquakes: A link between slip, subsidence, and subduction erosion?, *Journal of Geophysical Research*, *108*(B10), 2507, doi:10.1029/2002JB002072.

APPENDIX A

ADDITIONAL FIELD OBSERVATIONS OF THE SALAR GRANDE AND ANTOFAGASTA REGIONS

A.1 Introduction

This appendix contains additional observations made during my June–July 2003, August 2004, March 2006, and August 2006 field seasons. These notes provide additional descriptions of neotectonic structures in several locations of the northern Chilean forearc, supporting the conclusions of the chapters of this thesis. The field observations are divided by region, with the locations identified on Figure A.1.

A.2 Salar Grande region

In addition to the field observations presented in Chapter 2, there are several other localities in the Salar Grande region that exhibit important characteristics of the surface cracks in the region.

A.2.1 Quebrada Pica

Within the region of incised topography around the Quebrada Pica ("QP" on Figure A.1), there are several exposures of bedrock joint planes in Mesozoic granodiorite. Measurement of joint plane orientations and comparison to the strikes of surface cracks in the surrounding region indicates a relationship between planes of weakness in the bedrock and the cracks that are preserved at the surface. The distributions of joint plane and surface cracks strikes are similar (Figure A.2), suggesting that the multiple sets of joints existing in the bedrock have been reactivated by neotectonic stress, propagating to the surface to form cracks.

Figure A.1: Regional topography of the northern Chilean forearc, showing the field sites discussed in this chapter. The black boxes outline the Salar Grande (a, Section A.2) and Antofagasta (b, Section A.3) regions. Specific field sites are labeled as (Salar Grande region): QP — Quebrada Pica (Section A.2.1), AT — Alto del Toro (Section A.2.2); (Antofagasta region): MF — Mititus Fault (Section A.3.1), QF — Quebrada Ordóñez fault (Section A.3.2), SCF — northern Salar del Carmen fault (Section A.3.3), NPF — northern Paposo fault (Section A.3.4), MB — Mantos Blancos cracks (Section A.3.5).

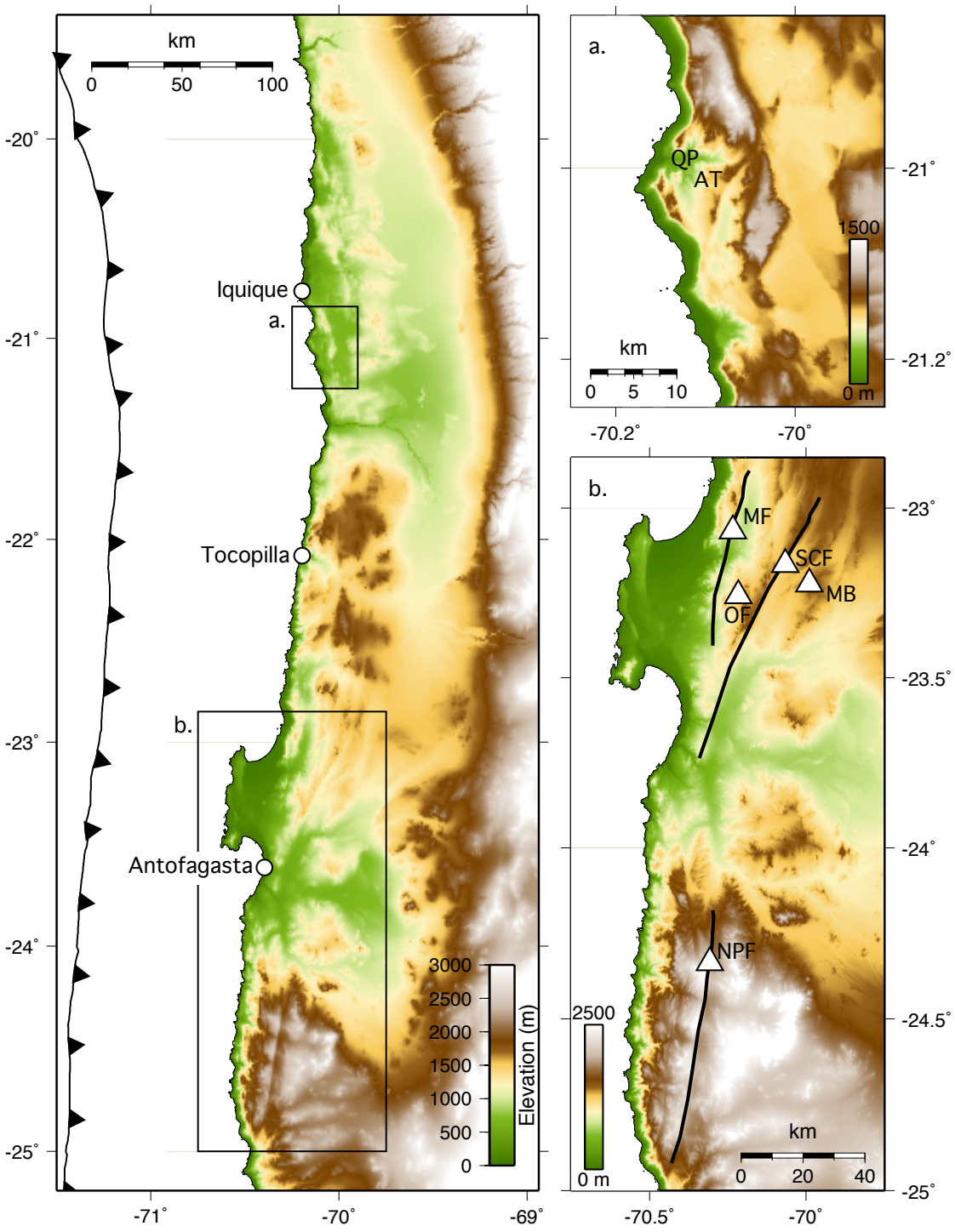
km
0
50
100
-20˚
-21˚
-22˚
-23˚
-24˚
-25˚
Iquique
a.
Tocopilla
b.
Antofagasta
3000
2500
2000
1500
1000
500
0
Elevation (m)
-71˚
-70˚
-69˚
a.
QP
AT
1500
0 m
km
0
5
10
-70.2˚
-70˚
-21˚
-21.2˚
b.
MF
SCF
MB
OF
NPF
2500
0 m
km
0
20
40
-70.5˚
-70˚
-23˚
-23.5˚
-24˚
-24.5˚
-25˚

A.2.2 South of Alto del Toro

South of the Quebrada de Pica and Alto del Toro ("AT" on Figure A.1, detailed image in Figure A.3) is a low-relief surface cut by NNW-striking en echelon cracks (arrow labeled "d" in Figure A.3). The bowl-shaped hill sides comprising the northern limit of this surface, as well as the flat-topped summits of these slopes, are affected by numerous hybrid cracks showing evidence of both opening and vertical separation of ∼1 m. Some of these cracks show an apparent genetic relationship to topography; cracks striking parallel to drainages (e.g., Figure A.3a), for example, may result from gravity-driven down slope slumping of gypsum-indurated regolith. Other cracks parallel topographic contours, striking parallel to the long axes of ridges separated by drainages (Figure A.3b). However, there is also cracking across relatively flat topography (Figure A.3c, d), suggesting that gravitational stresses are not the sole driver of crack evolution.

A.3 Antofagasta region

I surveyed several sites in the Antofagasta region in March 2006, accompanied by Holly Caprio, in order to find additional examples of the minor amounts of reverse motion superposed on otherwise normal fault, first observed by Rick Allmendinger and Gabriel González in the fall of 2005. In doing so, we visited several faults but found no further examples of this style of reactivation. Nonetheless, the Fortuna/Mititus and Quebrada Ordóñez faults featured several notable characteristics, which I describe in Sections A.3.1 and A.3.2. Additional detailed observations of reverse fault reactivation of the northern Salar del Carmen fault (Section A.3.3) and the northern Paposo fault (Section A.3.3) are also presented.

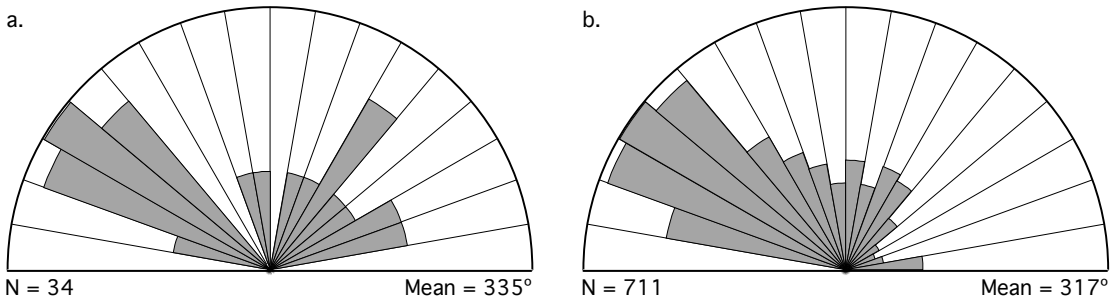

Figure A.2: Rose diagrams showing the strike distributions of joint planes measured in the field (A) and surface cracks measured in IKONOS imagery (B) in the rugged topography of the Quebrada Pica region. The similarity between the two populations suggests that deep-seated bedrock weaknesses are exploited by neotectonic stress to create the cracks evident at the surface.

A.3.1 Fortuna/Mititus fault

The Fortuna (*Delouis et al.*, 1998) or Mititus (G. González, personal communication, 2006) fault is located due east of the northern end of the Mejillones Peninsula (Figure A.1). At its southern end is an exposure of Miocene gravels in normal fault contact with Mesozoic basement (Figure A.4). Continuing north of this outcrop, the fault is expressed as a mountain-front scarp. I interpret the mountain front itself to have been constructed by multiple episodes of slip on a moderately to steeply east dipping normal fault. At the toe of the mountain front is a $\sim$2 m high (Figure A.5) with a 1 m free face and a relatively sharp profile relative to the smooth mountain front, suggesting that the most recent fault activity was localized on a splay fault cutting the hangingwall of the principal range-bounding structure. The footwall of this scarp is much more substantially incised than is the footwall, demonstrating further the normal faulting nature of the structure.

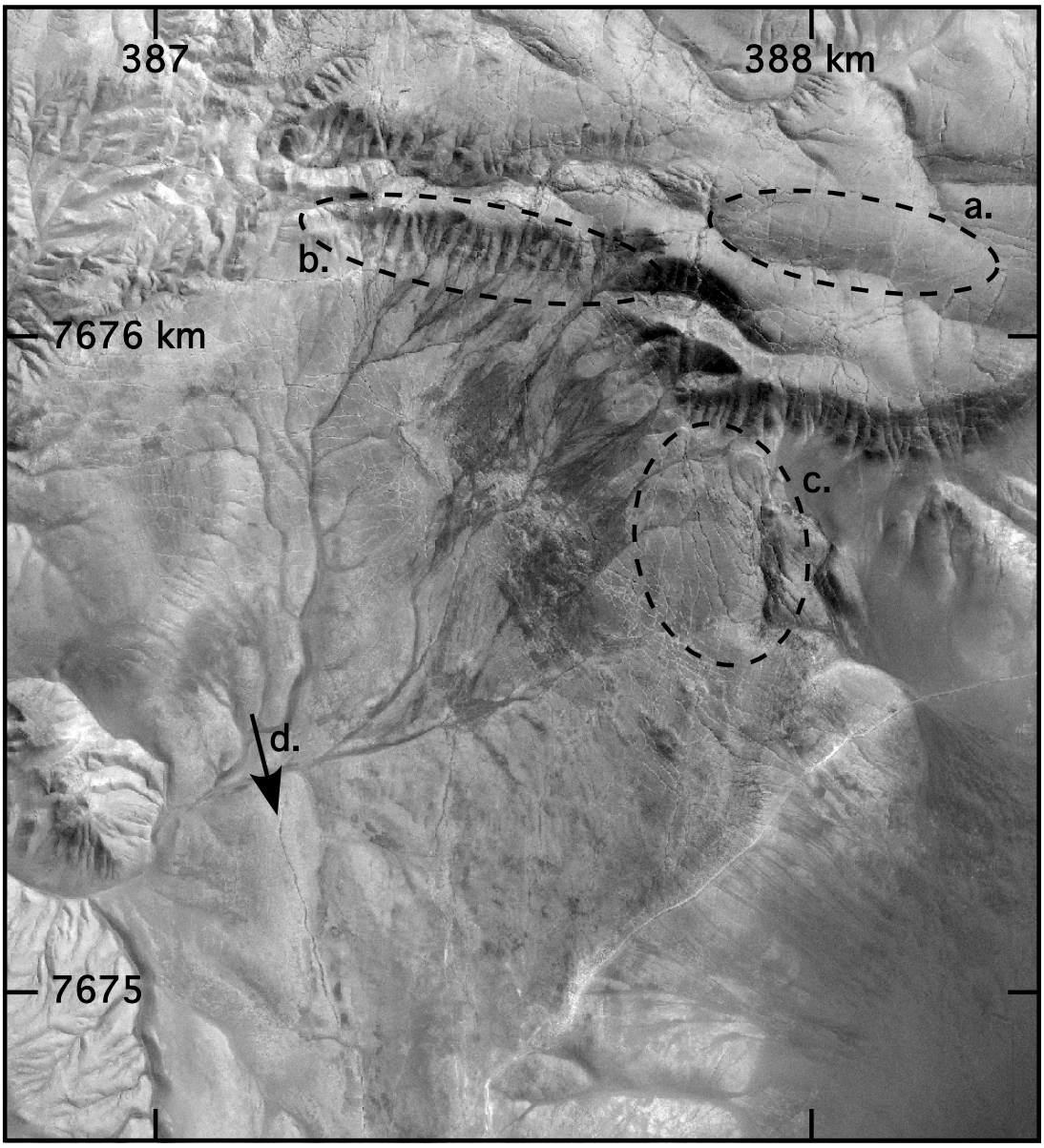

Figure A.3: IKONOS image of the Alto del Toro region, showing cracks affecting various topographic features. Some cracks are parallel to the trace of drainages (dashed oval A), others cut perpendicular to the long-axis of hillside ridges (B), which are separated by narrow drainages, and others still cut across relatively flat topography, such as those outlined in dashed oval C and the prominent, solitary en echelon crack identified by arrow D.

Figure A.4: Field photo showing the normal fault relationship between Mesozoic bedrock (west) and presumably Miocene gravels (east).

Figure A.5: Field photo showing the Mititus fault scarp near its southern extent. The larger hillside is interpreted to represent a smooth, cumulative scarp constructed from many episodes of east-side-down normal faulting, while the smaller, fresher scarp at the toe of the range, outlined by the dashed white line, represents more recent normal faulting.

A.3.2 Quebrada Ordóñez fault

East of the Mititus fault is the Quebrada Ordóñez fault (Figure A.1), a prominent scarp marked by a dramatic change in channel incision style (Figure A.6). From the fault trace westward, west-flowing drainages carve deep canyons with the sharpest incision localized in the immediate vicinity of the scarp (Figure A.6). Local drainages on the scarp itself reveal a normal fault relationship similar to that seen at the Mititus fault, with Miocene gravels in the hangingwall in fault contact with footwall Mesozoic bedrock (Figure A.7). The fault dips steeply to the east, and the normal faulting seen at outcrop scale is expressed at a larger scale by the

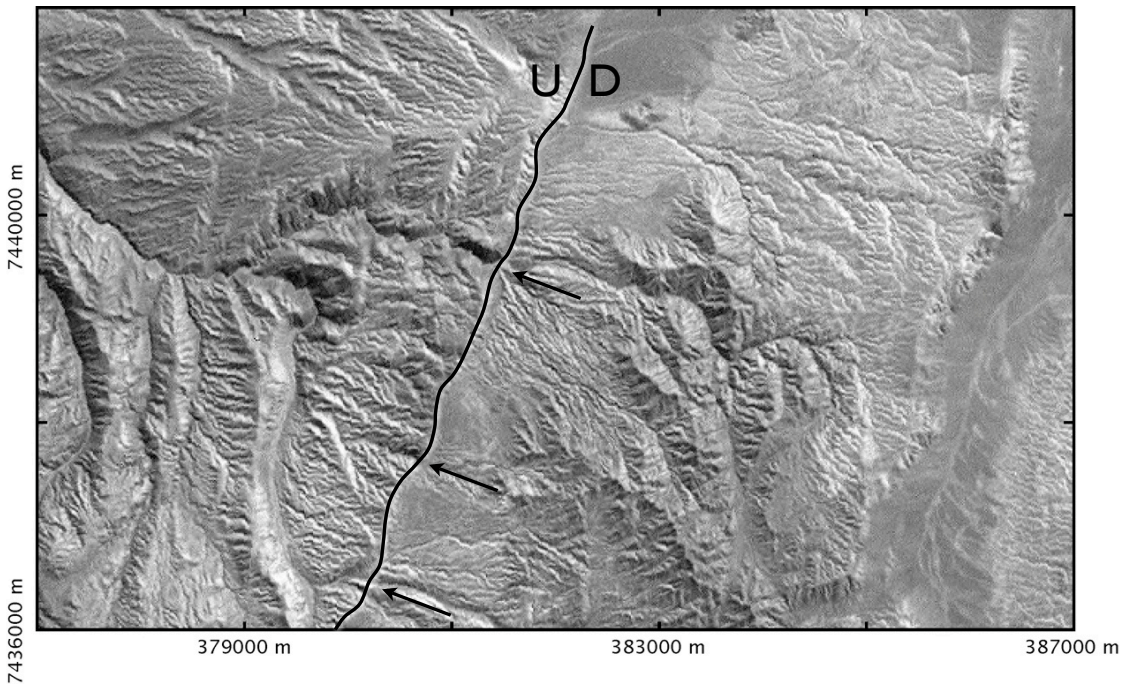

Figure A.6: Thematic Mapper image of the Quebrada Ordóñez fault. Westward drainages show a dramatic change in incision style at the fault trace, indicating uplift of the western block relative to the eastern block. This style of faulting is confirmed by the fault exposure seen in Figure A.7.

geomorphology, as down-dropping of the eastern block has required drainages to incise the western block in order to continue their westward path. In the field, it is apparent that both the hangingwall and footwall of the fault are covered uniformly by a cap of gypsum-indurated sediment (Figure A.7). This indicates that the fault has not experienced recent reactivation.

A.3.3 Northern Salar del Carmen fault

Using 0.6 m resolution imagery from the QuickBird satellite as a basemap (Figure 5.3), we made several observations of minor reverse reactivation on the northern extent of the Salar del Carmen fault (Figure A.1). As mentioned in Section 5.4.1,

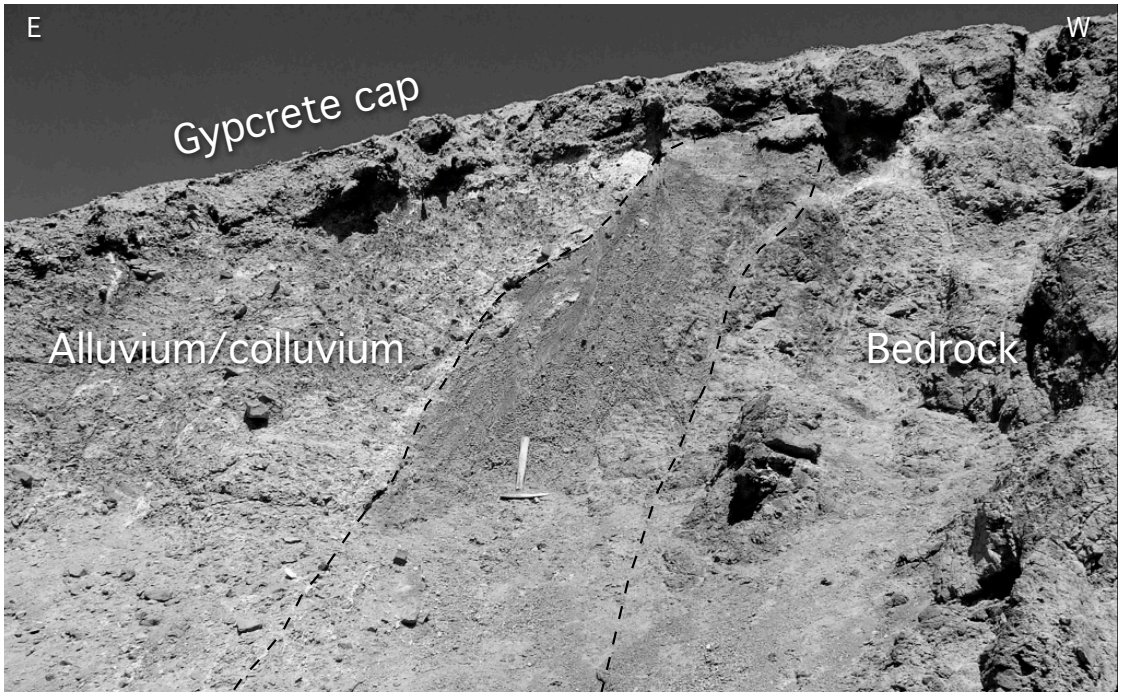

Figure A.7: Field photo showing the normal fault relationship between Mesozoic bedrock (west) and presumably Mio-Pliocene gravels (east). The fault zone is outlined by the black dashed line. The fact that both the hangingwall and footwall are uniformly blanketed by a cap of gypsum-indurated sediment indicates a relatively old age of the most recent episode of faulting. The fault relationship confirms the geomorphological signature of the fault seen in Figure A.6.

this part of the Salar del Carmen fault features an example of minor reverse motion on an otherwise normal fault. The fault scarp trends NE and its morphology suggests a moderate to steep east dip.

Canyons that crosscut the scarp provide opportunity to observe several key characteristics of the reverse fault reactivation. The fundamental observation — the upthrust basement wedge of the hangingwall — is exposed is several canyons, most notably that shown in Figure 5.4. Such exposures also establish the connection between the reverse faulting and a minor change in slope of the scarp (the "topographic bench"), which is marked by the accumulation of material darker

than that covering other parts of the hillside. The spatial coincidence of the bench and fault allows us to use its trace along the scarp to map the position of the underlying fault, which is particularly important in canyons that do not expose the reverse fault relationship. In general, the bench is narrower and more abrupt near the canyons where the fault is exposed and smoother and less distinct close to those drainages where the fault remains hidden. Based on this observation, we can not only use the location of the bench to trace the fault, but also the characteristics of the bench to estimate the relative burial depth of the fault tipline at any given location along the fault. Besides the break in slope represented by the topographic bench, the morphology of the drainages themselves provide information about the relative uplift of the lower part of the slope. In general, drainages are narrower and more slot-like below the topographic bench than above it, indicating enhanced incision of the lower slopes, which would result from uplift.

Several details of the reverse faulting are revealed in the canyon exposures. First, the gypcrete regolith cap that blankets the entire fault scarp surface is distinctly warped by the upthrust basement wedge (Figure 5.4a, inset). Second, the lithologic relationships that are seen reveal the relationship between the fault responsible for the upthrusting of the basement wedge with the primary normal fault that has constructed the overall scarp. The composition of the channel bed changes, from downstream to upstream, from bedrock to gypsum-indurated gravel and back to bedrock. The contact between the downstream bedrock and the intervening regolith coincides with the location of the reverse fault and topographic bench. The contact between the regolith and the upstream bedrock is not marked by a change in the topography and represents a stratigraphic contact. These lithologic relationships suggest that the reverse faulting takes place on a splay

fault located wholly within the footwall block of the larger normal fault. If reverse motion occurred on the main fault, much more offset than is observed would be required to thrust a basement block the surface; the reverse faulting would have to "erase" all of the accumulated normal motion. It is also possible that the reverse fault splay is contained within the hangingwall block of the larger normal fault, and the sediment component of the observed bedrock-sediment-bedrock pattern of channel bed composition represents a colluvial wedge generated during episodes of older normal faulting. This geometry seems less likely than the fault located within the footwall, as the intervening stretch of channel bed composed of sediment is shorter than the expected width of the colluvial wedge.

In some of the crosscutting channels, no bedrock wedge is exposed at the level of the topographic bench. Instead, the composition of the channel bed changes from uniformly sediment downstream of the bench to bedrock upstream. Furthermore, in these cases, the lithologic transition does not everywhere coincide with the location of the bench, but upstream of it. The fact that bedrock is not exposed within the channel at the location of the reverse fault suggests 1) reverse motion has been limited, such that only the the gypsum-indurated regolith is uplifted, 2) the location of reverse faulting is buried more deeply than in other canyons, or 3) reverse motion is taking place on a different fault splay, which may be located such that it uplifts a portion of the colluvial wedge constructed by primary normal faulting, rather than a slice of bedrock.

Figure A.8 shows an interpretation of the sequence of faulting events that have led to the present morphology of the northern Salar del Carmen segment. Like many segments of the Atacama Fault System, the Salar del Carmen segment is interpreted to have originated as a strike-slip fault in the Mesozoic (e.g., *Scheuber and*

Andriessen, 1990). Figure A.8a shows the first stage of neotectonic reactivation as a normal fault. Subsequent degradation of the scarp smooths the scarp profile and deposits a colluvial wedge at its base (Figure A.8b). The ongoing process of regolith development, here represented as a single step (Figure A.8c), blankets both the bedrock and colluvial wedge surfaces. A splay fault, or a plane of weakness within the fault zone (Figure A.8d) is constrained to lie either within the footwall or the hangingwall of the master normal fault, based on the channel-bottom lithologic relationships described above. When subject to fault-normal compression, the splay experiences reverse slip (Figure A.8e, f), creating the topographic bench at the surface above the upthrust basement wedge that is exposed within drainages that crosscut the scarp (Figure A.8e, inset). This schematic evolution oversimplifies the true evolution of the fault scarp. Scarp degradation and regolith development are ongoing processes rather than discrete steps as shown in Figure A.8. Similarly, episodes of both normal and reverse motion occur repeatedly to affect the morphology of the scarp, rather than in single "pulses" as shown.

A.3.4 Northern Paposo fault

A similar morphology to that seen at the northern Salar del Carmen segment is observed along a stretch of the northern part of the Paposo fault ("NPF" on Figure A.1, Section 5.4.2). Channels in this locality are not sufficiently deep to expose the reverse fault, but based on the presence of a topographic bench which marks a change in channel incision style — from less incised above to more incised below — we infer uplift of the hangingwall the alluvial fan relative to the rest of the scarp slope. An important characteristic of the Paposo scarp is the presence of relatively fresh normal and reverse fault scarps. The fact that hangingwall uplift

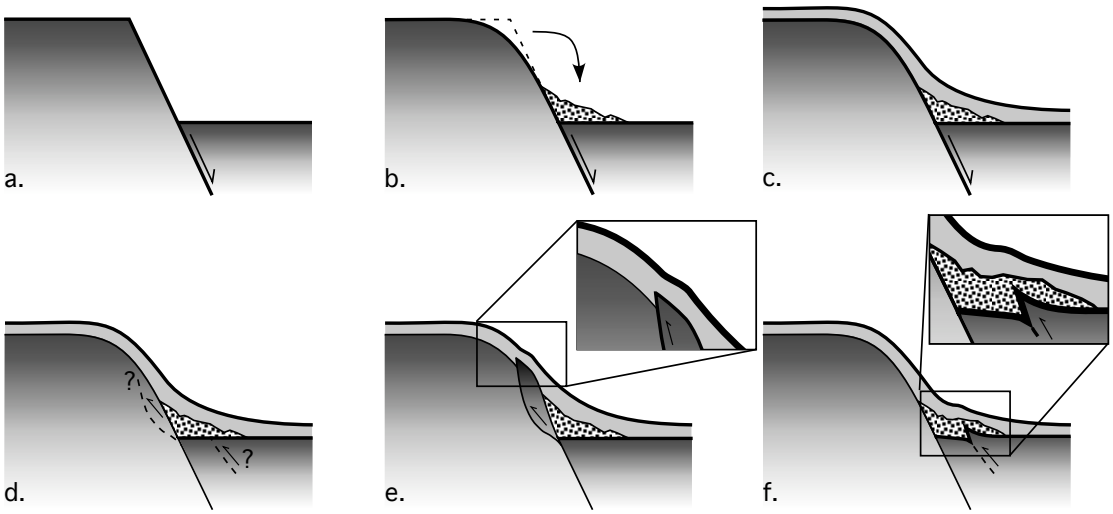

Figure A.8: Conceptual model of reverse fault reactivation, as seen at the northern end of the Salar del Carmen fault. Normal slip on the fault creates the initial fault scarp (a), which subsequently degrades, leaving colluvium at the scarp base (b). The ongoing process of regolith development (c) caps both the bedrock scarp and the colluvial wedge. When subject to fault-normal compression, a splay fault (d) experiences reverse motion (e, f), creating the subtle topographic bench observed at the surface and the upthrust basement wedge exposed in the drainages that crosscut the scarp. Based on the lithologic relationships observed in channels that crosscut the scarp, a splay fault in the footwall (e) or the hangingwall (f) of the master normal fault are both plausible.

is expressed by the change in stream incision into sediments indicates that the underlying reverse faulting is likely Quaternary. Furthermore, the upslope extent of the topographic bench is marked by a small (∼1–2 m high) normal fault scarp (Figure A.9). This suggests that the fault splay that accommodated reverse motion to create the topographic bench was reactivated as a near-surface normal fault.

An alternative explanation is that the topographic bench does not result from surface warping by a buried reverse fault, but rather slumping along a normal fault. In this case, the uplift of the hangingwall alluvial fan relative to upslope portions of the scarp would have been caused by rotation rather than fault transport.

Figure A.9: Field photo taken on the topographic bench, looking north along the strike of the fault scarp. The bench is subtle but can be identified by the gentler slope than the adjacent portions of the scarp (traced by dashed line). The interpreted normal fault scarp (white material) marks the upslope border of the topographic bench. Photo by R. W. Allmendinger.

A.3.5 Cracks near Mantos Blancos

In addition to the cracks in the Salar Grande region described in Chapters 1 and 2, Rick Allmendinger and I also visited the Mantos Blancos region (23.25°S) to investigate the style of cracking observed there. Cracks cut a large, relatively flat surface of gypsum-indurated sediments (Figure A.10). In general, apertures do not exceed ∼0.5 m, and most fissures are filled with windblown sediment, taking on a smooth, rounded profile shape. Cracks that transect a gentle south-southwest

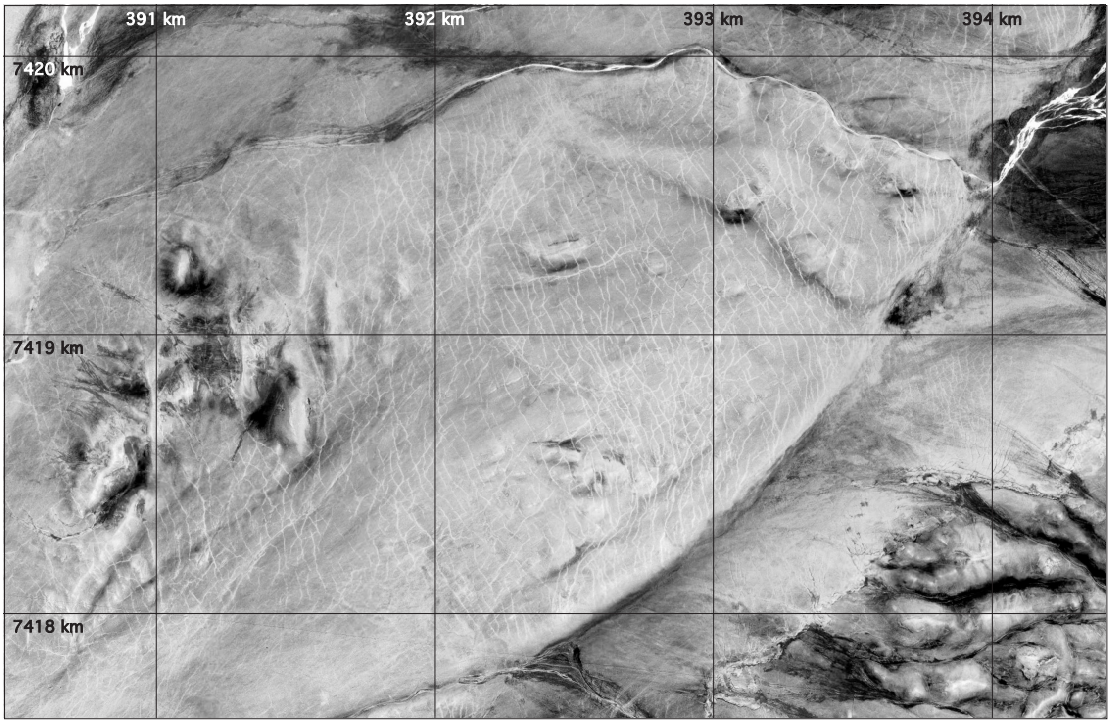

Figure A.10: Satellite image showing the Mantos Blancos area, cut by numerous meter-scale open cracks. The region is labeled as "MB" on Figure A.1. For the most part, crack strikes demonstrate a bimodal distribution in strike, with some cracks striking northwest and others northeast.

trending ridge show minor deflections in their strikes as they crest the hill, but overall maintain a relatively linear profile, indicating that topographic features exert some influence over crack propagation paths (Figure A.11a). In addition to cutting the regolith cover, some cracks affect bedrock. Such cracks are far more substantial than those restricted to the regolith, with apertures of 1.5–2 m and depths of up to 2 m (Figure A.11b).

Cracks in the Mantos Blancos region show a bimodal distribution in strike (Figure A.10, southernmost crack locality on Figure 3.1). Although there is range of strikes, the cracks most apparent in the field are those that strike northeast and those that strike northwest. As in the Salar Grande region, butting relationships

between cracks of different orientations are ambiguous (Chapters 1, 2); we can not clearly state that one set of cracks formed entirely before another. Instead, the butting relationships are more consistent with cyclic opening of each set of cracks. As discussed in Chapter 3, we observe that bimodal crack strike distributions occur primarily at known subduction earthquake segment boundaries. The obliquity between both sets of cracks and the plate boundary is consistent with the orientation of principal tension axes at the terminations of these rupture zones. In the case of the Mantos Blancos cracks, we suggest that the northeast striking features are activated by earthquakes on the Iquique segment of the plate boundary (18°–23°S), while those striking northwest are affected by events on the Antofagasta segment (23°–25°S). Alternatively, reopening of both sets of cracks may be induced by dynamic stress changes associated with an earthquake on either of those segments (Section 3.5.6).

We cannot state conclusively whether or not some of the cracks exposed at the Mantos Blancos site were opened or reactivated by the 1995 M_w 8.1 Antofagasta earthquake. The soil of the Mantos Blancos region shows evidence for induration with gypsum (gypsum nodules, high albedo, mm-scale polygonal cracking), but the sediment is not well consolidated. A suite of cracks located about 25 km southwest of Mantos Blancos and known to have opened as a result of the earthquake affected unconsolidated sediments (*González et al.*, 2003) and therefore the crack morphologies have been smoothed substantially by slow weathering processes over the past 12 years. Although we qualitatively evaluate the soil at Mantos Blancos as being more resistant to weathering than that at the coseismic crack site, it is possible that cracks did open coseismically here as well and have undergone weathering to produce their current, smoothly rounded morphology.

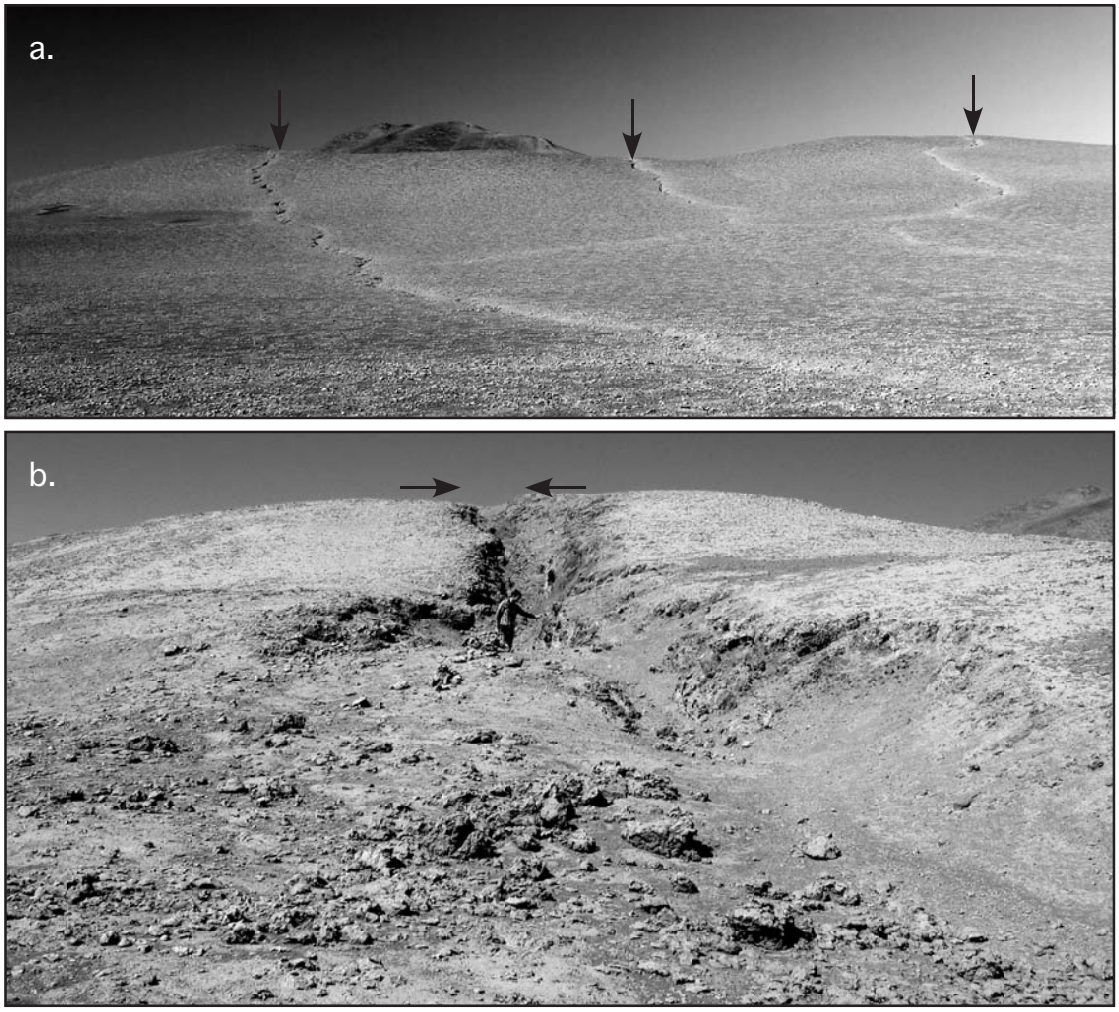

Figure A.11: a) Field photo showing the three cracks that crest a gentle hill. The intersections of the cracks with the hillcrest are marked by black arrows. While the hill does introduce some deflection in strike, cracks remain relatively linear across varying topography. b) Field photo of crack cutting bedrock in the Mantos Blancos region. The present crack depth is about 2 m, while crack aperture reaches 1.5–2 m. Photo by R. W. Allmendinger.

BIBLIOGRAPHY

Delouis, B., H. Philip, L. Dorbath, and A. Cisternas (1998), Recent crustal deformation in the Antofagasta region (northern Chile) and the subduction process, *Geophysical Journal International*, *132*, 302–338, doi: 10.1046/j.1365-246x.1998.00439.x.

González, G., J. Cembrano, D. Carrizo, A. Macci, and H. Schneider (2003), The link between forearc tectonics and Pliocene-Quaternary deformation of the Coastal Cordillera, northern Chile, *Journal of South American Earth Sciences*, *16*, 321–342, doi: 10.1016/S0895-9811(03)00100-7.

Scheuber, E., and P. A. M. Andriessen (1990), The kinematic and geodynamic significance of the Atacama fault zone, northern Chile, *Journal of Structural Geology*, *12*(2), 243–257.

APPENDIX B

SURFACE CRACK MAPPING AND PROCESSING TECHNIQUES

B.1 Introduction

The crack mapping and statistical analysis carried out in Chapters 1, 2, and 3 relied on several functions written in Matlab. This appendix describes the workflow used to process a map of cracks to create files containing a concise table containing statistical parameters, rose diagrams showing the strike distribution of cracks, and plots of crack density.

B.2 Workflow

The Matlab tools written to transform the raw files of crack vertex coordinates to useful statistical parameters are described below. Information about any program's function and use can be obtained by typing

```
>> help function
```

where `function` is the name of the tool to be used.

The crack vertex coordinates are determined by hand-tracing the cracks in GIS software. For most of the crack mapping, we used Canvas GIS, which allows for easy export of the coordinates. One caveat to exporting the coordinates is that Canvas becomes overwhelmed if too many vector objects are placed into "object edit mode" at once. I found that selecting subsets of 200–300 cracks at a time allowed for export with tolerable delays while Canvas "thought." The text files containing the subset coordinates can then be concatenated together after the fact, paying close attention to the fact that there must be a blank line separating the last vertex of one file with the first vertex of the next subset file. With the crack

vertex coordinates file available, run:

```
>> crackinfo(rawfile,infofile);
```

where `rawfile` is the raw coordinates file and `infofile` is the name of the desired output file. `crackinfo.m` calculates and outputs the number, starting coordinates, end coordinates, mean strike, and total length of all cracks. The length of the crack will be given in the same units as the input coordinates. The best strategy is to export the crack vertices from Canvas in UTM coordinates, but if the file is in decimal degrees, the raw coordinate file can be converted to UTM using:

```
>> convcracks(rawfile,rawconv,type);
```

where `rawfile` is the raw coordinates file, `rawconv` is the name of the desired output file containing the converted coordinates, and `type` specifies the type of coordinate transformation to be made (0 for geographic to UTM, 1 for UTM to geographic). This coordinate transformation is made using the called function `gmtutm.m`, which relies on having GMT installed on the system.

After producing the table of crack statistics with `crackinfo.m`, a file containing the length-weighted azimuths can be produced, with the intention of plotting a length-weighted rose diagram showing the strike distribution, by running:

```
>> lengthaz(infofile,lwazfile);
```

where `infofile` is the file produced by `crackinfo.m` and `lwazfile` is the desired length-weighted azimuth file. Following production of the length-weighted azimuth file, the rose diagram is plotting by running:

```
>> plotrose(lwazfile,bin,plotfile,{plottype});
```

where `lwazfile` is the azimuth input file, `bin` is an integer giving the degrees of strike per rose petal bin, `plotfile` is the name of the rose diagram plot to be saved, and the option argument `plottype` specifies the extension of the output

plot figure. The gaudy colors of the resulting plot are intentional, as it makes selecting various parts of the rose diagram by attribute very easy when inserted into a Canvas document, assuming no other parts of the document are similarly gaudy.

If a raw, non-length-weighted rose diagram is preferred, it can be produced using:

```
>> plotrose(infofile,bin,plotfile,{plottype});
```

as `plotrose.m` will simply extract the strike information from the statistical table contained in `infofile`.

Crack density, defined as the total length of cracking per unit area, can be calculated on a regularly-spaced grid using the function `new_density.m`. This program uses the coordinates contained in `infofile` and a specified grid interval to determine the length of cracks per grid cell, which can be plotted as a contour map. To run the program, type:

```
>> [x,y,dens] = new_density(infofile,densfile,grid);
```

where `x` and `y` are the center coordinates of the grid cells, `dens` is the density value for the grid cell, `infofile` is the statistical table produced by `crackinfo.m`, `densfile` is a Matlab `*.mat` file containing the grid cell coordinates, density values, and length-weighted mean strike value for each grid cell, and `grid` is the desired grid spacing in meters. A plot of the density and mean strike is generated automatically.

In order to use GMT create a map of the density grid that can be overlain by other geographic data, use the function `array2gmt.m`, which has several input arguments that can be used to customize the map's appearance. Before starting, make sure that GMT has been installed with the MEX tools that provide an

interface between it and Matlab, namely the function `gmtwrite.m`. `array2gmt.m` writes the crack density and/or azimuth array to a file readable by GMT, as well as a color scale and a UNIX shell script that can be manually modified to produce the desired final product. The built-in help information for `array2gmt.m` comprehensively explains the options for controlling its output.

APPENDIX C

MATLAB SCRIPTS FOR SUBDUCTION EARTHQUAKE CYCLE MODELING

C.1 Introduction

Four software packages were used in the mechanical modeling portions of this thesis. Poly3D, developed by David Pollard's geomechanics group at Stanford University (*Thomas*, 1993), was used for the actual calculations of deformation fields due to faulting. In order to prepare input files for Poly3D, I developed a suite of scripts in Matlab that, used in conjunction with the open source meshing program Gmsh (`http://www.geuz.org/gmsh`), produce boundary element meshes of faults. This appendix describes the use of these Matlab tools. File names and commands to be entered at the Matlab command prompt appear as

`>> command`.

The Matlab scripts are listed here in the logical order they would be used to construct input files for a subduction zone modeling problem. More information about each script can be provided by typing

`>> help (script name without .m extension)`.

C.2 Workflow

The first step that I used to model a subduction zone was defining its geometry. In order to take advantage of Poly3D's capability of using polygonal elements to accurately represent a non-planar geometry, I created subduction zone geometries that are curved surfaces. In order to do this, I used a GIS program to first load the 0, 50, and 75 km contour lines of the Wadati-Benioff zone. A global database of slab con-

tours can be found at `ftp://rses.anu.edu.au/pub/malcolm/RUM/slabs.tar.gz`. I then drew straight lines perpendicular to the local strike of the subducting slab, with three vertices per line, one on each of the contour lines. The contour depth was appended to the coordinates to create a three-column output file, with columns containing longitude, latitude, and depth:

```
-80.676   -9.191       0
-79.314   -8.355   50000
-78.884   -8.089   75000
-80.442   -9.576       0
-79.146   -8.741   50000
-78.732   -8.472   75000
      ⋮        ⋮       ⋮
-72.569  -30.819       0
-71.531  -30.857   50000
-71.165  -30.875   75000
```

These data are then further appended with a fourth column that contains the depths defining the updip extent of the fully-locked portion of the interface, the downdip extent of this portion, and the downdip extent of the "transition zone" between the locked and sliding parts of the interface (see Section 5.5.1.2 for more details). Because these values are assigned for every downdip profile, the depth of locking can vary along strike. The appended input file should be of the form:

```
-80.676   -9.191       0   20000
-79.314   -8.355   50000   35000
-78.884   -8.089   75000   50000
-80.442   -9.576       0   20000
-79.146   -8.741   50000   36000
-78.732   -8.472   75000   51000
      ⋮        ⋮       ⋮       ⋮
-72.569  -30.819       0   20000
-71.531  -30.857   50000   32000
-71.165  -30.875   75000   47000
```

with the fourth column showing an example of variation in locking depth.

The slab geometry file is processed with `adjustarc.m`, which uses the 0-50-75 km "triplets" to define the downdip curvature of the plate boundary, as an arc is defined by any three points. `adjustarc.m` interpolates the slab coordinates, resulting in a densified array of coordinates defining the slab geometry. The geometry is defined as three sections: the updip (seaward) transition zone, the fully-locked zone, and the downdip (landward) transition zone. These coordinates are then processed with `gmsh_write.m`, which converts the raw coordinates into a `*.geo` file readable by Gmsh. This file is then meshed, creating an assemblage of triangular elements that preserve the along-strike and downdip curvature of the plate boundary. In order to convert the Gmsh `*.msh` file to a format readable by Poly3D, either the function `gmsh2poly.m` or `gmsh2poly_old.m` is used, depending on the version of Gmsh used to create the mesh; for version 2 or newer, use `gmsh2poly.m`.

The next step is optional and allows the plate boundary mesh to be "corrected" for forearc topography using the function `polytopo.m`, using the method of *Flück et al.* (1997). This function uses a digital elevation model and the slab geometry to determine the total vertical distance between the element nodes and the overlying ground surface (Figure C.1a). The mesh geometry is adjusted such that the distance between topography and slab is equal to the distance between the flat, half-space surface and the modeled nodes. The adjusted mesh geometry is written to a new Poly3D input file.

If the end goal is to run an interseismic model, the model mesh must be converted into a format readable by the dislocation code DISL3D (*Flück et al.*, 1997; *Wang et al.*, 2003). This program is called in order to calculate the magnitude and rake of backslip to be applied to each triangular element, based on its position with respect to the Euler pole describing relative plate motion between the

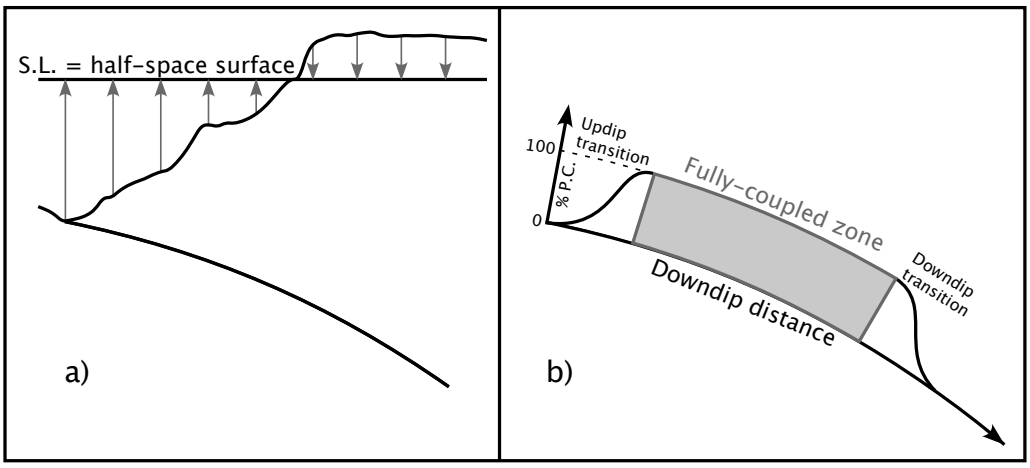

Figure C.1: Corrections applied to the backslip modeling of a subduction zone. A) Correction to topography, which assures that the distance between the half-space surface and the modeled fault is equal to that between slab and the ground surface. B) Gaussian shape applied to the backslip magnitude in the "transition zones" both up- and downdip of the fully-coupled portion of the plate boundary in order to minimize abrupt transitions in applied backslip between adjacent elements.

subducting and overriding plates. The conversion is carried out using the function `poly2dis.m`. Ideally, a new Matlab function should be written to assign the backslip magnitudes without having to call DISL3D.

After running DISL3D, the calculated backslip magnitudes and rakes must be inserted as displacement discontinuity boundary conditions into the Poly3D input file, using `dis2poly.m`. This function creates a file containing the mesh geometry that then must be modified to include the elastic constants and observation arrays that complete the Poly3D input file. An additional modification that must be made to the source mesh file is that unique object identifiers must be inserted so that the two transition zones and the fully locked zones (see Section 5.5.1.2) are distinct parts of the geometry. As of now, this must be done by hand by using the

object identifiers contained in the output of the `gmsh2poly.m` program.

The next step is to calculate the tapered slip within the transition zones. As described in Section 5.5.1.2, I model the transitional slip using a Gaussian function (Equation 5.1, Figure C.1b). The function `polygauss.m` uses the geometry of the subduction zone mesh as well as the "raw" backslip magnitudes calculated by DISL3D to taper the transition zone slip. The modified transition zone boundary conditions are written to a new Poly3D input file.

An additional optional step modulates the backslip magnitudes based on a map of gravity anomalies. *Song and Simons* (2003) and *Wells et al.* (2003) present observations that correlate regions of high magnitude coseismic slip during great subduction earthquakes to regions of negative gravity anomalies. *Bürgmann et al.* (2005) extend this theory to the distribution of interseismic strain, suggesting that the modeled backslip magnitude should be greater in regions of negative gravity anomalies. The function `polygrav.m` uses a map of trench-parallel gravity anomalies ("TPGA," a term defined by *Song and Simons* (2003) to describe the small-scale anomalies in the gravity field) to adjust the magnitude of calculated backslip. To calculate the TPGA required for this adjustment, use the function `tpga.m`, which converts a raw gravity anomaly map, such as that available from `http://topex.ucsd.edu/marine_grav/mar_grav.html`, into TPGA for a specified region.

After any step in which a Poly3D input or mesh file is written, the geometry and boundary conditions can be confirmed graphically using the function `polymesh.m`, which plots any of the three boundary condition components, or the overall boundary condition magnitude.

Once the Poly3D input file is constructed, Poly3D should be run to calculate

stress, strain, and/or displacement at the specified observation points. After the run is complete, use the function `poly3d_out.m` to extract the elemental displacements and tractions (if calculated) as well as the stress, strain, and displacement values at each observation node. This function scans the input file to determine which parameters were calculated, then extracts the values from the output file, places them into arrays, and saves the collection of arrays to a Matlab `*.mat` file. After running `poly3d_out.m`, the results can be plotted using any of Matlab's graphical functions. The function `poly3d_plot.m` streamlines the calculation and plotting of the Coulomb stress change, which is the parameter I used most often in my subduction zone modeling.

BIBLIOGRAPHY

Bürgmann, R., M. G. Kogan, G. M. Steblov, G. Hilley, V. E. Levin, and E. Apel (2005), Interseismic coupling and asperity distribution along the Kamchatka subduction zone, *Journal of Geophysical Research*, *110*, B07405, doi:10.1029/2005JB003648.

Flück, P., R. D. Hyndman, and K. Wang (1997), Three-dimensional dislocation model for great earthquakes of the Cascadia subduction zone, *Journal of Geophysical Research*, *102*(B9), 20,539–20,550.

Song, T.-R. A., and M. Simons (2003), Large trench-parallel gravity variations predict seismogenic behavior in subduction zones, *Science*, *301*(5633), 630–633, doi: 10.1126/science.1085557.

Thomas, A. L. (1993), Poly3D: A three-dimensional, polygonal element, displacement discontinuity boundary element computer program with applications to fractures, faults, and cavities in the Earth's crust, M.S. thesis, Stanford University, Stanford, CA.

Wang, K., R. Wells, S. Mazzotti, R. D. Hyndman, and T. Sagiya (2003), A revised dislocation model of interseismic deformation of the Cascadia subduction zone, *Journal of Geophysical Research*, *108*(B1), 2026, doi:10.1029/2001JB001227.

Wells, R. E., R. J. Blakely, Y. Sugiyama, D. W. Scholl, and P. A. Dinterman (2003), Basin-centered asperities in great subduction zone earthquakes: A link between slip, subsidence, and subduction erosion?, *Journal of Geophysical Research*, *108*(B10), 2507, doi:10.1029/2002JB002072.

APPENDIX D

ADDITIONAL BOUNDARY ELEMENT MODELS OF UPPER PLATE FAULTING IN THE SALAR GRANDE REGION (SUPPLEMENT TO CHAPTER 2)

D.1 Introduction

In Chapter 2, I present models showing the perturbation to a regional stress field induced by the presence of upper plate faults. In addition to the preferred models presented in that chapter, I explored several additional sets of boundary element model parameters for each of the four fault zones. This appendix contains descriptions of all tested permutations and plots of the calculated stress perturbations and vertical displacement fields.

D.2 Tested parameters

D.2.1 Depth-dependent traction boundary conditions

For models of normal faulting, we test two types of boundary conditions applied to the fault surface. One set of boundary conditions, used in the preferred models of Chapter 2, allows the faults to slip freely both along strike and down dip, but prohibits fault-normal motion in response to an applied uniaxial tension, T. The other class of models employs variable traction boundary conditions, which permit fault opening near the surface. These boundary conditions are determined following the approximate lithostatic method of *Crider and Pollard* (1998). The fault surface is everywhere affected by lithostatic stress, which serves to clamp the two sides of the fault interface together. At shallow levels, the lithostatic stress may

be less than the remote tension resolved in the direction of the element normal, defined as $-t_3^e(0)$, which leads to opening-mode displacements. The boundary conditions applied to the fault elements are determined based on the element geometry and the magnitude of T and in all cases serve to oppose the applied tension. At depths where the lithostatic stress exceeds the remote tension resolved onto the fault element, we prescribe fault-normal traction equal and opposite to the resolve remote stress, such that the resulting fault-normal displacement is nominally zero. At shallower depths, where the lithostatic stress is less than the remote tension magnitude, the fault is allowed to open an amount proportional to the difference between the remote and lithostatic stresses. On all elements, the boundary conditions are parameterized as:

$$
\begin{aligned}
t_1^e &= 0 \\
t_2^e &= 0 \\
t_3^e &= \begin{cases} \rho g x_3 & \text{if } 0 > x_3 \geq -\frac{t_3^e}{\rho g}, \\ -T \sin^2 \delta \cos\theta \sin\theta & \text{if } x_3 < -\frac{t_3^e}{\rho g}. \end{cases}
\end{aligned}
\tag{D.1}
$$

where t_1^e is the traction on the fault element in the downdip direction, t_2^e is the traction in the along-strike direction, and t_3^e is the traction acting normal to the fault plane, with positive traction acting outwards from the element centroid; ρ is the density of the elastic medium (assumed to be 2750 kg/m^3), g is gravitational acceleration, x_3 is the depth of the element centroid, δ is the dip of the fault element, and θ is the angle between the element strike and the azimuth in which the uniaxial tension T is directed. A schematic diagram of these boundary conditions is presented in Figure D.1.

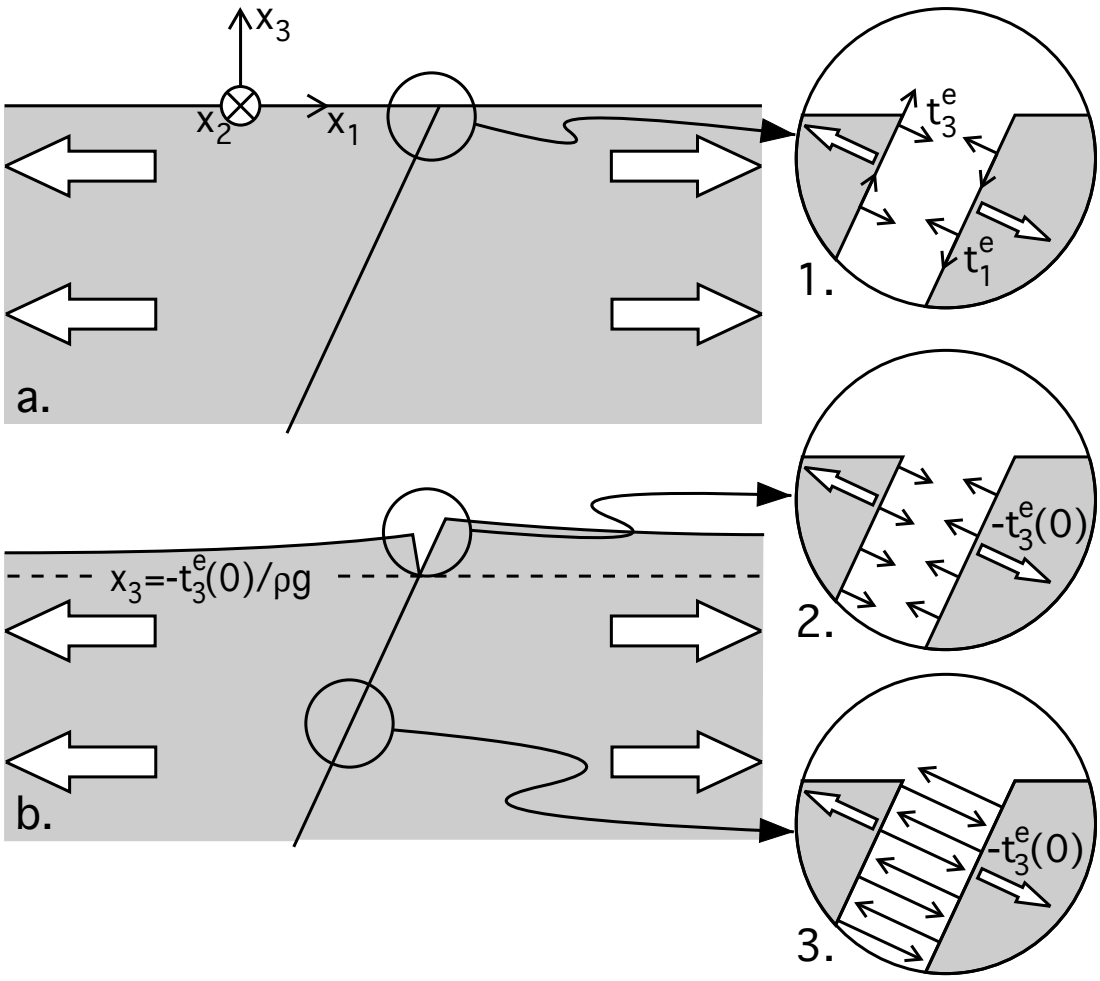

Figure D.1: Schematic diagram showing the boundary conditions applied to the fault elements for the depth-dependent traction models. a. Element traction boundary conditions are applied to each fault element, using an element-local coordinate system. t_1^e and t_2^e (inset 1; t_2^e acts into the page but is not labeled) are assigned to be zero, allowing free slip on the fault. The lithostatic traction t_3^e acts normal to the fault, opposing the remote traction (large white arrows). b. Where the remote tension resolved onto the fault plane (equal to $-t_3^e(0)$) exceeds the "clamping" traction t_3^e, the fault opens (inset 2). Below the depth $x_3 = -t_3^e(0)\rho g$, the lithostatic stress is sufficiently great to keep the fault clamped, i.e. the magnitude of the applied t_3^e equals the remote tension resolved in the direction of the element normal (inset 3). After *Crider and Pollard* (1998).

D.2.2 Remote stress promoting reverse faulting

In Chapter 2, models in which reverse faulting was encouraged were subject to uniaxial compression in the direction of plate convergence. Here, I we test four remote stress compression scenarios. In all cases, the horizontal principal axes of remote stress trend parallel and perpendicular to the direction of plate convergence, but the relative magnitudes vary. These permutations are meant to span a range of uniaxial and biaxial compression that would result in the "constrictional" deformation field proposed by *Carrizo et al.* (2007). Each reverse faulting model was subject to 1) uniaxial compression of 2×10^6 Pa directed 075°, 2) uniaxial compression of 2×10^6 directed 165°, 3) 2×10^6 Pa of compression directed 075°, 1×10^6 Pa of compression oriented 165°, and 4) 1×10^6Pa of compression along the azimuth 075°, 2×10^6 Pa directed 165°. All reverse model figure panels show a schematic diagram denoting the directions and relative magnitudes of the remote stress axes.

D.3 Model results

D.3.1 Hombre Muerto fault

We test both normal and reverse fault parameter sets for the Hombre Muerto fault. Although unlikely, there exists the possibility that the trenched faults (*Carrizo et al.*, 2007) represent secondary structures, and the principal fault that forms the scarp is actually an east-dipping normal fault, so we investigate models using this geometry and uniaxial tension as remote stress. The applied remote stress tensor that drives fault slip is reasonably consistent with the geomorphology of the fault scarp. Drainages off the mountain front directly east of the Hombre Muerto fault

are either diverted by the fault scarp or are dammed but show some evidence of previous continuity on the upthrown western fault block. In all cases, the preserved continuity shows no clear lateral offset relative to the upstream segment of the drainage, suggesting that fault motion has been primarily dip-slip. This implies that the principal axes of the remote stress field are oriented such that minimal strike-slip motion is induced, i.e. one principal axis is nearly perpendicular to the fault and the other is nearly parallel. If the Hombre Muerto fault is a normal fault, it slips in response to remote tension applied approximately east-west, as is likely induced in this region by strong subduction zone earthquakes (Chapter 3) or possibly flexural effects during the interseismic period (Chapter 5). If it is a reverse fault, as suggested by the trenching and therefore assumed in our preferred model (Section 2.6.1), motion is driven by compression oriented east-west, which may arise from plate convergence or a concentrated zone of compression during a subduction zone earthquake, depending on the exact slip distribution during that earthquake (Chapter 4).

For both the normal and reverse cases, we test two cases to treat the transition zone geometry. Given the lack of topographic expression of the fault between the northern and southern segments, it is possible that the fault is discontinuous or segmented. For both the normal and reverse faulting cases, we test scenarios in which the fault is modeled as a single, through-going fault as well as two distinct segments. It is important to note that in both cases we fix the maximum depth D of modeled faults to be $L/2$, and so in the case of the segmented fault models, the maximum fault depth is about half that of the single fault simulations, due to the different fault lengths. The segmented fault cases also employ variable burial depth B: due to the fact that the scarp of the southern segment is much more

subdued than that of the northern segment, we interpret it as more deeply buried ($B = L/20$ for the southern segment and $B = L/200$ for the northern segment). When modeled as a single fault, we bury the discontinuity to $B = L/200$ along its entire length.

Figure D.2 and D.3 show the patterns of normal stress resolved onto vertical planes striking 000° that result from remote stress imposed on the modeled Hombre Muerto fault. Figure D.2 shows the stress fields for the remote uniaxial tension conditions and demonstrate the effects of fault interaction around the transition zone. Figures D.2a and c show the simulations in which no opening displacement is allowed on the modeled faults, while panels b and d show the cases in which the variable traction boundary conditions are employed, allowing opening of the fault near the surface. Restriction of opening in the single fault model (Figure D.2a) produces a tensional stress field along the footwall that decreases in width around the transition zone, which is inconsistent with the wider extent of cracking in that area. Conversely, the opening, single fault model (Figure D.2b) shows a slight bulge in the tensional stress field around the transition zone. Regions of tension in the segmented fault models (Figures D.2c, d) are similar regardless of whether or not opening is allowed. The width of the tensional stress field in the footwall is narrower than that of the single fault models, which results from the smaller downdip extent of the individual fault segments. Even so, the regions in which cracking is encouraged contain most of the mapped cracks. The transition zone itself is characterized by low-magnitude tension encompassing most of the mapped cracks. As in the case of the single fault models, the case in which near-surface fault opening is allowed produces a stress field more consistent with the mapped cracks than the non-opening model.

Figure D.2: Results of modeling in which the Hombre Muerto fault region is subject to uniaxial tension directed 255° (represented by the double-headed arrow), simulating the stress generated either by a strong subduction zone earthquake or interseismic flexure. Bold black lines show the surface trace of the modeled faults and thin black lines show the mapped surface cracks. The color map shows the distribution of tensile stress resolved onto vertical planes striking 000°, approximating the mean crack strike within this region (see rose diagram in Figure 2.8). From the total calculated stress field, we subtract the magnitude of remotely applied tension resolved onto planes striking 000°, so that the stress field shown represents solely the perturbation to the stress field caused by the presence of and slip on the modeled faults. Where tensile stress is non-zero, opening is encouraged on such planes.

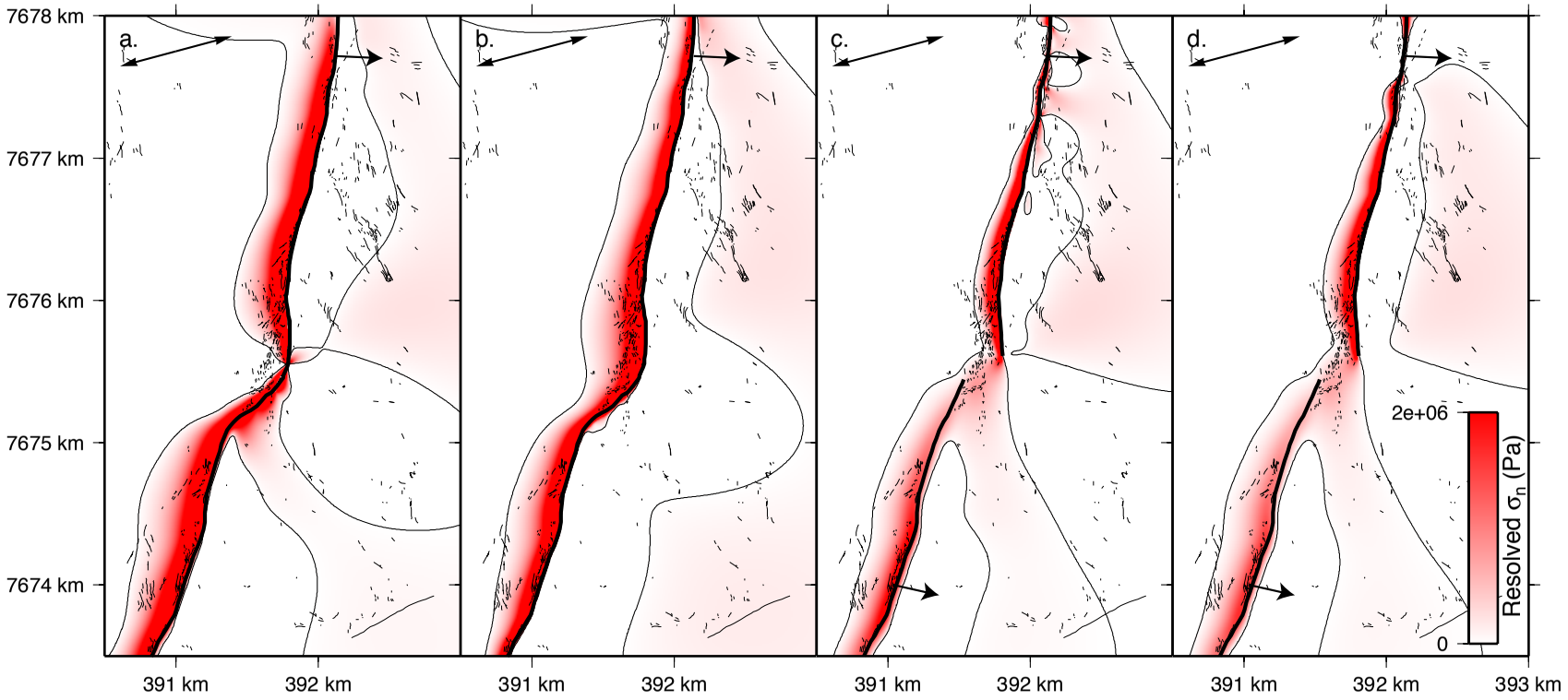
7678 km
7677 km
7676 km
7675 km
7674 km
a.
b.
c.
d.
391 km
392 km
391 km
392 km
391 km
392 km
391 km
392 km
393 km
2e+06
0
Resolved σn (Pa)

When the west-dipping modeled faults are subject to uniaxial or biaxial compression, the resulting patterns of stress perturbation are relatively similar to those of the normal fault models (Figure D.3). Models experiencing uniaxial compression directed 075° (Figure D.3a, e), or biaxial compression with the larger magnitude axis trending 075° (Figure D.3c, g) show a narrow zone of tension concentrated along the scarp crest, consistent with the zone of enhanced cracking observed along the fault. However, these models do not predict tensional stress around the transition zone. Simulations in which compression directed 165° dominates the remote stress field (Figures D.3b, d, f, h) do show an enhancement of tensional stress around the transition zone, but the reverse-sinistral fault slip vectors and vertical displacement fields (e.g., Figure D.4b) resolved from these models are inconsistent with the geomorphology of the region, which indicates little lateral offset along the linear fault.

The deeper burial of the southern segment of the Hombre Muerto fault significantly affects the extent of the tensional stress field at the surface (Figure D.3e-h). Only in the case of uniaxial compression directed 165° (Figure D.3f) is the hanging-wall stress field tensional, but again, this model is inconsistent with the cumulative slip on the fault as recorded by the geomorphology (Figure D.4b). As discussed in Section 2.6.1, it is possible that the transition zone is underlain by several short fault segments, and the collective perturbation that they introduce into the stress field may be consistent with the diffuse deformation we observe there.

When modeled as a two-segment normal fault system, the general patterns of predicted uplift and subsidence along the Hombre Muerto fault (D.4a) agree reasonably well with the observed fault-related topography, which can be discerned from the IKONOS image shown in Figure 2.8. Because of the near-surface burial

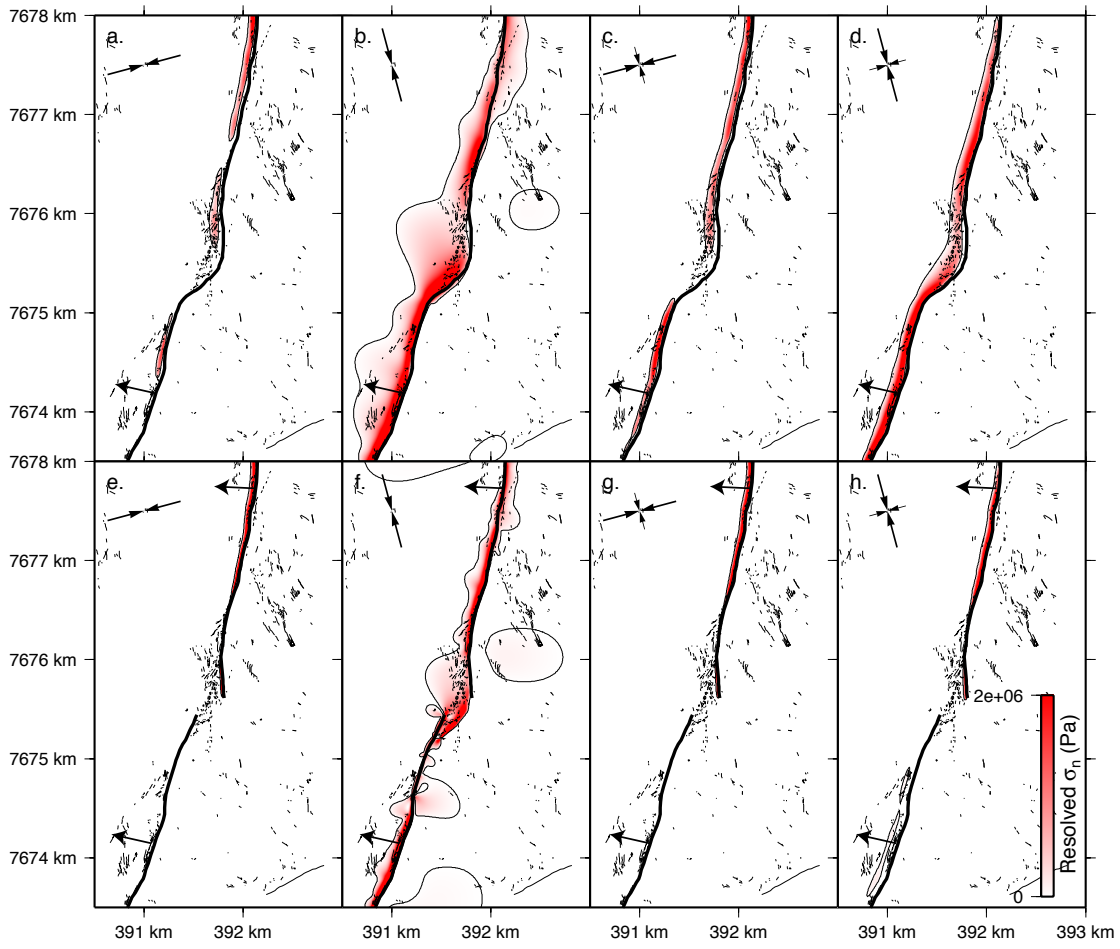

Figure D.3: Results of modeling in which the Hombre Muerto fault is simulated as a structure dipping 75°W, broadly consistent with the trenching observations of *Carrizo et al.* (2007), and subject to various compressional remote stress conditions. All symbols are the same as in Figure D.2 except that all reverse fault models, the stress field shown is not corrected for remote stress, as any tensional stress in the reverse fault models results exclusively from localized effects due to fault-related processes. The top row (a–d) shows the results of simulations in which the fault is modeled as a single, continuous structure, whereas the the bottom row (e–h) shows the results for the two segment models. The four columns show the field of tensional stress for models subject to different remote stress conditions, expressed by the black arrows: a, e) uniaxial compression directed along the azimuth 075°, b, f) uniaxial compression oriented 165°, c, g) biaxial compression, with the magnitude of compression oriented 075° twice that oriented 165°, and d, h) compression oriented 165° twice the magnitude of that directed 075°.

depth of the northern segment, the resulting fault scarp is higher and more abrupt than the subdued scarp of the deeper-buried southern segment. In the transition zone between segments, the horizontal gradient of the vertical displacement field is less than that along the fault segments, consistent with the continuous slope that is cut by continuous drainages in that area (D.4a). Patterns of vertical displacement for the reverse fault simulation subject to uniaxial compression directed 165° (Figure D.4b) do not closely resemble the topography. Elevated regions are not elongated parallel to the fault trace but rather are dome-shaped. The greatest uplift predicted by this model occurs within the transition zone (Figure D.4b), which is inconsistent with the through-going drainages in that region. Figure D.4c shows the vertical deformation for the two-fault model subject to constriction, with the compression oriented 075° twice the magnitude of that directed south-southeast (i.e., the model shown in Figure D.3g), which closely resembles the displacement fields of the models shown in Figure D.3e and h. Like the normal faulting displacement field, Figure D.4c shows elongated zones of uplift and corresponding valleys parallel to the fault, consistent with the scarp topography observed. Furthermore, the relief across the transition zone is relatively low, which would allow for the continuity of drainages from east to west across the fault zone. The vertical displacement fields shown in Figure D.4a and c both resemble the accumulated fault-related topography, indicating that repeated episodes of fault slip can explain the resulting surficial expression.

D.3.2 Punta de Lobos fault

The Punta de Lobos fault is curious in that the region of adjacent cracking extends across the alluvial fan for about 1 km from the fault trace. Based on preliminary

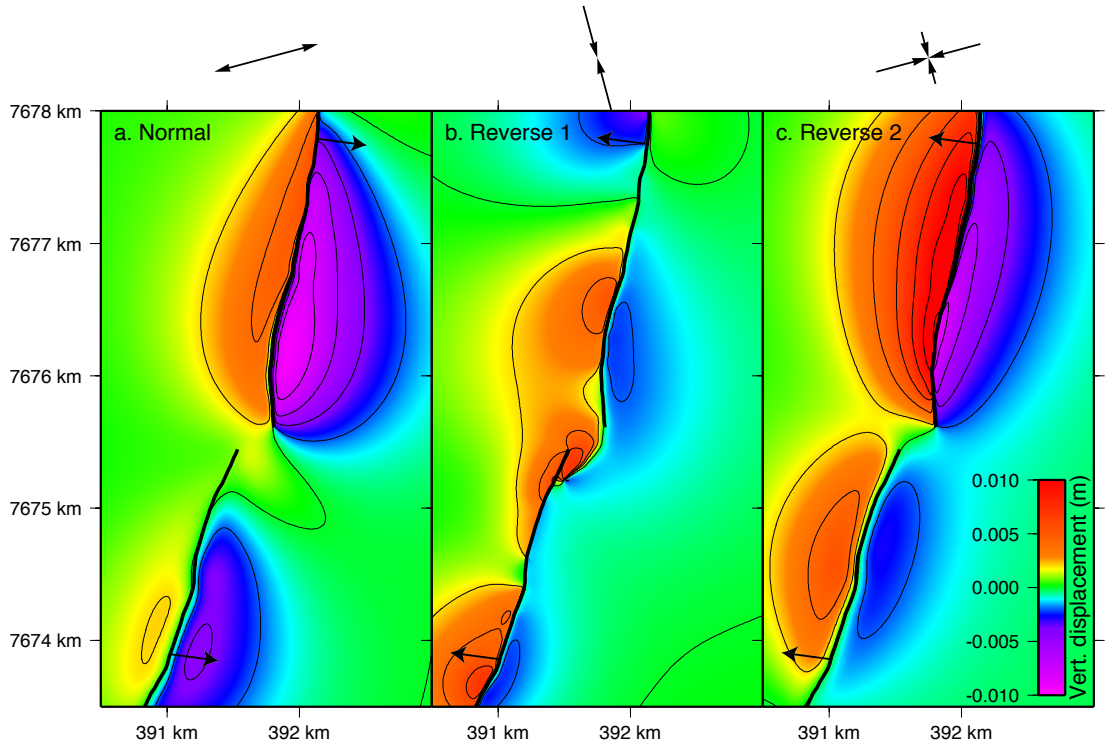

Figure D.4: Vertical displacement field for three of the Hombre Muerto models: A) normal fault model, subject to uniaxial tension directed 255°, B) reverse fault model subject to uniaxial compression along azimuth 165°, and C) constrictional model, with compression directed 075° twice the magnitude of that directed 165°. The patterns seen in C are very similar to those seen for the other reverse fault remote stress conditions. The fields of A and C are relatively similar, characterized by linear zones of uplift and subsidence along the fault trace, with little uplift in the transition zone between fault segments, consistent with the topography. Vertical displacement shown in B is inconsistent with the topography, as the zone of greatest predicted uplift coincides with the transition zone, where fault-related relief is low. However, the model corresponding to B is the reverse fault simulation producing the stress field most consistent with the distribution of cracks.

modeling, if these cracks are exclusively related to the stress perturbation generated by the presence of the fault, the fault must extend to great depth and/or dip gently. Because we know the dip of the fault at the surface to be 82°E, the gentle dip hypothesis is either incorrect, or the inclination shallows at depth, suggesting a listric geometry. Despite a deep incision into the alluvial fan sediments that comprise the hangingwall, we have little information about bedding dips on either side of the fault that could shed light on whether or not the fault is listric. If the fault were listric, we would expect cracking to be accentuated around the crest of a rollover anticline in the hangingwall. As mentioned before, cracks show little change in aperture or spacing across the alluvial fan, indicating little enhancement due to any structure. Nonetheless, we test a listric geometry in our simulations of the Punta de Lobos fault, the dip of which decreases from 82°E at the surface to horizontal at a distance 3 km away from the surface trace and a depth of 2 km. We also test two aspect ratios for planar faults ($D = L/2$ and $D = L$) to address the possibility that a planar yet deep fault imposes a stress perturbation over a wide region.

The fault kinematics of the Punta de Lobos fault are constrained by the surface exposure described by *González et al.* (2003), and so all results shown in Figure D.5 compare only the effects of fault geometry, and not the applied remote stress tensor. The fault-normal traction conditions imposed on the modeled Punta de Lobos fault exert strong influence over the resulting surface stress pattern, which is plotted as normal stress resolved on vertical planes striking 350°. For the planar fault models in which near-surface fault opening is prohibited (Figure D.5a, b), there is a zone of tension predicted along the footwall of the fault, the width of which is greater for the $D = L$ fault model (Figure D.5b) than the $D = L/2$

model (Figure D.5a). This feature is absent in the stress fields of models in which opening is allowed (Figure D.5d, e). In the opening, planar fault models, a region of low-magnitude tension in the hangingwall extends eastward from a point just a few hundred meters from the fault trace, whereas the zero-value stress contour line for models in which opening is prohibited is located about 1 km from the fault. The zone of tension encompasses most of the cracks mapped in the hangingwall alluvial fan, but the small magnitude may not be capable of driving the evolution of these cracks. North of the fault plane exposure site (white circle in Figure 2.11), cracks located in the footwall lie within the zone of tension predicted by the non-opening models (Figure D.5a, b). Near the northern terminus of the modeled fault, the numerous cracks lie within a region where tension is not predicted by any model. The actual trace of the fault in this area is difficult to identify, and it may terminate with branched ends rather than as a discrete plane, which could explain the wider extent of cracking observed.

Further tests not presented here show that the stress field resulting from larger magnitudes of tension (i.e., 10×10^6 Pa as opposed to 2×10^6 Pa) applied to faults that are permitted to open have a slightly different pattern, in that tension is predicted on both the hangingwall and, to a lesser extent, the footwall sides of the fault, rather than being almost exclusively restricted to the hangingwall side. Such a pattern is consistent with the occurrence of cracks immediately to both east and west of the Punta de Lobos fault, but the magnitude of tension required to produce such a field is greater than that predicted by our models of subduction zone earthquakes. It is possible that the dynamic stress associated with a large earthquake could result in such a magnitude.

When the Punta de Lobos fault is simulated as a listric fault (Figure D.5c,

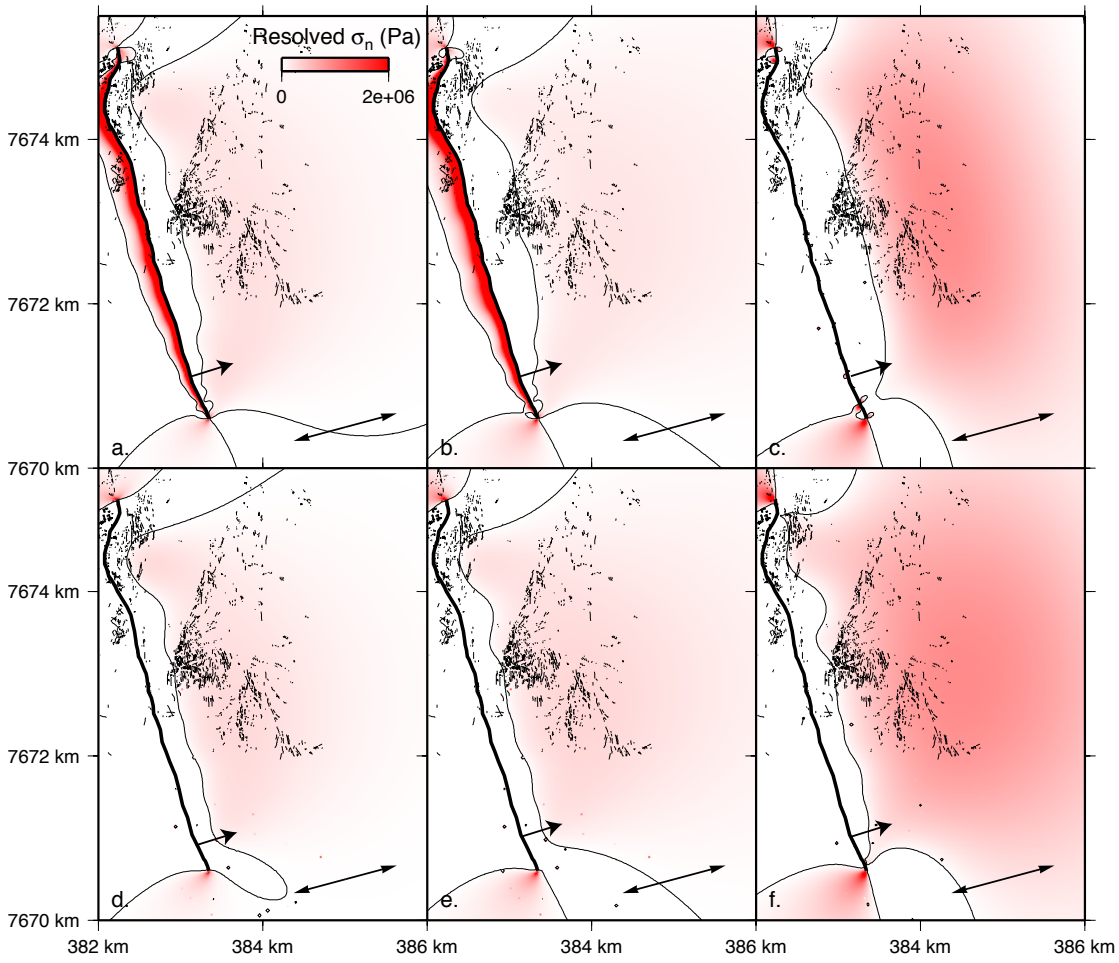

Figure D.5: Tension resolved onto vertical planes striking 350° around the Punta de Lobos fault. All models are subject to 2×10^6 Pa of uniaxial tension directed 255°, causing normal slip on the fault. In the top row models (A-C), the fault is not permitted to open, while the variable traction boundary conditions are applied to the bottom row models (D-F). The planar fault in models in the first column (A, D) dips 80°E, consistent with the observations of *González et al.* (2003), and has an aspect ratio of $D = L/2$, while the modeled fault in the second column (B, E) has an aspect ratio of$D = L$. The third column models (C, F) show the stress field resulting from slip on a listric fault, which has a surface dip 80°E that decreases to horizontal 3 km from the surface trace at a depth of 2 km.

f), tension in the hangingwall is greater in magnitude than that predicted by the planar fault models. When near-surface opening is allowed on the listric fault, the zone of tension again extends from a location nearer the fault trace than that of the non-opening model. These models emphasize the fact that the rollover anticline generated by slip on a listric fault does produce tensional stress at the surface and is therefore a plausible mechanism for crack enhancement. However, as is the case with the planar fault models, the low magnitude of the induced tension may not be sufficient to drive the cracking, indicating that the evenly-spaced cracks we observe cannot be explained exclusively by fault-related processes, but rather by larger scale stresses.

D.3.3 Antena-Bahía Blanca faults

For both the normal and reverse faulting cases of the Antena Norte, Antena Sur, and Bahía Blanca fault segments, we test fault dips of 60°, 75°, and 80°, with aspect ratios of $D = L/2$. For the 75° dip cases, we also test an aspect ratio of $D = L$.

The scarp above the Antena Sur segment is subtle, yet it comprises a topographic anomaly sufficient to dam alluvial sediments transported from the west (Figure 2.13b). As in the case of the southern Hombre Muerto segment, the subtler topography of this segment as compared to the Antena Norte and Bahía Blanca scarps may suggest that the Antena Sur fault is inactive and has undergone substantial degradation, or that the fault is deeply buried, subduing its surface expression. We model the fault assuming the latter characteristic, burying the Antena Sur fault to $B = L/20$ and the Antena Norte and Bahía Blanca to a nearly surface-breaking depth of $B = L/200$.

Figure D.6: Tension, resolved onto vertical planes striking 345°, resulting from modeling the Antena-Bahía Blanca segments as normal faults subject to 2×10^6 Pa of uniaxial tension oriented 255°. Modeled faults in the top row (A-D) are prevented from opening, while near-surface opening is allowed on the bottom row models (E-H). The first three columns contain planar faults of the noted dip whose aspect ratio is $D = L/2$, while the aspect ratio of faults in the final column is $D = L$.

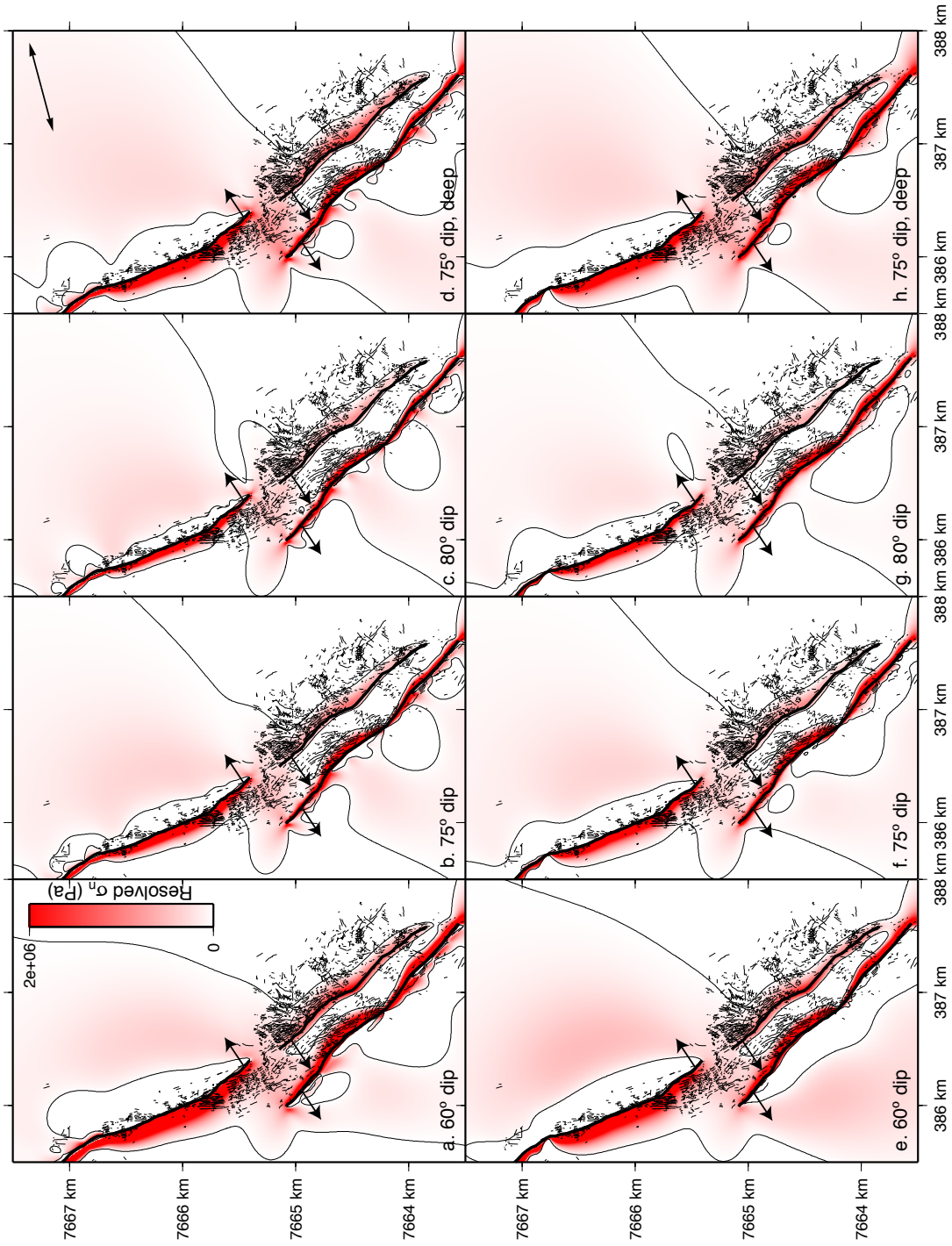
Resolved σn (Pa)
2e+06
0
a. 60° dip
b. 75° dip
c. 80° dip
d. 75° dip, deep
e. 60° dip
f. 75° dip
g. 80° dip
h. 75° dip, deep
7667 km
7666 km
7665 km
7664 km
386 km
387 km
388 km

Figure D.7: Same as Figure D.6, but faults dip in the opposite direction and are subject to compressional boundary conditions, resulting in reverse oblique motion. Each row of models represents the results using a different set of remote stress conditions, with each column representing different fault geometries as described for Figure D.6. Row 1 (A-D): 2×10^6 Pa of uniaxial compression directed 075°; row 2 (E-H): 2×10^6 Pa of uniaxial compression directed 165°; row 3 (I-L): 2×10^6 Pa of compression directed 075°, 1×10^6 Pa of compression directed 165°; row 4 (M-P): 1×10^6 Pa of compression along 075°, 1×10^6 Pa along 165°.

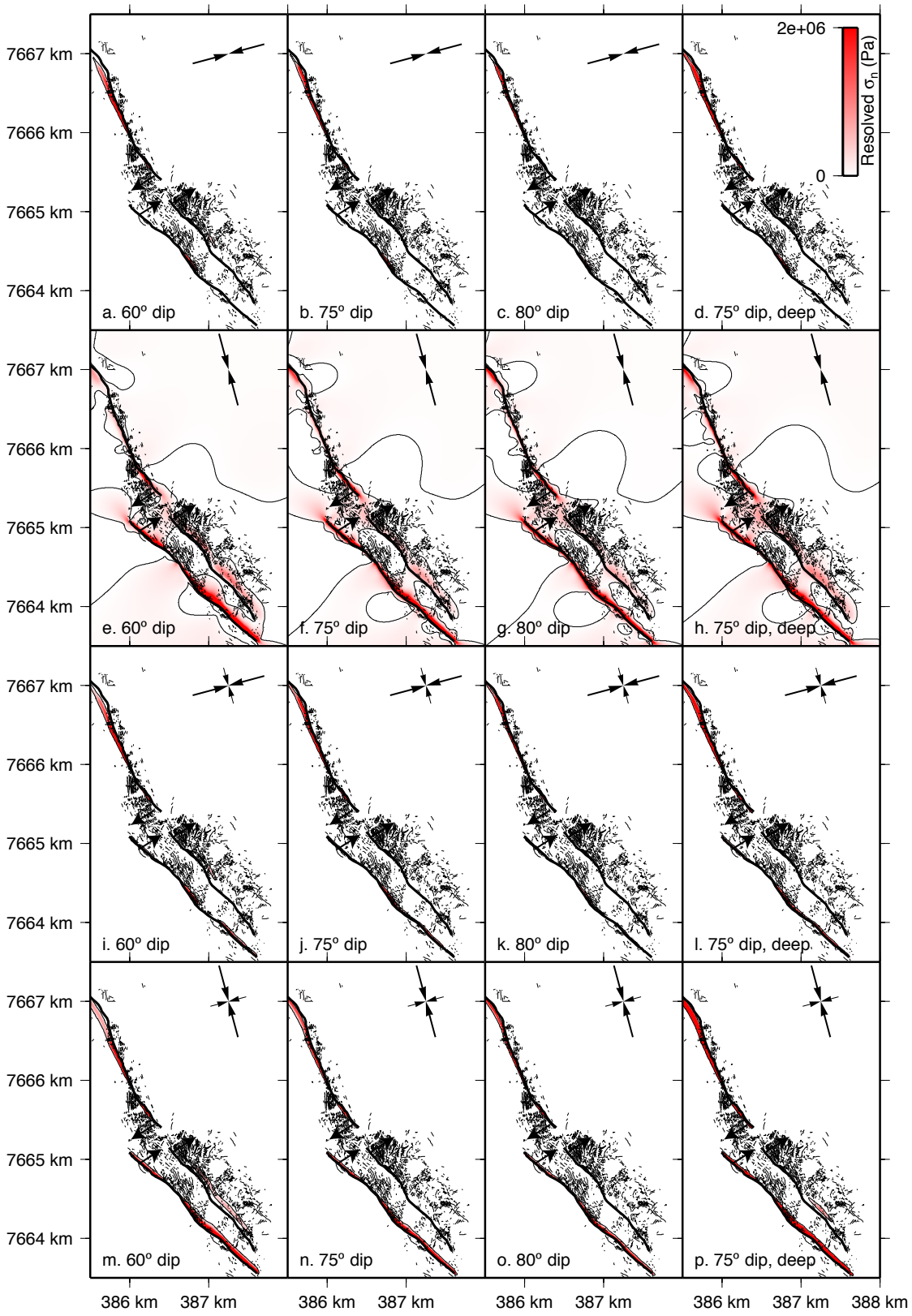
2e+06
0
Resolved σ_n (Pa)
7667 km
7666 km
7665 km
7664 km
a. 60° dip
b. 75° dip
c. 80° dip
d. 75° dip, deep
e. 60° dip
f. 75° dip
g. 80° dip
h. 75° dip, deep
i. 60° dip
j. 75° dip
k. 80° dip
l. 75° dip, deep
m. 60° dip
n. 75° dip
o. 80° dip
p. 75° dip, deep
386 km
387 km
388 km

When modeled as a normal fault system, the Antena-Bahía Blanca faults introduce stress perturbations that are more consistent with the distribution of surface cracking than those predicted by the reverse fault simulations (Figures D.6, D.7). For all models in this region, we evaluate the results by plotting the tension resolved onto vertical planes striking 345° and compare the stress fields with the extent of cracks. Uniaxial tension induces normal fault slip on all faults, resulting in the west-side-down motion on the Bahía Blanca and Antena Sur segments, and east-side-down motion of the Antena Norte segment (Figure D.8a). Models permitting near-surface opening of the fault (Figure D.6e-h) produce stress fields similar to simulations in which fault opening is prohibited (Figure D.6a-d), though the extent of the tensional stress field is slightly larger in the opening models. As mentioned in Section D.3.2, a larger magnitude of applied T forces opening of fault elements to a greater depth, which results in a wider zone of tension surrounding the fault at the surface. Some cracks striking approximately parallel to the faults lie outside of the zone of induced tension, suggesting that a process or parameter not considered by our simple models contributes to their formation.

Regardless of the fault dip and aspect ratio used, all of the normal fault models predict displacement fields relatively consistent with the geomorphology and topography of the region. Oblique dextral-normal slip is induced on all faults, resulting in a vertical displacement field (representative field shown by Figure D.8a) that closely resembles the topographic features of the fault system, which can be inferred from the satellite imagery in Figure 2.13. Even small details of the topography are reproduced by the models: the region of slight uplift lying between the two elongated zones of maximum uplift along the Bahía Blanca segment coincides with the region in which drainages have broken through the scarp topography,

suggesting that the barrier impeding incision is lower there (Figure 2.13). Also, the vertical displacement pattern between the Bahía Blanca and Antena Sur segments is very similar to the subtle topography of the region. Zones of negligible uplift, shown in green in Figure D.8a, are located where the less consolidated, younger, darker material has accumulated (Figure 2.13b), which occurs in slight depressions. Conversely, the zones of slight uplift between the Bahía Blanca and Antena Sur segments, shown in yellow in Figure D.8a, roughly coincide with the lighter-colored, gypsum-indurated sediments which are perched above the younger, darker alluvium (Figure 2.13b). Although the actual magnitude of uplift is greater on the Antena Sur segment, the slope of the vertical displacement field is far less than that across the Bahía Blanca segment, meaning that the scarp topography is less abrupt, as observed. In the transition zone between the two southern segments and the Antena Norte segment, negligible vertical displacement is predicted, consistent with the lack of a topographic scarp developed in this region. The pattern of uplift and subsidence along the Antena Norte segment mimic the linear trace of that fault, though the changes in scarp height that coincide with wide regions of cracking are not considered by the model and therefore are not expressed in the vertical displacement field.

When modeled as reverse faults, the Antena-Bahía Blanca faults produce perturbations to the regional stress field that are restricted to bands on the hanging-wall side of the faults that are far narrower than the extent of observed cracking (Figure D.7). The models subject to uniaxial compression directed 165° (Figure D.7e-h) show wider zones of tension that are more consistent with the distribution of cracks, including the region of enhanced cracking in the zone between the northern and southern faults, but the vertical displacement field does not resemble the

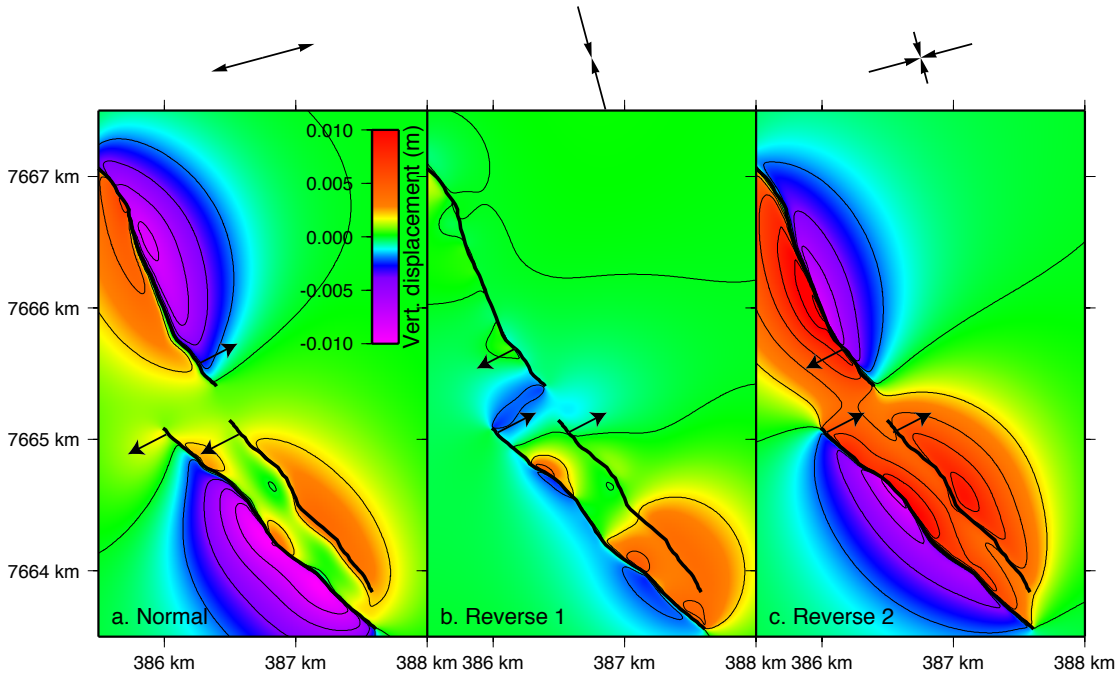

Figure D.8: Distribution of vertical displacement resulting from various models of the Antena-Bahía Blanca system. A) Vertical displacement from preferred normal faulting model (corresponding to Figure D.6h). B) Displacement field resulting from the model shown in Figure D.7h, which shows the stress field most consistent with the distribution of open cracks but vertical displacements that do not resemble the topography. C) The patterns of uplift and subsidence are very similar for all reverse fault models in rows 1, 3, and 4 of Figure D.7, so we show only a representative example here, corresponding to the model shown in Figure D.7o. The vertical displacement field of the normal fault model (A) is similar to the fault-related topography of the region, indicating that repeated episodes of fault slip are capable of constructing the observed topography. Vertical displacement shown in C is reasonably similar to that shown in A, suggesting that cumulative reverse faulting is also capable of producing the fault-related topography, but the corresponding surface stress field is less consistent with the crack distribution than the normal fault models (compare Figures D.6 and D.7, rows 1, 3, and 4). Further discussion appears in the text.

fault-related topography of the region (Figure D.8b). Reverse fault models subject to any of the other remote stress conditions show vertical displacement fields that approximate the fault-generated topography of the region as in the case of the normal fault models (Figure D.8c), yet the stress perturbation that they induce is less consistent with the extent of cracking.

D.3.4 Geoglifos fault

Cracks along the Geoglifos scarp appear to dominantly reflect fault-related deformation, but some clusters of cracks are affected by the NW-striking structure that intersects the northern part of the Geoglifos fault. While focusing on the interaction between cracks and the Geoglifos fault, we also model the intersecting structure as a vertical frictionless discontinuity to examine its effects on the local stress field, particularly around the point of intersection. Furthermore, we examine the effects of the southern Geoglifos segment, which is exposed at the surface with reported dip of 78°E (*Carrizo et al.*, 2007). As in the case of the Hombre Muerto and Antena-Bahía Blanca faults, we test both east and west dips of the fault subject to tensional and compressional remote stress conditions, respectively, in order to explore a wide range of possible fault kinematics.

Figures D.9 and D.10 show the stress perturbations caused by the Geoglifos fault (and splays from it) as a result of the tensional (Figure D.9) and compressional (Figure D.10) remote loading conditions. For this fault, we present the tensional stress resolved on vertical planes striking 350°. Cracks along the fault scarp are restricted to a narrow band at the scarp crest, roughly coincident with the zone of tension predicted by the reverse faulting models (Figure D.10) and wholly within the region of tension surrounding the normal fault models (Figure D.9). The dense

concentration of cracks around 7652 km N (cluster of thin black lines on Figures D.9 and D.10) is contained within the tensional stress predicted by all normal fault models, but the scarp-top tension predicted by the reverse fault models is anomalously thin at that latitude (Figure D.10).

The normal models considering the southern Geoglifos and northwest-striking splay faults (Figure D.9b, c) show patterns of stress perturbation that vary substantially from the single Geoglifos fault model (Figure D.9a). Interaction between the three faults is evident from the distribution of tensional stress, which is more consistent with the distribution of cracking than is the single fault model, particularly in terms of the northwest striking array of cracks that splays off of the northern part of the Geoglifos fault. The three-fault models subject to compressional boundary conditions (Figure D.10, bottom row) show zones of tension similar to those predicted by the corresponding single fault models (Figure D.10, top row). Only the model subject to uniaxial compression directed 165° (Figure D.10f) shows evidence for interaction between the modeled faults, yet this remote stress condition predicts a displacement field that does not resemble the scarp topography, mainly in that dome-like uplifts are predicted rather than the more linear ridge that results from the other compressional remote stress conditions (compare Figure D.11b and D.11c). Furthermore, the tension resolved onto northwest-striking planes is of low magnitude in these simulations. The model subject to NNW-SSE compression twice the magnitude of that direction ENE-WSW (Figure D.10h) shows some evidence for interaction between the Geoglifos fault and the northwest striking fault, as the zone of tension immediately surrounding the intersection is slightly larger than in that in Figure D.10e or g.

None of the reverse fault models demonstrate a zone of tension near the inter-

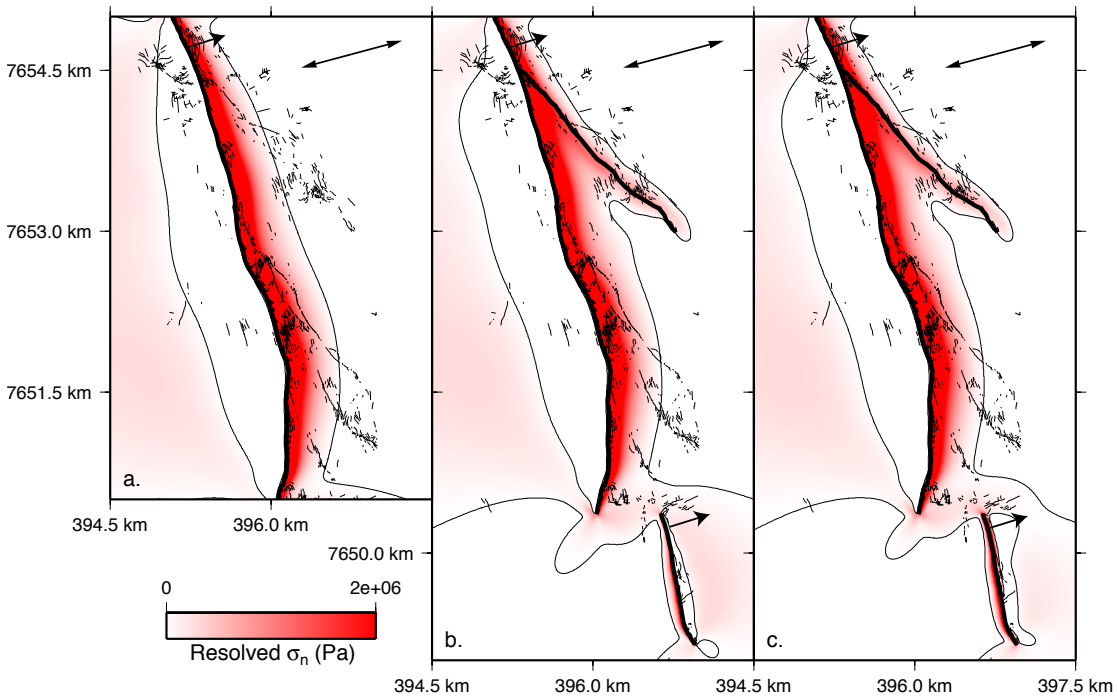

Figure D.9: Stress field resulting from the Geoglifos fault and associated splays, subject to 2×10^6 Pa of remote tension oriented 255°. The main strand of the Geoglifos fault (longest bold black line with NNW strike) dips 75°W and has an aspect ratio of $D = L/2$. A) Results of modeling a single fault. The distribution of tension, resolved onto planes striking 350°, is consistent with the extent of cracking localized on the scarp crest, but the several arrays of northwest-striking cracks lie outside of this predicted tension. B) Model incorporating three faults. The northwest striking fault in the north is modeled as a vertical fault with aspect ratio $D = L/2$. The southern fault has the same aspect ratio but dips 75°E, consistent with the fault plane observations of *Carrizo et al.* (2007). The interaction between these two subsidiary faults and the main Geoglifos fault results in a stress field more consistent with the distribution of cracking than the single fault model. C) Same as (B), but opening is allowed on the southernmost fault. Opening does not occur on the northern two faults, because they are buried to a depth such that the lithostatic stresses hold the fault clamped together; this burial depth was chosen based on the smoothness of fault-related topography and lack of surface exposure. The stress distribution is similar in B and C, except for minor details surrounding the southern fault.

Figure D.10: Stress fields resulting from the reverse fault modeling of the Geoglifos fault and related splays. The top row models show the stress fields resulting from the single Geoglifos fault, while the bottom row models show the stress perturbation caused by three modeled faults. Each column shows the results from the different applied remote stress tensors, as described for the other reverse fault models. Only the model subject to uniaxial compression directed 165° shows evidence for interaction between the northwest-striking striking and the main Geoglifos fault, as demonstrated by the low-magnitude zone of tension surrounding the fault intersection. All models except for those in the second column show an anomalously narrow region of tension in an area where surface cracks are concentrated (around 7652 km N) and show no interaction between the main Geoglifos fault and the southern splay. However, many of the cracks restricted to the scarp crest do lie within the zone of predicted tension for most models.

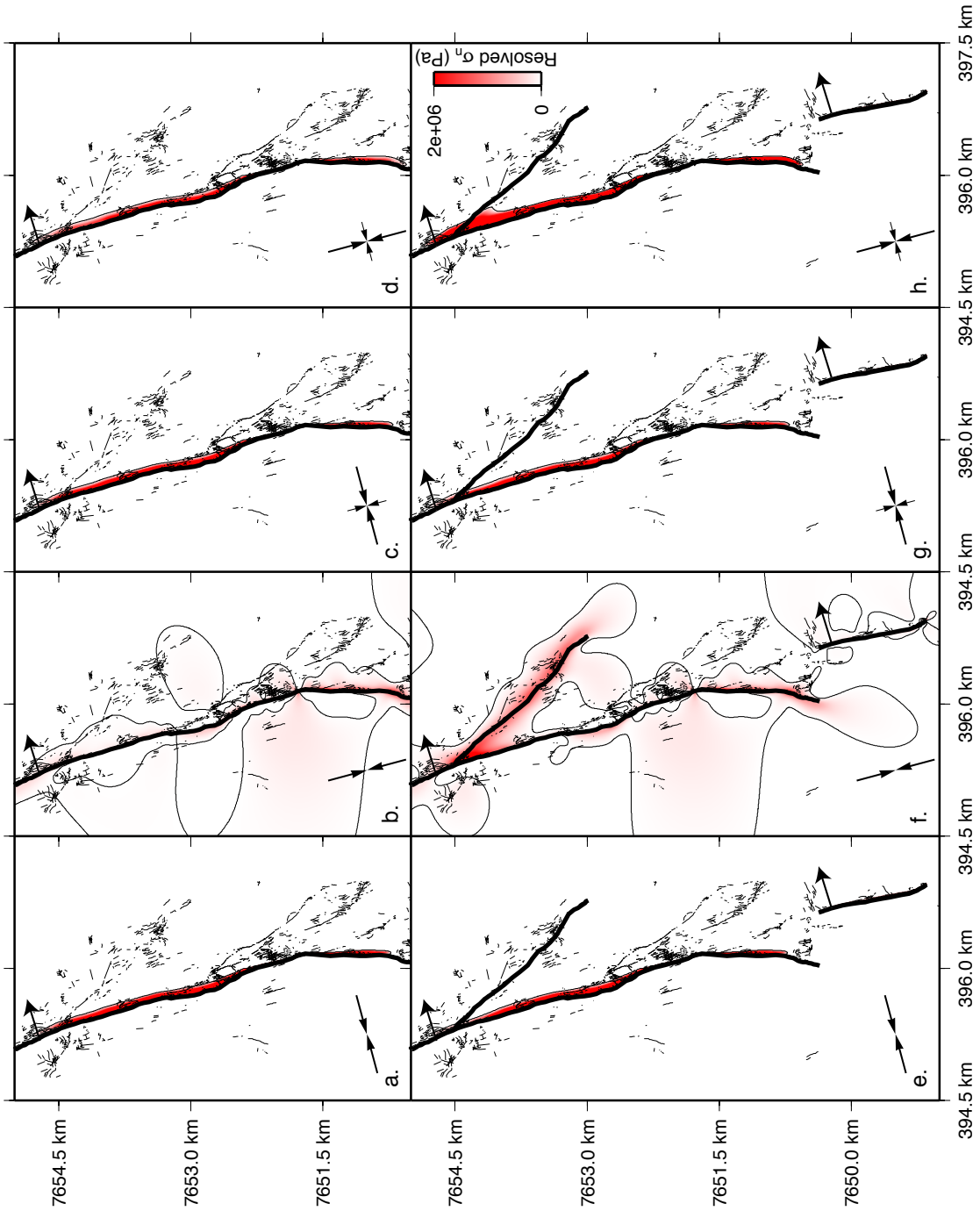
a.
b.
c.
d.
e.
f.
g.
h.
Resolved σn (Pa)
2e+06
0
7654.5 km
7653.0 km
7651.5 km
7650.0 km
394.5 km
396.0 km
394.5 km
396.0 km
394.5 km
396.0 km
397.5 km

acting segments of the Geoglifos fault with its southern extension (Figure D.10), whereas the normal fault models show regions of low to moderate magnitude tensional stress within a "transition zone" between the two fault segments (Figure D.9b, c), consistent with the diffuse cracking in that region.

We did not explicitly model the southernmost northwest-striking array of en echelon open cracks as a fault because it has no topographic expression along its trace. However, we expect that inclusion of a buried, vertical discontinuity similar to that which represents the northern array of northwest-striking open cracks would result in little change to the stress field of the reverse faulting models while perturbing the normal faulting models in a manner similar to that of the northern fault. This would make the extent of tensional stress of the normal fault models more consistent with the distribution of cracks, particularly in terms of the dense cluster located near the intersection of the northwest-striking array and the main Geoglifos fault.

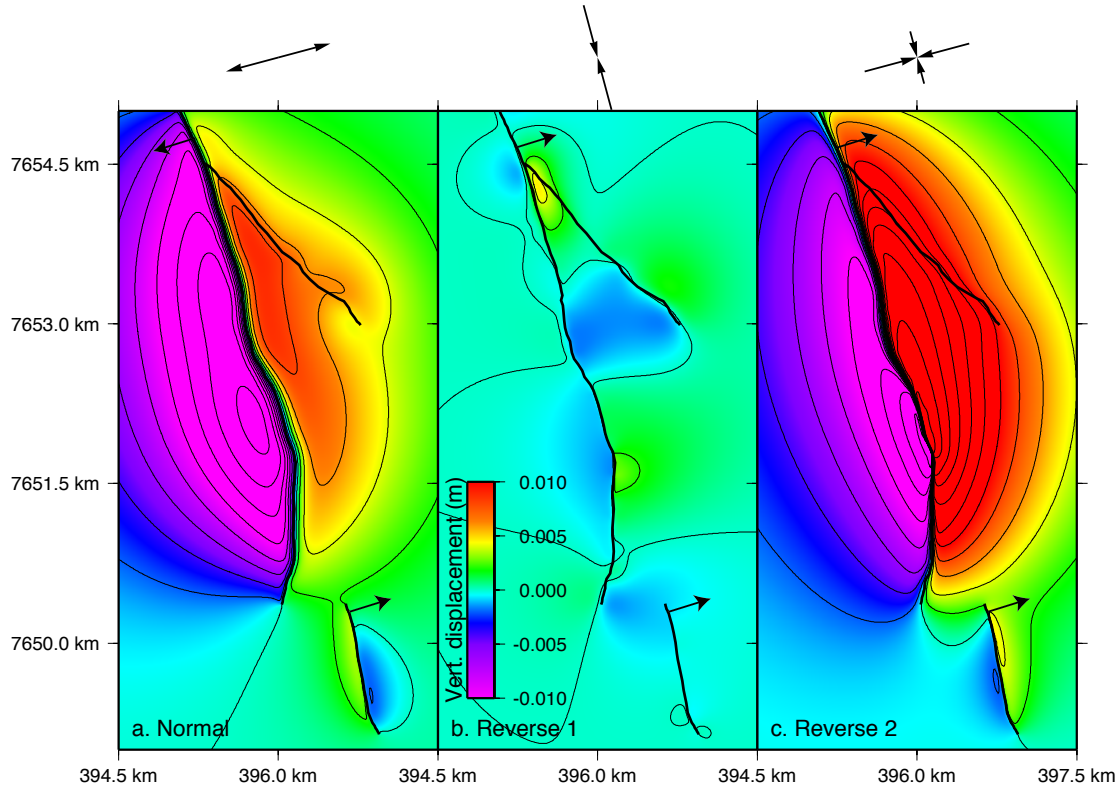

Figure D.11: Patterns of vertical deformation resulting from the Geoglifos fault modeling. A) Vertical displacement field predicted by the model corresponding to Figure D.9c. B) Vertical displacement field corresponding to the model shown in Figure D.10f, which is the reverse faulting model that produces the stress field most consistent with the extent of cracking. The low-magnitude, dome- and bowl-like shapes of predicted uplift and subsidence zones are inconsistent with the linear nature of the fault scarps. C) Representative model showing vertical uplift patterns that result from the other reverse fault models, which are relatively similar to each other. These patterns are similar to those of the normal faulting model, and thus suggest that the fault-related topography can be explained by accumulated slip on the modeled faults. In C, no anomalous topography is predicted along the northwest striking splay fault, as it is in A and as is observed in the field. However, the sense of displacement along the southern splay fault in A is opposite its observed morphology, which is accurately represented in panel C.

BIBLIOGRAPHY

Carrizo, D., G. González, and T. Dunai (2007), Constricción neógena en la cordillera de la costa norte de Chile: Neotectónica y datación de superficies con ^{21}Ne cosmogénico, *Revista Geológica de Chile*, *34*, in review.

Crider, J. G., and D. D. Pollard (1998), Fault linkage: Three-dimensional mechanical interaction between echelon normal faults, *Journal of Geophysical Research*, *103*(B10), 24,373–24,391.

González, G., J. Cembrano, D. Carrizo, A. Macci, and H. Schneider (2003), The link between forearc tectonics and Pliocene-Quaternary deformation of the Coastal Cordillera, northern Chile, *Journal of South American Earth Sciences*, *16*, 321–342, doi:10.1016/S0895-9811(03)00100-7.

APPENDIX E

REGIONAL CRACK MODELING DETAILS (SUPPLEMENT TO CHAPTER 3)

E.1 Crack-based inversion strategy

To explore the range of coseismic slip distributions that would result in deformation consistent with that exhibited by the surface cracks, we invert the permanent strain field shown by the cracks for motion on the subduction thrust. Elastic dislocation theory (e.g., *Okada*, 1985, 1992) shows a linear relationship between a displacement discontinuity (i.e., relative motion) on a modeled fault and the displacement and strain fields throughout an elastic medium. Therefore, any displacement or deformation data throughout the medium can be inverted to solve for the distribution of slip on the modeled fault. If the fault geometry is known, the inversion is linear and computationally inexpensive, whereas solving for fault geometry in tandem with the slip distribution is a complicated, nonlinear problem (e.g., *Simons et al.*, 2002). We use the three-dimensional elastic boundary element code Poly3DInv (*Maerten et al.*, 2005) to invert the crack-based strain field for slip on the subduction thrust. This program permits various constraints to be applied during the inversion, notably the ability to simultaneously minimize the misfit between model and data and the roughness of the slip distribution, and to limit the sense of strike- and dip-slip to a specified direction through use of a weighted non-negative least-squares inversion (e.g., *Menke*, 1984; *Maerten et al.*, 2005). In all of our inversions, we restrict slip to be reverse and/or left-lateral, consistent with the direction of plate convergence. Furthermore, we prohibit slip on the elements that line the edges of the modeled fault.

We carry out a series of inversions with varying parameters to investigate which resolved properties of the slip distribution are most robust. All modeling assumes a known subduction thrust geometry which we constructed by fitting a three-dimensional curved surface to the Wadati-Benioff zone contours of *Cahill and Isacks* (1992) between depths of 0 km (trench) and 75 km, then discretized with triangular elements in order to retain the curvature (Figure E.1). We group the inversions in four subsets based on permutations of two parameters: use of crack density-weighted strain magnitudes versus identical strain magnitudes at each cluster ("u" suffix in Table E.1), and use of a coarse fault mesh versus a denser mesh ("d" suffix in Table E.1). The crack density-based strain magnitude is equal to the mean of the total length of cracking within 90 m resolution cells throughout each crack population divided by the area of each grid cell, to yield crack density in m/m^2 or m^{-1}. The range of this value amongst all 16 crack populations is 0.058–0.124 m^{-1}. We convert the crack density to strain magnitude by modulating the density value by an exponent. Test inversions of the crack dataset indicated that multiplying crack density by 10^{-5}, yielding strain magnitudes of 5.8×10^{-7} – 1.24×10^{-6}, resolved maximum slip values of ∼7 m, with an overall moment magnitude of 8.5. This is similar to the estimates of maximum slip and moment for the 1877 earthquake (*Nishenko*, 1985). For the uniform strain models, we chose a magnitude of 1×10^{-6}, which resolved a maximum slip value of 8 m and moment magnitude of 8.5, also consistent with the estimated parameters.

For each of the four combinations of variable/uniform strain magnitudes and coarse/dense meshes, we generate a model using four subsets of the constraining data (Figure E.2). One model in each group uses the mean strike of all crack populations ("A" prefix in Table E.1), while the three other models use datasets that

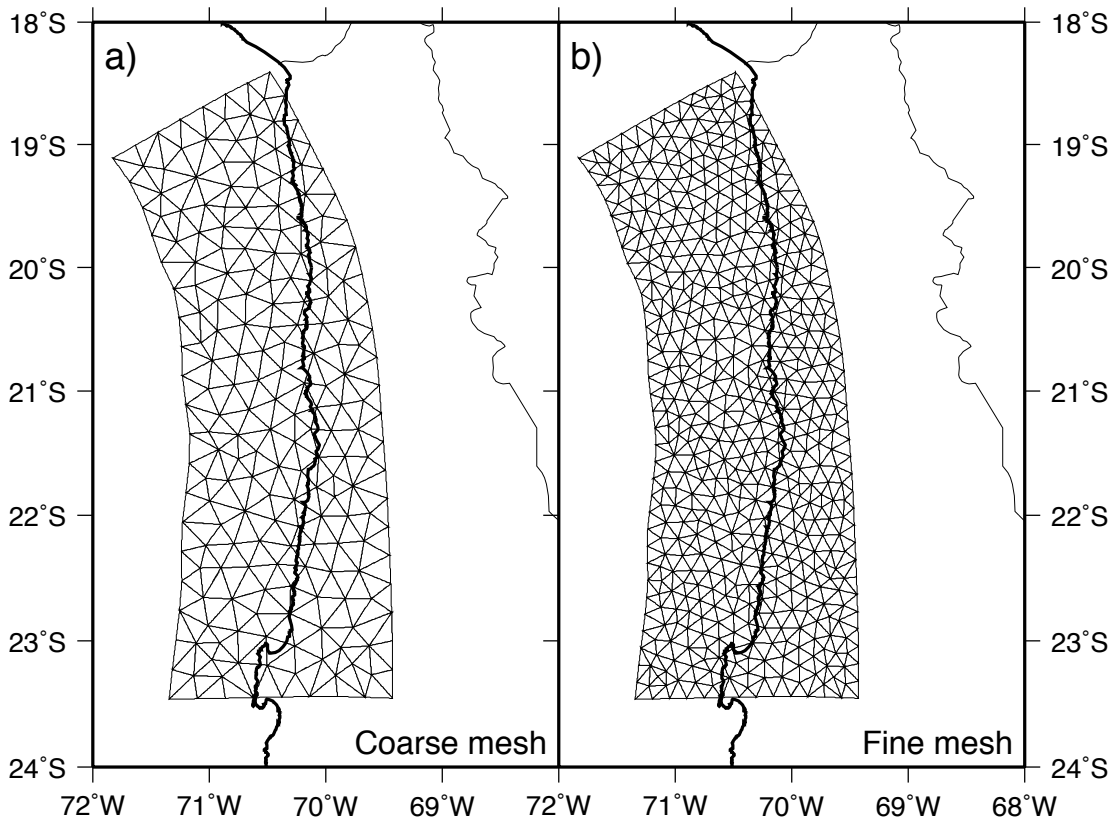

Figure E.1: Coarse (369 elements, a) and fine (1009 elements, b) triangular discretization of the Iquique segment of the plate boundary used in the inverse modeling.

Table E.1: Inversion model parameters

Model[a]	N_E[b]	Moment (N-m)[c]	M_w	Slip (m)		Slip az.[d]	Angular error[e]			
				Mean	Max.		Min.	Max.	Mean	Total
A	369	6.3×10^{21}	8.5	2.1	8.0	242	0.2	75.1	18.2	291
S1	369	3.0×10^{21}	8.2	0.9	8.0	199	7.6	63.9	34.4	550
S2	369	3.0×10^{21}	8.3	1.0	8.0	229	0.1	68.0	19.0	304
S3	369	2.2×10^{21}	8.2	0.7	8.0	213	2.8	75.7	26.9	430
Au	369	6.8×10^{21}	8.5	2.3	8.0	239	0.3	30.3	13.1	210
S1u	369	3.4×10^{21}	8.3	1.1	8.0	204	4.1	43.0	18.3	293
S2u	369	3.7×10^{21}	8.3	1.2	8.0	224	0.4	28.4	9.0	144
S3u	369	2.3×10^{21}	8.2	0.7	8.0	228	6.7	72.1	23.4	374
Ad	1009	8.9×10^{21}	8.6	2.9	8.0	237	0.8	59.5	15.8	253
S1d	1009	4.3×10^{21}	8.4	1.4	8.0	192	0.8	49.4	15.1	242
S2d	1009	3.5×10^{21}	8.3	1.1	8.0	225	2.5	56.2	20.3	325
S3d	1009	2.3×10^{21}	8.2	0.7	8.0	235	3.3	48.8	21.0	336
Adu	1009	6.2×10^{21}	8.5	2.0	8.0	240	0.4	33.4	13.5	217
S1du	1009	5.3×10^{21}	8.4	1.8	8.0	205	3.2	40.7	15.0	241
S2du	1009	3.8×10^{21}	8.3	1.2	8.0	218	0.3	27.5	11.3	181
S3du	1009	3.5×10^{21}	8.3	1.1	8.0	229	8.6	43.5	18.8	300
Adux	1009	7.0×10^{21}	8.5	2.3	8.0	235	0.9	44.1	15.3	260
S1dux	1009	5.4×10^{21}	8.4	1.8	8.0	198	1.2	43.6	17.4	295
S2dux	1009	4.0×10^{21}	8.3	1.3	8.0	222	1.2	26.1	12.5	213
S3dux	1009	4.6×10^{21}	8.4	1.5	8.0	216	1.1	41.4	14.8	251

[a]Leading number refers to constraining dataset used in the inversion. "A" indicates that all crack data were used in the inversion, while "S" denotes the subset of data used (subset 1, 2 or 3; see Figure E.2). Appended "u" indicates uniform strain magnitude assumed for all constraining data, "d" indicates a denser-spaced element mesh (Figure E.1), and "x" indicates models including the supplementary postulated data point at 22°S (Section E.2.4).

[b]Number of elements

[c]Moment is defined as the modulus of rigidity (3×10^{10} N/m^2) times the sum of the slip times area of all fault patches.

[d]Mean azimuth of the element slip vector projected onto the half-space surface. The mean value is weighted by the slip magnitude.

[e]Angular difference between the mean observed crack strike in each cluster and calculated most-compressional principal stress axis at the cluster location.

exclude information from up to 7 of the 16 clusters (S1, S2, or S3 prefix in Table E.1). These subsets were chosen to reduce the number of closely-spaced control points (S1 and S2) or to distribute more evenly the control points along the coastline (S3, Figure E.2). However, the lack of any crack population between 21.5° and 22.5°S limits the resolution of slip within those bounds. As mentioned in the main text, high topography in this region impedes development of the gypsum-indurated sediment crust, which plays a key role in crack preservation. Therefore, coseismic stress fields in this segment are likely capable of producing and reactivating cracks, but the lack of a durable surface crust prevents their long-term preservation.

E.2 Inversion results

We use the resolved slip distributions to calculate the principal stress axes at each crack population location. Before carrying out this forward modeling, we scale the resolved earthquake slip such that the maximum slip magnitude is 8 m, roughly consistent with the maximum value estimated for the 1877 earthquake (*Nishenko*, 1985; *Comte and Pardo*, 1991). The pattern of slip — and therefore the calculated orientations of principal stress at the surface — does not change as a result of this modification. We evaluate the goodness-of-fit of each inverse model by calculating the angular difference between the mean crack strike observed within each cluster and the most-compressional principal stress axis calculated at the cluster location. As mentioned in the main text, the strike of a mode 1 crack is parallel to the σ_1 direction of the stress field that created it. We calculate the minimum, maximum, and mean angular difference between the observed and predicted crack strike, and we summarize the overall model misfit by summing the angular discrepancies between model and data for all crack populations (Figures E.3-E.6, Table E.1).

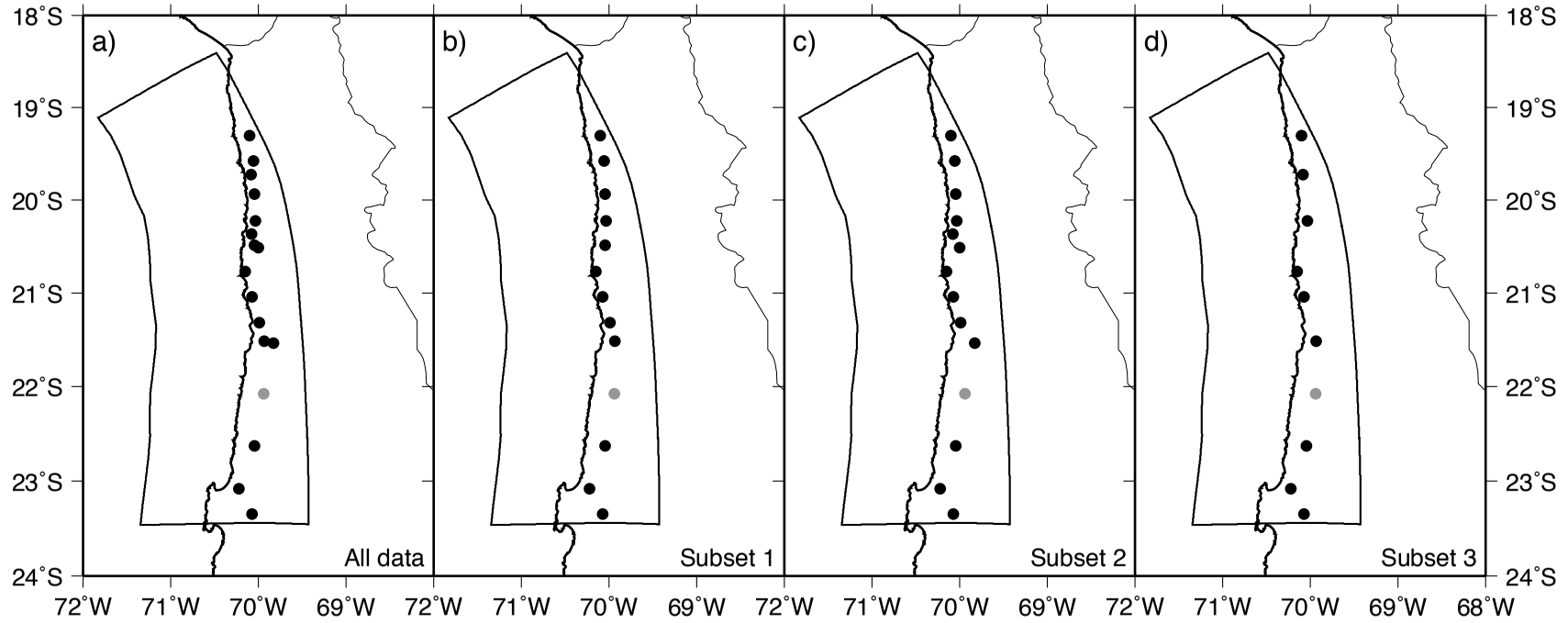

Figure E.2: Subsets of crack strain data used in the inversions. Black dots show locations of crack clusters that comprise each set. The gray dot indicates the position of the additional strain tensor used to fill the large gap in constraining data between 21.5° and 22.5°S (see Section E.2.4).

There are several fundamental differences between the models. For all permutations of geometry and data subsets, the slip distributions constrained using a uniform strain magnitude for all crack locations produce a stress field that better fits the observations than the corresponding model that used the variable, crack density-based strain magnitudes. The mean slip azimuth, defined as the mean surficial projection of the element slip vector, weighted by slip magnitude, is consistently rotated southwest from the expected direction opposite the plate convergence azimuth of 255° (Table E.1). Inversions of the full crack dataset resolve a mean slip vector closest to this expected value, while use of subset 1 results in slip vectors with a stronger sinistral component than expected.

E.2.1 Slip distribution

The spatial distribution of slip varies substantially between models. For the most part, "A" models show widely distributed slip and thus are characterized by larger moments than the corresponding "S" models (Figure E.3, Table E.1). One curious feature of the A models is that the resolved slip distribution is such that contour lines do not close towards the termination of the modeled rupture zone. This is particularly evident along the northern part of the updip edge of the model, where the 7 m slip contour is open as it approaches the trench (e.g., Figure E.3c). This suggests that, if the modeled geometry were larger, slip would be resolved over a greater area. In the case of the open contours near the trench, extending the model geometry is physically unreasonable, as the western edge of the modeled fault marks the extent of the plate boundary. S1 models show a concentration of slip off the coast of Iquique, as well as a region of slip just north of 23°S latitude (Figure E.4). The slip on this southern patch is strongly partitioned, with the deeper

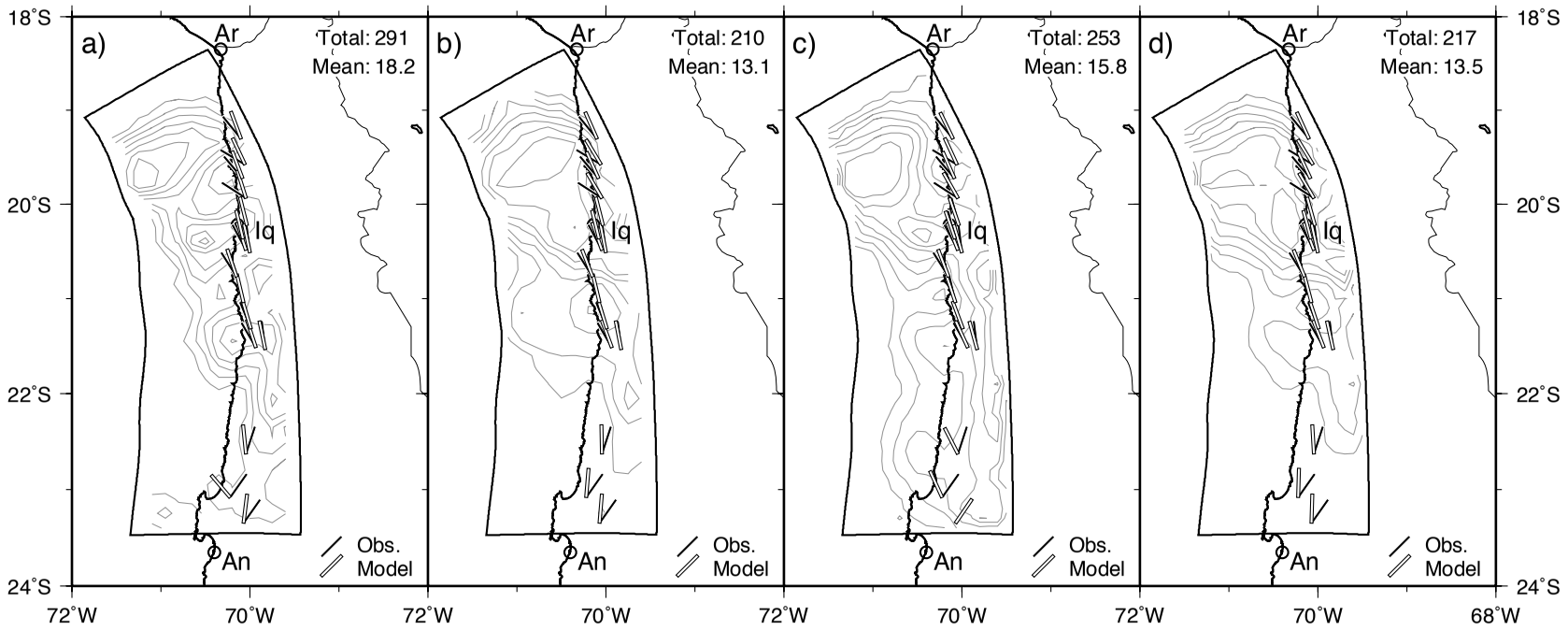

Figure E.3: Slip distributions resolved using all crack populations as constraining data and forward modeling results. The slip magnitude are represented by the contour lines (1 m slip interval). Population locations are shown in Figure E.2a. In each panel, the solid vectors show the observed mean crack strike at each crack location, and the hollow vectors show the σ_1 direction calculated using the slip distribution. The total and mean angular errors, defined as the angular difference between the observed and calculated orientations, are shown in the upper right corner of each panel. City names are abbreviated as Ar (Arica), Iq (Iquique), and An (Antofagasta). a) Model using coarse mesh and crack density-based strain magnitudes ("A" in Table E.1). b) Model using coarse mesh and uniform strain magnitudes for all crack populations (Au). c) Model using fine mesh and variable strain magnitudes (Ad). d) Model using fine mesh and uniform strain magnitudes (Adu).

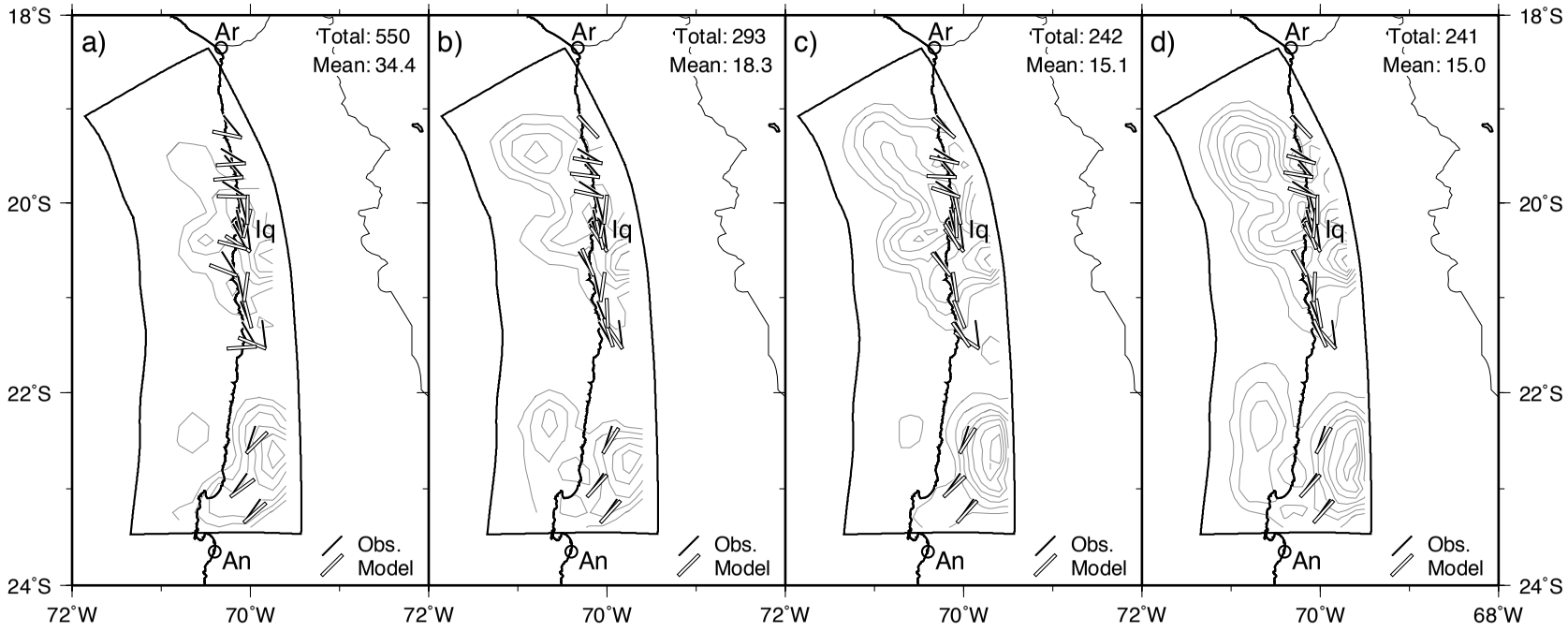

Figure E.4: Slip distributions resolved using subset 1 of the crack data, with locations shown in Figure E.2b. a–d) Models with parameters as described in Figure E.3.

part of the patch (around 75 km depth) dominated by nearly dextral slip and the shallower portion characterized by dominantly reverse slip. Inversions based on the S2 dataset also show a concentration of slip offshore Iquique, which tapers reasonably smoothly in all directions, except for some open contours along the down-dip extent of the model geometry (Figure E.5). A patch of lower magnitude slip ($\sim$1 m) near the southern extent of the modeled rupture geometry is also present in S2 models. In contrast to the southern patch of slip in the S1 models, the S2 patch is located around 30 km depth and is dominantly reverse slip. The S3 models also show a slip distribution very similar to that of the S1 models (Figure E.6) in terms of the concentration of slip near Iquique and the partitioning of slip in the southern slip patch. The similarities between the S1 and S3 slip distributions indicates that the crack orientation data omitted in the S3 inversions (Figure E.2) does not affect large-scale patterns of earthquake slip. As the goodness-of-fit statistics indicate, however, the small-scale patterns of slip resolved due to the inclusion of additional data in S1 models as compared to S3 models produce a surface stress field that is more similar to the deformation exhibited by the cracks.

E.2.2 Effects of data subsampling and uniform strain

The two modifications to the constraining data that we explore in the inverse modeling exclusion of strain information from some of the crack populations and assigning a uniform strain magnitude to all populations generally improve the statistical fit between the observed and predicted crack strikes. In all cases, inversions using the uniform strain magnitude produce better fits to the data than the corresponding crack-density based strain magnitude models. The uniform strain

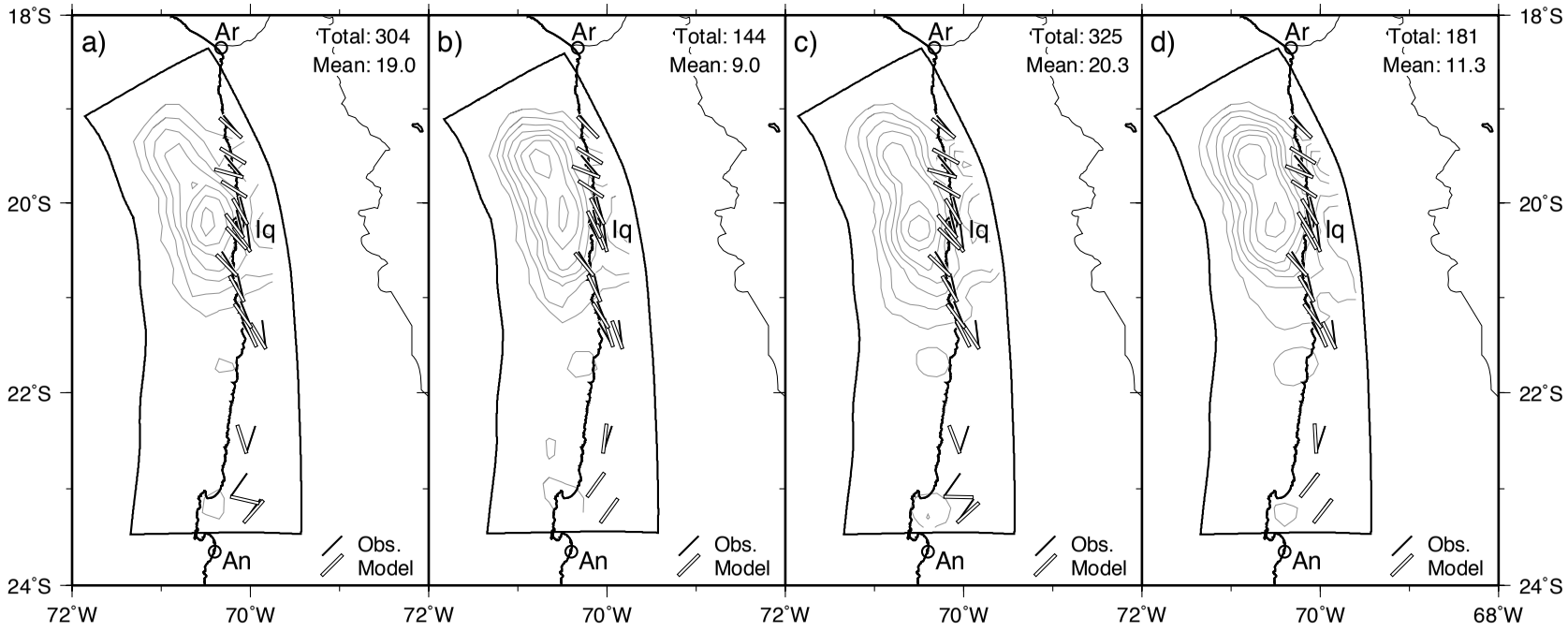

Figure E.5: Slip distributions resolved using subset 2 of the crack data, with locations shown in Figure E.2c. a–d) Models with parameters as described in Figure E.3.

S2 models, which exclude strain data from 3 of the 16 crack populations (Figure E.2), show the best statistical fit to the data (Figure E.5b, d; Table E.1). Inversions based on all crack populations (A models) predict principal stress directions consistent with the mean crack strikes of many of the clusters north of 22°S but inconsistent with the three southern populations (Figure E.3). S1 and S3 models show, in general, poor fits between the predicted and observed crack strikes for those populations not used as constraining data. The aforementioned patch of almost purely dextral slip on deep portions of the southern extent of the S1 models produces a stress field consistent with the crack orientations in the three southern populations, but this sense of slip is physically unreasonable considering the known plate convergence direction and expected rake of the coseismic slip vectors.

E.2.3 Effect of fault mesh density

The density of the fault mesh also affects the statistical fit between the predicted and observed crack strikes. In the majority of cases, slip resolved onto the dense mesh produces a stress field more consistent with the crack data than the corresponding inversion using the coarse mesh. In the S2 and uniform strain A models, however, the coarse mesh model results in a better fit. This likely results from the smoothing routine involved in the inversion. Because the dense mesh contains elements that are more numerous and closer-spaced than the coarse mesh, the overall slip distribution is smoother. The more abrupt changes in slip magnitude between adjacent elements of the coarser mesh allow for more heterogeneity in the slip distribution, which in some cases provides a better fit than the corresponding fine mesh model.

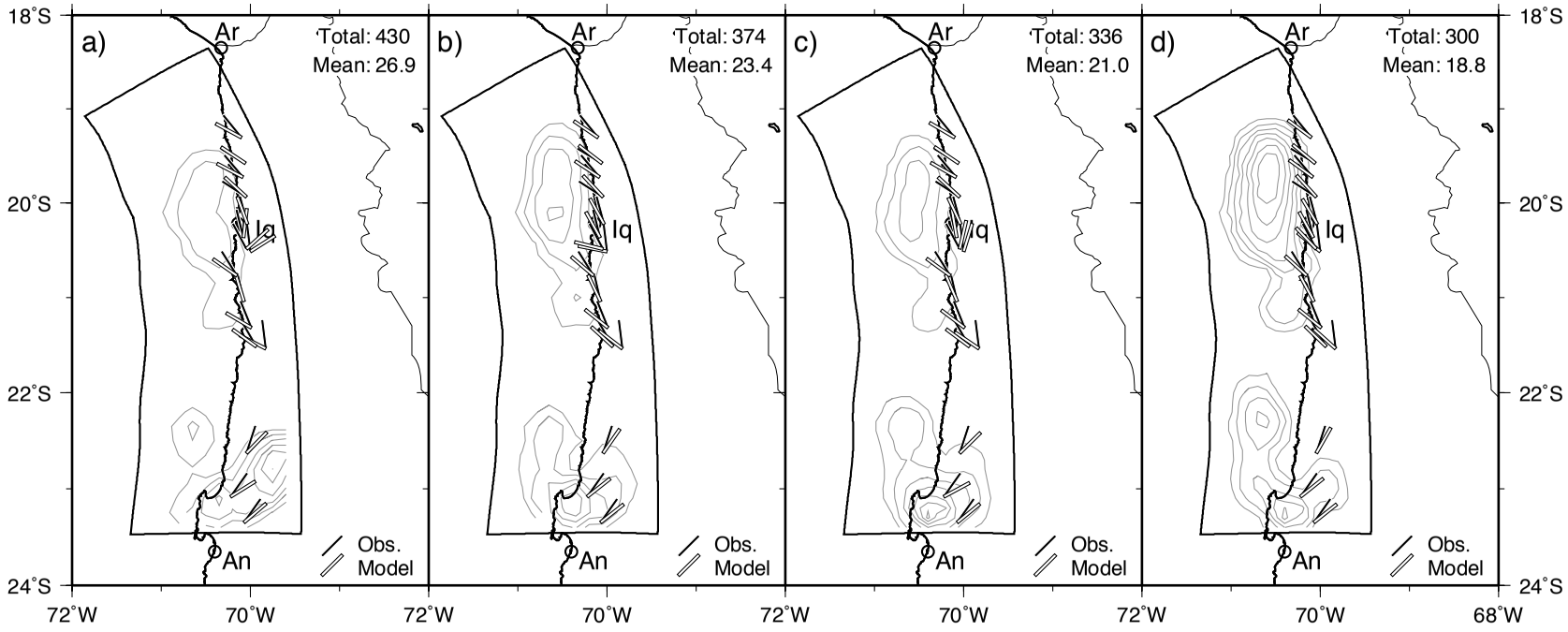

Figure E.6: Slip distributions resolved using subset 3 of the crack data, with locations shown in Figure E.2d. a–d) Models with parameters as described in Figure E.3.

E.2.4 Addition of an inferred crack population

Because of the large gap in the constraining data between 21.5° and 22.5°S and the resulting lack of slip resolved within this latitude range, we add a strain tensor to each subset of the crack-based strain data to investigate the differences in the resolved coseismic slip. This additional data point lies at the average of the latitude and longitude of the crack populations bounding it (gray circle, Figure E.2), with principal strain directions assigned to the mean of those of the bounding populations. As mentioned above and in the main text, the lack of cracking observed in this region may result exclusively from the topographic and climatic conditions that inhibit crack preservation. We assume that earthquakes are capable of producing cracks around this latitude and postulate a supplementary data point to reflect that. The results of the inversion for the supplemented strain data sets are shown in Figure E.7.

Addition of the postulated strain tensor in the data gap does not substantially affect the slip distribution of any of the 4 models (compare Figure E.7 with the corresponding results shown in panel (d) of Figures E.3-E.6). Inclusion of the supplementary strain tensor resolves minor slip further south in model A (Figure E.7a), connects two distinct patches of slip in model S1 (Figure E.7b), is virtually indistinguishable from model S2 (Figure E.7c), and slightly enhances both the magnitude and extent of the southern slip zone of model S3 (Figure E.7d). The total angular error of model S3 with the supplementary data point is actually less than the original model, but in all other models the total angular error predictably increases with the addition of the data point. For the most part, the fit between the models and crack strike of the supplementary data point is good, with an angular error less than 25° in all cases (Figure E.7).

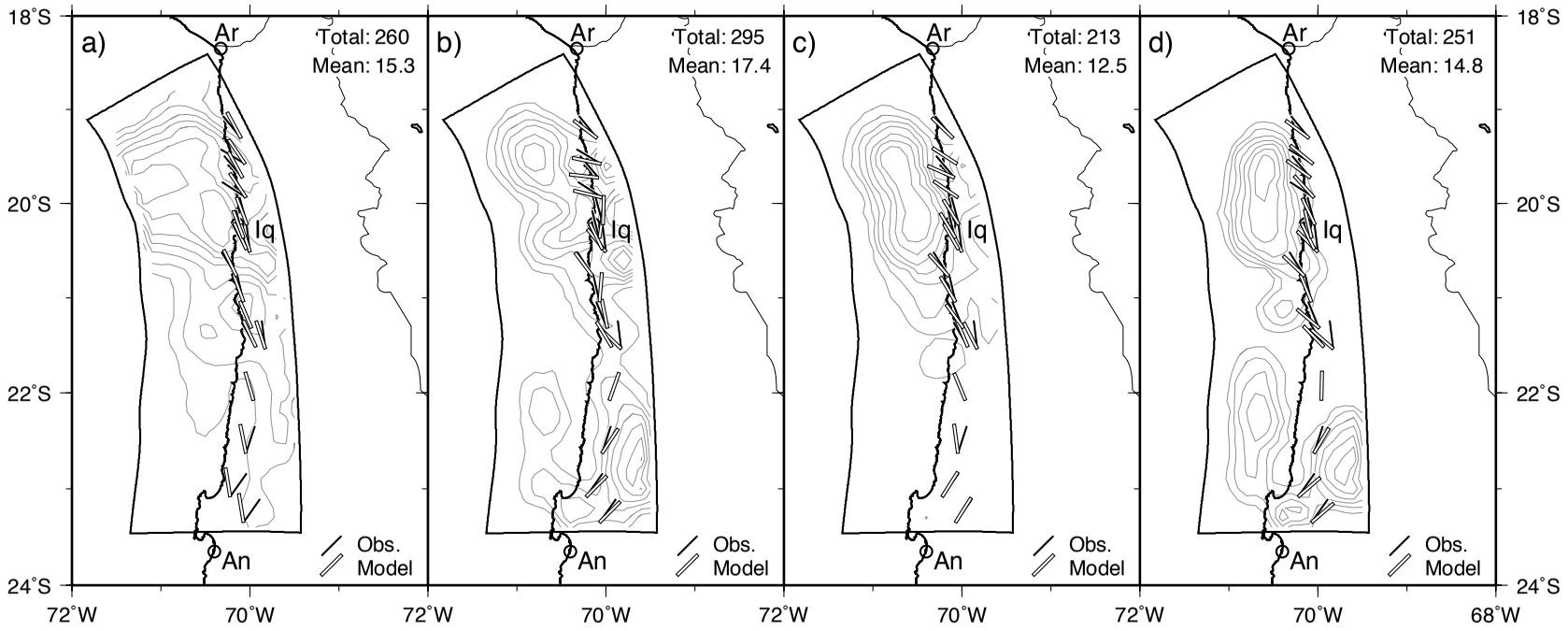

Figure E.7: Slip distributions resolved onto the dense mesh using the crack-based strain data sets supplemented by an additional strain tensor at ∼22°S. This artificial data point fills the large gap in the constraining data (see Figure E.2). Angular error results are shown for the supplemented A (a), S1 (b), S2 (c), and S3 (d) data sets. Symbols in each panel are as described in Figure E.3.

E.2.5 Effect of smoothing parameter

To investigate the effects of the smoothing parameter on the slip distribution and resulting fit of the predicted crack strike to the observations, we vary the smoothing parameter for model S2du, which is the statistically best-fitting dense mesh model. Keeping all other model parameters equal, we vary the smoothing parameter from 0.05 to 1 in increments of 0.05. We present the slip distributions and predicted crack strike results for four inversions, with smoothing parameters 0.1, 0.3, 0.7, and 0.9, in Figure E.8. Figure E.9 shows the relationship between the smoothing parameter and the angular error of the models with respect to the crack data. The inversion using the smoothing parameter of 0.7 produces a stress field most consistent with the deformation shown by the cracks (Figure E.8c, E.9). A local minimum in the smoothness versus error plot occurs at smoothing factor 0.35.

E.2.6 Preferred model

We chose model S2u as our preferred model discussed in the text. This was based upon the low mean and total error and the fact that the resolved slip lies within the modeled geometry. The geometry extends to 75 km depth, which lies below the presumed down-dip limit of seismogenesis of 45–50 km (*Tichelaar and Ruff*, 1991; *Comte et al.*, 1994). Slip may, however, originate at the locus of maximum moment release and propagate up-dip, down-dip, and along strike. The plate interface below the seismogenic zone is thought to be characterized by velocity-strengthening behavior (*Oleskevich et al.*, 1999), so slip that propagates into this region should in theory decrease to zero with increasing depth. Therefore, resolved slip that reaches a maximum within the seismogenic zone and smoothly decreases in magnitude towards both the trench and the down-dip extent of the seismogenic

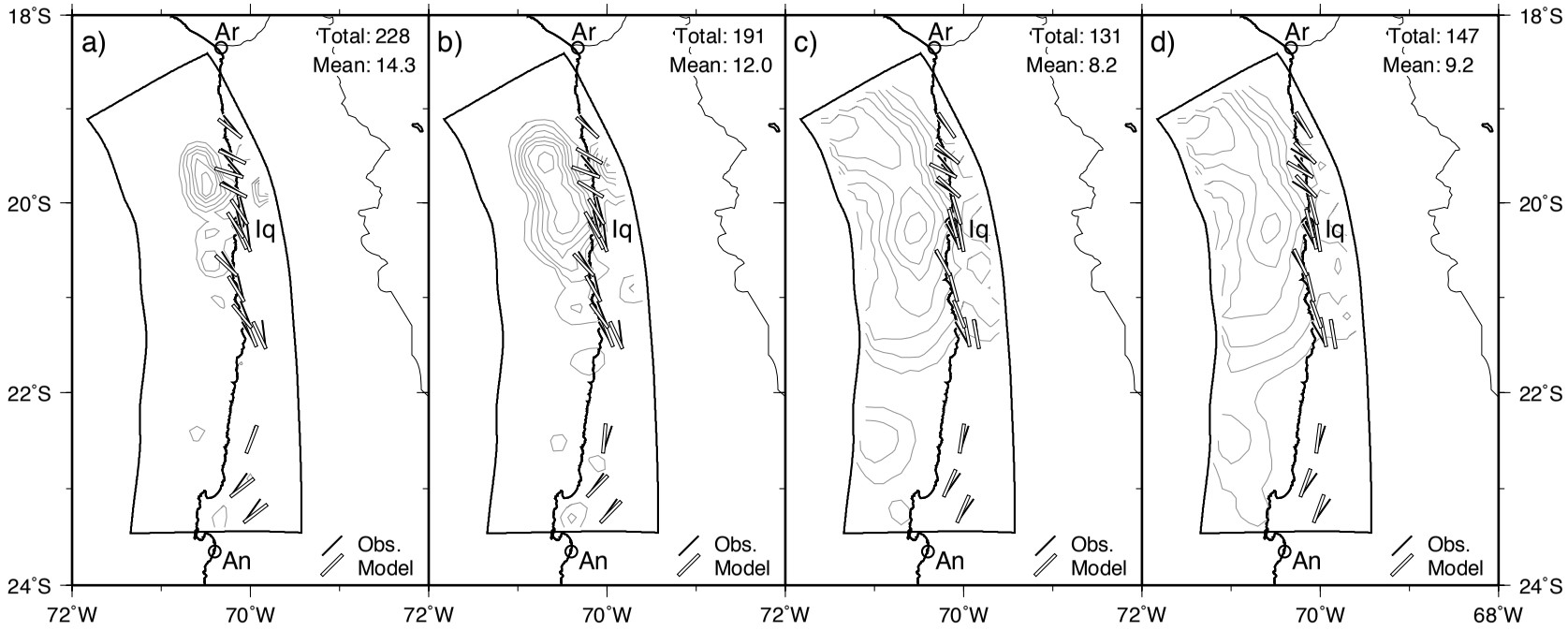

Figure E.8: Slip distributions resolved onto the dense fault mesh by inverting uniform strain magnitudes at the S2 subset crack locations, with smoothing parameters of a) 0.1, b) 0.3, c) 0.7, and d) 0.9. Annotation of the panels is as described in the caption for Figure E.3.

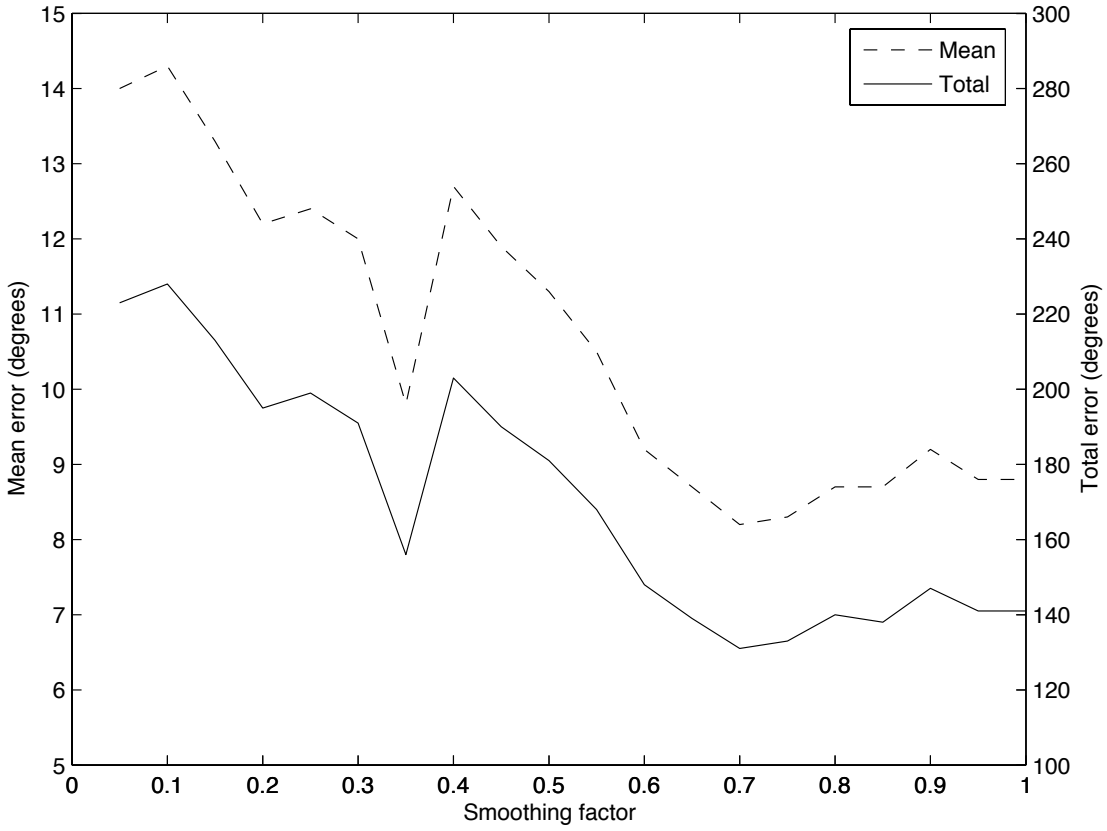

Figure E.9: Plot of smoothing parameter versus angular error for variants of the S2ud model. Mean (dashed, left axis) and total (solid, right axis) angular errors between model and data were calculated for S2ud models with smoothing parameters from 0.05 to 1 in increments of 0.05.

zone is physically plausible. Conversely, patterns of slip showing an increase in magnitude outside of the seismogenic zone are suspect. We distinguish plausible and suspect slip patterns based on the closure of contours near the edges of the model geometry: models in which contours are closed near the down-dip edge, such as model S2u (Figure E.5b) and most S3 models (Figure E.6b-d) are plausible, while those that show open contours near the boundaries, such as the near-trench contours in the A model (Figure E.3) are less reasonable. We prefer model S2u over the variant of S2ud with a smoothing parameter of 0.7. The latter results in a slightly better fit to the data (total angular error of 131 versus 144 for S2u), but shows many open slip contours near the model edges (Figure E.8c).

E.3 Dynamic stress change modeling

The associated electronic material contains two animations (`antodyn.mp4` and `areqdyn.mp4`) that show the temporal evolution of the principal stress axes resulting from the 1995 Antofagasta and 2001 Arequipa earthquakes. Animation `antodyn.mp4` shows the first 100 seconds of the Antofagasta event, with a time interval of one half second per frame. Figure `areqdyn.mp4` shows the first 175 seconds of the Arequipa earthquake, also with a half-second per frame time interval. The models were calculated using the method of *Cotton and Coutant* (1997), the one-dimensional seismic velocity model of *Husen et al.* (1999), and the spatiotemporal distributions of coseismic slip of *Pritchard et al.* (2006, 2007).

Animation `antodyn.mp4`. Animation, in `*.mp4` format, showing the temporal evolution of the horizontal principal stress axes at the surface due to the 1995 Antofagasta earthquake. The animation shows the principal stress axes calculated at half-second intervals for the first 100 seconds of the event. Red axes represent principal tension and blue axes represent principal compression. Note that in some cases, both axes are tensional or compressional (see Chapter 3).

Animation `areqdyn.mp4` Animation showing the temporal evolution of principal stress axes due to the 2001 Arequipa earthquake. The stress field is calculated at half-second intervals for the first 175 seconds of the event. Symbols are as described for Animation `antodyn.mp4`.

BIBLIOGRAPHY

Cahill, T. A., and B. L. Isacks (1992), Seismicity and shape of the subducted Nazca Plate, *Journal of Geophysical Research*, *97*(B12), 17,503–17,529.

Comte, D., and M. Pardo (1991), Reappraisal of great historical earthquakes in the northern Chile and southern Peru seismic gaps, *Natural Hazards*, *4*(1), 23–44, doi:10.1007/BF00126557.

Comte, D., M. Pardo, L. Dorbath, C. Dorbath, H. Haessler, L. Rivera, A. Cisternas, and L. Ponce (1994), Determination of seismogenic interplate contact zone and crustal seismicity around Antofagasta, northern Chile using local data, *Geophysical Journal International*, *116*(3), 553–561, doi:10.1111/j.1365-246X.1994.tb03279.x.

Cotton, F., and O. Coutant (1997), Dynamic stress variations due to shear faults in a plane-layered medium, *Geophysical Journal International*, *128*, 676–688, doi:10.1111/j.1365-246X.1997.tb05328.x.

Husen, S., E. Kissling, E. Flueh, and G. Asch (1999), Accurate hypocentre determination in the seismogenic zone of the subducting Nazca Plate in northern Chile using a combined on-/offshore network, *Geophysical Journal International*, *138*(3), 687–701, doi:10.1046/j.1365-246x.1999.00893.x.

Maerten, F., P. Resor, D. D. Pollard, and L. Maerten (2005), Inverting for slip on three-dimensional fault surfaces using angular dislocations, *Bulletin of the Seismological Society of America*, *95*(5), 1654–1665, doi:10.1785/0120030181.

Menke, W. (1984), *Geophysical Data Analysis: Discrete Inverse Theory*, 285 pp., Academic Press, New York.

Nishenko, S. P. (1985), Seismic potential for large and great interplate earthquakes along the Chilean and southern Peruvian margins of South America: A quantitative reappraisal, *Journal of Geophysical Research*, *90*(B5), 3589–3615.

Okada, Y. (1985), Surface deformation due to shear and tensile faults in a half-space, *Bulletin of the Seismological Society of America*, *75*(4), 1135–1154.

Okada, Y. (1992), Internal deformation due to shear and tensile faults in a half-space, *Bulletin of the Seismological Society of America*, *82*(2), 1018–1040.

Oleskevich, D. A., R. D. Hyndman, and K. Wang (1999), The updip and downdip limits to great subduction earthquakes: Thermal and structural models of Cascadia, south Alaska, SW Japan, and Chile, *Journal of Geophysical Research*, *104*(B7), 14,965–14,991, doi:10.1029/1999JB900060.

Pritchard, M. E., C. Ji, and M. Simons (2006), Distribution of slip from 11 $M_w > 6$ earthquakes in the northern Chile subduction zone, *Journal of Geophysical Research*, *111*, B10302, doi:10.1029/2005JB004013.

Pritchard, M. E., E. O. Norabuena, C. Ji, R. Boroschek, D. Comte, M. Simons, T. Dixon, and P. A. Rosen (2007), Geodetic, teleseismic, and strong motion constraints on slip from recent southern Peru subduction zone earthquakes, *Journal of Geophysical Research*, *112*, B03307, doi:10.1029/2006JB004294.

Simons, M., Y. Fialko, and L. Rivera (2002), Coseismic deformation from the 1999 M_w 7.1 Hector Mine, California, earthquake as inferred from InSAR and GPS observations, *Bulletin of the Seismological Society of America*, *92*(4), 1390–1402, doi:10.1785/0120000933.

Tichelaar, B. W., and L. J. Ruff (1991), Seismic coupling along the Chilean subduction zone, *Journal of Geophysical Research*, *96*(B7), 11,997–12,022.